Epitaxial heterostructures of topological insulators: band engineering and electronic transport

DISSERTATION

zur Erlangung des
Doktorgrades der Naturwissenschaften (Dr. rer. nat.)
der Fakultät für Physik der Universität Regensburg

vorgelegt von

Thomas Mayer

aus Ingolstadt

2021

Das Promotionsgesuch wurde eingereicht am 21.04.2021.

Die Arbeit wurde angeleitet von Prof. Dr. Dominique Bougeard.

Contents

Contents

II   Epitaxy and methods

III   Experimental results

Contents

IV

1

Introduction and motivation

Two of the most fundamental concepts in condensed matter physics are the band theory of crystalline solids and Landau's classification of phases of matter. The former, among other aspects, allows the understanding of the electronic properties of insulators, conductors, and semiconductors [1] and hence lies at the heart of the vast progress of solid state theory and technological breakthroughs of the last century. The latter, based on the seminal work of Lev Landau, provides a universal theoretical framework to describe most phase transitions of matter by means of spontaneous breaking of symmetries specified by an order parameter [2, 3]. For example, in magnetic materials, the net magnetization serves as the order parameter distinguishing the low-symmetry ferromagnetic from the high-symmetry paramagnetic state, being non-zero (ferromagnetic) below and zero (paramagnetic) above the critical Curie temperature T_C [4]. The discovery of the integer quantum Hall effect (IQHE) in 1980 [5], however, did not only earn it's discoverer, Klaus von Klitzing, the Nobel price 1985, but also challenged both of these highly successful concepts and triggered an extension of the theories with notions of topology. Neither does the quantum Hall state break any symmetries, nor does it show electronic properties described by the, at the time, established band theory [6]. Already a few years earlier, in 1972, J. Michael Kosterlitz and David J. Thouless had proposed a *topological* phase transition in two-dimensional systems that does not break any symmetries [7, 8]. In a later work, Thouless et al. were able to connect the quantized Hall response of the quantum Hall state to a topological invariant [9]. This not only explained the quantization, but also the precise values of the Hall conductance even under perturbations. Moreover, the topological approach to the description of the IQHE allowed Duncan Haldane to conceptualise this exotic state of matter in the absence of an external magnetic field. In his 1988 paper, he showed that a quantized, non-zero Hall conductance can emerge without the system's band spectrum forming Landau levels: only the breaking of time reversal symmetry (TRS) was a necessary factor in his model [10]. For their pioneering contributions to the implementation of topological concepts to condensed matter theory,

Kosterlitz, Thouless, and Haldane were awarded the Nobel price of physics in 2016. By then, their groundwork had lead to the emergence of a whole research field of topological band theory. After Charles Kane and Gene Mele had extended Haldane's model and discovered a new and different topological phase for two-dimensional systems with unbroken time-reversal symmetry in 2005 [11, 12] - the quantum spin Hall insulator - this non-trivial state was quickly theoretically predicted [13] and experimentally verified [14] in HgCdTe quantum wells. In contrary to the topological class of the IQHE with broken TRS, this new phase could be generalized to a non-trivial, three-dimensional state, the three-dimensional topological insulator (TI) [15–17]. In theory, the insulating bulk of a TI is wrapped by a conductive surface layer with a Dirac-like, linear dispersion that is topologically protected by TRS against disorder and non-magnetic perturbations. These topological surface states (TSS) furthermore feature a helical spin texture, where the spin of a carrier is perpendicularly locked to its momentum [4, 6].

Besides their fundamental meaning to the progress of theoretical and experimental solid state physics, the unique characteristics of TIs inspire a variety of possible technological applications. For example, the topological protection of the surface states drives ambitions to combine TIs with superconductors in the search for Majorana fermions, hence aiming to realize new architectures for robust quantum computing [18–22]. Due to the spin-momentum locking (SML) of surface charge carriers, TIs are moreover promising candidates for implementation in novel concepts of electronics and spintronics. On the one hand, TIs could provide an ideal platform for the generation of spin currents for spintronic operations. Furthermore, SML leads to a suppression of direct backscattering of electrons, reducing the resistance for electronic transport of the TSS and therefore possibly opening a path to electronic devices with lower power consumption [23–26].

A promising candidate to realize these applications is the family of $(Bi_{1-x}Sb_x)_2(Te_{1-y}Se_y)_3$ (BSTS) compounds, where a non-trivial topology was experimentally verified soon after the theoretical prediction of three-dimensional topological insulators [27]. However, especially concerning the desired exploitation of the unique TSS physics for electronic transport, this material class poses a major challenge: imperfections in the crystal lead to an unintentional doping of the compound, causing parasitic bulk conduction that can easily mask all effects stemming from the topological surface states. Many strategies have been employed in literature to overcome this issue. Successful compensation of unintentional dopants has for example been achieved in single-crystalline Bi-Sb-Te-Se solid solutions grown by the Bridgman technique, resulting in suppressed bulk conduction and high-mobility surface dominated transport in samples exfoliated from large bulk crystals [28]. However, considering thin crystalline films, *molecular beam epitaxy* (MBE) provides crucial advantages for many of the conceivable experimental and technological applications. For example, MBE offers quick adjustment of alloy stoichiometries, precise control of sample thickness down to single layers, and the capability of in-situ preparation of hybrid devices with well defined interfaces, all while opening a way to wafer-size scalability. However, sample quality has lagged significantly compared to other crystal growth methods and while the issue of parasitic bulk conduction due to structural disorder has not been conclusively solved for MBE grown samples, research especially concerning

the promising quaternary alloy BSTS, has stalled in recent years. This provides the main motivation for this thesis. In our investigations, we aim to employ methods of band structure engineering to enable the epitaxial preparation of high quality quaternary BSTS thin films with minimized parasitic bulk conduction. On the one hand, $(Bi_{1-x}Sb_x)_2(Te_{1-y}Se_y)_3$ directly allows a tuning of the band structure by varying the stoichiometric parameters x and y. A further method to modify the electronic properties of a sample is the creation of p-n-type heterostructures of thin TI layers with excess dopants of opposite charge, where compensation processes lead to an intrinsic band bending. Combining these two band structure engineering techniques lies at the heart of the results discussed in this work.

To present our investigations this thesis is structured as follows:
Part I introduces the fundamental theoretical concepts necessary for a deep understanding of the obtained experimental results. Therein, chapter 2 provides an overview of topological aspects in condensed matter theory. Starting from mathematical examples, the chapter demonstrates the connection between topology and electronic band structure, before introducing the $(Bi_{1-x}Sb_x)_2(Te_{1-y}Se_y)_3$ family as three-dimensional topological insulators.
Then, chapter 3 provides an overview of the theory of electronic transport. Including classical as well as quantum mechanical effects, the chapter lays the theoretical foundation for analyzing and interpreting the electronic transport measurements performed in this thesis.

Part II is dedicated to the methods employed to realize the experiments discussed in this work. After chapter 4 introduces the molecular beam epitaxy cluster and the growth procedure utilized to prepare the topological insulator thin film samples, chapter 5 considers the performed measurement methods. Besides additional sample characterization tools, the focus of this chapter lies on the Hall-bar patterning process, the four-point electrical transport technique and the setups used to perform the experiments.

Part III presents the experimental results of this thesis that cover three central aspects. The first is discussed in chapters 6 and 7. Therein, chapter 6 summarizes the findings of preliminary work that proved to be crucial for the development of high quality quaternary $(Bi_{1-x}Sb_x)_2(Te_{1-y}Se_y)_3$ alloys. Starting from the ternary $(Bi_{1-x}Sb_x)_2Te_3$, where direct evidence for the presence of topological surface states will be provided, we proceed with discussing first results on quaternary films and demonstrate common issues in the epitaxial preparation of such samples. As a crucial step towards the improvement of the quaternary BSTS epitaxy, the chapter presents the benefits of implementing a thin Bi_2Se_3 (BS) seed layer before the subsequent BSTS growth. However, these advantages for sample preparation come at the cost of a potentially large parasitic contribution to the bulk conductivity introduced by the Bi_2Se_3 layer.
A solution to this challenge is presented in chapter 7, where the two above mentioned

methods of band structure engineering will be combined to suppress the detrimental effect of the BS layer and to aim towards an overall minimized bulk conductivity: the concept discussed in this chapter uses the influence of the BSTS stoichiometry on its electronic properties to create layers with a slight surplus of excess acceptors. Subsequently, band bending effects are created within a heterostructure of the p-type BSTS with the intrinsically n-type BS layer that causes compensation of unintentional bulk dopants. The chapter will demonstrate this using a systematic magnetotransport study with respect to the individual thicknesses of the heterostructure constituents.

An important tool to gain information on the underlying processes that contribute to the electronic transport of such topological insulator samples is the analysis of the modulation of the electrical resistance by applying external magnetic fields. As the second key aspect of our results, a deep analysis of the magnetoresistance will be given in chapter 8, where a rich field of different effects will be uncovered, including classical contributions from the bulk states as well as two types of effects stemming from quantum mechanical interferences.

The detailed investigations of chapters 7 and 8 not only present some of the central results towards reaching the objectives of this thesis and help to provide a deeper understanding of the electronic properties of our TI samples, but also identify ongoing challenges for future sample design. As the third central aspect of this thesis, a first approach aiming to optimize the p-n heterostructure concept will be discussed in chapter 9.

Finally, chapter 10 provides a conclusion of this thesis, where the status quo of our research on epitaxial bismuth-based topological insulators will be summarized and a broad spectrum of future perspectives based on the results of this work will be presented.

Theoretical fundamentals

<div style="text-align: right; font-size: 4em;">2</div>

Introduction to topological aspects in condensed matter theory

All of the experimental work presented in this thesis aims to investigate or utilize the unique physics of topological insulators. While the theoretical concepts behind this exotic phase of matter are complex, TIs still just pose the tip of the iceberg of a vast field of topological band theory and represent only one example of a topologically non-trivial class. In contrary to the Landau formalism, topological phases are not classified by spontaneous breaking of symmetries, but by global quantities, *topological invariants*, that are not changed by smooth variations of the system and allow a definition of separated topological equivalence classes. The literature concerning concepts of topology in condensed matter theory in general and topological insulators in particular is expansive. Detailed elaborations can, for example, be found in Refs. [4, 6, 29–33]. The following will provide a brief introduction. Starting from basic principles such as the Berry phase and topological examples from mathematics, the manifestation of topological notions in condensed matter physics will be discussed. Then, the theory of topological insulators is presented with a particular emphasize on the family of bismuth-based 3D TIs that is experimentally investigated in this thesis.

2.1 Basic principles

2.1.1 Topology in mathematics

Topology is a branch of mathematics that classifies mathematical spaces in terms of homeomorphic functions [34]. A function $f : X_1 \rightarrow X_2$ between two topological spaces X_1 and X_2 is homeomorphic, if it is continuous and has a continuous inverse function $f^{-1} : X_2 \rightarrow X_1$. If such a function exists, the sets X_1 and X_2 are *topologically equivalent* with respect to f. In simplified terms: two spaces, or, more intuitively, two geometrical objects are topologically equivalent, if they can be transformed into each other by a continuous deformation. One of the most common examples is shown in Fig. 2.1 a).
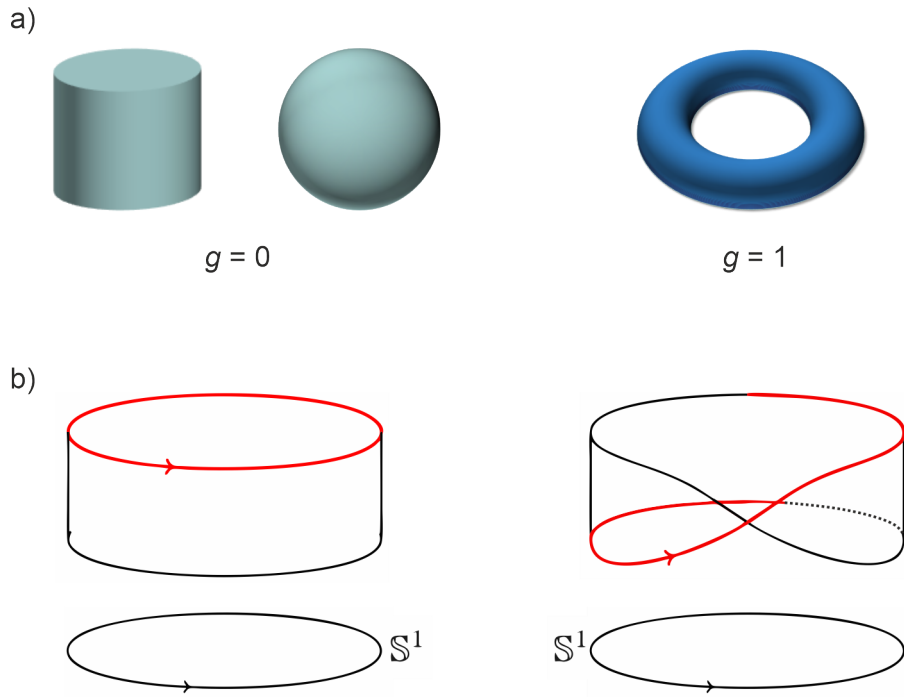
Figure 2.1: Examples of topological classification in mathematics. a) Cylinder and sphere have genus $g = 0$ and are topologically equivalent. The torus has $g = 1$ and belongs to a different equivalence class. b) Example with a different underlying topological classification. The cylinder (left) is topologically not equivalent to the Möbius strip (right) over the circle $\mathbb{S}^1$. Panels b) adapted from Ref. [32].

Comparing the three depicted geometrical shapes, the cylinder, the sphere, and the torus, provides a straightforward illustration of a topological classification. Intuitively, a cylinder can be continuously deformed into a sphere and vice versa. The quantity that is conserved under this homeomorphic transformation and that uniquely defines the topological class is the topological invariant. In the given example, the considered invariant is the *genus* of the two-dimensional surfaces that can be understood as the number of holes within the three-dimensional shapes when assuming shapes without boundaries. Cylinder and sphere then share a genus of $g = 0$ and are therefore topologically equivalent in this regard. In contrast, the torus has $g = 1$ and belongs to a different equivalence class, since adding a hole to the shape does not represent a continuous transformation. More precisely, for a compact, orientable, and boundary-less surface, or in general, Riemannian manifold M, the genus can be calculated by the simplified Gauss-Bonnet-theorem [35]:

$$\int_M K \, da = 4\pi(g - 1). \tag{2.1}$$

Here, da is an infinitesimal area element and K the Gaussian curvature. K has dimension of inverse area and is given by the product of the principal curvatures κ_1 and κ_2 that are the maximal and minimal curvatures at any given point of the surface. From this simple example, two conclusions can be drawn that will become essential in the context of topological band theory: first, Eq. (2.1) shows the robustness of the topological invariant. The integral of the Gaussian curvature over the manifold is proportional to an integer that is constant for any shape within the same equivalence class and is hence unaffected by external deformation of the cylinder to a sphere, or to any other shape with no holes. The respective changes of the principal curvatures always cancel in the integral and the topological class stays unchanged. Second, the example shows that a topological treatment of a system allows to extract global information from the local geometry. The number of holes in the shape can be calculated from its local curvature.

At this point, it is important to emphasize that categorizing shapes with respect to their genus is only one example of a topological classification. A mathematically different instance of a topological classification is displayed in Fig. 2.1 b), where the topology of so-called fiber bundles over a circular base manifold $\mathbb{S}^1$ is illustrated. The cylinder (left) is trivial, whereas the twisted Möbius strip (right) is non-trivial and no continuous transition between the two exists. The mathematical details of this topological description can be found in Ref. [32]. The important aspect here is the identification of the existence of different kinds of topological classifications with varying underlying topological invariants, since also in condensed matter theory different types of topologically non-trivial material classes exist.

2.1.2 Berry-phase, -connection, and -curvature of adiabatic processes

A second basic notion that will be important in the context of a topological classification of material systems is the Berry phase, introduced as a "geometrical phase" by Michael V. Berry in Ref. [36]. Already in the early 1980's, and therefore not in the context of topological band theory that was developed later, Berry considered a quantum mechanical system to acquire a geometrical phase in addition to the conventional dynamical phase, when a state of the system is adiabatically transported along a closed path C. A common classical example unrelated to quantum mechanics, but illustrating the underlying concept of a geometrical phase, is the parallel transport of a vector on a curved real space surface, e.g. a sphere. When a vector starting at time $t = 0$ at point r_0 at the surface travels along a closed path C enclosing the area $S > 0$ and returns to r_0 at $t = t^*$, it will point into a different direction than at $t = 0$ [37]. The mathematical expressions for the quantum mechanical Berry phase and the associated Berry connection and curvature can be straightforwardly derived, mainly following Refs. [4, 38].
Consider a Hamiltonian $H(\mathbf{R}(t))$ that depends on a set of arbitrary time-dependent parameters $\mathbf{R}(t) = (R_1, R_2, R_3, ...)$. With the n-th eigenvalue $E_n(\mathbf{R}(t))$ and respective eigenvector $|n(\mathbf{R}(t))\rangle$, the Schrödinger equation of the system is given by

$$H(\mathbf{R}(t)) |n(\mathbf{R}(t))\rangle = E_n(\mathbf{R}(t)) |n(\mathbf{R}(t))\rangle .\qquad(2.2)$$

Following the adiabatic theorem [39], a system starting in the non-degenerate n-th eigenstate at time $t = 0$ will remain in the n-th eigenstate, when the parameters $\mathbf{R}(t)$ are varied slowly along the path C.[1] The eigenvector $|n(\mathbf{R})\rangle$ is defined up to a phase $\theta(t)$ that can vary during the adiabatic transport in parameter space. The n-th eigenstate of the system in a generalized form thus reads

$$|\psi(t)\rangle = e^{-i\theta(t)} |n(\mathbf{R}(t))\rangle ,\qquad(2.3)$$

and follows the time evolution

$$H(\mathbf{R}(t)) |\psi(t)\rangle = i\hbar \frac{d}{dt} |\psi(t)\rangle .\qquad(2.4)$$

Inserting the equations (2.2) and (2.3) into Eq. (2.4) gives

$$e^{-i\theta(t)} E_n(\mathbf{R}(t)) |n(\mathbf{R}(t))\rangle = i\hbar \frac{d}{dt} e^{-i\theta(t)} |n(\mathbf{R}(t))\rangle ,\qquad(2.5)$$

and performing the derivative on the right hand side leads to

$$E_n(\mathbf{R}(t)) |n(\mathbf{R}(t))\rangle = \hbar \left(\frac{d}{dt}\theta(t) \right) |n(\mathbf{R}(t))\rangle + i\hbar \frac{d}{dt} |n(\mathbf{R}(t))\rangle .\qquad(2.6)$$

---

[1]What is considered "slow" in this context depends on the energy gap of the n-th to the nearest other eigenstate of the system.

Calculating now the scalar product with $\langle n(\mathbf{R}(t))|$ on both sides of the equation under the assumption of a normalized n-th eigenvector with $\langle n(\mathbf{R}(t))|n(\mathbf{R}(t))\rangle = 1$ and after some rearranging finally

$$\hbar \frac{d}{dt}\theta(t) = E_n(\mathbf{R}(t)) - i\hbar \langle n(\mathbf{R}(t))| \frac{d}{dt} |n(\mathbf{R}(t))\rangle \tag{2.7}$$

is obtained. Thus, the solution for $\theta(t)$ is given by

$$\theta(t) = \underbrace{\frac{1}{\hbar} \int_0^t E_n(\mathbf{R}(t'))dt'}_{\text{dynamical phase}} - \underbrace{i \int_0^t \langle n(\mathbf{R}(t'))| \frac{d}{dt'} |n(\mathbf{R}(t'))\rangle \, dt'}_{\text{Berry phase}}. \tag{2.8}$$

The first term of Eq. (2.8) represents the aforementioned conventional dynamical phase that is connected to the energy eigenvalues of the system, the second term is the Berry phase. In contrast to the dynamical term that explicitly depends on time, such an explicit time dependence can be removed from the Berry phase, which will be defined below as γ_n, by

$$\gamma_n = i \int_0^t \langle n(\mathbf{R}(t'))| \frac{d}{dt'} |n(\mathbf{R}(t'))\rangle \, dt'$$

$$= i \int_0^t \langle n(\mathbf{R}(t'))| \nabla_{\mathbf{R}} |n(\mathbf{R}(t'))\rangle \frac{d\mathbf{R}}{dt'} dt' \tag{2.9}$$

$$= i \oint_C \langle n(\mathbf{R})| \nabla_{\mathbf{R}} |n(\mathbf{R})\rangle \, d\mathbf{R}$$

For the last equality the parameters $\mathbf{R}(t)$ are assumed to travel a closed path C in a time t^* such that $\mathbf{R}(t = 0) = \mathbf{R}(t = t^*)$. The Berry phase is thus expressed as a circuit integral over C and does hence only depend on the path taken, not on the elapsed time, reasoning the name "geometrical phase".[2] From Eq. (2.9) the expressions for the Berry connection $\mathbf{A}_n(\mathbf{R})$ and the Berry curvature $\mathbf{B}_n(\mathbf{R})$ can be directly defined:

$$\gamma_n = \oint_C i \langle n(\mathbf{R})| \nabla_{\mathbf{R}} |n(\mathbf{R})\rangle \, d\mathbf{R} \tag{2.10a}$$

$$\equiv - \oint_C \mathbf{A}_n(\mathbf{R})d\mathbf{R} \tag{2.10b}$$

$$= \int_S \mathbf{B}_n(\mathbf{R})d\mathbf{S}. \tag{2.10c}$$

---

[2] Note that the Berry phase γ_n is real, since $\langle n(\mathbf{R})| \nabla_{\mathbf{R}} |n(\mathbf{R})\rangle$ is purely imaginary. See Ref. [4] for proof.

The last equality is obtained by means of Stokes' theorem, where $\mathcal{S}$ is the surface enclosed by the path C. Berry connection and curvature are thus given by

$$\mathbf{A}_n(\mathbf{R}) = -i \langle n(\mathbf{R}) | \nabla_{\mathbf{R}} | n(\mathbf{R}) \rangle, \tag{2.11a}$$

$$\mathbf{B}_n(\mathbf{R}) = \nabla_{\mathbf{R}} \times \mathbf{A}_n(\mathbf{R}). \tag{2.11b}$$

2.2 Integer Quantum Hall effect in a topological context

As mentioned in the introduction of this thesis, the quantum Hall effect, experimentally discovered by von Klitzing et al. in 1980 [5], challenged conventional band theory. It was observed that the low-temperature Hall conductivity σ_{xy} of a two-dimensional, non-interacting electron system in the presence of a strong perpendicular magnetic field B is quantized in steps of

$$\sigma_{xy} = \nu \cdot \frac{e^2}{h}, \tag{2.12}$$

with the integer filling factor $\nu \in \mathbb{Z}$. In the "conventional" approach, the appearance of chiral edge modes, that subsequently lead to the observed quantized values, are described in the context of a formation of Landau levels of the energy spectrum and taking into account disorder and the edge potential at the sample boundaries. The topological nature of the IQHE was revealed in 1982 by **T**houless, **K**ohmoto, **N**ightingale, and den **N**ijs in deriving their **TKNN** equation in Ref. [9]. Several years later, in 1988, Duncan Haldane realized in Ref. [10] that the IQHE effect is part of a whole class of topologically non-trivial systems, the so-called Chern insulators. Below, the key concepts will be briefly introduced.

2.2.1 TKNN equation: connecting IQHE, Berry phase, and topology

Before coming to the TKNN equation, let us reiterate the formulation of the Berry phase and the connected entities introduced in Sec. 2.1.2 in the context of Bloch electrons moving through a crystal lattice. The following mainly follows Refs. [40, 41].
Consider a periodic rectangular lattice within the x-y-plane with lattice constant a in x- and b in y-direction. The energy spectrum forms a band structure, where the energy of each band of index n depends on the quasimomentum $\mathbf{k} = (k_x, k_y)$, which is the wave vector in the according Bloch function:

$$|\psi_{n\mathbf{k}}(\mathbf{r})\rangle = e^{i\mathbf{k}\mathbf{r}} |u_{n\mathbf{k}}(\mathbf{r})\rangle. \tag{2.13}$$

Here, $\mathbf{r}$ is the positional vector and the function $u_{n\mathbf{k}}(\mathbf{r})$ parameterizes the lattice periodicity. The possible values for $\mathbf{k}$ are $-\pi/a < k_x \leq \pi/a$ and $-\pi/b < k_y \leq \pi/b$, which spans

the periodic Brillouin zone (BZ) in k-space. Important for the concept of a Berry phase is the existence of a continuous parameter space. The periodicity of the BZ in x- and y-direction, which gives it the shape of a torus, represents such a parameter space, where a state can travel a closed path. Thus, when a state $\psi_{n\mathbf{k}}$ in band n at some wave vector $\mathbf{k}$ is swept through the entire BZ on a closed path, it acquires a Berry phase.[3] This is associated with a Berry connection $\mathbf{A}_n$ and a Berry curvature $\mathbf{B}_n$ of

$$\mathbf{A}_n(\mathbf{k}) = -i \langle u_n\mathbf{k}| \nabla_{\mathbf{k}} |u_n\mathbf{k}\rangle , \tag{2.14a}$$

$$\mathbf{B}_n(\mathbf{k}) = \nabla_{\mathbf{k}} \times \mathbf{A}_n(\mathbf{k}) = -i \left\langle \frac{\partial u_{n\mathbf{k}}}{\partial k_y} \middle| \frac{\partial u_{n\mathbf{k}}}{\partial k_x} \right\rangle + i \left\langle \frac{\partial u_{n\mathbf{k}}}{\partial k_x} \middle| \frac{\partial u_{n\mathbf{k}}}{\partial k_y} \right\rangle . \tag{2.14b}$$

With this the connection between the Hall conductivity in the IQHE regime and the Berry phase can be illustrated via the TKNN equation. In Ref. [9], Thouless et al. considered a two-dimensional system of non-interacting electrons in a perpendicular magnetic field, where the Fermi energy is located in a gap between two bands. Summing over all filled bands n, they theoretically showed that the Hall conductivity can be derived as

$$\sigma_{\mathrm{xy}} = \frac{e^2}{2\pi h} \sum_n \int_{\mathrm{BZ}} d^2k \ \ i \left\langle \frac{\partial u_{n\mathbf{k}}}{\partial k_y} \middle| \frac{\partial u_{n\mathbf{k}}}{\partial k_x} \right\rangle - i \left\langle \frac{\partial u_{n\mathbf{k}}}{\partial k_x} \middle| \frac{\partial u_{n\mathbf{k}}}{\partial k_y} \right\rangle . \tag{2.15}$$

The argument of the integral in Eq. (2.15) precisely coincides with the negative of the Berry curvature $\mathbf{B}_n$ provided in Eq. (2.14b). Importantly, it can be shown that integrating this over the Brillouin zone yields an integer multiple of 2π and it follows

$$\sigma_{\mathrm{xy}} = -\frac{e^2}{h} \sum_n m_n, \tag{2.16}$$

where m_n is the integer *Chern number* corresponding to the band with index n. Thus, the total Chern number of the system is the sum of m_n over all filled bands, which equals the filling factor ν in Eq. (2.12). This illustrates the topological nature of the IQHE, as the TKNN equation (2.15) to calculate the Hall conductivity mirrors the form of the Gauss-Bonnet theorem introduced in Eq. (2.1) with the filling factor ν taking the place of the genus as the integer invariant. Like the genus does not change by continuous deformations of the geometrical shape it corresponds to, the filling factor in the IQHE is invariant under smooth transformations of the underlying Hamiltonian. This explains the universally observed quantized Hall conductances in the IQHE regime showing precisely the same values independent of the used material system and robust against external influences.

---

[3]Under the additional assumptions that the Fermi energy of the system resides between bands and the electrons of the system are non-interacting
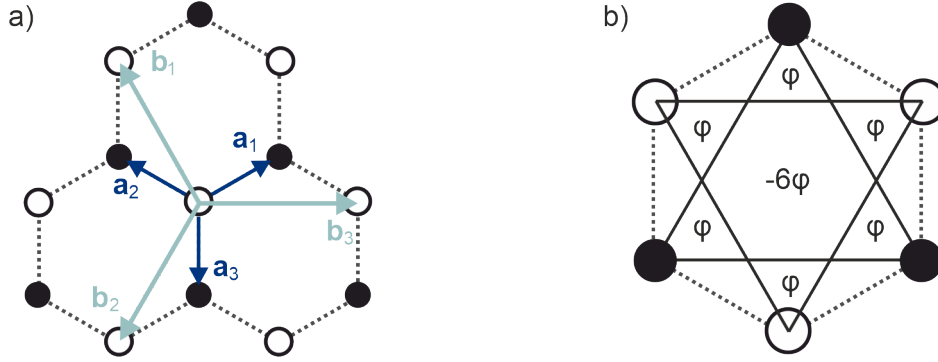
Figure 2.2: Illustrations for Haldane's model. a) Hexagonal lattice spanned by the vectors $\mathbf{a}_i$ and $\mathbf{b}_i$ consisting of two triangular sublattices (solid and open circles). b) Possible distribution of magnetic fluxes φ through one hexagonal cell, such that the total flux through the cell vanishes. Panels adapted from Ref. [32].

2.2.2 Haldane's model and Chern insulators

The two necessary ingredients for the non-trivial topology, i.e. non-vanishing Chern number and quantized Hall conductance, of the IQHE discussed above are the two-dimensionality of the considered electron system and the presence of an external magnetic field. However, in Ref. [10] Haldane showed that the latter is not necessary to yield a non-zero Chern number and the underlying topological equivalence class can be generalized to a matter of time-reversal symmetry (TRS) breaking.

Haldane's model considers spinless electrons in a two-dimensional hexagonal lattice as shown in Fig. 2.2 a), which is spanned by the vectors $\mathbf{a}_i$ and $\mathbf{b}_i$ and consists of two non-equivalent, triangular sublattices of different atoms identified by solid and open circles, respectively. Following the notation of Ref. [32] the real space Hamiltonian $\mathcal{H}$ of the model is given by

$$\mathcal{H} = t_1 \sum_{\langle i,j \rangle} |i\rangle \langle j| + t_2 \sum_{\langle\langle i,j \rangle\rangle} |i\rangle \langle j| + M \left(\sum_{i \in A} |i\rangle \langle i| - \sum_{j \in B} |j\rangle \langle j| \right). \tag{2.17}$$

Here, $i \in A$ represents a lattice site in sublattice A (solid circles), $j \in B$ in sublattice B (open circles), and $\langle i, j \rangle$ in the first sum and $\langle\langle i, j \rangle\rangle$ in the second sum denote nearest and next nearest hopping, respectively, with hopping probabilities of t_1 and t_2. Moreover, the parameter M defines an on-site energy and has opposite sign for the sublattices, which breaks inversion symmetry. Figure 2.2 b) illustrates a possible allocation of magnetic fluxes φ, such that the total magnetic flux through the hexagonal cell vanishes. However, if such a flux distribution is imposed on the system, an electron acquires an Aharonov–Bohm phase Φ in a next-nearest hopping process, which breaks time-reversal symmetry. Fourier transforming the Hamiltonian of Eq. (2.17) to k-space and including the magnetic fluxes

leads to [32]

$$\hat{H}(\mathbf{k}) = h^\mu(\mathbf{k})\sigma_\mu, \tag{2.18}$$

with $\mu \in \{0, x, y, z\}$, the Pauli matrices σ_μ ($\sigma_0 = \mathbb{1}$), and the $h^\mu(\mathbf{k})$ taking the form of

$$h_0 = 2t_2 \cos(\Phi) \sum_{i=1}^{3} \cos(\mathbf{k} \cdot \mathbf{b}_i), \quad h_z = M - 2t_2 \sin(\Phi) \sum_{i=1}^{3} \sin(\mathbf{k} \cdot \mathbf{b}_i),$$

$$h_x = t_1(1 + \cos(\mathbf{k} \cdot \mathbf{b}_1) + \cos(\mathbf{k} \cdot \mathbf{b}_2)), \quad h_y = t_1(\sin(\mathbf{k} \cdot \mathbf{b}_1) - \sin(\mathbf{k} \cdot \mathbf{b}_2)). \tag{2.19}$$

It can be shown that for specific values of M/t_2 with respect to the Aharonov–Bohm phase, a non-zero Chern number can be obtained, even though no net magnetic field is penetrating the system.

This result essentially renders the IQHE as a part of a topological equivalence class, the so-called Chern insulators, where the breaking of time-reversal symmetry is the necessary ingredient for a non-trivial topology. In the case of the IQHE the external magnetic field is the parameter that breaks TRS. As the filling factor, or more generally the Chern number, can take any integer value, the Chern insulators are said to have $\mathbb{Z}$ topology.

2.3 $\mathbb{Z}_2$ topology of time-reversal symmetry conserving systems

Historically, after the description of the Chern insulators, the breaking of time-reversal symmetry was widely considered to be essential for a condensed matter system to possess non-trivial topology. In 2005, however, C.L. Kane and E.J. Mele theoretically predicted the existence of a non-trivial phase for TRS conserving systems [11, 12], which was a leap for topological band theory. Like Haldane, Kane and Mele used a hexagonal lattice as a 2D model system, but taking into account the electron spin and spin-orbit coupling without requiring the breaking of TRS. Similar to Fig 2.1, where two purely mathematical examples were presented with a different underlying topological description, this new phase is part of a topological class different from the Chern insulators. In two dimensions this class is called *quantum spin Hall insulator* (QSHI). In contrast to the Chern insulator, this topological classification can be generalized to a phase in three dimensions, which was termed *topological insulator* [6].[4] Importantly, whereas the topological invariant in the Chern insulator class can take any integer value $\in \mathbb{Z}$, quantum spin Hall and topological insulators have $\mathbb{Z}_2$ topology, meaning the invariants can only take the values 0 or 1, i.e. trivial or non-trivial.

---

[4]In literature, this nomenclature is not used consistently and the QSHI is also often called "topological insulator". Hence, to emphasize the three dimensionality, often the term "3D topological insulator" is used.

2.3.1 Time-reversal symmetry for spin-$\frac{1}{2}$ particles and Kramers' theorem

Time-reversal symmetry operator

Let the operator that reverses time t be defined as

$$\mathcal{T} : t \to -t. \tag{2.20}$$

Physical quantities can be even or odd under a time-reversal operation. For example, the position operator $\hat{x}$ is even, while the momentum operator $\hat{p}_x$ in x-direction is odd due to the sign reversal of the velocity, i.e.

$$\mathcal{T} \hat{x} \mathcal{T}^{-1} = x, \qquad \mathcal{T} \hat{p}_x \mathcal{T}^{-1} = -p_x. \tag{2.21}$$

For *spinless* particles a form for $\mathcal{T}$ can be easily obtained considering Eq. (2.20) and the canonical commutation relation $[\hat{x}, \hat{p}_x] = i\hbar$ [4]:

$$\mathcal{T} [\hat{x}, \hat{p}_x] \mathcal{T}^{-1} = -[\hat{x}, \hat{p}_x] = -i\hbar. \tag{2.22}$$

Thus, for spinless particles, $\mathcal{T}$ is equal to the complex conjugation operator $\mathcal{K}$.
If now spin is added to the particle, an additional action is required to account for the spin being odd under time reversal. The operator takes the form [4, 32]

$$\mathcal{T} = e^{-i\pi S_y} \mathcal{K}, \tag{2.23}$$

where S_y is the y-component of the Spin operator and the term $e^{-i\pi S_y}$ represents the rotation of the spin by π along the y-axis. Note that the y-axis is arbitrarily chosen by convention and $\mathcal{T}$ of Eq. (2.23) remains proportional to $\mathcal{K}$, since Eq. (2.22) must still hold. For spin-$\frac{1}{2}$ particles, it can be shown that $\mathcal{T}^2 = -1$ [4], which is crucial for the formulation of Kramers' theorem.

Kramers' theorem and time-reversal invariant momenta

An important consequence of the above formulated time-reversal operator for spin-$\frac{1}{2}$ particles is Kramers' theorem, which states that every eigenstate of a Bloch Hamiltonian of a TRS preserving system is at least doubly (and always even number) degenerate.
The Bloch wave function was introduced in Eq. (2.13), where $|u_{n\mathbf{k}}\rangle$ is a cell-periodic eigenstate of the Bloch Hamiltonian $\hat{H}(\mathbf{k})$ with energy $E_{n\mathbf{k}}$ [38]:

$$\hat{H}(\mathbf{k}) |u_{n\mathbf{k}}\rangle = E_{n\mathbf{k}} |u_{n\mathbf{k}}\rangle . \tag{2.24}$$

If the system preserves time-reversal symmetry, it can be shown that [4]

$$\mathcal{T} \hat{H}(\mathbf{k}) \mathcal{T}^{-1} = \hat{H}(-\mathbf{k}), \tag{2.25}$$

such that the time-reversal operation transforms the Hamiltonian at $\mathbf{k}$ to $-\mathbf{k}$ and $\mathcal{T} |u_{n\mathbf{k}}\rangle$
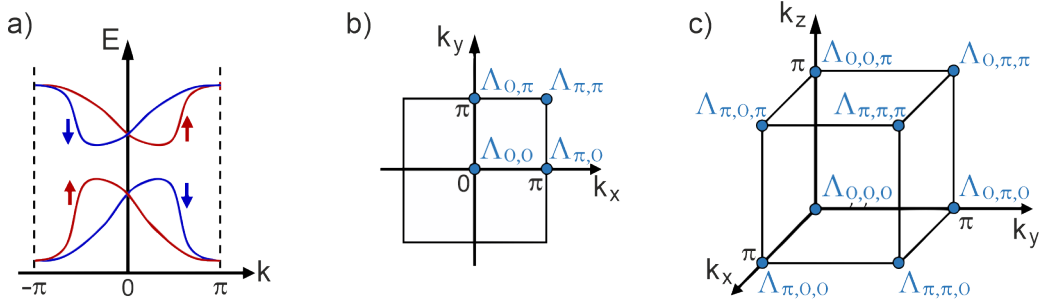
Figure 2.3: a) Kramers pairs of spin-split bands that intersect at the TRIM for $\mathbf{k} = 0$ and $\mathbf{k} = +\pi = -\pi$, where $\mathbf{k} \equiv$ **-k** (assuming a lattice constant of $a = 1$). The red and blue colors and the respective arrows indicate the spin orientation of each band. b) TRIM Λ of a two-dimensional, square Brillouin zone. c) TRIM Λ of a three-dimensional, cube Brillouin zone. Panels adapted from Ref. [38].

is an eigenstate of $\hat{H}(-\mathbf{k})$. It follows [4]

$$\hat{H}(-\mathbf{k})\mathcal{T}\,|u_{n\mathbf{k}}\rangle = \mathcal{T}\,\hat{H}(\mathbf{k})\,\mathcal{T}^{-1}\mathcal{T}\,|u_{n\mathbf{k}}\rangle = \mathcal{T}E_{n\mathbf{k}}\,|u_{n\mathbf{k}}\rangle = E_{n\mathbf{k}}\mathcal{T}\,|u_{n\mathbf{k}}\rangle, \qquad (2.26)$$

where the last identity is justified by $E_{n\mathbf{k}}$ being a real number. Thus, the time-reversed eigenstate $\mathcal{T}\,|u_{n\mathbf{k}}\rangle$ at $-\mathbf{k}$ has the same energy as $|u_{n\mathbf{k}}\rangle$ at $\mathbf{k}$. Furthermore, from the spin-$\frac{1}{2}$ nature of the considered electrons it follows that these two states can not be identical. If $|u_{n\mathbf{k}}\rangle = \mathcal{T}\,|u_{n\mathbf{k}}\rangle$ would be true, then also $\mathcal{T}\,|u_{n\mathbf{k}}\rangle = \mathcal{T}^2\,|u_{n\mathbf{k}}\rangle$ would hold and hence $\mathcal{T}^2 = +1$, which contradicts the above stated property of $\mathcal{T}^2 = -1$ for spin-$\frac{1}{2}$ particles. Subsequently, the eigenstates come in so-called *Kramers pairs* with energies $E_{n\mathbf{k}} = E_{n-\mathbf{k}}$. Neglecting spin-orbit coupling, this degeneracy is provided by the spin degeneracy [6]. An illustrating sketch of the situation in the presence of SOC is displayed in Fig. 2.3 a), where two pairs of spin-split bands are shown that fulfill $E_{n\mathbf{k}} = E_{n-\mathbf{k}}$. Importantly, to still meet this condition, the pairs are required to intersect at $\mathbf{k} = 0$ and $\mathbf{k} = +\pi = -\pi$, as there $\mathbf{k} \equiv$ **-k**. These points within the Brillouin zone are called time-reversal invariant momenta (TRIM) Λ.[5] Figure 2.3 b) shows the four TRIM for a two-dimensional, square Brillouin zone that follow from its periodicity. For a three-dimensional, cube Brillouin zone 8 TRIM can be identified, which is illustrated in Fig. 2.3 c).

2.3.2 Kane-Mele model

Section 2.2.1 considered systems with broken time-reversal symmetry and showed how a non-zero Chern number yields a topologically non-trivial phase. If TRS is preserved, however, the Chern number always vanishes as for the $\mathbf{k}$-dependent Berry curvature $\mathbf{B}_n(-\mathbf{k}) = -\mathbf{B}_n(\mathbf{k})$ holds and subsequently the integral in the TKNN equation (2.15) goes to zero for all filled bands n [4].

---

[5]Here, a lattice constant of $a = 1$ is assumed. If $a \neq 1$ the Brillouin zone is periodic in π/a and the subsequent TRIM coordinates are 0 and $\pm\pi/a$ along the x- or y-axis, respectively.

The model introduced by Kane and Mele in Refs. [11, 12] discussed a different type of topological classification for TRS preserving systems. Like Haldane, they used a two-dimensional hexagonal lattice (see Fig. 2.2), but without magnetic fluxes and with identical atoms on the sublattices A and B [6]. In this graphene-like setup the mass term h_z in Eq. (2.18) vanishes and a trivial insulator is obtained within Haldane's framework. Kane and Mele, however, showed that when the half integer spin of the electrons and spin-orbit coupling is added to the model, a new mass term emerges that does not break TRS. The result is essentially a decoupling into two Haldane models, one for each spin, with Hall conductivities of opposite signs. As σ_{xy} and spin are both odd under time reversal, this does not violate TRS. The total Hall conductivity of the system is zero, but a quantized *spin Hall* conductivity can be observed, hence the name quantum spin Hall insulator (QSHI). Like the Chern insulators, the QSHI phase features gapless edge states that are, however, helical instead of chiral, as the two spin orientations propagate in opposite directions. Furthermore, the topology of the QSHI is determined by a $\mathbb{Z}_2$ invariant, which is sometimes called *spin Chern number* and that can only take the values 0 or 1, corresponding to a trivial or a non-trivial topology. Several mathematical approaches have been reported to obtain this invariant for a given system. An intuitive method, which proved to be a powerful tool to predict non-trivial $\mathbb{Z}_2$ topology in real materials, was introduced by Fu and Kane in Ref. [15] for systems that preserve inversion symmetry additional to TRS.

They showed that under these conditions the invariant η is obtainable via

$$(-1)^\eta = \prod_i^{N_i} \delta_i = \prod_i^{N_i} \prod_m^{N_m} \xi_m(\Lambda_i), \qquad (2.27)$$

where the second product regards the N_m Kramers pairs of occupied bands m and the first product goes over the N_i time-reversal invariant momenta Λ_i. The term $\xi_m(\Lambda_i)$ is the parity eigenvalue of pair m at the TRIM Λ_i and can thus take values of ± 1. In two dimensions the Brillouin zone contains four TRIM, as was exemplarily shown for a square BZ in Fig. 2.3 a) within the previous subsection. Evaluating and multiplying the parity eigenvalues of the occupied states at these points yields a value of ± 1, which subsequently renders the $\mathbb{Z}_2$ invariant as 0 or 1 in Eq. (2.27).

As stated above, Kane and Mele considered graphene for their theoretical model. However, spin-orbit coupling is too weak in graphene to experimentally observe the topologically non-trivial QSHI phase. In Ref. [42] Bernevig et al. proposed CdTe/HgTe/CdTe quantum wells as a suitable material system and the experimental evidence of the QSHI in such structures was found by König et al. in Ref. [43]. CdTe possess a typical semiconductor band structure with s-like (even parity) states at the conduction band edge and p-like states (odd parity) at the valence band edge. In HgTe, on the other hand, the bands invert at the Γ-point in the Brillouin zone, when a critical thickness d_c is exceeded. This changes the sign of the parity at this point, which leads to $\eta = 1$ and hence a non-trivial topology by means of Eq. (2.27).

2.3.3 Three-dimensional topological insulators

To obtain the $\mathbb{Z}_2$ invariant for a three dimensional, time-reversal and inversion symmetric system, the approach introduced in Sec. 2.3.2 of evaluating the parity eigenvalues at the TRIM of the Brillouin zone is directly transferable. An exemplary cubic 3D Brillouin zone containing eight TRIM was shown in Fig. 2.3 b). Within the six two-dimensional planes of the cube with $x = 0$, $x = \pm\pi$, $y = 0$, $y = \pm\pi$, and $z = 0$, $z = \pm\pi$ all symmetries of the 2D Brillouin zone are preserved and hence each plane possess a $\mathbb{Z}_2$ invariant, labeled as x_0, x_1, y_0, y_1, z_0, and z_1. However, i.e. $x_0 x_1 = y_0 y_1 = z_0 z_1$ as each of these pairs contains all eight TRIM and hence the product of the two invariants is respectively identical. This reduces the situation to four independent $\mathbb{Z}_2$ invariants η_0, η_1, η_2, and η_3 [16, 38]. The position of the eight TRIM within the 3D Brillouin zone can be expressed in terms of reciprocal lattice vectors $\mathbf{b}_i$ ($i \in 1, 2, 3$) as $(n_1\mathbf{b}_1 + n_2\mathbf{b}_2 + n_3\mathbf{b}_3)$ with $n_j = 0, 1$. Utilizing this notation, the four invariants are obtained in analogy to Eq. (2.27) by [44]

$$(-1)^{\eta_0} = \prod_{n_j=0,1} \delta_{n_1 n_2 n_3}, \tag{2.28a}$$

$$(-1)^{\eta_{i=1,2,3}} = \prod_{n_{j\neq i}=0; n_i=1} \delta_{n_1 n_2 n_3}. \tag{2.28b}$$

The invariant η_0 in Eq. (2.28a) follows from the product over all eight TRIM and renders the system to a *strong* topological insulator for $\eta_0 = 1$. If $\eta_0 = 0$, the three other invariants, each obtained over four TRIM by Eq. (2.28b), further distinguish the trivial insulator for $(\eta_0, \eta_1, \eta_2) = (0, 0, 0)$ from *weak* topological insulator phases. In such weak topological insulators, which are basically stacked two-dimensional quantum spin Hall insulators, the emerging surface states are not protected by TRS and perturbations like disorder can lift the topologically non-trivial distinction [6, 44].[6]

---

[6]In literature, especially experimental literature, the term "topological insulator" usually refers to the *strong* topological insulator phase, if not further specified. This also applies for the remainder of this thesis.
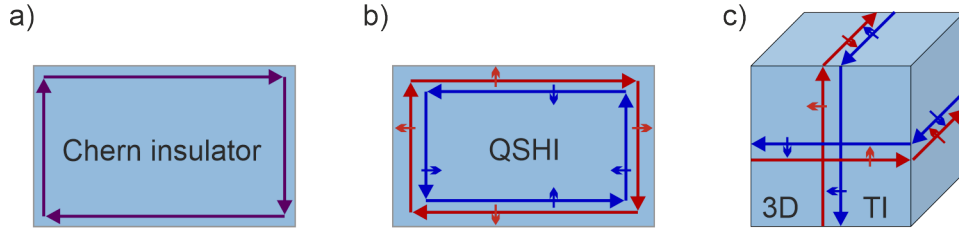
Figure 2.4: Real space sketches of the three topologically non-trivial phases discussed in this chapter. The systems are each assumed to be surrounded by a trivial insulator (e.g. air). a) 2D Chern insulator with Chern number 1 and hence one chiral edge state. b) 2D quantum spin Hall insulator with helical edge states. c) 3D topological insulator with helical surface states.

2.4 Edge and surface states of topologically non-trivial systems

The most important consequence, especially for experimental purposes, of a non-trivial topology of a condensed matter system is the emergence of edge or surface states at the boundary to a topologically trivial material. This is illustrated in Fig. 2.4, where real space sketches of the three topological classes discussed above are shown that are assumed to be surrounded by a trivial insulator (e.g. air). For the two-dimensional Chern insulators (panel a)) the edge channels are spin-degenerate with chiral propagation. The sketch shows one such channel for a system with Chern number 1. As the Chern number can take any integer value, multiple chiral edge states can be present at the systems' boundary, which then leads to a different quantized Hall conductivity.[7] Figure 2.4 b) shows the helical edge states of a two-dimensional quantum spin Hall insulator, where opposite spin electrons have opposite propagation direction. Essentially, the spin-up electrons exhibit a chiral integer quantum Hall effect, while the spin-down electrons exhibit an anti-chiral IQHE [29], where the spin orientation is always perpendicular to the propagation direction as indicated by the small arrows with the respective color in Fig. 2.4 b). As the three-dimensional topological insulator is the 3D equivalent of the QSHI, similar helical surface states span the six surfaces of the cuboid system sketched in Fig. 2.4 c).

The emergence of edge or surface states as a consequence of the topology of a system is also called *bulk-boundary correspondence*, as bulk properties (e.g. band inversion) determine the electronic characteristics at the sample boundaries. This is also responsible for the robustness of these boundary states to external influences, since the topological invariant can not be changed by smooth perturbations that do not affect any of the necessary symmetries.

---

[7]In the classical description of the integer quantum Hall effect, these edge channels are explained by skipping orbits of electrons at the sample boundaries.

Figure 2.5: Illustration of the interface of a non-trivial Chern insulator (Chern number 1) and a trivial insulators at the real space coordinate $y = 0$. The blue dashed line indicates the mass term $m(y)$ changing sign at the boundary. The red solid line illustrates the probability density $|\psi|^2$ of the edge state. Figure adapted from Ref. [32].
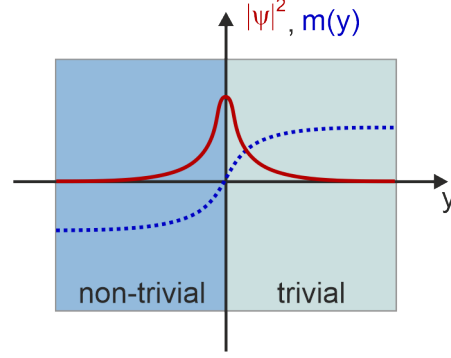
2.4.1 Jackiw-Rebbi model

An intuitive model that illustrates the requirement of a gap closing by edge states is inspired by the findings of Jackiw and Rebbi within 1D field theory in Ref. [45] and discussed in the context of topological condensed matter in Refs. [6, 32, 46].

A band gap in the electronic structure of a condensed matter system is parameterized in the Hamiltonian by a non-zero mass term. This mass term is positive for trivial and negative for non-trivial insulators. Figure 2.5 shows two such materials interfaced at the real space coordinate $y = 0$. Tracing the mass term $m(y)$, which is illustrated in Fig. 2.5 by the blue dashed line, across the boundary of the two systems, it is required to change sign at $y = 0$ and hence $m(0) = 0$, implying a gap closing at the interface. A derivation of the according domain wall state is provided in Ref. [32], where the topologically non-trivial material is assumed to be a Chern insulator with Chern number 1. The Hamiltonian for this setup was provided in Eq. (2.18), which takes the real space form

$$\mathcal{H} = -i\nabla\sigma_{2d} + m(y)\sigma_z = \begin{pmatrix} m(y) & -i\partial_x - \partial_y \\ -i\partial_x + \partial_y & -m(y) \end{pmatrix}. \tag{2.29}$$

After a basis rotation the solution of the Schrödinger equation yields

$$\psi(x, y) \propto e^{ik_x x} \exp\left(-\int_0^y dy' m(y')\right)\begin{pmatrix} 1 \\ 1 \end{pmatrix}, \tag{2.30}$$

with the energy $E(k_x) = E_F + \hbar v_F k_x$. Thus, the state crosses E_F at $k_x = 0$ with positive group velocity v_F and linear dispersion. Furthermore, it is localized at the boundary of the two systems, which is illustrated by the red line in Fig. 2.5 corresponding to the probability density $|\psi|^2$ of the wave function. This edge state hence describes the chiral state sketched in Fig. 2.4 a).
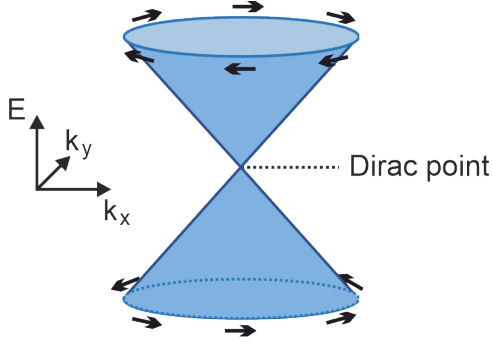
Figure 2.6: Illustration of electronic dispersion of topological surface states in a 3D TI. The helical spin texture is indicated by the black arrows. The spin texture and the crossing at the Dirac point are required by Kramers' theorem.

2.4.2 Surface sates of three-dimensional topological insulators

In its most simple manifestation, a three-dimensional topological insulator possess a spin-orbit coupling induced band inversion at the Γ-point in the Brillouin zone, which leads to a negative Dirac mass in the Hamiltonian. Equivalently to the above discussion, the mass thus has to change sign at the boundary to a trivial insulator. This essentially leads to the emergence of a two-dimensional metal at the surface of the 3D TI. As time-reversal symmetry is preserved in the system, in contrast to the Chern insulator phase, Kramers' theorem has to be fulfilled, which has important consequences for the electronic structure of the surface states. For each state at $\mathbf{k} = (k_x, k_y)$ it requires the existence of a state of the same energy at $-\mathbf{k}$ with opposite spin [6] and moreover forces a twofold degeneracy at the Γ-point in reziprocal space, where $\mathbf{k} = -\mathbf{k} = 0$. The resulting electronic dispersion thus takes the form of a Dirac cone, with the Dirac point at the crossing at $\mathbf{k} = 0$. The simplest form is illustrated in Fig. 2.6, with the dispersion being circular in k_x and k_y and linear in E.[8] The spin texture of these surface states is helical, as indicated in Fig. 2.6 by the black arrows, with the spin oriented perpendicular to $\mathbf{k}$, which is called spin-momentum locking. From the helicity follows that the spin of an electron traveling a closed loop around the Fermi surface must come back to its original orientation, which leads to a non-trivial π Berry phase in the wave function. This π Berry phase leads to a suppression of direct backscattering for surface state electrons, which manifests in quantum transport experiments in a weak anti-localization effect, which will be discussed in more detail in Sec. 3.2. The requirement of Kramers' theorem that the surface states are degenerate at $\mathbf{k} = 0$ moreover prevents a gap opening induced by perturbations that do not break TRS. The surface states are thus topologically protected and hence termed *topological surface states*.

---

[8]Real material systems can show a deviation from the linear dispersion for $\mathbf{k}$ away from the Dirac point, or a deformation of the circular behavior in the k_x-k_y-plane, which is called hexagonal warping [47].

Figure 2.7: Illustration for band inversion in Bi_2Se_3. Starting from the atomic levels (I), a modulation of the states is caused by chemical bonding (II), crystal-field splitting (III), and spin-orbit coupling (IV). In stage (IV) a parity inversion takes place that leads to the non-trivial topology of the material. Figure adapted from Ref. [27].
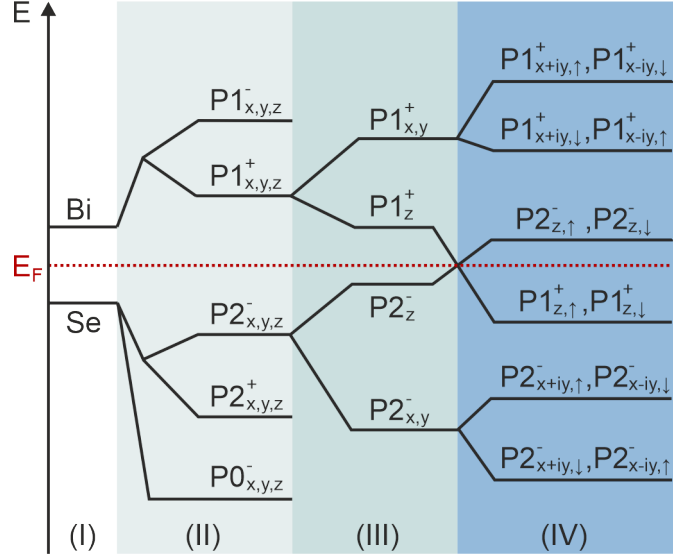
2.5 $(Bi_{1-x}Sb_x)_2(Te_{1-y}Se_y)_3$ materials as three-dimensional topological insulators

In section 2.4.2 the most simple type of a three-dimensional topological insulator was associated with a band inversion at the Γ-point in the Brillouin zone and the subsequent emergence of a single Dirac cone around $\mathbf{k} = 0$ at the surface. Manifestations of such a 3D TI system can be found within the $(Bi_{1-x}Sb_x)_2(Te_{1-y}Se_y)_3$ material family. A standard example is the binary alloy Bi_2Se_3, which was predicted to possess a spin-orbit coupling induced band inversion at the Γ-point and hence a non-trivial topology hosting a single Dirac cone in Ref. [27]. Following the reasoning of this publication, the appearance of a band inversion in Bi_2Se_3 at the Γ-point can be illustrated using Fig. 2.7. The elements bismuth and selenium haven an atomic number $Z_{Bi} = 83$ and $Z_{Se} = 34$, respectively, and an electron configuration of $Bi:[Xe]4f^{14}5d^{10}6s^26p^3$ and $Se:[Ar]3d^{10}4s^24p^4$. Thus, the states near the Fermi surface mainly stem from p-orbitals. Starting from the atomic energy levels, corresponding to stage (I) in Fig. 2.7, stage (II) includes the chemical bonding between Bi and Se atoms, where the subsequent hybridization of the Bi and Se states leads to a splitting of the atomic energy levels into 5 states. These states are labelled as $\left|P1^{\pm}_{x,y,z}\right\rangle$, $\left|P2^{\pm}_{x,y,z}\right\rangle$, and $\left|P0^{-}_{x,y,z}\right\rangle$, where $\pm$ respectively denotes an even (+) or odd parity (-) of the state. A reduction of degeneracy of these states is induced by crystal field splitting, sketched in area (III) of Fig. 2.7, separating the p_z orbital from the $p_{x,y}$ orbitals. Finally, stage (IV) includes spin-orbit coupling, which ultimately leads to a respective crossing of the Fermi level E_F by the $\left|P1^+_{z,\uparrow}\right\rangle$, $\left|P1^+_{z,\downarrow}\right\rangle$ levels and the $\left|P2^-_{z,\uparrow}\right\rangle$, $\left|P2^-_{z,\downarrow}\right\rangle$ states manifesting the parity inversion and hence rendering Bi_2Se_3 as a three-dimensional topological insulator.

Underlying the theoretical predictions for the electronic structure provided in Ref. [27], Bi_2Se_3 could be considered as a close to "ideal" 3D TI system for many types of

experimental applications, as the topologically protected Dirac states reside in the center of a comparatively large bulk band gap, intersected by the Fermi level directly in the Dirac point. The three other binary compounds from the $(Bi_{1-x}Sb_x)_2(Te_{1-y}Se_y)_3$ family, Bi_2Te_3, Sb_2Te_3, and Sb_2Se_3 show less favorable electronic characteristics, with, for example, a smaller bulk energy gap in Sb_2Te_3 or a shift of the Dirac point below the valence band edge for Bi_2Te_3. The compound Sb_2Se_3 is predicted in Ref. [27] to be a trivial insulator, which will play an important role in chapter 9 of the experimental part of this thesis.

Lastly, while especially the prototypical Bi_2Se_3 provides a promising basis for the experimental investigation of three-dimensional topological insulators, an important aspect for all materials from $(Bi_{1-x}Sb_x)_2(Te_{1-y}Se_y)_3$ family is the complex defect chemistry. Naturally occurring atomic vacancies and anti-sites within the crystal lattice can lead to large unintentional and hardly controllable doping of the material. In Bi_2Se_3, for example, this causes a shift of the Fermi level from the theoretically predicted position within the bulk energy gap to the bulk conduction band, preventing the full exploitation of the unique physics of the topological surface states. This motivates the concept of band structure engineering, which lies at the core of the experimental investigations presented in this thesis. Expanding, for example, the $(Bi_{1-x}Sb_x)_2(Te_{1-y}Se_y)_3$ material from a pure binary compound to a tertiary or quaternary alloy largely influences all aspects of the electronic structure of the 3D TI and can particularly yield a compensation of unintentional bulk doping. The same goal can be approached by creating TI heterostructures of opposite excess dopant type, aiming to create a depletion zone within the bulk of the TI material. More details on such band structure engineering approaches and the obtained experimental results, will be discussed in part III of this thesis.

3

Electronic transport

The key instrument to characterize the topological insulator samples investigated in this thesis are electronic transport experiments. In such measurements a complex behavior of a typical TI sample can be expected, as transport can be mediated by a mixture of different kinds of bulk and possible surface state contributions that moreover underlie influences of classical as well as quantum mechanical effects. Thus, to provide a thorough analysis of the experimental data presented in this thesis, a good understanding of the underlying theory of electronic transport in solids is necessary, for which the following sections aim to provide a basis. First, section 3.1 will discuss the semi-classical Drude theory of electronic transport of metals and semiconductors, especially in terms of their dependencies on temperature and external magnetic fields. The presented overview mainly follows Refs. [48–50], where extensive reviews of the topic can be found. Then, section 3.2 will consider the influence of quantum interference effects. After introducing the notion of phase coherence of electronic wave functions, possible quantum corrections to a systems' conductivity induced by weak anti-localization and electron-electron interactions will be discussed.

3.1 Semi-classical description

In a semi-classical approach to describe the electronic transport in solids, the conduction electrons are modelled as packets of superimposed Bloch waves moving through the periodic potential of the crystal lattice. In an ideal crystal at $T = 0\,\mathrm{K}$, the packets travel unimpeded. Crystal defects, (charged) impurities, and phonons at non-zero temperature, however, lead to scattering of the electrons. The mean free path ℓ is defined as the distance traveled by the electrons between two scattering events and is connected to the respective mean free time τ via $\ell = v_{\mathrm{th}}\tau$, with the average thermal velocity of the electron v_{th}. Without external forces, the electrons move randomly within the material and no current is observed. Biasing the system with an electric field $\mathbf{E}$, however, creates a net
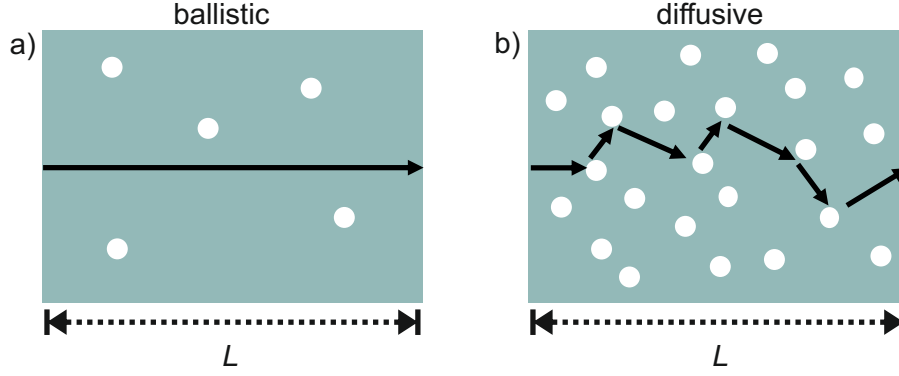
Figure 3.1: Illustration of transport regimes in a system of size L. a) Ballistic transport for $\ell \gg L$. b) Diffusive transport for $\ell \ll L$

transport of electrons where the density of scattering centers separates two fundamental regimes. As illustrated in Fig. 3.1, for a scarce number of scattering events, the mean free path ℓ is much larger than the system size L and the transport is *ballistic*. On the contrary, the transport is *diffusive*, if $\ell \ll L$. In the diffusive regime, the ensemble of N electrons on average acquires a drift velocity $\mathbf{v}_d$ that leads to a net electric current of density

$$\mathbf{j} = -|e|n\mathbf{v}_d = -\frac{|e|n}{N} \sum_{i=1}^{N} \mathbf{v}_i \tag{3.1}$$

Here, e is the elementary charge and n the electron density. The conductivity σ, or respectively the resistivity ρ, of the system can then be defined by Ohm's law as

$$\sigma = \frac{1}{\rho} = \frac{\mathbf{j}}{\mathbf{E}}. \tag{3.2}$$

3.1.1 Diffusive transport in metals and semiconductors

Metals
In metals, the overlap of conduction and valence band leads to a presence of free electrons at the Fermi surface that mediate the electronic transport. The resistivity of a metal is therefore determined by the scattering events mentioned above, i.e. lattice imperfections and especially phonons. According to Matthiessen's rule, the total resistivity of the material is obtained by the summation of single resistivities ρ_i of the i-th scattering channel:

$$\rho = \sum_i \rho_i. \tag{3.3}$$

With respect to temperature T, the effective resistivity of a metal can then be dissected into

$$\rho(T) = \rho_R + \rho_T(T), \tag{3.4}$$

with the temperature-independent residual resistance ρ_R and the temperature-dependent resistance ρ_T. The main contribution to ρ_T are thermally activated phonons with resistivity

$$\rho_{ph}(T) = \rho_0 \left(\frac{T}{T_0}\right)^n,\tag{3.5}$$

where ρ_0 is the resistivity at the reference temperature T_0. Typically, above the critical Debye temperature T_D, a linear dependence of the resistivity on temperature is observed, hence $n = 1$. For $T < T_D$, the scattering of conduction electrons with phonons becomes less efficient and $n = 5$. Due to saturation of the phonon contribution and hence ρ_T, the resistivity of the system approaches ρ_R for $T \ll T_D$.

Semiconductors

For semiconductors, the above mentioned scattering processes and their influence on the resistivity are still valid. However, in contrast to metals, the ability of electrical conduction in semiconductors is highly dependent on the density n of available charge carriers. For intrinsic semiconductors with an activation energy Δ, n depends exponentially on temperature:

$$n \sim \exp(-\Delta/2k_B T).\tag{3.6}$$

Therefore, the resistivity increases with decreasing T due to the freeze out of thermally activated carriers. Another distinctive feature of semiconductors is the possibility of ambipolar transport of electrons and holes. Applying an electric field $\mathbf{E}$ to a sample creates a current density $\mathbf{j}$ according to Eq. (3.2), where σ generalizes to

$$\sigma = q_e n_e \mu_e + q_h n_h \mu_h.\tag{3.7}$$

Here, n_i and μ_i are the density and mobility of electrons (i=e) and holes (i=h) and q_i denotes the respective charge with $q_h = -q_e = e$. The temperature dependencies and the ratio of contributing charge carrier types in semiconductors can furthermore be largely influenced by extrinsic doping of the material. Usually, the charge carrier density of intrinsic semiconductors is comparatively low and hence their resistivities are much larger than that of metals. By addition of dopants, however, the charge carrier density can be increased by orders of magnitude, leading to an almost metal-like conduction in the extreme case. If the dopants are donors, the dominant charge carriers are electrons. For acceptors the current is carried by holes.

3.1.2 Diffusive transport in magnetic fields

Applying an electric *and* a magnetic field $\mathbf{B}$ to the system leads to an additional Lorentz force acting on the charge carriers. For an ensemble of carriers inside a solid, this modifies the mean drift velocity $\mathbf{v}_D = \langle \mathbf{v} \rangle$ introduced in Eq. (3.1) to

$$\mathbf{v}_D = \frac{q_i \tau}{m}(\mathbf{E} + \mathbf{v}_D \times \mathbf{B}),\tag{3.8}$$

where m is the effective carrier mass and q_i is the elemental charge, being negative for electrons ($q_e = -e$) and positive for holes ($q_h = e$). With the cyclotron frequency $\omega_c = \frac{|e|B}{m}$ and choosing $\mathbf{B} = (0, 0, B_z)$, $\mathbf{v}_D$ can be dissected into its cartesian components

$$\mathbf{v}_D^x = -\omega_c \tau \left(\frac{E_x}{B_z} + \mathbf{v}_D^y \right), \tag{3.9a}$$

$$\mathbf{v}_D^y = -\omega_c \tau \left(\frac{E_y}{B_z} + \mathbf{v}_D^x \right), \tag{3.9b}$$

$$\mathbf{v}_D^z = -\omega_c \tau \left(\frac{E_z}{B_z} \right). \tag{3.9c}$$

Using this and the Eqs. (3.1) and (3.2) introduced above yields a current density for a solid in electric and magnetic fields of

$$\begin{pmatrix} j_x \\ j_y \\ j_z \end{pmatrix} = \frac{\sigma_0}{1 + \omega_c^2 \tau^2} \begin{pmatrix} 1 & -\omega_c \tau & 0 \\ +\omega_c \tau & 1 & 0 \\ 0 & 0 & 1 + \omega_c^2 \tau^2 \end{pmatrix} \begin{pmatrix} E_x \\ E_y \\ E_z \end{pmatrix}. \tag{3.10}$$

In absence of a magnetic field, ω_c is zero and Eq. (3.10) reproduces Eq. (3.2) with the conductivity σ_0. From this expression, important relations of the Hall- and magnetoresistance-effects can be derived.

Hall effect

Choosing $\mathbf{E} = (E_x, 0, 0)$ creates a current density $\mathbf{j} = (j_x, 0, 0)$. With $\mathbf{B} = (0, 0, B_z)$ the charge carriers are deflected in y-direction by the Lorentz force, giving rise to an electric field E_y. The Hall field E_y builds up until the created electric force $\mathbf{F}_E = q_i \mathbf{E}_y$ compensates the Lorentz force $\mathbf{F}_L = q_i (\mathbf{v}_D \times \mathbf{B})$. Hence, $j_y = 0$ for the stationary case and from Eq. (3.10) follows

$$E_y = -\omega_c \tau E_x = \frac{q_i B_z \tau}{m} \frac{j_x}{\sigma_0} = R_H B_z j_x, \tag{3.11}$$

with the Hall coefficient R_H. For conduction in metals or highly doped semiconductors, where the density of one type is much larger than the other, it is given by

$$R_H = \frac{1}{n q_i}, \tag{3.12}$$

with the charge carrier density n and its sign being determined by the sign of q_i depending on the charge carrier type. If the current density j_x is carried by electrons *and* holes, the derivation becomes more complicated. The total current density is then given by the sum

of two densities $\mathbf{j}_{1,x}$ and $\mathbf{j}_{2,x}$, yielding two equations of the type of relation (3.10). In this case, the Hall coefficient takes the form

$$R_{\mathrm{H}} = \frac{n_{\mathrm{h}}\mu_{\mathrm{h}}^2 - n_{\mathrm{e}}\mu_{\mathrm{e}}^2}{|e|(n_{\mathrm{h}}\mu_{\mathrm{h}} + n_{\mathrm{e}}\mu_{\mathrm{e}})}. \tag{3.13}$$

Due to their opposite charge *and* opposite drift velocity, both charge carrier types will be deflected in the same direction, leading to a (partial) compensation. The dominant charge carrier type depends on the respective density n_i and mobility μ_i of the electrons and holes and manifests in the sign of R_{H}. In the chosen geometry, a longitudinal conductivity σ_{xx} along the x-axis and a perpendicular Hall conductivity σ_{xy} can be defined and Eq. (3.10) is transformed to

$$\begin{pmatrix} j_{\mathrm{x}} \\ j_{\mathrm{y}} \end{pmatrix} = \begin{pmatrix} \sigma_{\mathrm{xx}} & -\sigma_{\mathrm{xy}}, \\ \sigma_{\mathrm{xy}} & \sigma_{\mathrm{xx}} \end{pmatrix} \begin{pmatrix} E_{\mathrm{x}} \\ E_{\mathrm{y}} \end{pmatrix}. \tag{3.14}$$

For an arbitrary number N of contributing transport channels they can be obtained as [51, 52]

$$\sigma_{\mathrm{xx}} = \sum_i^N \frac{|q_i \cdot n_i \cdot \mu_i|}{1 + (\mu_i \cdot B)^2} \tag{3.15a}$$

$$\sigma_{\mathrm{xy}} = \sum_i^N \frac{q_i \cdot n_i \cdot \mu_i^2 \cdot B}{1 + (\mu_i \cdot B)^2}, \tag{3.15b}$$

The respective longitudinal and Hall resistivities are obtained by tensor inversion that yields

$$\rho_{\mathrm{xx}} = \frac{\sigma_{\mathrm{xx}}}{\sigma_{\mathrm{xx}}^2 + \sigma_{\mathrm{xy}}^2}, \tag{3.16a}$$

$$\rho_{\mathrm{xy}} = \frac{\sigma_{\mathrm{xy}}}{\sigma_{\mathrm{xx}}^2 + \sigma_{\mathrm{xy}}^2}. \tag{3.16b}$$

Classical magnetoresistance effects

In general, the relative magnetoresistance is defined as the percentage change of the longitudinal resistance ρ_{xx} with applied magnetic field:

$$MR^{\mathrm{rel}} = \frac{\rho_{\mathrm{xx}}(B) - \rho_{\mathrm{xx}}(0)}{\rho_{\mathrm{xx}}(0)} = \frac{\delta\rho_{\mathrm{xx}}(B)}{\rho_{\mathrm{xx}}(0)}. \tag{3.17}$$

Choosing again $\mathbf{E} = (E_x, 0, 0)$ and $\mathbf{B} = (0, 0, B_z)$ and assuming only a single type of freely moving carriers contributing to j_x, it is easily shown that $MR^{\text{rel}} = 0$: for the stationary case, equation (3.10) yields $\omega_c \tau E_x + E_y = 0$ and it follows by inserting this expression of E_y into Eq. (3.10)

$$j_x = \frac{\sigma_0}{1 + \omega_c^2 \tau^2}(E_x - \omega_c \tau E_y) = \frac{\sigma_0}{1 + \omega_c^2 \tau^2}(E_x + \omega_c^2 \tau^2 E_x) = \sigma_0 E_x. \tag{3.18}$$

The current density j_x and hence ρ_{xx} are not dependent on B, since, as stated above, the Lorentz force and the electric force created by the Hall field exactly cancel. As for the Hall effect discussed above, the situation for the longitudinal resistance complicates, if multiple transport channels are present. For two charge carrier types with respective Hall coefficients $R_{H,1}$ and $R_{H,2}$, a general expression can be derived:

$$\rho_{xx}(B) = \frac{\rho_{xx,1}\rho_{xx,2}(\rho_{xx,1} + \rho_{xx,2}) + (\rho_{xx,1}R_{H,2}^2 + \rho_{xx,2}R_{H,1}^2)B^2}{(\rho_{xx,1} + \rho_{xx,2})^2 + (R_{H,1} + R_{H,2})^2 B^2}. \tag{3.19}$$

If $R_{H,1} = R_{H,2}$, the system effectively resembles the single carrier case and Eq. (3.19) is independent of B. However, for e.g. compensated metals, where $R_{H,1} = -R_{H,2}$ and $\rho_{xx,1} = \rho_{xx,2}$, both $\rho_{xx}(B)$ and MR^{rel} are proportional to B^2.

Naturally, these specific examples can not account for the experimental observations of a measurable positive magnetoresistance in most non-magnetic metallic systems and the presented model is too simplified. A more general, empirical description of the magnetoresistance in metals is provided by Kohler's rule. It states that

$$\frac{\Delta\rho_{xx}(B)}{\rho_{xx}(0)} = F\left(\frac{B}{\rho_{xx}(0)}\right), \tag{3.20}$$

where the function F is material specific. Since the magnetoresistance should not depend on the sign of the magnetic field, F can only contain even powers of B. Hence, for small fields, $MR^{\text{rel}} \sim B^2$.

3.2 Quantum interference effects

At the beginning of chapter 3.1, two characteristic length scales, the system size L and the mean free path ℓ, were introduced to separate ballistic from diffusive transport. Especially at low temperatures, when quantum effects of the electrons' wave nature become important, the phase coherence length l_φ defines an additional *quantum diffusive* regime, if $\ell \ll L$ and $\ell \ll l_\varphi$. In classical diffusive transport, the electrons are assumed to follow classical trajectories in between scattering events. This assumption breaks down in the quantum diffusive regime, where interference effects of coherent electron wave functions have to be taken into account. The condition $\ell \ll l_\varphi$ implies that the conduction electrons of the system are scattered many times during the transport before they lose their phase

coherence. This causes two types of quantum corrections to the classical conductivity: first, an electron can essentially interfere with itself, when its path intersects itself to from a closed loop. Depending on the sign of this interference and considering the subsequent effect on the conductivity, this is called weak localization or weak anti-localization. On the other hand, also the interaction between different electrons, the electron-electron interaction (EEI), influences the transport behavior and provides a second correction term to the conductivity. As will be discussed below, both effects not only show a characteristic dependence on temperature, but also on external magnetic fields. Before introducing the quantum corrections to conductivity, however, a more thorough definition of phase coherence and a brief overview of decoherence mechanisms will be given.

3.2.1 Phase coherence and dephasing mechanisms

When describing dynamical processes such as scattering, a time dependent treatment of the quantum mechanical system is necessary. The wave function $\Psi(\mathbf{r}, t)$ of an electron in a static potential then reads [53]

$$\Psi(\mathbf{r}, t) = \psi(\mathbf{r})\mathrm{e}^{-i\omega t} = \psi(\mathbf{r})\mathrm{e}^{-i\epsilon t/\hbar} = \psi(\mathbf{r})\mathrm{e}^{-i\varphi(t)}, \tag{3.21}$$

where $\psi(\mathbf{r})$ is the time-independent wave function, ω the frequency, ϵ the electron's energy, t the time variable, $\hbar$ the reduced Planck constant, and $\varphi(t) = \epsilon t/\hbar$ the phase factor. For elastic scattering events from the static disorder of the lattice, where the electron energy ϵ remains constant, the term $\mathrm{e}^{-i\epsilon t/\hbar}$ does not change. The time and the distance travelled between such events are the mean free time τ and path ℓ introduced above. If, however, interactions causing energy transfer with the environment are present, the variation of ϵ causes a variation of $\mathrm{e}^{-i\epsilon t/\hbar}$. Here, the time and distance the electron travels before a significant change of ϵ, are the phase coherence time τ_φ and length l_φ. The two quantities are connected via the diffusion constant D following

$$l_\varphi = \sqrt{D\tau_\varphi}. \tag{3.22}$$

The phase of a wave function is no physical observable and only the phase difference $\Delta\varphi$ of two waves is well defined [54]. The energy exchange with the environment $\Delta\epsilon$ becomes significant to dephase two originally coherent wave functions, when $\Delta\varphi \approx \frac{\Delta\omega}{2\pi}\tau_\varphi \approx \pi$ and hence $\Delta\epsilon = \hbar\omega \approx \frac{h}{\tau_\varphi}\pi$ [55]. The processes responsible for the change of energy are inelastic electron-phonon and inelastic electron-electron scattering, as well as electron-electron interactions with small energy transfer. Above temperatures of a few Kelvin, the inelastic scattering events with energy transfer of order of $\approx k_\mathrm{B}T$ usually dominate. For lower temperatures and especially in reduced dimensions, however, the EEI causing only small energy variations, which is hence termed *quasi-elastic*, often determines τ_φ [54–56]. It can be interpreted as the interaction of an electron with the fluctuating electromagnetic field created by the ensemble of other electrons, the *Nyquist noise* [56]. This quasi-elastic process can significantly contribute to dephasing, since the requirement of $\Delta\epsilon \approx \frac{h}{\tau_\varphi}\pi$ to
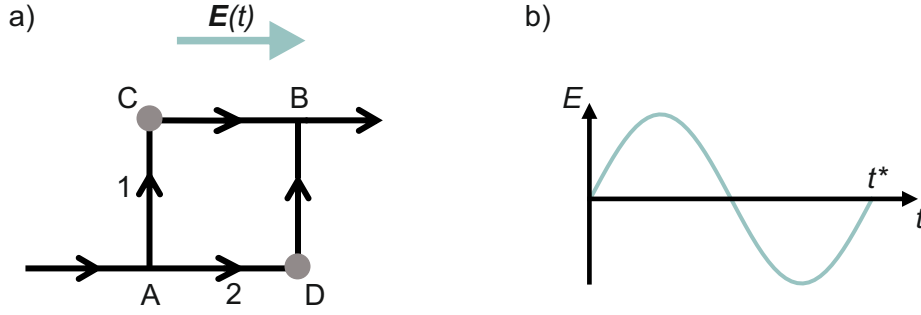
Figure 3.2: Exemplary toy model for dephasing by Nyquist noise. a) Propagation of two partial waves along paths 1 and 2 in a time-varying electric field $\mathbf{E}(t)$. To travel from point A to B the partial waves take the time t^* that equals the periodicity of E(t) as indicated in b). Figure adapted from Ref. [55].

cause wave decoherence is orders of magnitude smaller than k_BT. For a more intuitive understanding of how Nyquist noise leads to dephasing, the following will discuss a toy model of two partial waves in a time-varying electric field $\mathbf{E}(t)$ introduced in Ref. [55] and illustrated in Fig. 3.2. An electron wave shall come in from the left entering $\mathbf{E}(t)$. It splits into two partial waves at point A that travel along paths 1 and 2, elastically scatter at points C and D at time $t = t^*/2$, respectively, and recombine at point B after a time t^* that is equivalent to the periodicity of $\mathbf{E}(t)$. When the propagation of one of the waves is perpendicular to the electric field, its energy does not change. On path 2 the electron wave moves parallel to $\mathbf{E}(t)$ travelling from point A to D and its energy decreases due to its negative charge. Partial wave 1, however, moves from C to B after the time $t^*/2$, when $\mathbf{E}(t)$ has changed sign as indicated in Fig. 3.2 b). Its energy hence increases and the two waves have dephased when recombining at point B. Obviously, this artificial model only serves as an illustration. In a real system any kind of interaction between electrons and a fluctuating electromagnetic field can lead to dephasing of electron waves and, importantly, no inelastic scattering events with large energy transfer are necessary.

An experimental method to determine quantitative values for l_φ are quantum transport measurements in external magnetic fields. The quantum interference effects, that will be discussed in the preceding section, lead to a correction of the classical conductivity, but are destroyed in external magnetic fields. The magnitude of the magnetic field necessary to suppress the quantum interference is directly correlated to l_φ. The temperature dependence of the obtained values then allows to draw conclusions on the underlying dominant dephasing process. Usually, the phase coherence length follows a power law in temperature, i.e. $l_\varphi \sim T^p$, where p depends not only on the dephasing process, but also on the dimensionality of the system. The quasi-elastic EEI for example leads to $p = \frac{1}{3}$ in one-, $p = \frac{1}{2}$ in two-, and $p = \frac{3}{2}$ in three dimensions [56, 57].
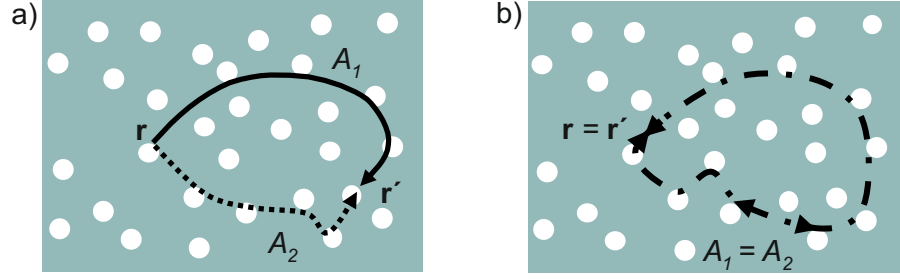
Figure 3.3: Illustration of electron trajectories in the quantum diffusive regime. a) Two arbitrary trajectories with probability amplitudes A_1 and A_2 from point **r** to **r**´. b) A closed loop with **r** = **r**´, where the two trajectories have the same amplitude ($A_1 = A_2$), but opposite propagation direction (adapted from Ref. [58]).

3.2.2 Weak localization and weak anti-localization: the Hikami-Larkin-Nagaoka theory

Interference between coherent electron waves in the quantum diffusive transport regime can have a pronounced effect on the classical conductivity introduced in Ch. 3.1. Semiclassically and disregarding the electron spin, the total probability $P(\mathbf{r}, \mathbf{r'}, t)$ for an electron to diffuse from point **r** to **r'** during the time t is given by the squared magnitude of the sum over all individual probability amplitudes A_n of the n possible trajectories [58]:

$$P(\mathbf{r}, \mathbf{r'}, t) = \left| \sum_n A_n \right|^2 . \tag{3.23}$$

In the quantum diffusive regime, however, where an electron elastically scatters many times before losing its phase coherence ($\ell \ll l_\varphi$), additional interference terms between trajectories have to be considered and Eq. (3.23) expands to

$$P(\mathbf{r}, \mathbf{r'}, t) = \left| \sum_n A_n \right|^2 = \underbrace{\sum_n |A_n|^2}_{\text{semiclassical}} + \underbrace{\sum_{n \neq m} A_n A_m^*}_{\text{quantum interference}} . \tag{3.24}$$

Consider arbitrary pairs of two partial wave trajectories with amplitudes A_1 and A_2 between points **r** and **r'**. In the case sketched in Fig. 3.3 a), where **r** ≠ **r'**, the interference terms are always negligible, because the trajectories 1 and 2 generally have uncorrelated phases. In the summation over all possible pairs to obtain the total probability P the interference contributions then average out. For closed loops with **r** = **r'** illustrated in Fig. 3.3 b), however, every trajectory can be paired with its respective time-reversed path of opposite propagation direction such that $A_1 = A_2 \equiv A$. The contribution to $P(\mathbf{r}, \mathbf{r'}, t)$

of one such pair is given by

$$|A_1 + A_2|^2 = |A_1|^2 + |A_2|^2 + A_1 A_2^* + A_1^* A_2. \tag{3.25}$$

If the time t to cover the trajectory is larger than τ_φ, the interference terms again do not contribute and $P = 2|A|^2$. However, for $t < \tau_\varphi$, the time-reversed partial waves coherently interfere at $\mathbf{r} = \mathbf{r'}$ and the probability is doubled to $4|A|^2$. In a spin-less consideration, this is always equivalent to an enhanced back scattering probability leading to a decrease of the system's conductivity [50, 53, 54, 58]. This effect is hence termed *weak localization* (WL). For a two-dimensional film the absolute correction $\delta\sigma_{\mathrm{WL}}$ to the conductivity σ is given by [53]

$$\delta\sigma_{\mathrm{WL}} = -\int_\tau^{\tau_\varphi} dt \, \frac{e^2}{\pi h} \cdot \frac{1}{t} = -\frac{e^2}{\pi h} \ln\left(\frac{\tau_\varphi}{\tau}\right) = -2\frac{e^2}{\pi h} \ln\left(\frac{l_\varphi}{\ell}\right). \tag{3.26}$$

For the last equality, relation (3.22) and $\ell = \sqrt{D\tau}$ for the mean free path ℓ was used. When considering the electron spin, a more thorough treatment is necessary. Now, each trajectory contains two electrons of opposite spin projection of $\pm\frac{1}{2}$, that each generate a pair of waves. If the spin projections remain unchanged, each wave interferes at the starting point with its complementary time-reversed counterpart as discussed above. However, in the presence of spin-orbit coupling (SOC) the spin can be flipped by an elastic scattering event and the two pairs of waves mix. This mixing can be modelled by *Cooperon* quasi-particles that consist of pairs of electron states before and after back scattering. The wave function $\Xi_{j,m}$ of such a Cooperon therefore has four components [53]:

$$\Xi_{j,m} = \begin{pmatrix} \Xi_{0,0} \\ \Xi_{1,-1} \\ \Xi_{1,0} \\ \Xi_{1,1} \end{pmatrix} = \begin{pmatrix} \frac{1}{\sqrt{2}}(\psi_+^{(1)}\psi_-^{(2)} - \psi_-^{(1)}\psi_+^{(2)}) \\ \psi_-^{(1)}\psi_-^{(2)} \\ \frac{1}{\sqrt{2}}(\psi_+^{(1)}\psi_-^{(2)} + \psi_-^{(1)}\psi_+^{(2)}) \\ \psi_+^{(1)}\psi_+^{(2)}, \end{pmatrix} \tag{3.27}$$

where the $\psi_s^{(i)}$ are the wave functions of the first $(i = 1)$ and second $(i = 2)$ electron and $s = (+, -)$ denotes the electron spin of $+\frac{1}{2}$ and $-\frac{1}{2}$, respectively. The subscripts j and m of $\Xi_{j,m}$ are the quantum number for the total angular momentum and its projection. The first row of Eq. (3.27) has zero angular momentum and represents the singlet channel of the Cooperon, the remaining rows form the triplet channel with $j = 1$. For the correction to the conductivity $\delta\sigma$ now the sum of interferences of all four components has to be considered and equation (3.26) is modified to [53]

$$\delta\sigma = -\int_\tau^{\tau_\varphi} dt \, \frac{e^2}{\pi h} \cdot \frac{1}{t} \left(\frac{3}{2} e^{-t/\tau_{\mathrm{so}}} - \frac{1}{2}\right). \tag{3.28}$$

The parameter τ_{so} denotes the characteristic time until a spin-flip occurs during the diffusive motion of the electron. Since not every elastic scattering event causes the spin to flip, it is much larger than the mean free time, i.e. $\tau_{\text{so}} \gg \tau$. The second term in the brackets within the integral of Eq. (3.28), $-\frac{1}{2}$, stems from the singlet channel of the Cooperon, whereas the term $\frac{3}{2}e^{-t/\tau_{\text{so}}}$ accounts for the triplet and depends on the strength of spin-orbit coupling that determines τ_{so}. For $t \ll \tau_{\text{so}}$, the factor $e^{-t/\tau_{\text{so}}} = 1$ and Eq. (3.28) reproduces the essentially spin-less case of weak localization given in equation (3.26). However, if the SOC is strong and hence $\tau_{\text{so}} \ll t < \tau_\varphi$, the exponential function goes to zero and the bracket in Eq. (3.28) yields a factor of $-\frac{1}{2}$. In this case, the quantum interference hence changes the sign of $\delta\sigma$ and therefore *increases* the conductivity with half magnitude. This effect is termed *weak anti-localization* (WAL). Reducing the consideration to these two extreme cases with respect to spin-orbit coupling, thus allows to define a parameter α that modifies the quantum correction derived for weak localization in Eq. (3.26) by

$$\delta\sigma = \alpha \cdot \delta\sigma_{\text{WL}}, \qquad (3.29)$$

with $\alpha = 1$ for weak and $\alpha = -\frac{1}{2}$ for strong spin-orbit coupling.

To provide a qualitative but more intuitive picture: as mentioned above, the triplet channel of the Cooperon causes a positive, the singlet a negative contribution to α. Without spin-orbit coupling, the triplets outnumber the singlets, α is positive and localization is observed. However, in the presence of strong SOC the triplet channels are "destroyed", since it acts like a spin-dependent scattering. The singlet channel with $j = 0$, on the other hand, is unaffected and the quantum interference leads to a positive correction to the conductivity [59]. This possible crossover from WL to WAL for systems with increasing spin-orbit coupling was shown for the first time in Ref. [60] for thin film systems by Hikami, Larkin, and Nagaoka. Therein, the case $\alpha = 1$ is termed *orthogonal* and the anti-localization regime with $\alpha = -\frac{1}{2}$ is called *simplectic*. The unitary case defined in Ref. [60] for systems with strong magnetic scattering and $\alpha = 0$ will not be regarded in this thesis. Variation of the temperature or the application of an external magnetic field both affect the correction to the conductivity in a characteristic way. Experimentally, this can not only be used to prove the presence of quantum interference, but also to gain insight to certain material properties. To avoid later ambiguities, the quantum correction to the conductivity caused by weak localization or weak anti-localization will be symbolized by $\delta\sigma_{\text{HLN}}$ in the following, where the WL or WAL origin enters the respective equations via the pre-factor α.

Influence of temperature on $\delta\sigma_{\text{HLN}}$

The temperature does not explicitly modify $\delta\sigma_{\text{HLN}}$, but enters via the T-dependence of the phase coherence. For the two-dimensional case, it was shown in Ch. 3.2.1 that $l_\varphi \sim T^p$, where p is determined by the dephasing process. From Eqs. (3.26) and (3.28) hence always follows

$$\delta\sigma_{\text{HLN}} \sim -\alpha p \ln(T). \qquad (3.30)$$

The quantum correction effect is strongest at low temperatures. At high T the conduction electrons dephase too quickly and no coherent interference is possible. To provide an explicit formula for $\delta\sigma_{\mathrm{HLN}}(T)$, a characteristic temperature T_0 has to be defined at which the quantum correction vanishes. It follows [61]

$$\delta\sigma_{\mathrm{HLN}} = -\alpha p \frac{e^2}{\pi h} \ln\left(\frac{T}{T_0}\right). \tag{3.31}$$

Influence of a magnetic field on $\delta\sigma_{\mathrm{HLN}}$

So far, the behavior of $\delta\sigma_{\mathrm{HLN}}$ has been considered in the absence of an external magnetic field **B**. Under influence of **B**, the electrons travelling along a closed loop acquire an additional Aharonov-Bohm phase factor φ_{AB} of [50, 53]

$$\varphi_{\mathrm{AB}} = \pm \pi \frac{BS}{\Phi_0}. \tag{3.32}$$

Here, B is the magnitude of the magnetic field, $\Phi_0 = h/2e$ is the magnetic flux quantum, and S the area of the enclosed loop projected to the plane perpendicular to **B**. The sign of φ_{AB} depends on the propagation direction of the electron. Since the two interfering waves travel the loop oppositely, they obtain a total phase difference of $\Delta\varphi_{\mathrm{AB}} = 2|\varphi_{\mathrm{AB}}|$ that modifies the quantum interference terms in Eq. (3.25) such that [50]

$$|A_1 + A_2|^2 = |A_1|^2 + |A_2|^2 + 2|A_1||A_2|\cos(\Delta\varphi_{\mathrm{AB}}). \tag{3.33}$$

Hence, the quantum interference term would remain unaffected for $\cos(\Delta\varphi_{\mathrm{AB}}) = 1$, but completely vanish for $\cos(\Delta\varphi_{\mathrm{AB}}) = 0$. For a single loop with enclosed area S, this would yield an oscillatory behavior of $\delta\sigma_{\mathrm{HLN}}$ in B with period Φ_0. In a macroscopic sample, however, many loops of different S are present, the cosine thus averages to zero for any $B \gg 0$, and the quantum interference is destroyed. Only around zero magnetic field it is $\cos(\Delta\varphi_{\mathrm{AB}}) \approx 1$ for all S and hence $|\delta\sigma_{\mathrm{HLN}}| > 0$. This vanishing of the quantum correction with an increasing magnetic field leads to the observation of a distinct magnetoconductivity. The magnetic field range in which this effect is observed depends on the magnitudes S of the contributing loops. The boundaries of S are approximately given by $\ell^2 \lesssim S \lesssim l_\varphi^2$, with ℓ being the mean free path [50]. Requiring $\Delta\varphi_{\mathrm{AB}} = \pi$, such that the interference term in Eq. (3.33) entirely vanishes, therefore yields with Eq. (3.32) a magnetic field range of

$$\frac{h}{4el_\varphi^2} \lesssim B \lesssim \frac{h}{4e\ell^2}. \tag{3.34}$$

The sign of $\delta\sigma_{\mathrm{HLN}}(B)$ depends on the type of quantum interference. In the case of weak anti-localization, the conductivity is increased in the absence of a magnetic field. When the effect is suppressed by $B > 0$, the conductivity hence decreases and a negative magnetoconductivity is observed. The situation is opposite for weak localization. In Ref. [60] Hikami, Larkin, and Nagaoka provide a theory that allows a quantitative analysis of

the quantum correction in two-dimensional systems accounting for both WL and WAL. They derive the general formula

$$\delta\sigma_{\text{HLN}}(B) = \sigma_0 - \frac{e^2}{2\pi^2\hbar}\left[\psi\left(\frac{1}{2} + \frac{1}{b\tau_{\text{e}}}\right) - \psi\left(\frac{1}{2} + \frac{1}{b\tau_1}\right)\right.$$
$$\left. + \frac{1}{2}\psi\left(\frac{1}{2} + \frac{1}{b\tau_2}\right) - \frac{1}{2}\psi\left(\frac{1}{2} + \frac{1}{b\tau_3}\right)\right],$$

(3.35)

for a two-dimensional sample in the x-y-plane and a perpendicular magnetic field along the z-axis. Here, σ_0 is the classical conductivity at $B = 0$, ψ denotes the digamma function, $b = 4eDB/\hbar$, and the contained characteristic times are[1]

$$\frac{1}{\tau_{\text{e}}} = \frac{1}{\tau} + \frac{2}{\tau_{\text{so}}^{\text{x}}} + \frac{1}{\tau_{\text{so}}^{\text{z}}},$$

(3.36a)

$$\frac{1}{\tau_1} = \frac{2}{\tau_{\text{so}}^{\text{x}}} + \frac{1}{\tau_{\text{so}}^{\text{z}}} + \frac{1}{\tau_{\varphi}},$$

(3.36b)

$$\frac{1}{\tau_2} = \frac{1}{\tau_{\varphi}},$$

(3.36c)

$$\frac{1}{\tau_3} = \frac{4}{\tau_{\text{so}}^{\text{x}}} + \frac{1}{\tau_{\varphi}}.$$

(3.36d)

The parameters $\tau_{\text{so}}^{\text{x}}$ and $\tau_{\text{so}}^{\text{z}}$ are the spin-flip times along the respective axis and τ_{e} is the effective mean free time including corrections to τ due to spin-orbit scattering. As for the phase coherence given in Eq. (3.22), all characteristic times are connected with the respective length via the diffusion constant D via $l_{\text{i}} = \sqrt{D\tau_{\text{i}}}$. For large arguments x the digamma function $\psi(x)$ can be approximated by $\psi(x) \approx \ln(x)$. Hence, when B approaches zero, Eq. (3.35) goes to

$$\delta\sigma_{\text{HLN}}(B \to 0) =$$
$$\sigma_0 - \frac{e^2}{2\pi^2\hbar}\left[\ln\left(\frac{1}{b\tau_{\text{e}}}\right) - \ln\left(\frac{1}{b\tau_1}\right) + \frac{1}{2}\ln\left(\frac{1}{b\tau_2}\right) - \frac{1}{2}\ln\left(\frac{1}{b\tau_3}\right)\right].$$

(3.37)

With equations (3.35) and (3.37) the magnetoconductivity caused by the quantum interference $\Delta\sigma_{\text{HLN}}(B) = \delta\sigma_{\text{HLN}}(B) - \delta\sigma_{\text{HLN}}(B \to 0)$ can therefore be calculated

---

[1]In the original formula given in Ref. [60] also spin-flips by scattering at magnetic impurities are considered that enter the equation via a time τ_{s}. Since such magnetic scattering is not relevant in this thesis, this parameter is disregarded in the given equations.

by

$$\Delta\sigma_{\text{HLN}}(B) = \frac{e^2}{2\pi^2\hbar} \left[\ln\left(\frac{1}{b\tau_{\text{e}}}\right) - \psi\left(\frac{1}{2} + \frac{1}{b\tau_{\text{e}}}\right) \right.$$

$$- \ln\left(\frac{1}{b\tau_1}\right) + \psi\left(\frac{1}{2} + \frac{1}{b\tau_1}\right)$$

$$+ \frac{1}{2}\ln\left(\frac{1}{b\tau_2}\right) - \frac{1}{2}\psi\left(\frac{1}{2} + \frac{1}{b\tau_2}\right)$$

$$\left. - \frac{1}{2}\ln\left(\frac{1}{b\tau_3}\right) + \frac{1}{2}\psi\left(\frac{1}{2} + \frac{1}{b\tau_3}\right) \right].$$

(3.38)

The term $1/b\tau_{\text{e}}$ can be assumed to be large for all B, since τ_{e} is very small in the diffusive regime. Hence, the terms containing τ_{e} in Eq. (8.2.3) cancel. Implementing the parameter α as introduced above then simplifies the equation to

$$\Delta\sigma_{\text{HLN}}(B) = \alpha\frac{e^2}{2\pi^2\hbar} \left[\psi\left(\frac{1}{2} + \frac{1}{b\tau_\varphi}\right) - \ln\left(\frac{1}{b\tau_\varphi}\right) \right],$$

(3.39)

where α takes the same values as above. In the absence of spin-orbit scattering (orthogonal case) with thus $1/\tau_{\text{so}}^{\text{x}} = 1/\tau_{\text{so}}^{\text{z}} = 0$, Eq. (3.39) directly reproduces Eq. (8.2.3) for $\alpha = 1$, yielding a positive magnetoconductivity as expected for weak localization. In the simplectic regime with large spin-orbit scattering and $1/\tau_2 = 1/\tau_\varphi \ll 1/\tau_1, 1/\tau_3$, α takes the value $-\frac{1}{2}$ and a negative, WAL-type magnetoconductivity is observed. In the limits of $b\tau_\varphi$ Eq. (3.39) shows a quadratic or respectively a logarithmic behavior in B:

$$\Delta\sigma_{\text{HLN}} = \begin{cases} \sim B^2, & b\tau_\varphi \ll 1 \\ \sim \ln(B), & b\tau_\varphi \gg 1. \end{cases}$$

(3.40)

3.2.3 Conductivity corrections from electron-electron interactions

Weak localization and anti-localization essentially stem from interferences of electrons with themselves. In turn, also the interaction of wave functions of different electrons can lead to a quantum correction to the classical Drude conductivity of the system. Within the Landau theory of Fermi liquids even strong correlations between electrons in a metal can be disregarded, since they merely lead to a renormalization of parameters like the density of states [62]. However, the Landau theory requires a homogeneous system and interactions between electrons can become important in the presence of disorder. Note that the intricacies of the many-body treatment are highly complex and the following will only provide a brief overview of the corrections to the conductivity originating

Figure 3.4: Schematic real space illustration of electron-electron interaction. Two electrons diffuse from $\mathbf{r_1}$ to $\mathbf{r'_1}$ and $\mathbf{r_2}$ to $\mathbf{r'_2}$. If the solid line trajectories cross twice within a time $t \lesssim \hbar/\Delta\epsilon$ they interfere coherently with the dashed line trajectories (adapted from Ref. [65, 66]).
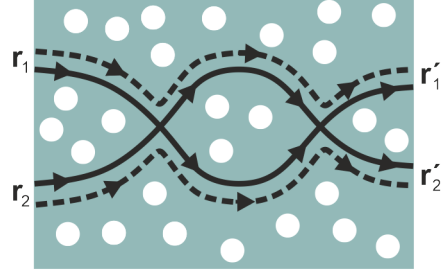
from interelectron interference, which are relevant for the discussion of the experimental findings of this thesis. Extensive reviews can be found in Refs. [61, 63]. Within the theoretical formalism, electron-electron interactions are usually further subdivided into a *Cooper-* and a *diffusion* channel, sometimes also termed particle-particle and particle-hole channel, respectively. For the consideration provided here the Cooperon channel can be neglected [64]. Figure 3.4 visualizes the diffusion channel of the interaction simplified to two electrons and highlights the importance of disorder.

Two electrons diffuse from left to right, respectively starting at $\mathbf{r_1}$ and $\mathbf{r_2}$, along the trajectories marked by the solid lines to the points $\mathbf{r'_1}$ and $\mathbf{r'_2}$. The distances between starting and end points are assumed to be much larger than the mean free path, such that the trajectories undergo several scattering events and paths with one or multiple crossings exist. Let the first crossing of the trajectories define the time $t = t_0 = 0$. In a ballistic regime the distance r between the electrons would increase with $r \sim v_F t$ for $t > 0$, where v_F is the Fermi velocity. However, under diffusive conditions scattering keeps the electrons closer together such that $r \sim v_F \sqrt{\tau t}$ and the trajectories cross a second time at $t = t_1$ with a finite probability. The phase factor of an electron wave with energy ϵ was given above to be $\varphi(t) = \epsilon t/\hbar$. Hence, if $t_1 \lesssim \hbar/\Delta\epsilon$, where $\Delta\epsilon$ is the difference of the electron energies, the two trajectories maintain coherence between the crossings (assuming $\tau < \tau_\varphi$). The energy spectrum of diffusing electrons in a system at temperature T is given by [53]

$$E_F - k_B T \lesssim \epsilon \lesssim E_F + k_B T \tag{3.41}$$

and thus $\Delta\epsilon \sim k_B T$ on average. With this, a characteristic time for the electron-electron interaction τ_{ee} can be defined as

$$\tau_{ee} \approx \frac{\hbar}{k_B T}. \tag{3.42}$$

As already defined in the discussion of weak (anti-)localization (see Eq. (3.24)), the probability $P(\mathbf{r}, \mathbf{r'}, t)$ of a *single* electron to travel from $\mathbf{r}$ to $\mathbf{r'}$ during the time t is given by

$$P(\mathbf{r}, \mathbf{r'}, t) = \left| \sum_n A_n \right|^2,$$

where A_n is the probability amplitude of trajectory n. This can be rewritten to [65]

$$P(\mathbf{r}, \mathbf{r'}, t) = \left| \sum_n A_n \right|^2 = \sum_{n,m} A_n^+ A_m^-, \qquad (3.43)$$

with $A^- = (A^+)^*$. In a theoretical interpretation, A^+ and A^- can be viewed as the amplitudes of a propagating electron and hole, respectively, justifying the denotation as *particle-hole* channel [65].[2] If only a single electron is considered, like in the description of weak (anti-)localization, coherent interference of trajectories is only possible for closed, time-reversed loops. In the case sketched Fig. 3.4 the situation slightly changes. Now, the probability for two electrons to travel from $\mathbf{r_1}$ to $\mathbf{r'_1}$ and $\mathbf{r_2}$ to $\mathbf{r'_2}$ is given by [65]

$$P(\mathbf{r_1}, \mathbf{r'_1}, t)P(\mathbf{r_2}, \mathbf{r'_2}, t) \sim \sum_{n,m,l,k} A_n^+(\mathbf{r_1}, \mathbf{r'_1}, t) A_m^-(\mathbf{r_1}, \mathbf{r'_1}, t)$$
$$\times A_k^+(\mathbf{r_2}, \mathbf{r'_2}, t) A_l^-(\mathbf{r_2}, \mathbf{r'_2}, t), \qquad (3.44)$$

which can be viewed as the propagation of two electron-hole pairs. Usually, all interference terms contained in Eq. (3.44) would average out. As discussed above, however, if two trajectories cross twice within a time $t \lesssim \hbar/\Delta\epsilon$, coherent interaction is possible. The electron-hole pairs essentially "switch" at the crossing points, leading to the paths represented by the dashed lines in Fig. 3.4). Solid- and dashed line trajectories interfere and yield a quantum correction to the conductivity $\delta\sigma_{\mathrm{EEI}}$ that enhances for large disorder and small $\Delta\epsilon$. The complexity behind the underlying processes becomes apparent, if one takes into account that exchange as well as coulombic interactions need to be considered, where an arbitrary amount of electrons are involved [61, 63–67].

Influence of temperature on $\delta\sigma_{\mathrm{EEI}}$
From the definition of the relevant time scale $\tau_{\mathrm{ee}} \approx \hbar/k_\mathrm{B}T$ the importance of temperature T for $\delta\sigma_{\mathrm{EEI}}$ is obvious. By comparing the theoretical description provided for WL/WAL and EEI, it is furthermore natural that the respective corrections to the conductivity show a functional similarity. In Ref. [61, 63] $\delta\sigma_{\mathrm{EEI}}(T)$ is derived in two dimensions to be

$$\delta\sigma_{\mathrm{EEI}} = (1 - \frac{3}{4}\tilde{F}_\sigma)\frac{e^2}{\pi h}\ln\left(\frac{T}{T_{\mathrm{EEI}}}\right), \qquad (3.45)$$

where $\tilde{F}_\sigma$ is an interaction, or also called Coulomb screening factor and T_{EEI} is the characteristic temperature, where the interaction effect vanishes.

---

[2] A^+ is the complex conjugate of A^-, but since both amplitudes "traverse" the trajectory in the same direction and $\mathbf{r} \neq \mathbf{r'}$ this is equivalent to the propagation of an electron and a hole. This also explains the name *diffusion* channel.

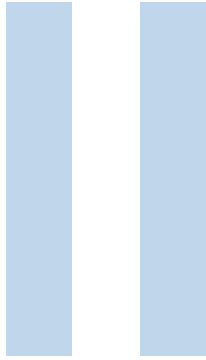**Influence of a magnetic field on $\delta\sigma_{\text{EEI}}$**

The effect of a magnetic field reveals a difference between the quantum corrections to the conductivity stemming from WL/WAL and EEI. In the case of electron-electron interactions the Aharonov-Bohm phase acquired by the wave functions due to the perpendicular component of a magnetic field cancels, since the two trajectories of the upper- and, respectively, lower arm of Fig. 3.4 travel in the same direction. However, the electron-electron interaction is spin-dependent and hence an applied magnetic field influences the quantum correction by means of a Zeeman splitting of spin-up and spin-down bands. The arising magnetoconductivity $\Delta\sigma_{\text{EEI}}(B,T)$ is always negative and is itself dependent on temperature. In two-dimensional systems it is given by [61]

$$\Delta\sigma_{\text{EEI}}(B,T) = \delta\sigma_{\text{EEI}}(B,T) - \delta\sigma_{\text{EEI}}(0,T) = -\frac{e^2}{\hbar}\frac{\tilde{F}_\sigma}{4\pi^2}g_2(h), \qquad (3.46)$$

where $h = g\mu_{\text{B}}B/k_{\text{B}}T$ and $g_2(h)$ is an integral function over the Fermi surface. It can be numerically calculated to take the form

$$g_2(h) = \begin{cases} 0.084h^2, & h \ll 1 \\ \ln(h/1.3), & h \gg 1. \end{cases}$$

Comparing this response to a magnetic field with the predicted dependence for weak (anti-) localization within the HLN formalism (see Eq. (3.40)) reveals a qualitatively similar behavior, being quadratic for small and logarithmic for large B. When the system is in the simplectic regime accompanied by weak anti-localization, the magnetoconductivities of WAL and EEI, furthermore, have the same sign. However, an important distinction between the two effects lies in the sensitivity to the penetration angle of the magnetic field. While for WL/WAL the magnetoconductivity is caused solely by the component of the magnetic field perpendicular to the surface, the spin-splitting effect causing the EEI response to B is isotropic. Note that the formula for $\Delta\sigma_{\text{EEI}}(B,T)$ given in Ref. [61] was derived for systems without spin-orbit coupling. If mixing between spin-up and spin-down channels is possible, the condition $g\mu_{\text{B}}B \gg \hbar/\tau_{\text{so}}$ must be fulfilled to observe a variation of the conductivity correction by the applied field. Two mechanisms can induce a deviation from the theoretically predicted isotropy of the effect: an anisotropy of the g-factor and an anisotropy of the spin-orbit coupling within the material. This will play an important role in Ch. 8 of the experimental part of this thesis.

II

Epitaxy and methods

4

Molecular beam epitaxy

All samples presented and discussed in this thesis were grown by Dr. Matthias Kronseder employing molecular beam epitaxy (MBE) in ultra high vacuum (UHV). Molecular beam epitaxy of topological insulators provides several crucial advantages over other growth techniques, such as the modified Bridgman method. Especially the quick growth of samples with varying alloy stoichiometries and the ability to prepare thin films of precisely adjustable thicknesses down to single layers are of crucial importance in this thesis. Moreover, MBE easily allows the preparation of TI heterostructures for band-structure engineering purposes, a concept that will be introduced in chapter 7 and that plays a key role for the majority of results presented in this work. The unique setup of the Regensburg MBE cluster further broadens the possibilities. In total, the cluster comprises four dedicated chambers that are interconnected by a vacuum tube, as schematically sketched in Fig. 4.1. The connecting tube allows the in-situ transfer of samples between the chamber of the system, which can, for example, be utilized to create topological insulator/ferromagnet heterostructures or the coating of semiconductor nanowires with topological insulator shells creating the platform for further experiments basing on the results of this thesis. Especially relevant for the samples of this work, the metals/oxides chamber is utilized to cap every sample, with a thin layer of aluminium oxide (AlOx) to prevent uncontrolled oxidation of the surface in ambient conditions.
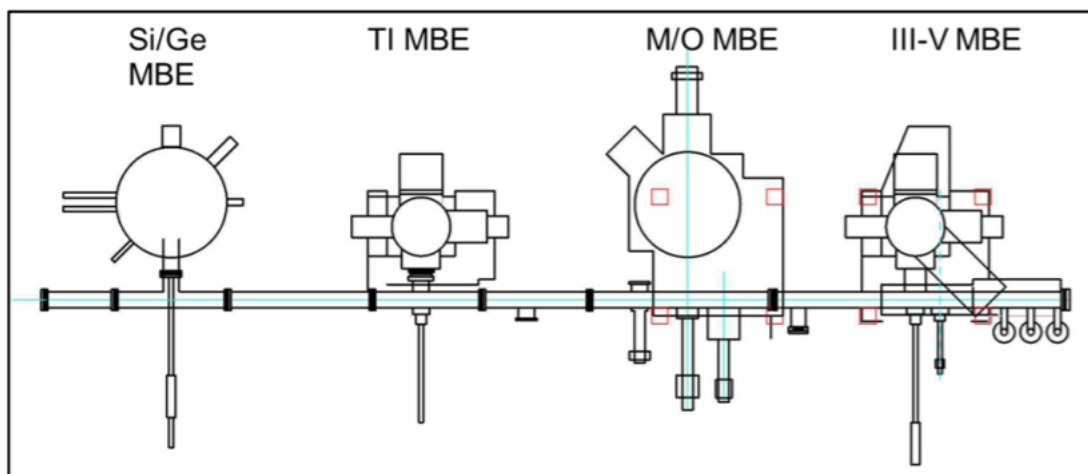
Figure 4.1: Technical drawing of the Regensburg MBE cluster with its four chambers dedicated to silicon/germanium (Si/Ge), topological insulator (TI), metals/oxides (M/O) and III-V semiconductor (III-V) growth.

4.1 MBE chambers

4.1.1 Topological insulator chamber

The chamber dedicated to the growth of topological insulators is of type *RIBER 32*. With a filled ℓN_2-shroud a base pressure below $3 \cdot 10^{-11}$ mbar is reached. Among others, it contains the materials bismuth, selenium, tellurium, and antimony, which are relevant for this thesis. With the exception of antimony, the elements are evaporated by standard Knudsen cells, where the effusion flux is adjusted by regulating the temperature of the crucible via heating filaments. Evaporation of antimony is facilitated by a more complex thermal cracker cell, which is necessary to guarantee the effusion of smaller Sb molecules instead of large clusters. The cell consists of a reservoir containing the Sb crucible and a cracker stage that can be heated individually. The reservoir is brought to the antimony sublimation temperature and the escaping flux of Sb molecules is controlled by a valve and guided to the cracker stage by an injector tube. At the tip of the cracker stage, that is heated to much higher temperatures than the reservoir, the Sb clusters are dissected to mainly Sb_2 molecules and evaporated into the chamber. The fluxes of all materials are determined by commercial Bayard-Alpert gauges. The manipulator installed in this chamber is equipped with a tantalum filament for heating of the substrate and is dedicated for sample holders for two-inch wafers. For monitoring the growth procedure the chamber is equipped with a reflection high-energy electron diffraction (RHEED) gun (see below).

4.1.2 Metal/oxide chamber

The metal/oxide chamber of type *Createc RS-3* is used for evaporating the AlOx capping layer implemented for all samples. As for the TI chamber, it also contains a ℓN_2 shroud and a base pressure of $< 9 \cdot 10^{-11}$ mbar can be reached. For the capping layer a home-built e-beam source is used to evaporate AlOx from a tablet of pressed powder. The material fluxes in this chamber are determined by the frequency modulation of quartz oscillators due to material deposition. Like the TI chamber, the M/O MBE is equipped with a RHEED gun and the manipulator is heated by a tantalum filament and can carry wafers up to two inches. A shutter can be adjusted such that the sample is exposed only partially to the respective material flux. This is crucial, since in every growth run one TI sample is prepared, where a small stripe is shielded from the AlOx exposure to allow post-growth determination of the sample's material composition via X-ray photoelectron spectroscopy (XPS) and the investigation of the topography of the pristine surface by means of atomic force microscopy (AFM) (see below).

4.2 Growth procedure

The following will provide an overview over the general growth procedure, detailed parameters utilized for the respective TI samples can be found in appendix A.
After the $SrTiO_3$ substrates are transferred into the UHV of the TI MBE chamber via a load lock and placed onto the manipulator, a pre-growth preparation routine is applied to remove possible contamination and to saturate dangling bonds to improve the interface with the subsequently grown TI material. The substrate temperature for the epitaxial process, set by the heating filament of the manipulator, has to be carefully adjusted. If it is too low, no single crystalline growth is possible, but if it is too high the evaporated atoms won't stick to the substrate surface. The *sticking coefficient* essentially specifies the probability of an impinging atom to stick to a surface and is not only dependent on the temperature, but also on structural details of the surface and the type and kinetic energy of the atom [68, 69]. Together with the provided fluxes of the used elements, this sticking coefficient determines the final composition of the TI sample. The fluxes are adjustable by the temperature of the Knudsen cells in the case of Bi, Se, and Te and by the valve opening of the cracker cell for Sb. The adjustment of the fluxes to precisely yield the targeted stoichiometry is highly complex and based on empirical values obtained from post-growth investigations of sample compositions via XPS. Due to a much lower sticking coefficient of tellurium and selenium at the used growth temperatures, the growth of the $(Bi,Sb)_2(Te,Se)_3$ V-VI compounds has to be performed in an overpressure regime of the group VI element. The V:VI ratio lies between at least 1:3 and approximately 1:10. Moreover, the experimental investigations presented in this thesis not only rely on fine adjustment of TI stoichiometry, but also on precise modulation of sample thicknesses. In principle, the thickness is varied simply by the growth time. However, since the growth time per QL depends on the fluxes of the single elements, it is dependent on the desired

stoichiometry and must be obtained from RHEED oscillations (see below), that are visible in our growth procedure even during rotated growth that is necessary to guarantee homogeneous exposure of the substrate. After the required thickness is reached, the samples are annealed under remaining group VI element overpressure and then transferred in-situ via the vacuum tube to the metal/oxide chamber. There, usually one of the three samples is covered by a 10 nm film of permalloy for spin-pumping experiments[1], before all three samples are capped by a 7 nm layer of inert AlOx for controlled passivation of the surface. As mentioned above, a small stripe of one of the samples without the FM layer is shielded from the AlOx exposure. After transferring the samples out of the MBE system, this stripe of pristine TI is used to verify the targeted stoichiometry by XPS and to image the surface topography via AFM. To prevent surface contamination, the sample is introduced into the vacuum environment of the XPS setup immediately after it is unloaded from the MBE, usually on a time scale below 15 minutes.

4.3 Growth monitoring

The complexity of the epitaxial preparation of the TI films requires thorough monitoring to enable sufficient sample quality and reproducible results. RHEED imaging is used to examine the TI crystallinity and to adjust the sample thickness, while XPS allows the precise determination of the sample stoichiometry. Like the growth procedure itself, these tools were applied by Dr. Matthias Kronseder.

4.3.1 Reflection high-energy electron diffraction

Basic principle
Reflection high-energy electron diffraction (RHEED) is a standard auxiliary tool for molecular beam epitaxy and all chambers of the Regensburg MBE cluster are equipped with the respective setup. The basic operating principle is sketched in Fig. 4.2 a). The sample is mounted to the manipulator and an electron beam generated by an electron gun (e-gun) of 15-20 keV is focussed onto the sample surface. Due to the gracing incidence angle, the beam gets deflected only by the topmost surface layer and the diffraction pattern gets converted into photons by a fluorescent screen and recorded by a CCD camera. From the obtained diffraction pattern conclusions concerning the sample's crystallinity and surface structure can be drawn [70].

Typical patterns
Typical RHEED patterns are displayed in Fig. 4.2 b) - d). For a perfect two-dimensional surface and ideal measurement conditions the electron beam would be diffracted onto spots on the zeroth order Laue circle above the shadow edge as indicated in the right

---

[1]Performed within a collaboration by the Group of Prof. Dr. C. H. Back of the Technical University of Munich.
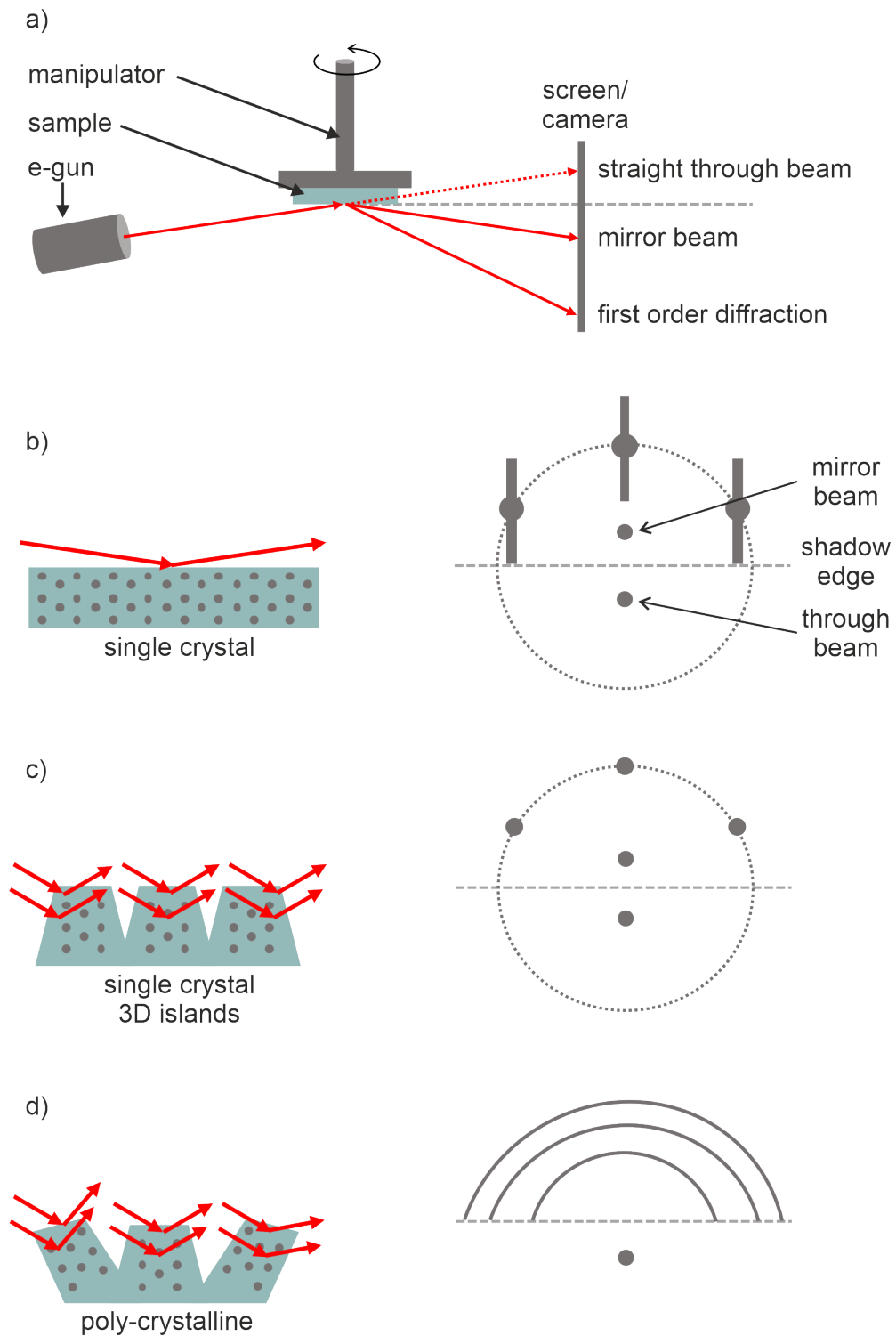
Figure 4.2: a) Basic principle of RHEED imaging. b) - c) Illustration of expected patterns for single crystal- (a), 3D island- (b), and poly-crystalline growth (c). Adapted from [70, 71].

panel of sub-figure b). Small imperfections, however, lead to an elongation of the spots into stripes. If a single crystalline sample has a three-dimensional surface, a regular pattern of spots away from the Laue circle (c) can be observed in the RHEED image. In the poly-crystalline case, sketched in panel d), where the sample consists of randomly distributed crystallites with different orientations, the diffraction yields a pattern of concentric rings. More details on the RHEED operating principle and the origin of the introduced diffraction patterns can be found in Refs. [70–73]. Such RHEED images have been obtained for every TI sample and only those samples showing the desired stripe patterns as shown in panel b) indicating single crystal growth were used for further experimental investigations.

Thickness determination

A further key capability of RHEED imaging is the tracking of sample thickness during the growth process by evaluating intensity oscillations of the mirror beam. If the crystal grows layer-by-layer, the mirror spot will reach its maximal intensity when the surface is completely closed. In between fully closed layers the intensity decreases and is minimal for half closed surfaces. Hence, the number of grown layers can be determined by counting the number of maxima of the obtained RHEED oscillations [70].

4.3.2 X-ray photoelectron spectroscopy

While no X-ray photoelectron spectroscopy (XPS) measurements will be directly shown in this thesis, the basic principle is still briefly introduced in the following, since this tool plays an important role for the calibration of the MBE beam fluxes to yield the desired TI stoichiometry, as well as validate the targeted composition after the growth process. Very similar to angle-resolved photoemission spectroscopy (see below), XPS is based on the photoelectric effect. The sample is exposed to electromagnetic X-ray radiation leading to an ejection of electrons from the surface-near layers. The kinetic energy E_{kin} of these photoelectrons is measured using a hemispherical analyser allowing to obtain the binding energy E_{bin} via

$$E_{bin} = h\nu - \Phi - E_{kin}, \tag{4.1}$$

where h is Planck's constant, ν the X-ray frequency and Φ the work function of the detector. This binding energy is characteristic for the atom the electron was bound to. Hence, by statistical analysis of the binding energies of the collected electrons the elemental composition of the sample can be determined. Extensive information about this technique can be found, for example, in Refs. [74–76].

<div align="right">

5

</div>

Measurement methods

The following chapter is dedicated to the measurement methods and setups utilized in this thesis. Magnetotransport serves as the ideal tool to investigate the electronic properties of the topological insulator samples. By varying the temperature down to cryogenic conditions, applying static gate voltages or magnetic fields with varying angle, we not only characterize our materials, but also obtain insight that helps to disentangle different contributions to transport and creates the necessary feedback for the improvement of the topological insulator quality throughout this thesis. In chapter 8, the same tools are, furthermore, used to explore the rich field of contributions to magnetoresistance (MR) in topological insulators, a crucial quantity for the understanding of electronic transport of such materials. As additional characterization tools, atomic force microscopy (AFM) and angle-resolved photoemission spectroscopy (ARPES) are used in this thesis to image the samples' surface topography and surface band structure, respectively.

5.1 Electronic transport measurements

5.1.1 Sample patterning and measurement geometry

To employ magnetotransport measurements, all samples were patterned into a Hall-bar geometry under clean-room conditions. The preparation process is schematically pictured in Fig. 5.1. The Hall-bar mesa is patterned by standard optical lithography, before the surface areas uncovered by photoresist are etched by chemical assisted ion beam etching (CAIBE), as illustrated in panel b). After removing remaining resist from the sample, another lithography step is employed to allow e-beam evaporation of $10\,\mathrm{nm}$ titanium and 100 gold onto the Hall-bar contact pads that are used for electrical contacting. Detailed recipes of the patterning process are given in appendix B. The finished Hall-bar is wire-bonded to a commercial 20-pin socket and used to perform standard four-point, low-frequency lock-in measurements to obtain the longitudinal resistance R_{xx} and, if a
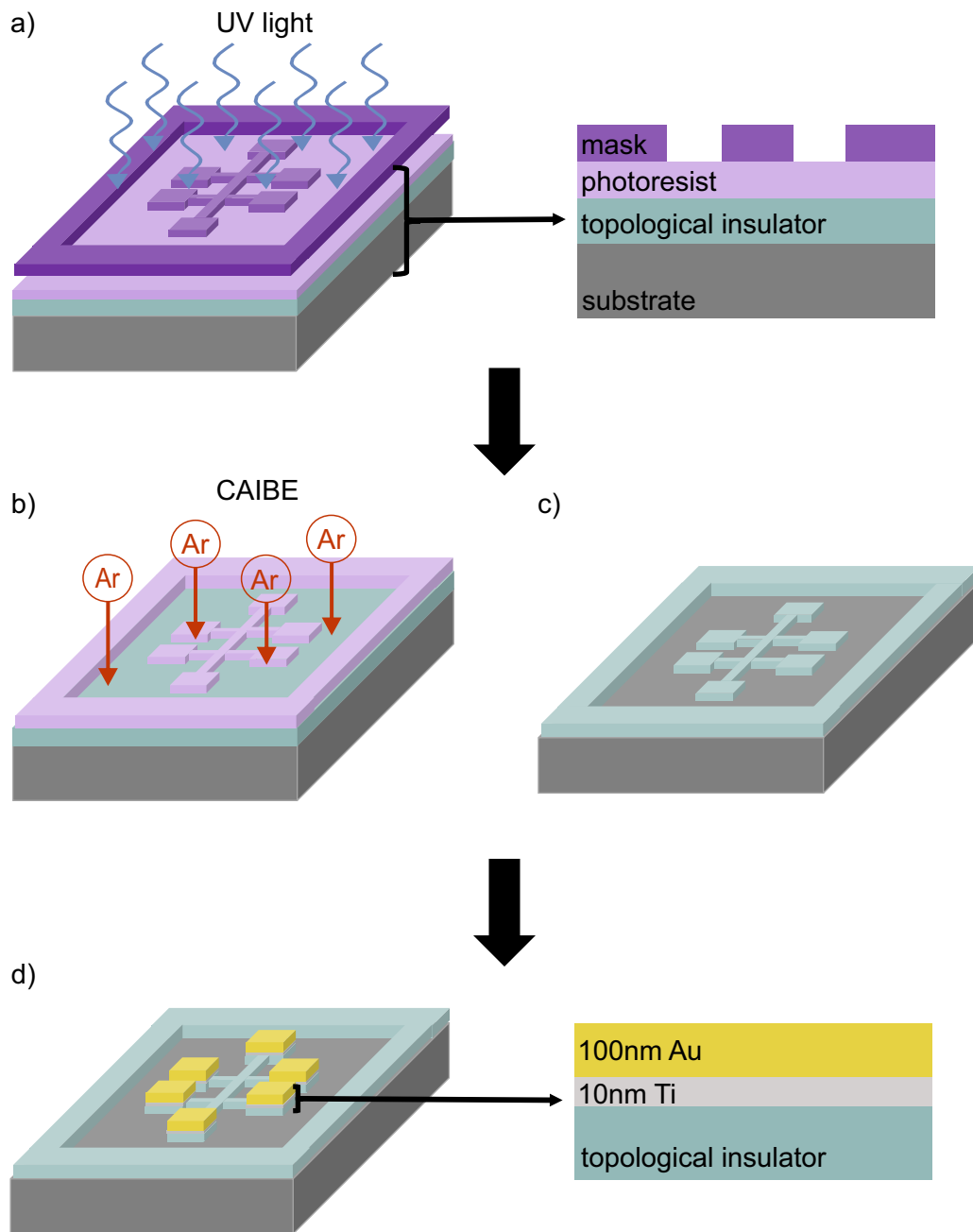
Figure 5.1: Illustration of the patterning process. a) Optical lithography of the resist covered sample using a shadow mas and ultra-violet (UV) light. b) Chemical-assisted ion beam etching (CAIBE) using argon. c) Patterned Hall-bar mesa after resist lift-off. d) Finished sample after electron beam evaporation of 10 nm titanium and 100 nm gold onto the contact pads.
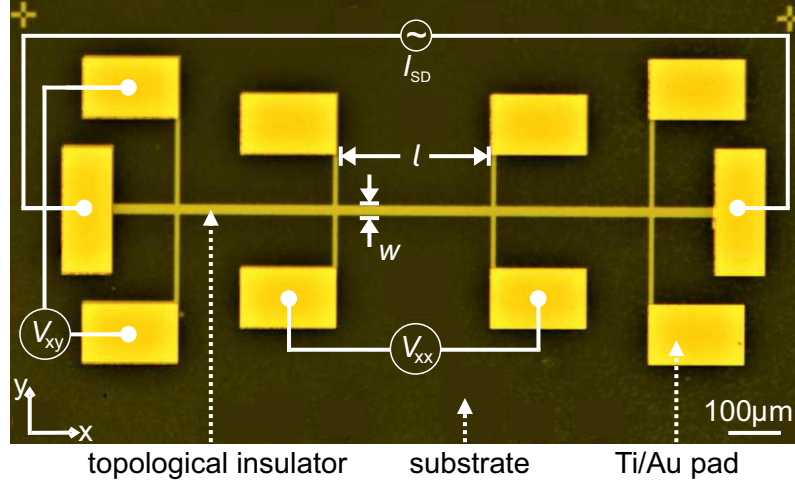
Figure 5.2: Optical photograph of the lithographically defined Hall-bar and indicated connections for I_{SD}, V_{xx}, V_{xy}, width $w = 20\,\mu m$, and length $l = 300\,\mu m$.

perpendicular magnetic field **B** is applied, the horizontal Hall resistance R_{xy} of the TI sample.

In the majority of the presented measurements, the internal oscillator of the lock-in generates a sinusoidal AC voltage of 5 V at a frequency of 7 Hz that is transformed into a current I_{SD} via a pre-resistor at the lock-in output of usually 10 MΩ. Figure 5.2 shows an optical image of a finished Hall-bar device and the measurement geometry. The current is applied between the source and drain contacts of the Hall-bar and measured simultaneously with the longitudinal and horizontal voltage drops V_{xx} and V_{xy} to obtain the resistances via

$$R_s = R_{xx} \cdot \frac{w}{l} = \frac{V_{xx}}{I_{SD}} \cdot \frac{w}{l} \tag{5.1a}$$

$$R_{xy} = \frac{V_{xy}}{I_{SD}}. \tag{5.1b}$$

Here, the sheet resistance R_s equals the measured longitudinal resistance R_{xx} normalized to the Hall-bar geometry by the dimensionless factor w/l, with the width $w = 20\,\mu m$ and length $l = 300\,\mu m$ for the Hall-bars used in this thesis (see Fig. 5.2). To highlight this normalization, R_s is given in units of *Ohms per square* ($\Omega/\square$). In general, the sheet conductance is given by [50]

$$G_s = \frac{R_s}{R_s^2 + R_{xy}^2}. \tag{5.2}$$

In absence of a perpendicular magnetic field ($\Rightarrow R_{xy} = 0$) or if $R_s \gg R_{xy}$ this simplifies to $G_s = 1/R_s$. A more detailed description of the four-point method in a Hall-bar geometry

can be found in e.g. Refs. [50, 77]. Throughout this thesis, such measurements have been performed with respect to magnetic field, temperature, and static gate voltage. A detailed measurement protocol including typical issues unique to the samples investigated will be given in appendix C.

5.1.2 Comments on quantitative analysis of Hall measurements

From a Hall-bar measurement in non-zero perpendicular magnetic field and underlying a semiclassical, two-dimensional Drude model for electronic transport of a *single* channel, one can in principle calculate the charge carrier density n and their respective mobility μ of a thin film as [50]

$$n = \frac{1}{q_i \cdot R_{xy}/dB|_{B=0}}, \tag{5.3a}$$

$$\mu = \frac{dR_{xy}/dB|_{B=0}}{R_s(B=0)}, \tag{5.3b}$$

where e is the elementary charge. In three dimensions, the charge carrier density and mobility for a sample of thickness t take the form $n^{3D} = n/t$ and $\mu^{3D} = \mu \cdot t$. However, the situation becomes more complex, when more than one transport channel is contributing to the electronic transport. Most generally, in a system consisting of N channels the longitudinal and horizontal conductivities result from the summations [51, 52]

$$\sigma_{xx} = \sum_i^N \frac{|q_i \cdot n_i \cdot \mu_i|}{1 + (\mu_i \cdot B)^2}, \tag{5.4a}$$

$$\sigma_{xy} = \sum_i^N \frac{q_i \cdot n_i \cdot \mu_i^2 \cdot B}{1 + (\mu_i \cdot B)^2}, \tag{5.4b}$$

where each channel i contributes with a charge carrier density n_i, mobility μ_i, and with $q_i = \pm e$ depending on the charge carrier type.

In research on topological insulators, where rarely only a single conduction channel is present, often two- [78–81] or even three-band [82] models are fitted to R_{xy} to extract quantitative values of n and μ for the respective channels. Such a procedure will not be applied within this thesis for the following reasons: first, when assuming a single conduction channel model, a completely horizontal behavior under applied magnetic field, which is expected for TI samples with the Fermi level located near the charge neutrality point, implies an infinite charge carrier density according to Eq. (5.3a), which is un-physical [38, 83, 84]. Second, underlying a multi-channel Drude model introduces at least four free parameters to the fit in the case of two channels (see Eq. (5.4b)), what
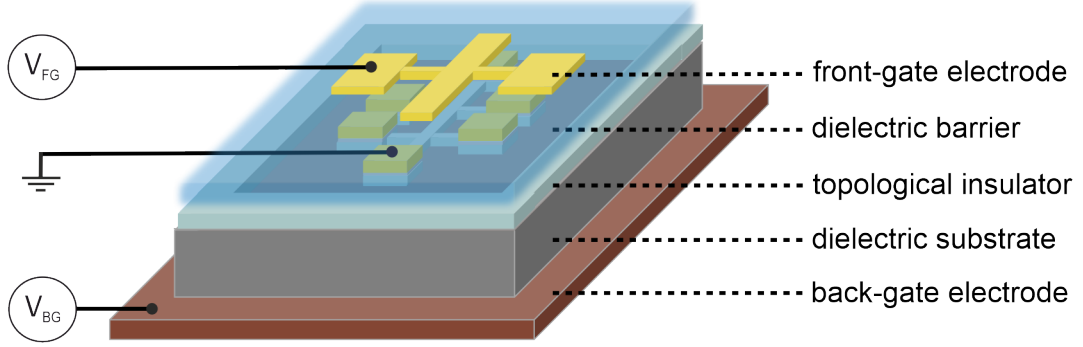
Figure 5.3: Schematic drawing of a dual-gated device.

renders the obtained values unreliable [38, 52, 85]. Often, the zero-field value of R_s is used as a constraint to increase the fit's precision, but this disregards strong influences to R_s by corrections to the conductivity like weak anti-localization or electron-electron interaction. Measurements of R_{xy} are still valuable, however, since the sign of the slope is determined by the dominant charge carrier type, providing additional insight into the underlying band structure contributing to transport. Moreover, sign reversal helps to monitor changes to the electronic properties introduced by gating or variation of the sample thickness.

5.1.3 Gate dependent electronic transport

Besides investigating the electronic transport behavior under varying temperatures or magnetic fields, electrostatic gating has been a key instrument employed in this thesis. Similar to a classical capacitor, applying a potential difference between the gate electrode and the sample leads to an accumulation or depletion of charge carriers in the TI by means of the field effect, allowing to externally tune the electronic properties of the topological insulators. The gating capability has been implemented in a back-gate (BG), as well as a front-gate (FG) geometry. Figure 5.3 shows a schematic of a device with both gates. To create a potential difference, a voltage V_{FG} or V_{BG} is applied to the FG or BG electrode, respectively, while the sample is held at ground potential via the Hall-bar contacts. An insulating, dielectric barrier separates both electrodes from the Hall-bar. For the FG, this dielectric is a thin layer of SiO_2/Al_2O_3 deposited by plasma-enhanced chemical vapor deposition (PECVD) and atomic layer deposition (ALD), respectively, and an electron beam evaporated Ti/Au electrode is placed directly above the Hall-bar channel. Details on the preparation process and common issues will be given in appendix B. To gain back-gate functionality, the majority of samples in this thesis were grown on $SrTiO_3$ (STO) substrates. Despite the large thickness of $500\,\mu m$, STO can function as the dielectric barrier due to its ultrahigh relative permittivity ϵ_r at cryogenic temperatures [86, 87]. A scan of ϵ_r^{STO} with respect to temperature will be shown in chapter 6. Rreliable implementation of the BG is achieved by using conductive silver epoxy to glue the samples to the likewise conductive bottom of the chip carrier that serves as the electrode.

5.1.4 Magnetotransport measurement setups

Concerning magnetotransport, mainly two setups have been utilized for the presented measurements. All TI samples were characterized by a standard protocol developed in this thesis in a ^{4}He dewar using a dipstick technique. For further investigations on magnetoresistance effects, selected samples were examined using an *Oxford Instruments Spektromag SM-4000* cryostat.

^{4}**He dewar**

In the ^{4}He dewar system, a magnet rod equipped with superconducting coils capable of generating magnetic fields up to ± 5 T is lowered directly into the liquid Helium (ℓHe) bath. Using a needle valve, the magnet rod can be filled with ℓHe. The sample, glued to a 20-pin socket, is mounted to a dipstick that connects every contact of the socket to the outside via coaxial cables and is inserted into the magnet rod such that the magnetic field is oriented perpendicular to the sample. During lowering of the sample rod, the temperature of the investigated TI steadily decreases from room temperature to 4.2 K, measured by a *Lakeshore DT-600* silicon Diode, allowing to obtain the temperature dependence of the sample resistance. The temperature data, as well as the obtained signals for, I_{SD}, V_{xx}, and V_{xy} measured by the connected lock-ins, is digitally transferred via a GPIB-interface to a computer and evaluated by a *Labview* program. Continuous magnetic field sweeps are performed between ± 5 T at 4.2 K. For gate dependent measurements, *Yokogawa 7651* and *Keithley 2410* voltage sources are connected to the gate electrode. More details concerning this measurement setup are elaborated in Refs. [88] and [89].

Oxford Instruments Spektromag SM-4000 cryostat

A schematic drawing of the *Oxford Instruments Spektromag SM-4000* cryostat is shown in Fig. 5.4. It provides two main additional functionalities over the ^{4}He dewar system: first, the inserted sample rod is rotatable by 360° along its vertical axis, allowing continuous adjustment of the magnetic field angle between out-of-plane (OOP) and in-plane (IP) orientation with respect to the sample surface. Second, due to the *variable temperature insert* (VTI) design, it is possible to hold the sample temperature constant between 1.4 K and 300 K while applying magnetic fields up to ± 7 T utilizing superconducting coils. The coils are installed inside the ℓHe bath that is surrounded by a liquid nitrogen shield. A needle valve controls the flow of ℓHe from the reservoir into the VTI, where a connected rotary pump reduces the vapor pressure. This yields a base temperature of 1.4 K that can be adjusted via two heating elements, one inside the VTI and one mounted to the sample rod, controlled with PID-regulated *intelligent temperature controllers* (ITCs) within 0.1 K precision. The temperature is measured by a *Cernox*-sensor located close to the sample. Equivalent to the ^{4}He dewar system, all 20 pins of the sample socket are connected by coaxial cables to the outside, where the connected lock-ins measure and transfer the signals via a GPIB-interface to a *Labview* program [70, 88].

Transfer tube entry

VTI top flange

20-pin socket with sample

liquid helium reservoir

Sample rod

VTI sample space

Magnet coils

Heat exchanger

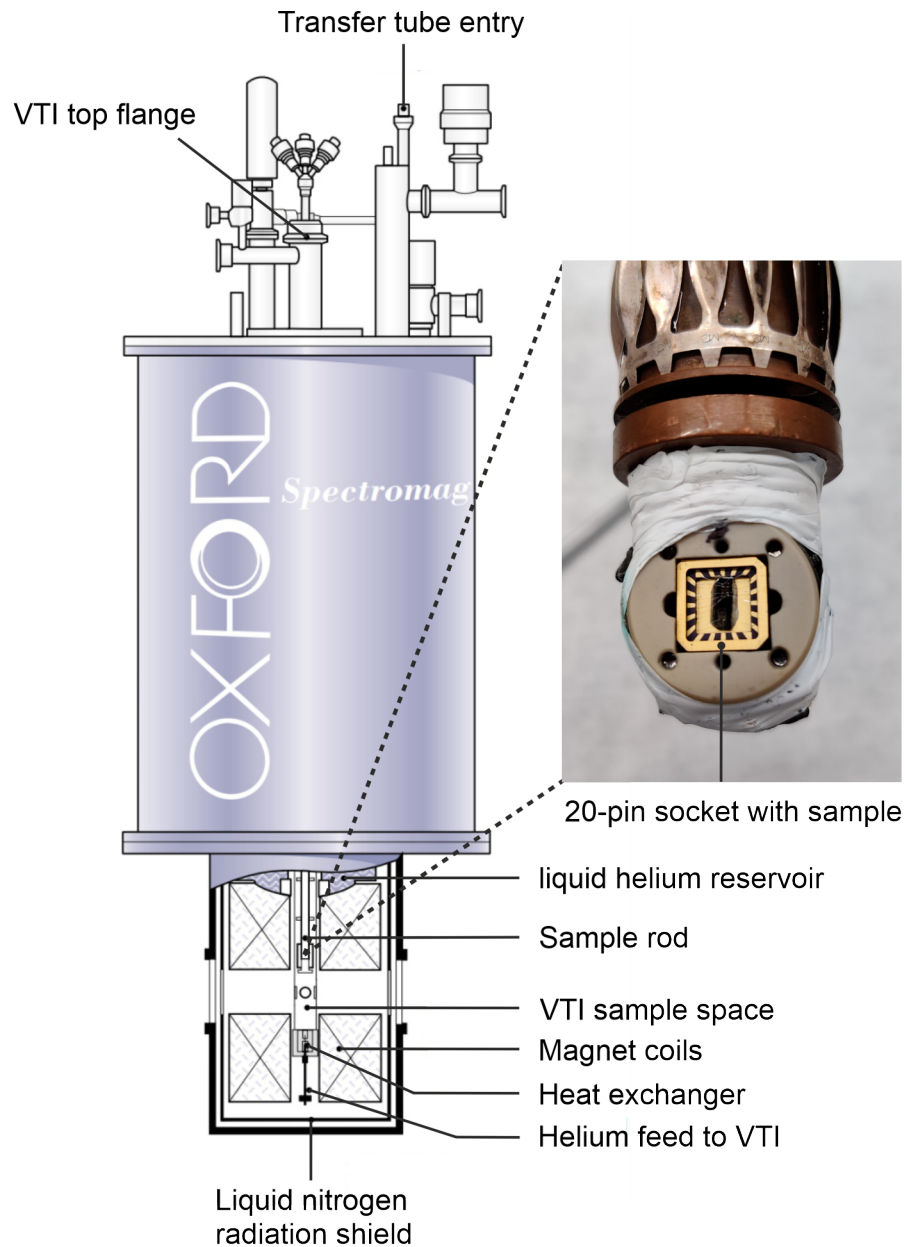Helium feed to VTI

Liquid nitrogen radiation shield

Figure 5.4: Schematic drawing of the Oxford Instruments Spektromag SM-4000 cryostat and image of a sample glued and bonded to a 20-pin socket and mounted to the sample rod (adapted from [70, 90]).

5.2 Additional characterization methods

As additional tools to characterize the samples, atomic force microscopy (AFM) and angle-resolved photoemission spectroscopy (ARPES) were utilized in this thesis to map the samples' surface topography as well as the surface band structure, respectively.

5.2.1 Atomic force microscopy

Atomic force microscopy (AFM) is a powerful technique to map the surface topography of solids. In this thesis a commercial *Bruker Dimension Icon-PT* system with a *NanoScope V* controller was utilized in ambient conditions and operated in *tapping mode*. To facilitate this microscopy technique, a sharp tip with a radius on the nanometer scale is mounted to a cantilever, closely approached to the sample and scanned over a user-defined area of the surface. Depending on the sample topography the interactions between surface and tip cause a deflection of the cantilever. The subsequent cantilever bending is measured by the deflection of a laser beam that is reflected from the cantilever back and measured via photo diodes. In tapping mode the cantilever is excited to oscillations by a piezo element with a constant frequency close to the the resonance frequency and slightly "taps" the sample surface. The forces between surface and tip cause a modulation of the oscillation amplitude from which a three-dimensional image of the surface topography over the scanned surface area can be obtained. Detailed introductions to atomic force microscopy can be found in Refs. [91–93]. In principle, the method is capable of atomic resolution. The images obtained for this thesis covered areas on the scale of $1\,\mu m^2$ to provide a mesoscopic overview of the surface roughness.

5.2.2 Angle-resolved photoemission spectroscopy

Angle-resolved photoemission spectroscopy is one of the most powerful tools to investigate the exotic surface electronics of topologically non-trivial materials. Closely related to XPS, ARPES as well utilizes high-frequency radiation to extract and analyze electrons from the investigated solids. However, instead of only determining the kinetic energy, ARPES maps the kinetic energy *and* the momentum of the emitted photoelectrons and therefore allows to directly image the electronic band dispersion of a crystalline solid up to the Fermi level. All ARPES measurements presented in this thesis were performed at the low energy *Advanced Photoelectric Effect* (APE-LE) beamline of the *Elettra* synchrotron radiation facility in Trieste, Italy. An extensive description of the experimental setup and the measurement technique is given in Refs. [94–97] and the references therein, based on which the following provides a brief introduction.

Equivalent to XPS, the sample is exposed to electromagnetic radiation of frequency ν and electrons are emitted due to the photoelectric effect with a kinetic energy E_{kin} of

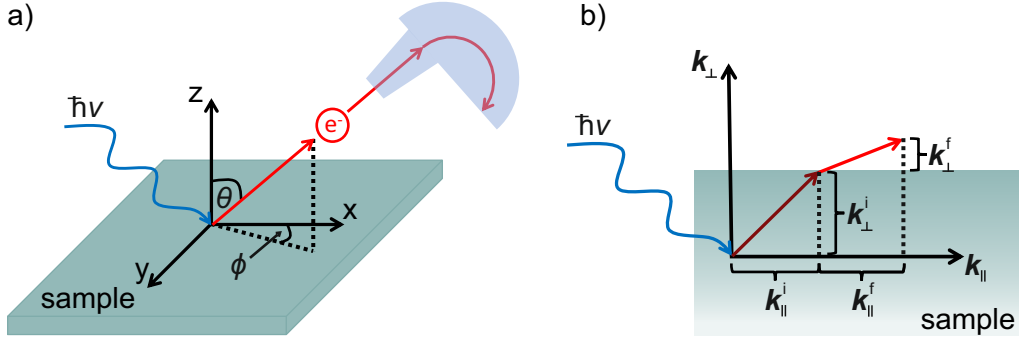$$E_{kin} = h\nu - \Phi - |E_{bin}|, \tag{5.5}$$

Figure 5.5: Illustration of ARPES measurement principles. a) Measurement geometry. b) Comparison of initial and final k-vectors.

where h is Planck's constant, Φ the detector's work function, and E_{bin} the binding energy of the state the electron occupied before emission. The final wave vector $\boldsymbol{k}^{\text{f}}$ of the photoelectron is connected with the kinetic energy via the final momentum $\boldsymbol{p}^{\text{f}}$ by the *de-Broglie* relation

$$\boldsymbol{k}^{\text{f}} = \frac{\boldsymbol{p}^{\text{f}}}{\hbar} = \frac{\sqrt{2m_{\text{e}}E_{\text{kin}}}}{\hbar}. \tag{5.6}$$

With the unit vectors $\hat{\boldsymbol{k}}_{\text{x,y,z}}$ and the polar (θ) and azimuthal angle (ϕ) (see Fig. 5.5a), $\boldsymbol{k}^{\text{f}}$ can be broken down into its components

$$\boldsymbol{k}^{\text{f}}_{\parallel} = \boldsymbol{k}^{\text{f}}_{\text{x}} + \boldsymbol{k}^{\text{f}}_{\text{y}} = \frac{1}{\hbar}\sqrt{2m_{\text{e}}E_{\text{kin}}}\sin\theta(\cos\phi \cdot \hat{\boldsymbol{k}}_x + \sin\phi \cdot \hat{\boldsymbol{k}}_y) \quad \text{and} \tag{5.7a}$$

$$\boldsymbol{k}^{\text{f}}_{\perp} = \boldsymbol{k}^{\text{f}}_{\text{z}} = \frac{1}{\hbar}\sqrt{2m_{\text{e}}E_{\text{kin}}}\cos\theta \cdot \hat{\boldsymbol{k}}_z. \tag{5.7b}$$

Using a hemispherical electron energy analyzer in UHV, the kinetic energy and the emission angle θ of the photoelectrons can be measured, directly yielding the binding energy E_{bin} and the magnitude of the final wave vector $\boldsymbol{k}^{\text{f}}$ following Eqs. 5.5 and 5.7, respectively. Due to the translational symmetry of the periodic lattice, the parallel component of the wave vector is conserved by the photoemission process (as sketched in Fig. 5.5b) and therefore the initial wave vector in the x-y-plane is

$$\boldsymbol{k}^{\text{i}}_{\parallel} = \boldsymbol{k}^{\text{f}}_{\parallel} \quad \text{with} \tag{5.8a}$$

$$|\boldsymbol{k}^{\text{i}}_{\parallel}| = |\boldsymbol{k}^{\text{f}}_{\parallel}| = \frac{1}{\hbar}\sqrt{2m_{\text{e}}E_{\text{kin}}}\sin\theta. \tag{5.8b}$$

From this, the dispersion of the binding energy parallel to the sample surface can be imaged, generating a complete picture of the electronic structure for two-dimensional

systems such as ultra-thin films or surface states. For three-dimensional (3D) materials with a non-zero dispersion in z-direction, also $k_\perp^i$ has to be reconstructed. Perpendicular to the sample surface the symmetry is broken and $k_\perp^i \neq k_\perp^f$, making this component not immediately accessible by the measurement. However, approximating the final state with a nearly free-electron model and assuming a parabolic dispersion of the 3D bands, $k_\perp^i$ is given by

$$k_\perp^i = \frac{1}{\hbar} \sqrt{2m_e(E_{kin}\cos^2\theta + V_0)}, \tag{5.9}$$

where V_0 is a material dependent constant that can be obtained by photo energy-dependent measurements.

In the utilized setup of the *Elletra* synchrotron, the sample is mounted to a rotatable manipulator in UHV, cooled to 77 K by liquid nitrogen and illuminated by X-ray radiation of energies between 15 and 90 eV in an angle of 45° with a spot size of 150 μm × 50 μm. The emitted photoelectrons are collected by a *Scienta DA30* hemispherical analyzer and focused onto a CCD camera. The setup is furthermore equipped with a vectorial spin polarimeter based on the very low energy electron diffraction (VLEED) technique that allows to spin-resolve the photoelectrons by exploiting the exchange coupling of the spin with a ferromagnetic target. Combining the angle- and the spin-resolution, this photoemission experiment allows direct demonstration of the spin-momentum-locked topological surface states in TIs.

III Experimental results

6

Towards quaternary
$(Bi_{1-x}Sb_x)_2(Te_{1-y}Se_y)_3$ alloys

Among the most widely investigated MBE-grown 3D TIs are the binary alloys of the $(Bi,Sb)_2(Te,Se)_3$ V - VI compound family, especially Bi_2Se_3 (BS). Its tetradymite crystal structure is built up by quintuple layers (1 QL $\approx$ 1 nm) with weak van der Waals (vdW) interlayer bonding, enabling successful growth on a variety of substrates via vdW epitaxy and high crystallinity was achieved by precise optimization of growth conditions [98, 99]. Furthermore, ab-initio calculations of BS showed a prototypical TI band structure with linearly dispersing topological surface states (TSS) within a comparably large band gap of approximately 300 meV and the Fermi level E_F intersecting the TSS at the Dirac point in the middle of the gap [27]. In real samples, however, angle resolved photoemission spectroscopy (ARPES) measurements routinely revealed a shift of E_F to the bulk conduction band [100, 101]. This shift is caused by lattice defects, mainly Se vacancies and Se_{Bi} anti-sites depending on the growth conditions, that have a low formation energy and effectively induce a large donor-type doping in the bulk of the material [102–104]. Due to the parasitic contribution of the resulting occupied bulk states at the Fermi level to electronic transport, exploiting the unique characteristics of the topological surface states is hampered. The large amount of unintentional bulk dopants is generally shared by all binary Bi-based 3D TI alloys, where the character of doping can be p-type (excess acceptors) or n-type (excess donators) depending on the specific material. For example, besides the intrinsically donor-heavy Bi_2Se_3, Sb_2Te_3 usually shows p-type character, whereas the excess dopant in Bi_2Te_3 depends on the growth conditions [102, 105, 106]. A possible strategy to counter parasitic bulk dopants is the alloying of different binary compounds with opposite excess charge carriers. A significant reduction of bulk carriers has for example been achieved by combining the n-type Bi_2Se_3 with p-type Bi_2Te_3 to the ternary compound Bi_2Te_2Se [98, 105, 107]. Another extensively studied ternary alloy is $(Bi_{1-x}Sb_x)_2Te_3$ (BST), formed by n-type Bi_2Te_3 and the p-type Sb_2Te_3. Here, the stoichiometric parameter x not only influences the density of bulk carriers, but the position of the Dirac point (DP), and the band gap size [108]. Further expansion of

the system to the quaternary alloy $(Bi_{1-x}Sb_x)_2(Te_{1-y}Se_y)_3$ (BSTS) in principle allows to compensate unintentional bulk dopants, while providing separate control over the key band structure parameters by varying x and y. This opens a pathway to custom band engineered 3D topological insulators with minimized bulk contributions to transport. However, MBE of ternary and especially quaternary alloys is challenging. Expanding the alloy complicates the growth procedure, increases the amount of atomic disorder naturally occurring in those systems, and reduces the amount of suitable substrates, since a large lattice mismatch induces crystal defects. One of the main goals of this thesis was to establish MBE-grown BSTS samples with predictable and reproducible electronic properties dependent on the stoichiometric parameters. This chapter is dedicated to the preliminary work towards the development of reliable quaternary samples. At first, Sec. 6.1 will introduce strontium titanate ($SrTiO_3(111)$, STO) as a substrate for the epitaxial preparation of our Bi-based three-dimensional topological insulator samples. To reduce the parameter space, we started our investigations with the ternary alloy BST utilizing magnetotransport and ARPES measurements, what will be presented in section 6.2. In Sec. 6.3, the first tests of BSTS growth directly onto a substrate will be discussed along with arising common issues, which we ascribe to insufficient crystallinity of the investigated films. A major leap in improving the crystal quality and simultaneously simplifying the growth procedure will be presented in Sec. 6.4, where the significant benefits of the implementation of a Bi_2Se_3 seed layer will be demonstrated. Utilizing this seed layer sample design is the starting point towards the establishment of high quality quaternary $(Bi_{1-x}Sb_x)_2(Te_{1-y}Se_y)_3$ alloys that are investigated more deeply in the subsequent chapters.

6.1 $SrTiO_3(111)$ as growth substrate

For the samples presented and discussed in this thesis $SrTiO_3(111)$ was used as the substrate for the molecular beam epitaxy.[1] Usually for epitaxial processes, the choice of substrate is of crucial importance as it bonds covalently or ionically to the deposited material and hence determines the crystal structure of the first layers. An optimized lattice matching of substrate and epitaxial film therefore leads to a minimization of strain and interface defects. For more loosely, van-der-Waals epitaxial materials like the Bi-based TIs, however, this requirement of lattice matching is less significant [109–111]. In Ref. [109], for example, Si(111) and InP(111) are compared for the growth of Bi_2Se_3. While Si(111) has a lattice mismatch of 7.8 %, the InP(111) is almost perfectly matched (0.2 %). Still, only slight differences were observed in terms of crystal quality and electronic properties of the topological insulator. STO(111) and $Al_2O_3(0001)$, on the other hand, have lattice mismatches to BS of 5.8 % and 13 %, respectively [112]. An important indicator for the growth quality is the surface topography. Figures 6.1 a) - d) compare AFM images of two sets of samples grown on STO and Al_2O_3 with a layer stack of

---

[1]With the exception of two samples discussed within Sec. 6.3, which will be highlighted there.

2 QL BS and 4 QL BSTS and 2 QL BS and 17 QL BSTS, respectively, where the color scale indicates surface roughness via the height z. While for the thicker samples in c) and d) the surface structure looks almost identical, the thinner samples show a slightly preferable topography for the STO substrate due to overall larger island sizes and less granular growth. Overall, however, all four samples show comparable roughness with two open layers on top of an almost completely closed film and hence no significant benefit of one substrate over the other is found in terms of sample topography.

The decisive advantage leading to the choice of STO as a substrate for the samples discussed in this thesis are its unique dielectric properties. Figure 6.1 e) shows the dielectric constant ϵ_r of STO with respect to temperature obtained from a capacitance measurement as sketched in panel f). A bare STO substrate of a thickness $t \approx 500\,\mu m$ and surface area $A = 14.4\,mm^2$ was covered by a thin layer of gold and glued using conductive silver epoxy to a socket compatible with the ^{4}He dewar setup described in chapter 5.1.4. The Au and Ag layers act as metallic plates of a classical capacitor with the STO as the dielectric. From a Lock-in amplifier an AC voltage $\tilde{V} = 0.03$ V with a frequency of $f = 1913\,Hz$ was applied and the resulting AC current $\tilde{I}$ was measured using the quadrature input channel of the Lock-in. From this, the relative permittivity can be obtained as

$$Z = \frac{\tilde{V}}{\tilde{I}} = \frac{1}{2\pi f C} \tag{6.1a}$$

$$\Rightarrow C = \epsilon_0 \epsilon_r \frac{A}{t} = \frac{\tilde{I}}{2\pi f \tilde{V}} \tag{6.1b}$$

$$\Rightarrow \epsilon_r = \frac{1}{2\pi f \epsilon_0} \frac{A}{t} \frac{\tilde{I}}{\tilde{V}}, \tag{6.1c}$$

where C is the capacitance and ϵ_0 the vacuum permittivity. Starting at room temperature, ϵ_r already shows a comparatively high value of ≈ 300 that is steadily enhanced when reducing T. Approaching $T \approx 100\,K$, the rate drastically reduces with a maximum at about 55 K. Below $T = 25\,K$, ϵ_r then saturates at a value of almost 7000. This dependence can be partly explained by temperature dependent changes in the crystal structure. STO, that has a direct band gap of 3.75 eV and an indirect of 3.25 eV [113], shows a cubic perovskite ordering at room temperature that changes to tetragonal at $T \approx 110\,K$ and to orthorhombic at $T \approx 65\,K$ [114]. Below the orthorhombic phase transition temperature the application of a static electric field can influence ϵ_r as the more loosely bound strontium atoms are displaced with respect to the tightly bonded oxygen and titanium. A detailed explanation of the microscopic processes causing these unique paraelectric characteristics are beyond the scope of this thesis and can be found e.g. in Ref. [114]. However, for practical purposes, due to this ultra-high relative permittivity at low temperatures, the STO substrate can function as back-gate dielectric allowing easy implementation of electrostatic gating to tune the electronic properties of the investigated samples.
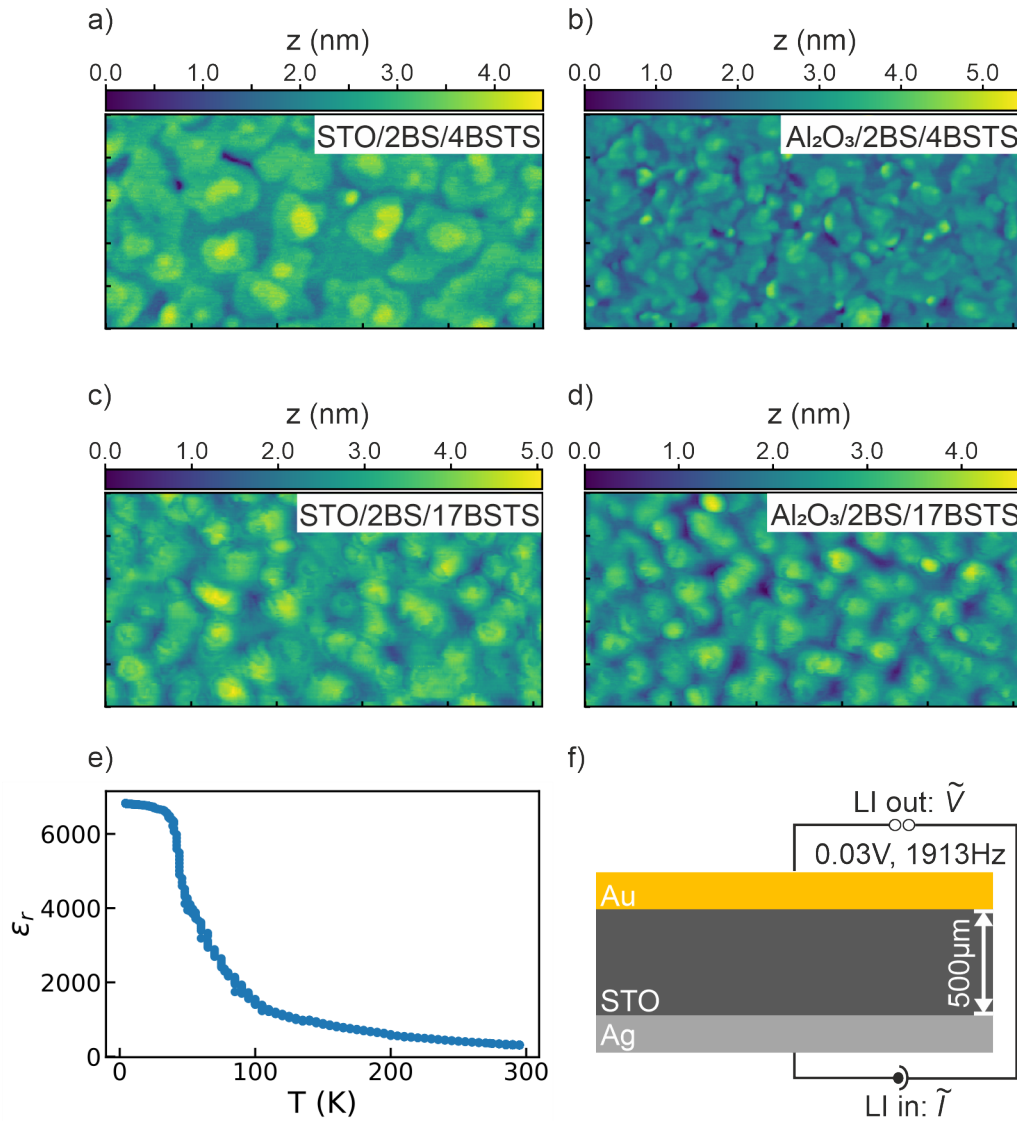
Figure 6.1: a) - d) AFM images of surface topography of 2BS/4BS and 2BS/17BSTS samples on STO (a, c) and Al_2O_3 (b, d). All four images show an area of $1\,\mu m \times 0.5\,\mu m$ and the height z is given by the color scale. For 17 QL BSTS no significant differences are observed, whereas the STO sample shows slightly larger island sizes in the case of 4 QL BSTS. e) Dielectric constant ϵ_r of STO measured with respect to temperature as sketched in panel f). Starting at room temperature, ϵ_r shows a value of ≈ 300 that increases to almost 7000, when the sample is cooled down to $4.2\,K$.

6.2 $(\text{Bi}_{1-x}\text{Sb}_x)_2\text{Te}_3$

Similar to Bi_2Se_3, the related binary alloys Bi_2Te_3 and Sb_2Te_3 have shown large parasitic bulk doping in magnetotransport studies. In Bi_2Te_3, when grown under Te-rich conditions, a n-type behavior is observed due to donor-type Te_{Bi} anti-sites and Te vacancies [31, 102, 108]. Sb_2Te_3, on the other hand, is dominated by acceptor-type Sb_{Te} anti-sites and Sb vacancies [31]. However, since the two compounds have the same crystal structure with similar lattice constants, alloying to the ternary $(\text{Bi}_{1-x}\text{Sb}_x)_2\text{Te}_3$ is possible with minimal strain [27], leading to a compensation of undesired excess bulk charges depending on the parameter x. Comparing the band structures of the binary constituents of BST furthermore reveals that its stoichiometric composition also influences the position of the Dirac point and size of the band gap. For Sb_2Te_3 ($x = 1$), the DP is located in the middle of the band gap that has a size below $200\,\text{meV}$ at the Γ-point. In the case of Bi_2Te_3 ($x = 0$), the band gap is slightly larger, but the DP is shifted below the valence band maximum [27]. Optimal characteristics in terms of these band structure parameters and the compensation of bulk carriers are hence found for intermediate x. In literature, a wide range of optimal x-values are reported for MBE-grown BST [98], ranging from $x = 0.88$ [108] for samples grown on Al_2O_3 to $x = 0.42$ using Si substrates [115]. Studies of samples on GaAs(111) [116] and SrTiO_3 [117] claim values of $x \approx 0.5$. This large discrepancy might not only stem from the choice of substrate, but also from differences in details of the growth conditions or procedure. Thus, purely relying on literature values for x is impractical and a separate study is necessary. In Ref. [108] the temperature dependence of the longitudinal four-point resistivity $\rho_{\text{xx}}(T) = t \cdot R_{\text{s}}$, where t is the film thickness and R_{s} the sheet resistance, was proposed as a reliable first indicator for the quality of the samples. As stated above, when large amounts of uncompensated bulk carriers are present in the sample, the Fermi level can be globally shifted from the band gap to the bulk conduction or valence band depending on the type of the dopant. In that case, a metal-like temperature dependence of $\rho_{\text{xx}}(T)$, i.e. a decreasing value with decreasing temperature is expected (see Ch. 3.1.1). If the excess donors and acceptors are compensated in the BST sample, on the other hand, E_{F} is located in the band gap. Then, decreasing T from room temperature should first yield an increase of $\rho_{\text{xx}}(T)$ due to the freezing out of thermally activated bulk carriers as observed in semiconductors, whereas at low temperatures a metal-like behavior should be observed due to dominant electronic transport by the metallic topological surface states. Figure 6.2 shows measurements of $\rho_{\text{xx}}(T)$ on $\text{SrTiO}_3/(\text{Bi}_{1-x}\text{Sb}_x)_2\text{Te}_3$ samples with x ranging from $x = 0.15$ to $x = 0.87$.[2] The behavior expected from a sufficiently compensated TI sample is observed in a pocket of $0.26 \leq x \leq 0.51$. For lower and higher values a metallic temperature dependence is measured that is expected to dominantly stem from bulk transport when the regime of the respective binary alloy is approached. The maximum value of ρ_{xx} is reached for $x = 0.37$,

---

[2]The presented measurements were performed by *Anton Frank* within his master thesis at the University of Regensburg (2017) under supervision of Dr. M. Kronseder, Prof. Dr. C.H. Back, and Prof. Dr. D. Bougeard.
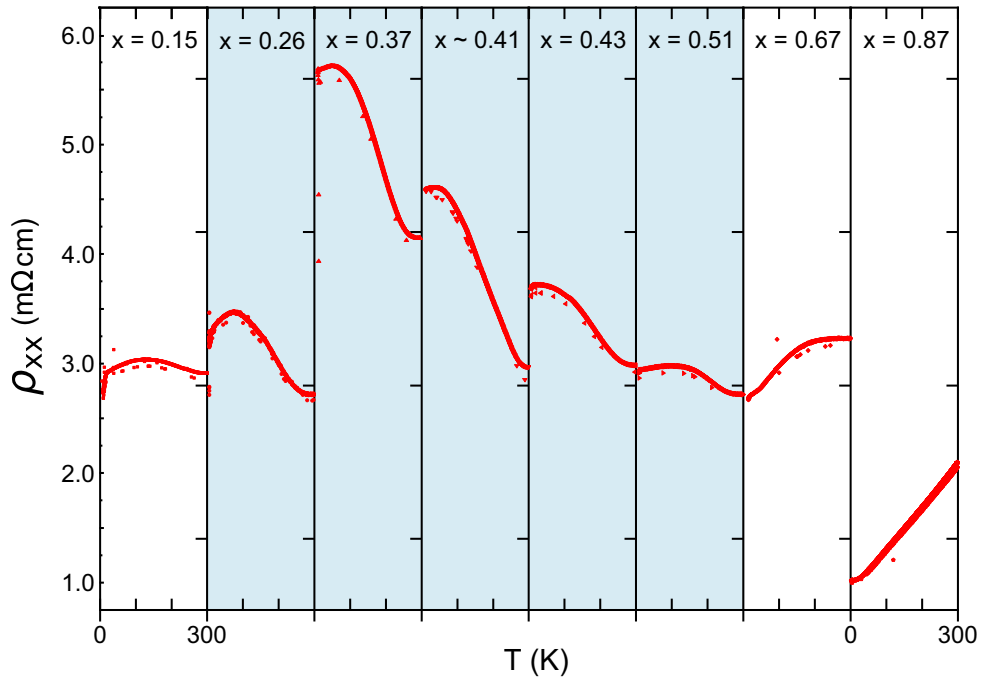
Figure 6.2: ρ_{xx} versus temperature T for $(\text{Bi}_{1-x}\text{Sb}_x)_2\text{Te}_3$ samples with varying x. The samples have a thickness of 15 QL and were grown on SrTiO_3 substrates. The values of x range from 0.15 to 0.87 and were verified by XPS measurements (except the sample with $x \sim 0.41$, where the value has been estimated from the growth parameters). The blue background highlights the pocket of x where the measurement shows the behavior of a compensated sample.

Figure 6.3: ARPES image of the surface band structure of the occupied states for a (Bi$_{1-x}$Sb$_x$)$_2$Te$_3$ sample with $x \approx 0.35$. The Fermi energy E_F is located in the band gap intersecting the topological surface states (TSS) above the Dirac point. The grey-scale represents the intensity. The measurement was performed at $T = 77\,\text{K}$ with a photon energy of 60 eV, for details see Ch. 5.2.2.
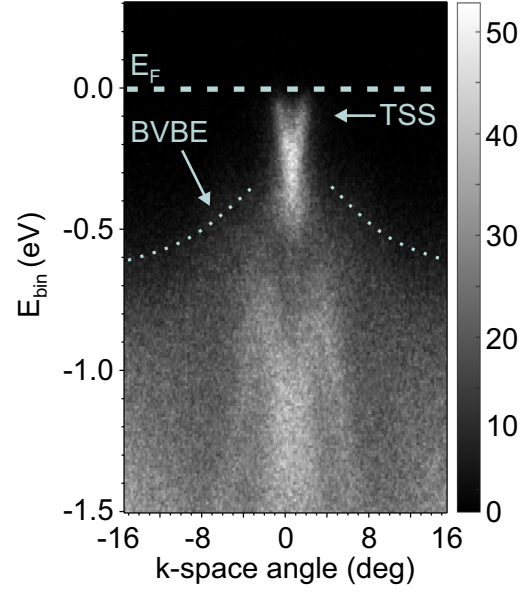
where the least amount of bulk carriers contributes to electronic transport and the Fermi level should be located in the energy gap intersecting the topological surface states.

A powerful tool to directly map the surface band structure up to E_F of a crystalline sample is angle resolved photoemission spectroscopy (ARPES). Figure 6.3 shows an ARPES image of a (Bi$_{1-x}$Sb$_x$)$_2$Te$_3$ sample with $x \approx 0.35$. In agreement with the $\rho_\text{xx}(T)$ measurements, the Fermi energy lies within the bulk band gap for the given stoichiometry. It intersects the linearly dispersing topological surface states above the Dirac point that is located at a binding energy of $E_\text{bin} \approx -0.35\,\text{eV}$ and is buried below the maximum of the bulk valence band edge (BVBE), which is expected for Te-rich BST samples. In the presented image, the onset of the bulk valence band edge is difficult to precisely identify due to low contrast and smeared-out bands, so the dotted lines in Fig. 6.3 only provide a guide-to-the-eye estimate. The intensity of the bulk states might be suppressed, since the photon energy was optimized to maximize the contrast of the surface states. More pronounced valence band states showing a clear dispersion are visible for binding energies $E_\text{bin} \lesssim -0.7\,\text{eV}$, as similarly observed in Refs. [115, 118]. A clear evidence of the topological nature of the observed surface states can be provided by the spin-resolved measurements shown in Fig. 6.4. Panel e) shows a zoom of Fig. 6.3. The vertical dotted lines at ± 1.5 deg indicate the k-space angles along which the spin polarization was recorded. Figures 6.4 a) and b) show the measured intensity of spin-up (I_up) and spin-down (I_down) electrons for the respective angle, whereas c) and d) show the corresponding polarization P given by $P = (I_\text{up} - I_\text{down})/(I_\text{up} + I_\text{down})$. Along the two angles an opposite, non-zero polarization is observed that changes sign at a binding energy coinciding with the Dirac point and directly reveals the helical spin structure expected from topological surface states. Above the DP, P reaches values of about 50 % agreeing well with the results found in Ref. [118]. For binding energies below the DP the polarization is lower due to the mixing of TSS and trivial bulk electrons. This also explains the higher absolute
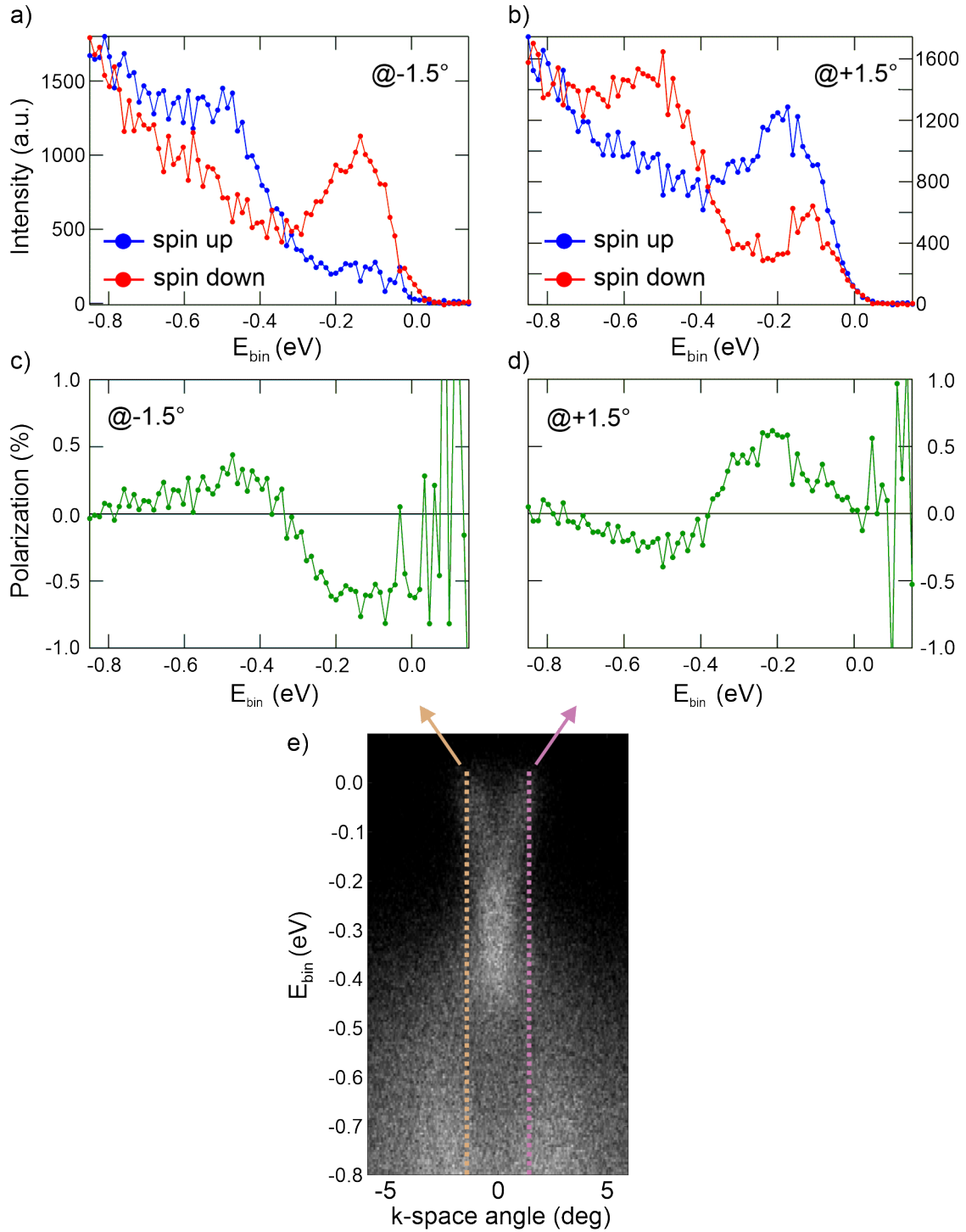
Figure 6.4: Spin-resolved ARPES measurements along fixed k-space angles of ± 1.5 deg. a) and b) show the spin-up and spin-down intensity and c) and d) the corresponding polarization for the respective k-space angle. The measurement was performed at $T = 77$ K with a photon energy of 60 eV.

intensity values recorded in this energy range in panels a) and b) of Fig. 6.4.

To conclude this section, varying x in $(Bi_{1-x}Sb_x)_2Te_3$ revealed the expected behavior in terms of the temperature dependence of the longitudinal resistivities. A maximum ρ_{xx} with a TI-typical temperature behavior was found for $x = 0.37$, where the Fermi level is hence expected to lie within the bulk energy gap. This was confirmed by ARPES imaging of a sample with similar stoichiometry. This agreement is important, since it is not necessarily expected due to the different capping procedures utilized for the respective samples. Without any capping layer, the surface of a Bi-based TI uncontrollably oxidizes in ambient conditions, possibly leading to an effective surface doping that can significantly shift the Fermi level and influence the electronic transport [119–122]. For ARPES, the selenium-capping was removed by heating in the UHV of the measurement system, such that the highly surface sensitive method has access to the pristine band structure of the sample. For the samples used in magnetotransport, this unscathed surface condition is aimed to be preserved after MBE growth by a controlled in-situ passivation of the surface by the thin and homogeneous layer of aluminium oxide (AlOx). The presented agreement between transport and ARPES observation suggests that no significant uncontrolled band bending occurs for AlOx-capped samples. Moreover, the observed large helical spin-polarization of the surface states further indicates the high quality of the investigated samples. However, ARPES also revealed a Dirac point location just at or even below the valence band edge, which is unfavorable for many experimental applications. The capability of a separate tuning of the Fermi level and the Dirac point is gained by expanding BST to the quaternary alloy $(Bi_{1-x}Sb_x)_2(Te_{1-y}Se_y)_3$.

6.3 $(Bi_{1-x}Sb_x)_2(Te_{1-y}Se_y)_3$

While MBE grown ternary and especially binary alloys from the family of Bi-based 3D TIs have been investigated extensively in the past, the quaternary $(Bi_{1-x}Sb_x)_2(Te_{1-y}Se_y)_3$ with $x, y \neq 0$ has received less attention. Expanding the system to the full alloy does lead to the maximal band structure engineering flexibility, but comes at the cost of a disproportionately more complex growth procedure and an increase of the relevant parameter space. In terms of stoichiometry, now x and y can be tuned between 0 and 1, where both parameters simultaneously influence the band structure characteristics and should hence primarily determine the electronic transport properties of the sample. Thus, a mapping of $(x|y)$ to the respective transport behavior is required.[3] Figure 6.5 summarizes the results obtained from a study of 12 samples with varying x and y values. As in the previous section, the temperature dependence of the longitudinal resistance was used as an indicator for the position of the Fermi energy. A metal-like behavior corresponds to E_F located in one of the bulk bands, whereas a semiconductor-like (semiC-like) dependence

---

[3]A detailed mapping of $(x|y)$ in terms of crystal structure and transport properties can be found in Ref. [109]. However, as was discussed in context of $(Bi_{1-x}Sb_x)_2Te_3$ in the previous section, a full reliance on literature values is problematic, since the properties can be very sensitive to minor variations in growth conditions or procedure.

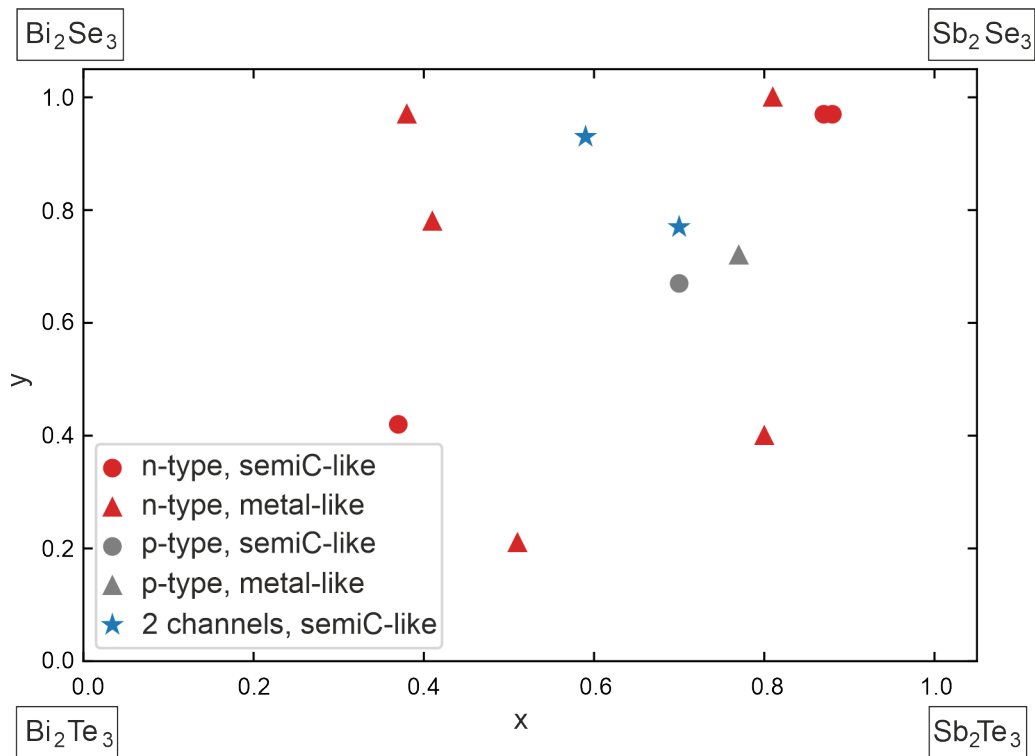**Figure 6.5:** Overview of investigated $(Bi_{1-x}Sb_x)_2(Te_{1-y}Se_y)_3$ samples with varying x and y values. Color and form of the marker represent the transport behavior as explained in the legend. All samples were grown on $SrTiO_3(111)$ substrates with exception of samples ($x = 0.51|y = 0.21$) and ($x = 0.77|y = 0.72$) where Al_2O_3 and InP were used, respectively.

suggests E_F lying in the energy gap. Additionally, the dominant charge carrier type at 4.2 K, n-type for electron- and p-type for hole-conduction, was obtained from the slope of the Hall resistance R_{xy} measured in a perpendicular magnetic field. Color and form of the markers, representing a specific ($x|y$) combination in Fig. 6.5, indicate the transport behavior of the samples as specified in the legend. Apparently, while the qualitative temperature dependence and the dominant charge carrier type should be determined by the stoichiometry, no systematic correlation with respect to both indicators was observed. Most samples showed a n-type Hall coefficient, whereas two samples clearly showed a hole-dominated transport and two more, represented by blue stars in Fig. 6.5, showed a non-linear Hall curve indicating two or more channel transport with different charge carrier types. Likewise, the occurrence of a metal- or semiC-like temperature dependence does not show correspondence to a specific range of x and y values. The origin of these seemingly arbitrary transport properties could be connected to similar erratic observations during the growth process, where RHEED imaging used to monitor the BSTS epitaxy revealed a high fluctuation of film crystallinity even between runs with the same growth conditions. While the samples presented in Fig. 6.5 collectively showed satisfying growth quality, minor differences could still largely influence the amount and type of unintentional bulk dopants and hence affect the transport behavior. Naturally, such a lack of controllability of growth quality and electronic transport characteristics is undesirable and prevents experimental reproducibility. A successful approach that resolves this predicament will be presented in the following section.

6.4 Implementation of a Bi$_2$Se$_3$ seed layer

A crucial advancement for the development of high quality epitaxial $(Bi_{1-x}Sb_x)_2(Te_{1-y}Se_y)_3$ was realized by the implementation of a Bi$_2$Se$_3$ seed layer. The benefit of introducing such a seed layer for the epitaxial preparation of BSTS becomes apparent when comparing typical RHEED images as shown in Fig. 6.6. Panel a) shows a pattern of a BSTS sample directly grown on SrTiO$_3$ (STO). Only faint vertical lines overlapped with circular features are visible. As explained in Sec. 4.3.1, the observation of concentric circles clearly indicates poly-crystalline growth. Inserting a BST seed layer, corresponding to Fig. 6.6 b), lead to improvements, but caused 3D features in the RHEED image apparent from the bright spots especially along the central reflex. In both cases, using different substrates or BSTS stoichiometries additionally compelled an adaptation of growth parameters and hence often required a tedious optimization process. When using a thin layer of BS as seed for the BSTS growth, however, the situation drastically improved. The RHEED image of such a BS/BSTS heterostructure grown on STO is shown in Fig. 6.6 c). The sharp vertical lines and the absence of poly-crystalline or 3D features indicate a high crystallinity.

Moreover, the BS layer facilitates high quality BSTS epitaxy using the same growth parameters even when the BSTS stoichiometry or the substrate is changed. Panels d) - f) exemplarily show RHEED patterns of BS/BSTS samples (right) and the respective
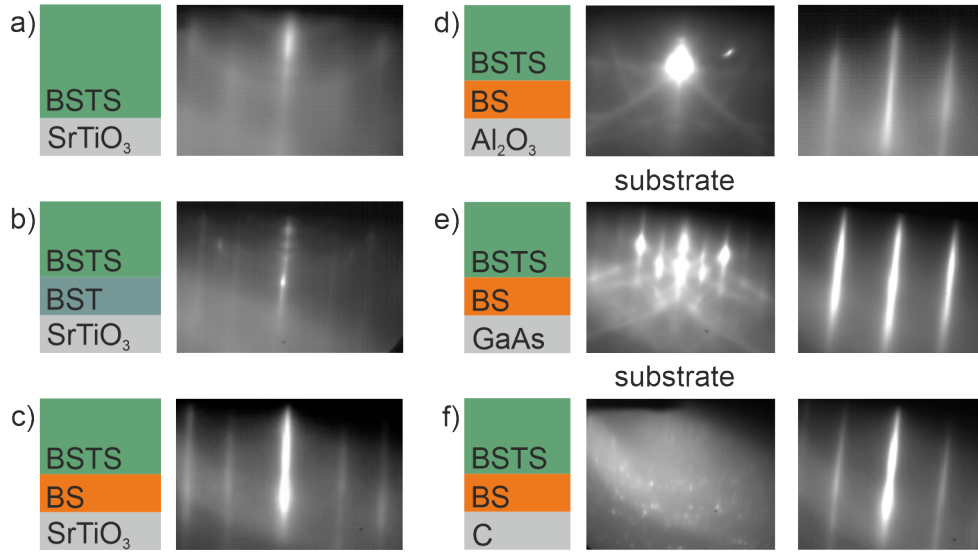
Figure 6.6: Comparison of RHEED images taken during sample growth of BSTS on different substrates and with varying seed layers. a) Direct growth of BSTS on $SrTiO_3$(111) b) Utilizing a BST seed layer. c) Utilizing a BS seed layer. d) - f) Exemplarily RHEED images for Al_2O_3(0001), GaAs(111), and C(111) substrates, where the middle panel respectively shows the RHEED pattern of the bare substrate.
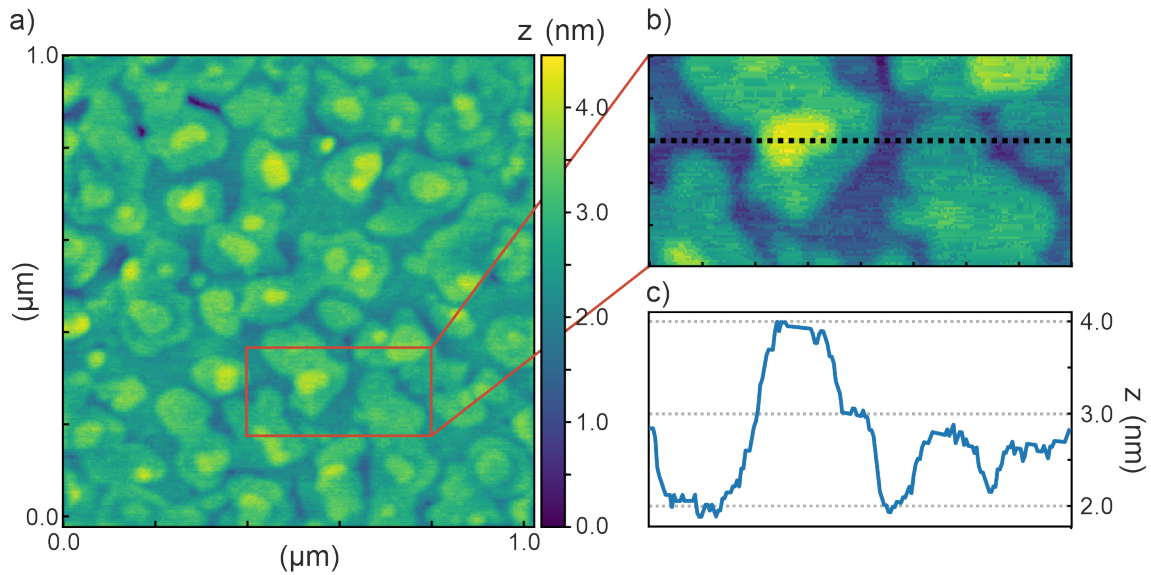
Figure 6.7: Surface topography of a typical BS/BSTS sample. a) AFM image of a surface section of area $1\,\mu m^2$, the color scale indicates the height z. b) Zoom to the red rectangle in picture a). c) Height profile along the dashed line in b) showing step sizes of 1 nm corresponding to the height of 1 QL.

substrate (middle) demonstrating single-crystalline growth on Al$_2$O$_3$(0001) d), GaAs(111) e), and even disordered C(111) f). In addition, successful growth was achieved on Al$_2$O$_3$(11-20), GaAs(001) and InP(111). Surprisingly, even a single quintuple layer of BS proved to be sufficient to yield this seed layer functionality and ease the vdW epitaxy of the subsequent BSTS. The surface topography of a finished BS/BSTS sample is shown in Fig. 6.7. Panel a) shows an AFM image of area $1\,\mu m^2$, where the color scale for z indicates the relative height profile. The topmost layer with $z \approx 4\,$nm consists of sparse, small islands sitting on top of bigger islands of the beneath layer ($z \approx 3\,$nm). Typical for the BS/BSTS samples, the third layer with $z \approx 2\,$nm is already almost completely closed. Figure 6.7 b) shows a zoom corresponding to the red rectangle in a). Along the dashed line a height profile is extracted and plotted in panel c). The step size between layers is approximately $1\,$nm, agreeing well with the expected height for one quintuple layer [98]. The presented RHEED and AFM images suggest high growth quality of the samples utilizing the BS/BSTS heterostructure design. However, the introduction of the Bi$_2$Se$_3$ layer also has important consequences for the electronic properties of the bilayer films. This will be the key topic of the following chapter.

7

Development of p-n-type BS/BSTS heterostructures

In the previous chapter, quaternary $(Bi_{1-x}Sb_x)_2(Te_{1-y}Se_y)_3$ samples grown directly onto the substrate were presented and the observation of an unpredictable transport behavior was attributed to small, difficult to control variations in sample crystallinity. A major leap for the improvement of growth quality was shown to be the implementation of a Bi_2Se_3 seed layer before the subsequent BSTS growth within the epitaxial procedure. In terms of the heterostructure's electronic properties, on the other hand, this poses a challenge. The main reason for expanding the binary TI compounds to the full quaternary alloy is the minimization of parasitic bulk conduction. However, the binary compound BS suffers from a large amount of unintentional n-type dopants, which potentially adds a significant bulk contribution to the electronic transport within such a BS/BSTS bilayer stack. An approach to counteract this issue and reduce parasitic bulk doping is the utilization of intrinsic band bending effects, when the n-type BS is interfaced with a p-type layer of BSTS. The concept of such vertical p-n-type heterostructures will be introduced in Sec. 7.1. In these samples, the electronic properties are largely determined by the thicknesses of the respective layers. To determine the strength of the as-grown compensation of bulk carriers and to investigate the arising transport channels, Sec. 7.2 will present a systematic study of three series with varying BS and BSTS thicknesses, employing temperature-, magnetic field-, and gate voltage-dependent electronic transport measurements. The main results of this study are published in Ref. [123]. Then, section 7.3 aims to provide a closer examination of the complex effects of electrostatic gating on the electronic properties of the samples, before a summary and a discussion of the presented results is given in section 7.4.
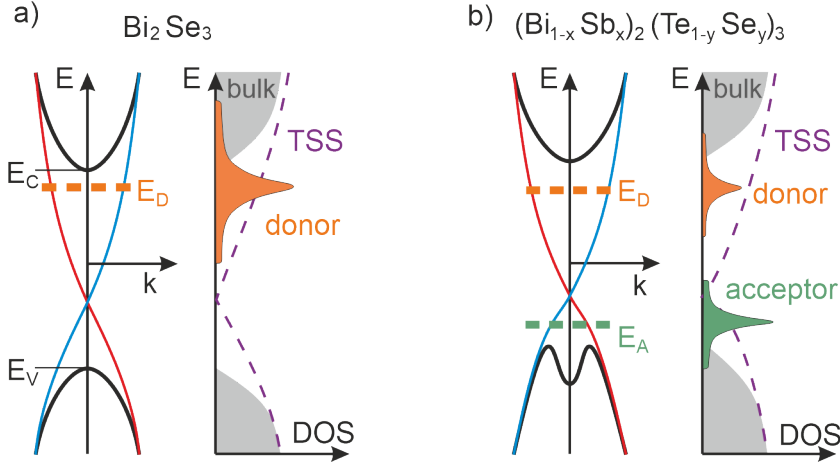
Figure 7.1: Sketches of band dispersion and density of states for Bi_2Se_3 (a) and $(Bi_{1-x}Sb_x)_2(Te_{1-y}Se_y)_3$ (b). The respective left panel of each sub-figure shows the energy dispersion indicating the bulk valence- (E_V) and conduction band (E_C) edges, the TSS within the band gap (red and blue lines), and the bulk dopant levels E_D (orange) and E_A (green) for donors and acceptors, respectively. The right panels illustrate the corresponding density of states.

7.1 Concept of $Bi_2Se_3/(Bi_{1-x}Sb_x)_2(Te_{1-y}Se_y)_3$ p-n heterostructures

In Bi_2Se_3, lattice defects cause a large bulk donor level that pins the Fermi energy to the conduction band as illustrated in Fig. 7.1 a). The left sketch shows the band dispersion with E_C and E_V being the bulk conduction and valence band edges, respectively, and the red and blue states within the energy gap indicate the topological surface states. The right panel represents the corresponding density of states (DOS) of the bulk donor level (orange), the TSS (purple), and the bulk continuum (gray). Due to the high amount of n-type dopants present in BS, implementing even a thin layer into a heterostructure with BSTS potentially adds a large contribution to the overall bulk conductance of the sample. In $(Bi_{1-x}Sb_x)_2(Te_{1-y}Se_y)_3$, on the other hand, generally both donor and acceptor dopants coexist[1] with the respective amount depending on the stoichiometry and hence being tunable by varying the alloy parameters x and y. Adjusting the stoichiometry to an acceptor surplus, as sketched in Fig. 7.1, thus opens the possibility to engineer vertical p-n heterostructures of the n-type BS with p-type BSTS layers, where intrinsic compensation effects could lead to a reduction of the total amount of unintentional dopants. In section 6.3, no systematic correlation between nominal stoichiometry and dominant charge carrier type of BSTS samples grown without a BS seed layer was found due to issues in epitaxial

---

[1]In principle, acceptor-type dopants are also present in BS. However, the three lattice defects with the lowest formation energy are donor-type and hence significantly exceed the acceptor defects [102]. The small acceptor level in BS is therefore omitted here for simplicity.

quality. To investigate the concept of p-n heterostructures we chose $0.70 \lesssim x \lesssim 0.74$ and $0.87 \lesssim y \lesssim 0.91$ within growth accuracy, aiming to cause excess acceptor dopants in the BSTS layer. Here, the high selenium ratio is chosen to target the maximum of the alloy's band gap [124], while x is used to adjust the dopant ratio. At a value of $x \approx 0.72$ we expect a slight acceptor surplus, while x is still low enough to avoid approaching a trivial insulator regime that is predicted for stoichiometries close to Sb$_2$Se$_3$ [109]. In section 7.2.2, the factual p-type character of this BSTS stoichiometry and the absence of the erratic behavior in terms of dominant charge carrier type will be proven experimentally. First, Fig. 7.2 introduces the concept of n-BS/p-BSTS heterostructures. By stacking the n-type BS with a p-type BSTS we aim to trigger an intrinsic band bending within the bilayer as similarly observed in Refs. [82, 125, 126] and illustrated in panels a) - c). For very thin BSTS, opposite excess charges may begin to compensate, but the effect is too small and the Fermi level stays above the conduction band minimum (CBM) (Fig. 7.2 c). This is revealed by ARPES on a heterostructure with 1 QL BS and 3 QL BSTS (1+3) in Fig. 7.2 d-i), where an occupation of the bulk conduction band can be observed up to binding energies of $E_{\text{bin}} \approx -0.1$ eV. The Dirac point, roughly indicated by the red circle, is positioned at $E_{\text{bin}} \approx -0.3$ eV. Increasing the BSTS thickness enhances the band bending until E_{F} is pulled below the CBM into the energy gap at the top surface (Fig. 7.2 b-ii)). The color grading towards iii) in b) indicates the evolution of the energy bands on further increase of the BSTS thickness. This band bending behavior is verified by ARPES in Fig. 7.2 d-ii) and iii) on samples of 1 QL BS and 6 QL (1+6) and 1 QL BS and 12 QL BSTS (1+12). Here, E_{F} is clearly pulled into the band gap accompanied by a pronounced shift of the Dirac point to higher binding energies. Ideally, at some point, the band bending is sufficient to pull the Fermi level into the band gap almost throughout the whole heterostructure by completely depleting the BS layer (Fig 7.2 e).

It is important to stress that while the ARPES measurements demonstrate the trend expected for this thickness-dependent band bending, they only image the energy bands at the very surface of the sample. Electrical transport properties, however, are governed by the complete band diagram throughout the whole thickness of the heterostructure. From the sketches displayed in Fig. 7.2 a)-c), three different contributions to transport can be expected as schematically illustrated in the respective lower panels. The most general case, with all three channels present, is represented by sub-figure b): additional to the top and bottom TSS (t-TSS, b-TSS), the bulk of the sample yields a metal-like contribution (m-bulk channel), where E_{F} intersects the conduction band and semiconductor-like (semiC-bulk channel), when it is positioned within the energy gap. In the case of Fig. 7.2 a), the Fermi level lies above the CBM throughout the sample thickness and hence the whole bulk is expected to show metal-like electronic transport properties. In the ideal case of Fig. 7.2 c), the BS seed layer is completely depleted and E_{F} lies in the band gap within the entire heterostructure.
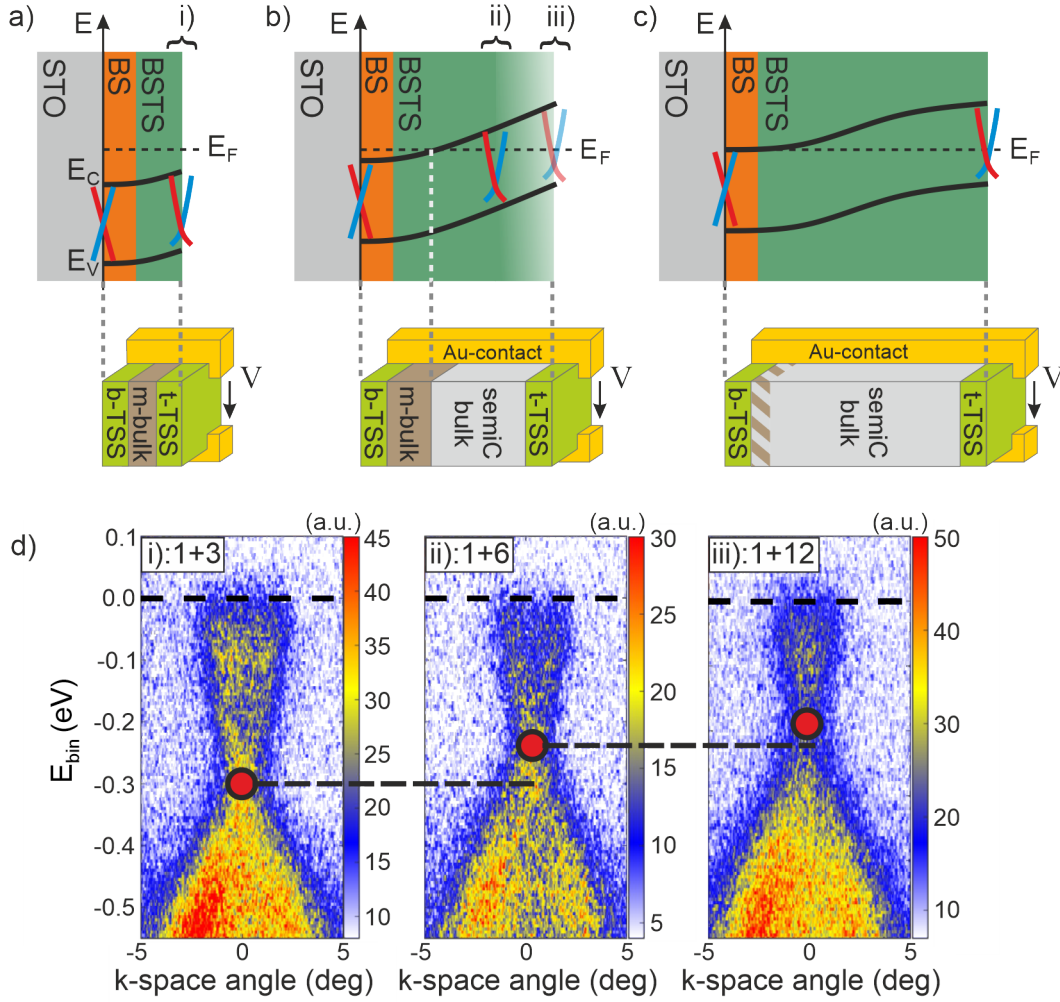
Figure 7.2: Heterostructure concept. a)-c) Illustration of thickness-dependent band bending within a p-n-type BS/BSTS heterostructure (upper panels) and the arising transport channels (lower panels). Additional to top and bottom TSS (t-TSS, b-TSS), a metal-like (m-bulk) or semiconductor-like (semiC-bulk) bulk contribution can be present in the sample depending on the position of the Fermi level E_F. d) ARPES at $T = 77$ K reveals the band bending evolution for samples of 1 QL BS and 3 QL (i), 6 QL (ii), and 12 QL (iii) BSTS. The horizontal black dashed lines at binding energies $E_{bin} = 0$ represent E_F, the red circles indicate the Dirac point position showing a shift to higher binding energies for increasing BSTS thickness.

7.2 Magnetotransport characterization of as-grown sample properties

To test the introduced band bending model and investigate the contributions of the anticipated transport channels to the electronic properties of the as-grown heterostructures, the following section presents a systematic magnetotransport study on three sample series. For each series, the BS layer thickness is fixed at 1 QL, 2 QL, or 4 QL, respectively, while the BSTS thickness is varied from 2 QL to 43 QL. In the following, the three series are hence termed 1+x, 2+x, and 4+x, where x is exchanged for the corresponding BSTS thickness, when a single sample is addressed.[2] A variation in the layer thicknesses is expected to influence the ratio of transport contributions of the m-bulk, the semiC-bulk, and the TSS and should thus manifest in the electronic behavior of the heterostructures. Below, this is investigated by temperature-, magnetic field-, and gate voltage-dependent magnetotransport measurements using a standard low frequency Lock-in technique in a four-point geometry and the ^{4}He dewar setup as introduced in Sec. 5.1.

7.2.1 Temperature dependence of the sheet resistance

The qualitatively different response to a variation of the temperature of classical metals and semiconductors has already been utilized in sections 6.2 and 6.3 to gain information about the electronic properties of BST and BSTS samples without a seed layer. There, as in the theoretical introduction of Sec. 3.1, a decreasing resistance with decreasing temperature was shown for metals due to the reduction of electron-phonon scattering, whereas an increasing resistance caused by reduced excitations of thermally activated carriers is observed for semiconductors. Disregarding quantum corrections in this context, also the TSS should behave like a metal, since their transport contribution stems from occupied states at the Fermi level. In Figure 7.3 a) - c) the temperature dependence between room temperature and 4.2 K of the normalized sheet resistance $R_s^{norm}(T) = R_s(T)/R_s(300\text{K}) - 1$ is shown for the three bilayer series. For the 1+x (a) and 2+x (b) series a clear competition between metal-like and semiC-like channels with respect to BSTS thickness can be observed. The samples with a thin layer of BSTS, where only a small band bending within the heterostructure is expected, indeed show a dominantly metallic behavior throughout the whole temperature range originating from states within the bulk conduction band. As predicted from the model of Fig. 7.2, this trivial metallic contribution gradually diminishes with increasing BSTS thickness. For samples 1+40 and 2+43 R_s^{norm} increases substantially starting from room temperature before showing a metal-like decrease below $T \approx 120$ K. This behavior has been reported for fully bulk compensated TIs, where the high temperature behavior is ascribed to a complete freeze-out of bulk carriers, whereas the low temperature decrease is attributed to dominant TSS transport [28, 128]. While a remaining metal-like contribution from a trivial m-bulk channel can not be excluded

---

[2]E.g. 1+12 for the sample with 1 QL BS and 12 QL BSTS, or 4+40 for 4 QL BS and 40 QL BSTS. The unit [QL] is omitted in the denomination.
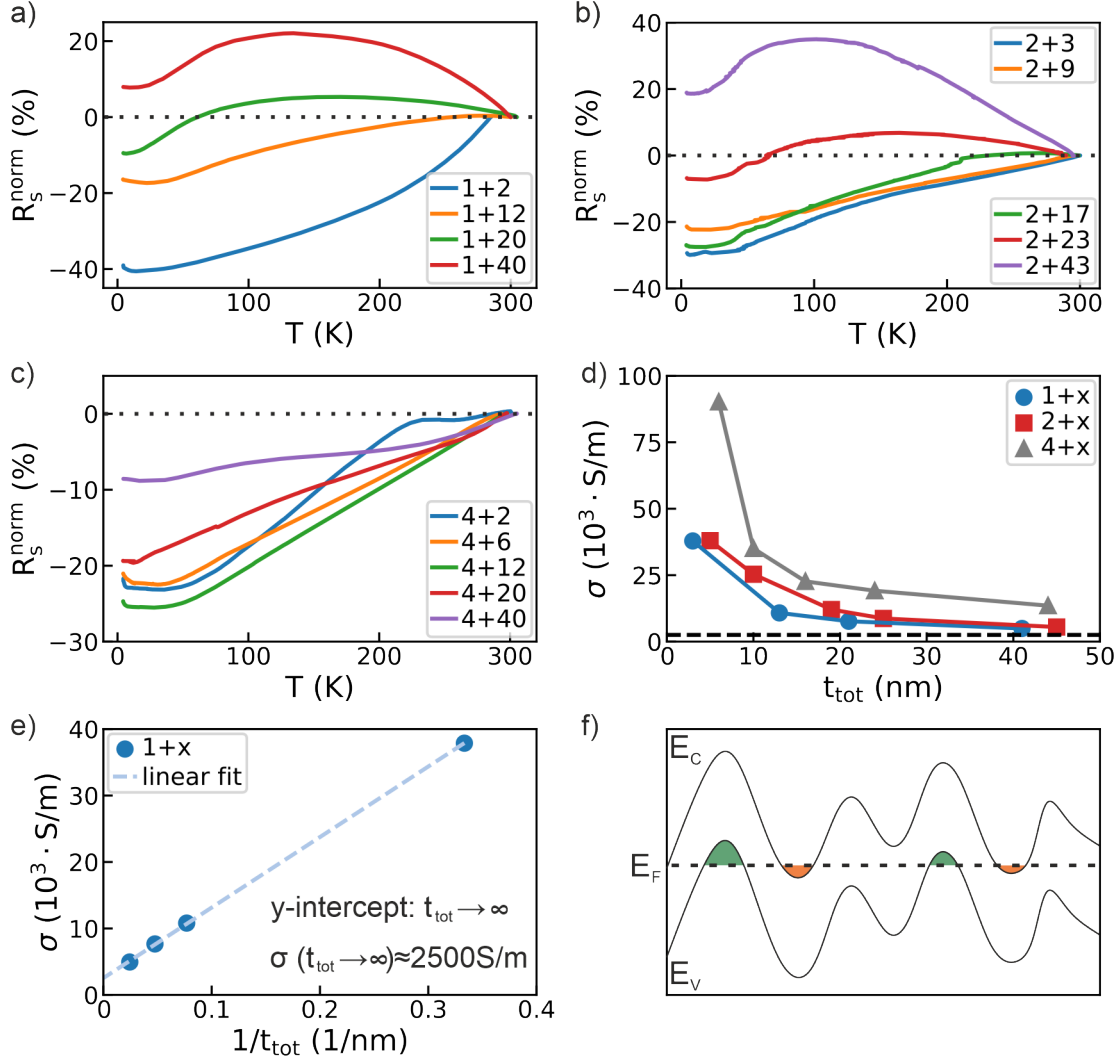
Figure 7.3: Temperature dependence of the normalized sheet resistance $R_s^{norm}(T) = R_s(T)/R_s(300\text{K}) - 1$ of the 1+x (a), 2+x (b), and 4+x (c) series. Whereas the 4+x series shows a metallic behavior for all BSTS thicknesses, an increasing semiconductor-like influence is observed for 1+x and 2+x. d) Conductivity σ at $T = 4.2$ K versus the total sample thickness t_{tot} showing a stark decrease with thickness for all three series and overall higher conductivity for the 4+x samples. e) Conductivity at $T = 4.2$ K of the 1+x series plotted against $1/t_{tot}$. From the y-intercept of the linear fit an estimate for the bulk BSTS can be extracted that has a value of ≈ 2500 S/m. f) Sketch of locally modulated conduction (E_C) and valence band edges (E_C) in a real space illustration (adapted from Ref. [127]). E_F is nominally positioned within the energy gap but occasionally crosses E_C or E_V causing electron- (orange areas) or hole puddles (green areas) that can transport a current by means of a variable range hopping process.

entirely from these measurements, the clear dominance of a semiC-like behavior at high and the comparatively small drop-off at low T already indicate that it becomes negligible for large BSTS thickness. This becomes more apparent when comparing the 1+x and 2+x series with the 4+x samples displayed in panel c). Here, the thicker layer of the highly n-type BS is expected to cause a considerably larger m-bulk contribution. This manifests in the observation of a metal-like behavior of $R_\text{s}^\text{norm}(T)$ for all temperatures independently of the BSTS thickness. The larger m-bulk contribution in the 4+x series also translates to higher absolute conductivity values. In Fig. 7.3 d) the conductivity $\sigma = 1/(R_\text{s}t_\text{tot})$ measured at $T = 4.2\,\text{K}$ is plotted versus the total sample thickness t_tot. All three series show a significant reduction of σ with increasing thickness. This behavior is per se unsurprising, since the thickness of the highly conductive BS is kept constant within the series and only the BSTS with lower charge carrier density is increased. However, the clear offset of the 4+x series is consistent with the large m-bulk channel present in these samples. Moreover, comparing the 1+x and 2+x series again indicates the vanishing of this trivial metallic contribution. While a small difference between 1+x and 2+x can be observed for small thicknesses, the two curves converge for $t_\text{tot} \gtrsim 20\,\text{QL}$, suggesting that σ becomes almost independent of the BS thickness. Both series asymptotically approach a dashed line that is obtained from Fig. 7.3 e). There, the conductivity values of the 1+x series are plotted with respect to $1/t_\text{tot}$. In this depiction a linear behavior is observed, where the y-intercept of the fit (light blue dashed line) corresponds to $t_\text{tot} \rightarrow \infty$ and hence represents an estimate value for the bulk BSTS conductivity that is approached by the blue and red curves in sub-figure d). Any offset from the dashed line is expected to mainly stem from contributions of the m-bulk channel or the TSS that are constant or even diminish with increasing BSTS thickness. If the BSTS was a perfect insulator in the bulk, $\sigma(t_\text{tot} \rightarrow \infty)$ would approach zero. From the linear fit in e), however, a comparatively small, but non-zero conductivity of $\approx 2500\,\text{S/m}$ is obtained. A possible origin of the bulk BSTS conduction are charge puddles that were suggested to be present in compensated TIs in Ref. [127] and have since been extensively discussed and investigated in literature [129–136]. In the binary TI alloys like BS, a high defect density of the same dopant type essentially shifts the Fermi level globally into the conduction band continuum leading to a metallic bulk behavior. In compensated materials, on the other hand, structural disorder can lead to a varying density of donors and acceptors fluctuating on small real space length scales and hence induce an inhomogeneous Coulomb potential landscape. The charged impurities then locally modulate and can shift the band edges above or below the Fermi level as sketched in Fig. 7.3 f), where a real space illustration of the corrugated conduction (E_C) and valence band edges (E_V) is shown. Even if E_F nominally lies within the energy gap, the bulk bands are locally intersected leading to electron (orange areas) or hole puddles (green areas). If these puddles are dense enough, they can carry a current by means of variable range hopping (VRH) and hence cause a non-zero bulk conductivity. It is important to stress, however, that if this conduction channel was dominant in our samples, a crossover from an activated behavior to a VRH-type temperature dependence would be expected for $T \lesssim 40\,\text{K}$, where $R_\text{s} \sim \exp\big[(1/T)^{0.5}\big]$ [129]. This is clearly not observed in our measurements shown in Fig. 7.3 a) - c), indicating only a small

contribution of charge puddle conduction.

7.2.2 Electronic transport in a perpendicular magnetic field

Further information about the as-grown electronic properties can be gained by applying a perpendicular magnetic field B at 4.2 K. Figures 7.4 a) and b) show the arising Hall resistance R_{xy} for the 1+x and 4+x series, where the primary charge carrier type determines the sign of the curves' slope. Most samples show dominant electron conduction, associated with a positive slope in our measurement geometry, which we ascribe to the large n-type contribution from the m-bulk channel. Sample 1+40, however, clearly switches to a p-type behavior (negative slope), proving not only the presence of an acceptor surplus for our BSTS with ($x \approx 0.72|y \approx 0.89$), but also the decline of m-bulk contribution to the transport for thin BS and thick BSTS layers. For 4 QL BS seed layer, where the m-bulk channel was shown above to largely govern the electronic transport, this switching is not observed within the series. Obtaining quantitative values for the charge carrier density and mobility of the samples by applying a Drude model to the Hall measurements is deliberately refrained in this thesis. The reasoning is explained in section 5.1.2. A further important observation drawn from these measurements is the absence of the unpredictable Hall-behavior that occurred for BSTS samples grown without seed layer and discussed in Sec. 6.3, where seemingly no correlation between sample stoichiometry and dominant charge carrier type was found. Clearly, the implemented BS layer not only improves the epitaxial quality, but also acts as an "electrostatic seed" layer. Its large amount of n-type dopants pins the Fermi level to the bulk conduction band and therefore reproducibly fixes the starting point for subsequent layers to an n-type foundation. At the opposite, aiming to grow compensated BSTS directly on a substrate can lead to band bending effects at the interface, where the direction sensitively depends on the defect configuration and is hence susceptible to minor fluctuations of growth conditions and epitaxial quality [133]. This uncontrolled up- or downward band bending can randomly shift the Fermi energy or even induce trivial n- or p-type conduction channels at the substrate/TI interface, possibly leading to the unpredictable Hall behavior observed in section 6.3.

An important quantity investigating the electronic properties of TIs is the longitudinal magnetoresistance (MR). Figures 7.4 c) and d) compare the absolute magnetoresistance $MR^{abs} = R_s(B) - R_s(0\,T)$ of the 1+x and 4+x series. By comparing the given values of the two series we conclude by elimination that the TSS are the main source of MR present in our heterostructures: as discussed above, the semiconductor-like bulk channel can be expected to increase with increasing BSTS thickness and should thus be accompanied by an increase of MR^{abs} if this channel was responsible for the observed magnetoresistance. This is not the case in both series. Moreover, a large metal-like bulk transport contribution clearly *decreases* the MR as apparent by the much smaller absolute values in the 4+x compared to the 1+x series. Hence, both bulk channels can be excluded, leaving the TSS as the origin of the MR. Depending on their respective strength, both bulk contributions
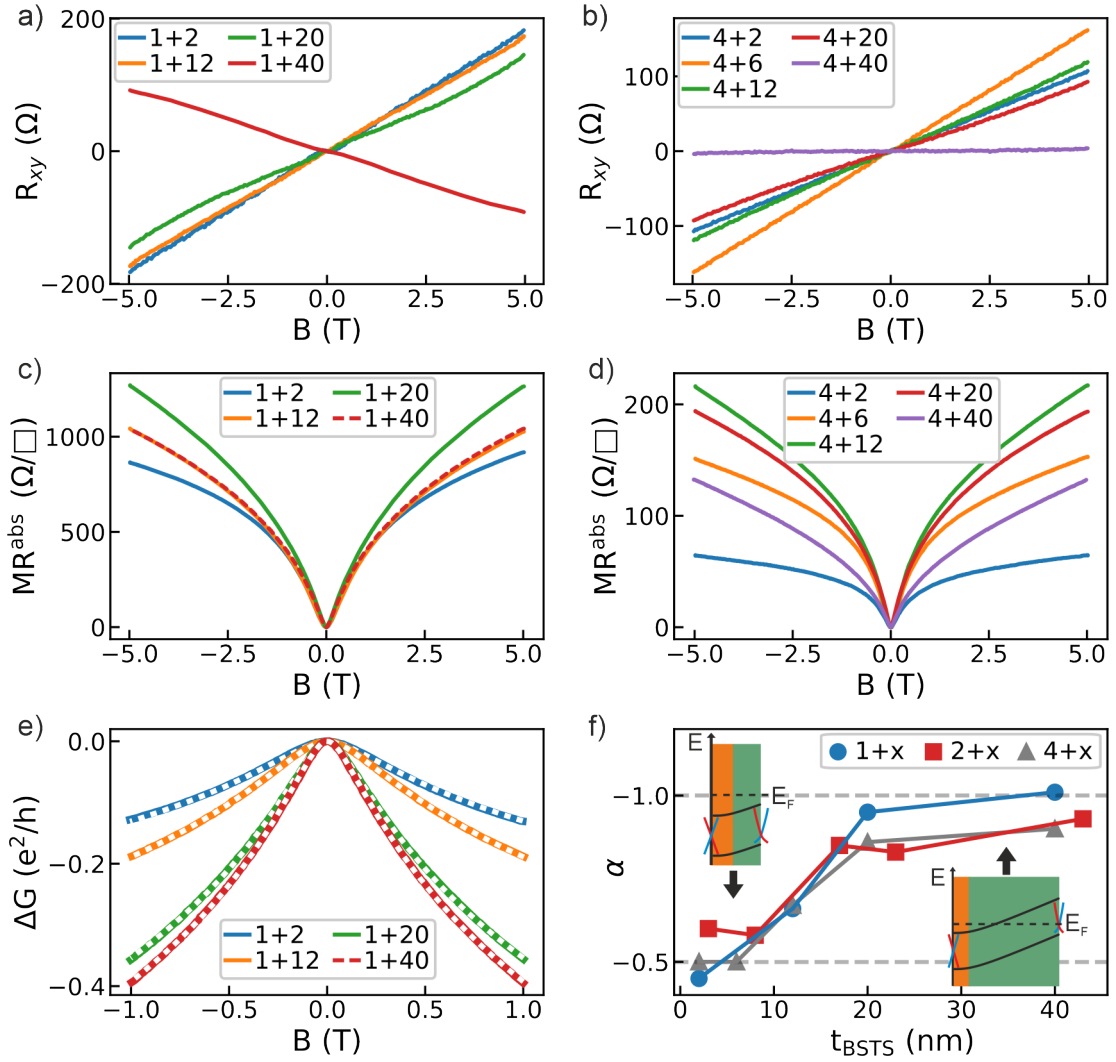
Figure 7.4: Magnetotransport properties at 4.2 K under application of a perpendicular magnetic field of ±5 T. a), b) Hall resistance of the 1+x and 4+x series, where a positive slope is associated with n-type and negative slope with p-type conduction. Sample 1+40 shows p-type conduction evidencing the acceptor surplus present in the BSTS layer with ($x \approx 0.72 | y \approx 0.89$). All other samples show electron conduction, which can mainly be ascribed to a large contribution of the n-type m-bulk channel. c), d) Magnetoresistance of the 1+x and 4+x series. From comparing the absolute values it can be concluded that the TSS are the main source of MR in our heterostructures. At least at small fields, this MR is expected to stem from weak anti-localization that can be analyzed by the Hikami-Larkin-Nagaoka theory. e) Exemplary fits (white dashed lines) of the simplified HLN formula to the obtained data (colored solid lines) demonstrating good agreement. f) Prefactor α obtained from the HLN fits plotted versus the BSTS thickness t_{BSTS} for all three series. Independent of BS thickness, an evolution of $\alpha \approx -0.5$ to $\alpha \approx -1$ is observed that corresponds to a decoupling of conduction channels on top and bottom surfaces of the samples.

act as parallel transport channels decreasing the ratio of current carried by the TSS and thus diminishing the overall MR as particularly evident for the m-bulk channel causing a large difference between the two series. Furthermore, bulk magnetoresistance effects in TIs are often shown to approximately follow a $\sim B^2$ dependence stemming from classical effects [82, 137], which is not observed in the measurements displayed in Figs. 7.4 c) and d). This again suggests the absence of sizeable transport contributions by (3D) bulk states in our samples. Within the investigated magnetic field range of ±5 T, all samples show a distinct cusp-shaped positive MR that is commonly described to stem from weak anti-localization (WAL). This quantum interference effect was theoretically introduced in section 3.2 for systems with strong spin-orbit coupling and is expected to be especially relevant for transport mediated by the surface states of topological insulators. Due to the arising π Berry phase of the TSS in the mass-less limit, the triplet channels of the Cooperon modelling the coherent back scattering process are essentially quenched and only the singlet channel remains [59, 138]. Since the singlet is responsible for WAL, whereas the triplets would lead to weak localization, the TSS are predicted to be subject to anti-localization. In other words: the spin-helicity of the Dirac cone requires an electron that is back scattered by $180°$ from a state k to $-k$ to reverse its spin. In the quantum interference this inevitably leads to destructive interference of time-reversed loops and hence a suppression of back scattering. Applying a perpendicular magnetic field destroys the effect, thus increases the resistance of the system and a positive MR is observed. It is important to note that many observations from our measurements indicate the presence of additional effects leading to a positive MR. Chapter 8 will present these observations and provide a more elaborate discussion. There, also the applicability of the Hikami-Larkin-Nagaoka (HLN) theory, which is a standard tool in literature for a quantitative analysis of the WAL effect, will be discussed in more detail. Especially for small fields, the cusp-shaped MR observed in topological insulators is predicted to stem dominantly from WAL [139–143] and the HLN formula is then used in the literature to fit the magnetoconductance. The simplified HLN formula was theoretically introduced in Eq. (3.39) of section 3.2 and is re-printed here [60][3]:

$$\Delta G_{\mathrm{HLN}}(B) = \alpha \frac{e^2}{2\pi^2 \hbar} \left[\psi \left(\frac{1}{2} + \frac{1}{b\tau_\varphi} \right) - \ln \left(\frac{1}{b\tau_\varphi} \right) \right]$$

$$= \alpha \frac{e^2}{2\pi^2 \hbar} \left[\psi \left(\frac{1}{2} + \frac{\hbar}{4eBl_\varphi^2} \right) - \ln \left(\frac{\hbar}{4eBl_\varphi^2} \right) \right].$$

Assuming $G(B) \approx 1/R_{\mathrm{s}}(B)$ and $\Delta G_{\mathrm{HLN}}(B) \approx \Delta G(B) \equiv G(B) - G(0\,\mathrm{T})$, the magnetoconductance for the HLN analysis can be directly obtained from the measurement

---

[3]Note that the HLN formula was given in section 3.2 for a conductivity $\Delta\sigma(B)$ instead of a conductance $\Delta G(B)$ to preserve the notation of the original publication in Ref. [60]. However, the formula yields values in units of e^2/h and not $\mathrm{m} \cdot e^2/h$ and thus corresponds to a conductance. This distinction was not made in Ref. [60] since the formula was derived for purely (quasi-) 2D systems.

of the longitudinal sheet resistance as $\Delta G(B) \approx 1/R_s(B) - 1/R_s(0\,\text{T})$. Figure 7.4 e) exemplarily shows HLN fits (white dotted lines) to $\Delta G(B)$ of the 1+x series measured at 4.2 K, where α and the phase coherence length l_φ are the free fit parameters and very good agreement of the theory and the obtained data is demonstrated within a field range of ± 1 T. In the simplectic case of the HLN theory, i.e. for systems with strong spin-orbit coupling and a WAL-type magnetoconductance as observed in our samples, the prefactor α is expected to yield a value of -0.5. However, if two parallel, uncoupled transport channels with similar phase coherence lengths are present in the system and equally contribute to the WAL effect, their contributions add up to yield $\alpha = -1$. This should, for example, be the case in a perfectly bulk insulating TI of sufficient thickness, where the top and bottom TSS both separately add a value of -0.5 to α [144, 145]. Figure 7.4 f) shows the evolution of α with increasing BSTS thickness t_{BSTS} for the three investigated series. Independently of the seed layer thickness, $\alpha \approx -0.5$ is observed for all samples with thin BSTS. When the BSTS thickness exceeds 8 QL, the value starts to increase approaching -1 for $t_{\text{BSTS}} \approx 20$ QL. In the thin film limit, the band bending model of our heterostructures predicts the Fermi level to lie mostly above the conduction band minimum as indicated by the upper inset of Fig. 7.4 f). Hence, we expect all conduction channels within the system to be strongly coupled via topologically trivial bulk states, consistent with the observation of $\alpha \approx -0.5$. It has furthermore been suggested that below a thickness of approximately 10 QL, $\alpha = -0.5$ would even be expected for separated channels due to coupling of top and bottom TSS mediated by tunneling or hopping [146, 147]. This could be the origin of the simultaneous increase in all three series starting around this threshold. As illustrated by the lower inset of Fig. 7.4 f), when the BSTS thickness is increased, we expect the upper TSS to start to become separated from the conduction channel at the bottom surface by the emergence of a semiconductor-like channel, where E_F is positioned in the band gap. While it was argued in section 7.2.1 that this channel is not completely insulating at 4.2 K, our HLN analysis argues in favor of its conduction to be small enough to allow an effective decoupling of a top and bottom conduction channel for sufficiently thick BSTS that triggers the evolution of α from -0.5 to -1. Hence, the trend presented here provides a further confirmation for the band bending model introduced in Sec. 7.1 and the low bulk conduction of the BSTS layer. Note, that at the same time they also contradict a common interpretation from literature that $\alpha = -1$ is associated with a completely insulating bulk of the TI. Not only does the BSTS layer that separates top from bottom channel show a remaining conduction, but especially the m-bulk channel was shown to not be completely depleted at least in the 4+x series. In Ref. [144] it has indeed been predicted that such a configuration, where the bottom TSS is strongly coupled to trivial bulk states from the m-bulk channel, can also yield $\alpha = -1$. Therein, also the evolution from -0.5 to -1 for increasing separation of two channels is theoretically modelled.

7.2.3 Back-gate dependence as sensor for as-grown properties

A further standard tool for magnetotransport experiments is the application of an electrostatic gate voltage. While the field effect naturally modulates the transport behavior of the sample, the triggered change of the longitudinal resistance also provides valuable information about the *as-grown* electronic characteristics, which will be described here. More details about the gate effect on the transport properties will be given in section 7.3. As explained in the beginning of the previous chapter (see Sec. 6.4), all samples presented here were grown on STO substrates that can function as the back-gate (BG) dielectric due to its ultrahigh relative permittivity, hence allowing an easy and reliable implementation of gate functionality. Whereas front-gate (FG) realization requires further lithography steps and thin-film deposition methods for the dielectric and electrode layers additional to the Hall-bar patterning, the sample is simply glued to a socket by conductive silver epoxy and contacted by wire bonding to enable the application of back-gate voltages between the sample and the Ag layer, using the STO as a dielectric barrier. Furthermore, thin-film dielectrics typically used as the FG barrier, like atomic-layer-deposited Al_2O_3, have been reported to damage the surface mobility [25, 148] and are moreover often vulnerable to leakage currents. The STO with its thickness of $500 \, \mu$m, on the other hand, proved to be very robust even up to voltages of several hundred volts. Applying a gate voltage V_G to the sample essentially leads to a shift of the Fermi level induced by the field effect and consequently modifies the transport behavior manifesting in a change of the longitudinal sheet resistance R_s. Figure 7.5 a) provides an illustration of the $R_s(V_G)$ evolution for the most simplified case. If the transport could be completely described by the prototypical band structure indicated in the insets, where only the bulk bands (black parabolas) and one set of surface states (red and black states) contribute and the as-grown Fermi energy E_F lies directly at the Dirac point, the displayed R_s behavior would be expected. Without any gate voltage the resistance shows a maximum due to the vanishing density of states at the Dirac point. For $V_G \neq 0$, the Fermi level is shifted away form the Dirac point and moves to higher energies for positive and to lower energies for negative voltages. The hence increasing density of states is accompanied by a reduction of the resistance that is most pronounced as long as E_F lies within the band gap (colored background). When the Fermi level is pushed into one of the bulk bands, the resistance obtains its lowest values and quickly saturates. Of course, the situation is much more complicated in real samples. Already the presence of a second TSS at the opposite surface and potential trivial bulk states pose additional contributions to transport that respond individually to the application of a gate voltage and hence inhibit the attribution of the resistance maximum directly to the Dirac point of a surface state. Following the terminology used for measurements in graphene and other 2D systems, this resistance maximum is thus often labeled *charge neutrality point* (CNP) in literature for generalization. Especially considering the heterostructure design of our samples, however, the description is still more complex. The samples are not two-dimensional in the sense that the field effect induced by the gate voltage will not tune the Fermi energy uniformly throughout the whole

thickness, which is amplified by the asymmetry of the BS/BSTS stacks. The presence of mobile charge carriers in surface or bulk states can partially or completely screen the electric field leading to a gradual attenuation. Thus, the applied voltage will also highly influence the intrinsic as-grown band bending that arises from the p-n-type character of the bilayers. Furthermore, all contributing transport channels can have different mobilities and hence changes of their respective density lead to an unequal impact on the overall resistance. Nevertheless, still a maximum in sheet resistance is expected to be observed for a certain gate voltage in our samples. To use a completely general terminology, this maximum will be labeled R_{peak} in the following. Figures 7.5 b) - c) show the evolution of the sheet resistance at 4.2 K normalized to its value under zero bias with respect to the applied back-gate voltage V_{BG}: $R_{\text{s}}^{\text{norm}}(V_{\text{BG}}) = R_{\text{s}}(V_{\text{BG}})/R_{\text{s}}(0\,\text{V}) - 1$. In panel c) the measurements on the 4+x series are presented. The thinnest samples, 4+2, 4+6, and 4+12, show a steep increase for negative voltages with $R_{\text{s}}^{\text{norm}}$ reaching large values of approximately 500 %, 200 %, and 100 %, respectively. However, even for voltages up to $-100\,\text{V}$ no maximum in the resistance is observed, which we ascribe to an effective screening of the BG-induced field effect before R_{peak} is reached. In theses samples with thick BS and thin BSTS layers our band-bending model for p-n heterostructures predicts the m-bulk channel to be large, leading hence to the presence of a highly conductive layer at the STO/TI interface that dominates the electronic transport. Applying a negative gate voltage partially depletes this channel, which causes the observed large relative increase of the resistance, but the high density of mobile charge carriers present in the m-bulk channel shields the electric field before a maximum in R_{s} is observed. Intriguingly, starting from a BSTS thickness of 20 QL the behavior changes and a maximum of $R_{\text{s}}^{\text{norm}}$ with respect to the voltage is reached that shifts towards 0 V for thicker samples. Sub-figure d) shows an enlarged depiction of the back-gate measurements on samples 4+20, 4+40, and 4+60. We interpret these observations as direct evidence for the compensation of opposite excess charges within the p-n-heterostructure: for thin BSTS, the metal-like bulk conduction channel at the STO/TI interface induced by the 4 QL of strongly n-type BS remains large enough to screen the static electric field. However, increasing the BSTS thickness from 2 QL to 6 QL and 12 QL the relative increase of R_{s} gradually diminishes, already indicating an as-grown reduction of the m-bulk contribution by intrinsic compensation effects. This trend continues for the samples 4+20, 4+40, and 4+60, where the m-bulk channel becomes sufficiently depleted that the back-gate can tune the Fermi level through a configuration with a resistance maximum R_{peak}. Figure 7.5 b) shows the $R_{\text{s}}^{\text{norm}}(V_{\text{BG}})$ measurements for the 1+x series[4]. From the investigations presented in Fig. 7.3 of section 7.2.1 it was concluded that sample 1+12 still shows a small remaining metal-like bulk channel as-grown that practically vanishes for 20 QL and 40 QL of BSTS. These observations directly manifest in the BG behavior of the respective samples: applying a positive gate voltage yields an upwards shift of the Fermi energy that hence increases

---

[4]To avoid hysteresis effects in these measurements, the sample was brought to room temperature in between back-gate sweeps in positive and negative direction. The two separate measurements are then digitally merged, leading to a small discontinuity at 0 V.
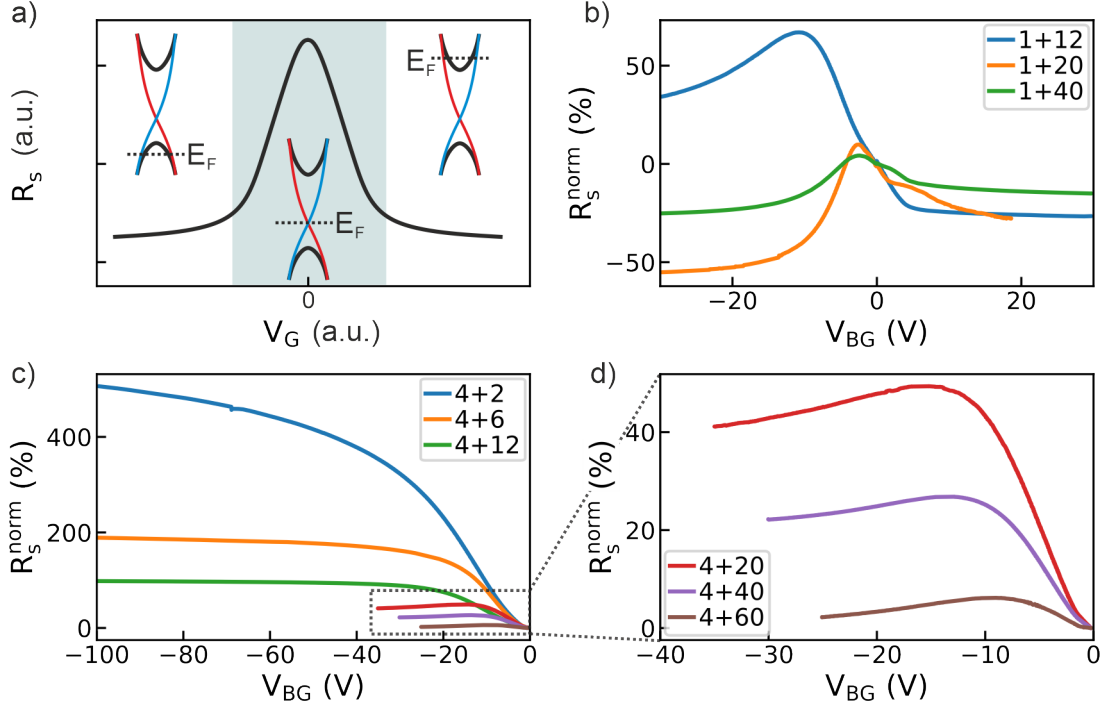
Figure 7.5: Effect of applied back-gate voltage on the longitudinal resistance R_s.
a) Simplified model to generally illustrate the expected R_s behavior under a gate
voltage V_G. If the band structure has the configuration of the insets, R_s shows a
maximum at 0 V, since the Fermi level E_F lies at the Dirac point with vanishing
density of states. Applying a voltage shifts E_F away from the Dirac point and the
resistance decreases due to the increasing density of states of the surface states
(red and blue states). It reaches the lowest values when E_F lies within the bulk
bands (black parabolas). b) Sheet resistance R_s^{norm} at 4.2 K normalized to the
unbiased value versus back-gate voltage V_{BG} for the 1+x series. Whereas sample
1+12 shows a large increase with a maximum at -10.5 V, samples 1+20 and 1+40
almost show no positive values of R_s^{norm} with a maximum at $V_{BG} \approx -2$ V. This
is ascribed to a complete depletion of the m-bulk channel for the two samples.
c) Measurements for the 4+x series. The three thinnest samples show large
changes in resistance, but no maximum is observed. For BSTS thickness of
20 QL and above an R_{peak} is observed, which is a direct evidence of the as-grown
intrinsic compensation of opposite excess charges within the p-n heterostructure.
d) Magnified depiction of samples 4+20, 4+40, and 4+60 shown in c).

the remaining n-type m-bulk channel in sample 1+12. For $+30\,\text{V} \geq V_{\text{BG}} \gtrsim +5\,\text{V}$ this channel is then large enough to screen the field effect, equivalent to the observations in thin 4+x samples. Thus, the resistance remains constant. Below $+5\,\text{V}$ the BG tunability is regained and $R_{\text{s}}^{\text{norm}}$ increases up to a pronounced maximum at $-10.5\,\text{V}$. In stark contrast, samples 1+20 and 1+40 only show a small increase with a maximum at $V_{\text{BG}} \approx -2\,\text{V}$, clearly indicating the complete as-grown depletion of the metal-like bulk channel induced by the BS seed layer. As observed for all other samples, any remaining contribution of this channel to electrical transport would be largely tunable by the field effect and therefore cause a significant increase of $R_{\text{s}}^{\text{norm}}$ for negative voltages in comparison to the unbiased measurement. The facts that both samples reach R_{peak} at the same gate voltage and almost no increase of R_{s} can be induced by the gate voltage suggests that the depletion of the m-bulk channel is already completed in sample 1+20.

In conclusion, investigating the behavior of the longitudinal resistance under a back-gate bias allowed to gain valuable information about the as-grown sample properties. It not only evidenced the intrinsic compensation of opposite excess charges within the p-n heterostructure, but also showed a complete depletion of the m-bulk channel introduced by the highly n-type BS layer for 1 QL BS and BSTS thicknesses above 20 QL. This strongly suggests that the BS seed layer functionality, that was shown above to be highly beneficial for the epitaxial preparation and the reproducibility of the electronic properties of the TI samples, can be utilized, while its parasitic contribution to the bulk conductivity can be minimized by choosing a p-type BSTS layer of sufficient thickness. The following section will provide a more detailed discussion on the effects of a back-gate voltage on the electronic transport properties of the heterostructures.

7.3 Electronic properties under electrostatic gating

The difficulty of interpreting the gating effects on electronic transport experiments, especially for our TI heterostructures, was already briefly discussed in the preceding section. All conduction channels present in the samples superimpose to yield the measured resistance, but are tuned to a different degree by the applied voltage. For example, whereas the m-bulk channel is expected to be directly depleted or populated by the field effect depending on the sign of the applied voltage, a contribution of the semiC-bulk channel, possibly stemming from charge puddle conduction, could be much less prone to a change of its conductivity by a shift of the Fermi level. Even if the BSTS stoichiometry is tuned to an overall acceptor surplus, n- and p-type puddles are simultaneously present and randomly distributed throughout the material as indicated in Fig. 7.3 f). When the Fermi level now is shifted to higher or lower energies, the density of states of one type of puddles will decrease, but the respective other will simultaneously increase, leading thus to an overall less pronounced and more difficult to predict modulation of the resistance. Furthermore, the distance of the respective channel from the dielectric plays an important
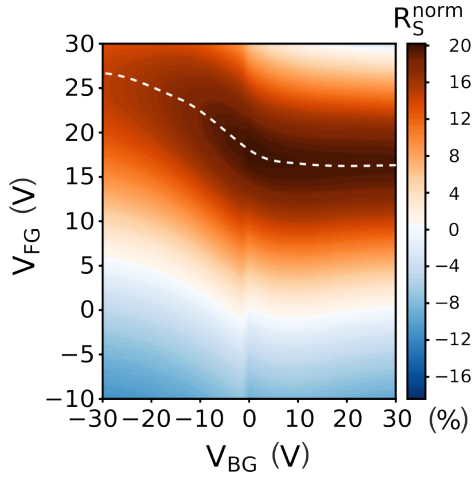
Figure 7.6: 2D color map of the normalized sheet resistance $R_{\mathrm{s}}^{\mathrm{norm}}$ obtained at 4.2 K with respect to back-gate- (V_{BG}) and front-gate voltage (V_{FG}). The white dashed line follows the maximum of $R_{\mathrm{s}}^{\mathrm{norm}}$ with respect to both gates. When it is horizontal, the BG is screened and does not influence the top surface. A non-zero slope indicates a capacitive coupling of the BG to the top surface.

role for the tunability of its conductivity due to screening effects. Naturally, when a back-gate is used, the field effect will be stronger at the bottom surface than on the top surface, especially if mobile bulk carriers are present, and hence the shift of the energy bands with respect to the Fermi level will be different for transport channels located at the respective surfaces, like the top and bottom TSS. In the measurements of the sheet resistance with respect to the applied back-gate voltage presented in Fig. 7.5 a maximum in resistance R_{peak} was obtained in most samples at a certain value of V_{BG}. While the observations discussed there evidenced the compensation effects within the heterostructures and suggested a possible full depletion of the m-bulk channel, they do not provide complete insight into the capability of the back-gate to tune the electronic bands throughout the whole sample thickness, since the observed curves could correspond solely to a variation of the conduction channels located at the bottom surface. For many practical scenarios, however, TI samples, where the top TSS could be shifted in energy by means of a back-gate voltage would be highly favorable, as this would leave the top surface free for e.g. surface sensitive optical experiments or even the addition of a further material layer like for example in TI/ferromagnet heterostructures. A tool to test the influence of the back-gate on the top surface is the implementation of an additional front-gate (FG) for dual-gate operation.

7.3.1 Capacitive coupling of top and bottom surfaces

The FG functionality was achieved by introduction of a bilayer dielectric between the sample and an e-beam evaporated layer of 10 nm titanium and 100 nm gold that is used as the electrode. The dielectric consisted of 30 nm of SiO_2 and 100 nm of Al_2O_3 deposited by plasma-enhanced chemical vapor deposition (PECVD) and atomic layer deposition (ALD), respectively. Details of the front-gate preparation process are given in appendix B.1. A dual-gated measurement at 4.2 K of sample 1+40 is shown in Fig. 7.6, where the applied back-gate voltage V_{BG} is plotted along the x-axis, the front-gate voltage V_{FG} along the y-axis and the normalized sheet resistance $R_{\mathrm{s}}^{\mathrm{norm}}$ is given by the color map. To acquire

this color plot, the back-gate was fixed at constant values in steps of 1.5 V, at which the front-gate was each swept from +30 V to −30 V. The remaining data points were obtained by digital interpolation. A precise description of the followed measurement procedure can be found in appendix C.3. The white dashed line in Fig. 7.6 tracks the behavior of R_{peak} obtained from every FG sweep with respect to both gate voltages. Following this line from right to left, its horizontal behavior for $+30\,\text{V} \geq V_{BG} \gtrsim +10\,\text{V}$ shows that the back-gate has no effect on the front-gate in this regime. At any V_{BG} within this interval, the conducted front-gate sweep showed a resistance maximum at a constant $V_{FG} \approx 16.5\,\text{V}$. Equivalently to measurements shown in Fig. 7.5, we ascribe this to the m-bulk channel being populated with mobile charge carriers induced by the positive back-gate voltage that leads to a screening of the BG electric field and hence prevents a coupling to the top surface. However, between 10 V and 0 V, where the m-bulk channel is expected to approach depletion, the maximum of R_s slowly starts to shift towards higher front-gate voltages. For $0\,\text{V} \gtrsim V_{BG} \gtrsim -12.5\,\text{V}$ this trend enhances, manifesting in the steepest slope of the white dashed line, before it starts to flatten again for larger negative voltages. The non-zero slope of the dashed line clearly indicates a capacitive coupling of the back-gate to the top surface showing that it is capable of tuning the Fermi level of the top TSS even for a sample thickness of 41 QL [84, 149–151]. At the same time, this observation again clearly suggests a very low bulk conductivity of our samples as long as the m-bulk channel is depleted. In Ref. [149] similar BSTS devices, however prepared by the Bridgman technique instead of MBE, were investigated in a dual-gate geometry. Therein, a capacitive coupling of top and bottom surface for a sample thickness of 42 nm and no coupling in a sample of 82 nm is reported. The authors ascribe this discrepancy to the presence of mobile bulk carriers induced by charge puddles in the thicker sample that prevent the BG electric field from penetrating the interior and claim an absence of puddles for samples thinner than 70 nm due to screening effects from the TSS. These screening mechanisms are also theoretically described in Refs. [127, 129]. In our heterostructures, as discussed above in Sec. 7.2.1, we do not assume a complete suppression of charge puddles in our samples due to the observation of a non-vanishing BSTS bulk conductivity. However, the conclusions drawn from Fig. 7.6 show that their density is small enough to allow the bulk penetration of an electric field.

7.3.2 Analysis of the $R_s(V_{BG})$ measurement

While the dual-gated measurement revealed a clear capacitive coupling of the back-gate to the top surface, an explicit interpretation of the sole back-gate effect on the sheet resistance $R_s(V_{BG})$, as presented within Fig. 7.5 in a normalized depiction, still requires a more detailed evaluation. Therefore, figure 7.7 compares $R_s(V_{BG})$ (lower panel) with the behavior of R_{peak} in the dual-gated measurement (upper panel) of sample 1+40.[5]

---

[5]Note that the measurements presented in Fig. 7.7 stem from separate halves of the same sample. The halve used for the $R_s^{norm}(V_{BG})$ measurement was not equipped with a front-gate and did hence also not go through the FG patterning process. Slight influences on the transport behavior can not be excluded.
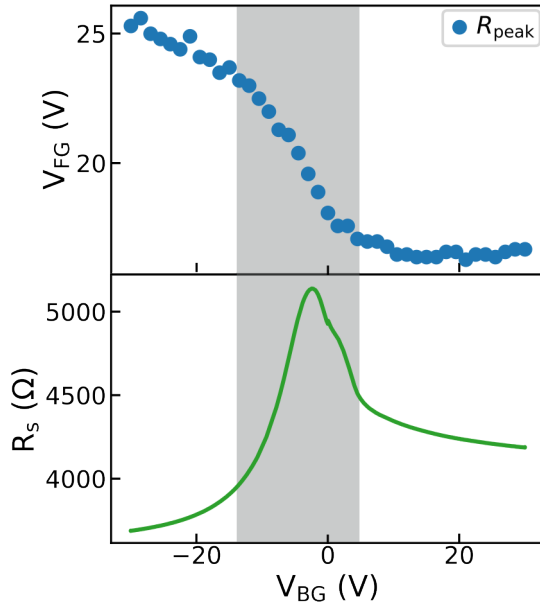
Figure 7.7: Comparison of the behavior of $R_{peak}(V_{FG})$ (upper panel) and the sheet resistance R_s (lower panel) with respect to the back-gate voltage of sample 1+40 and measured at 4.2 K. The largest coupling of the BG to the top surface, corresponding to the largest slope of the curve in the upper panel, agrees well with the maximum in R_s. As a guide to the eye, this region is highlighted by the gray background. From this it can be concluded, that the $R_s(V_{BG})$ curve mainly stems from the resistance variation of the bottom surface.

Corresponding to the white dashed line in Fig. 7.6, every point in the upper panel represents the value of V_{FG} at which the maximum resistance was found in each FG sweep at the respective BG voltage. The actual value of R_{peak} in general varies from point to point. As stated above, the slope of this curve is proportional to the capacitive coupling of the back-gate to the top surface. Intriguingly, a direct correspondence between this slope and the $R_s(V_{BG})$ measurement can be observed in Fig. 7.7. The largest capacitive coupling of the back-gate to the top surface is observed in a V_{BG} range between +6 V and -15 V (gray background), which agrees well with the maximum observed in $R_s(V_{BG})$. On the other hand, especially for large positive voltages, where the m-bulk channel is expected to be populated, the observed low sheet resistance corresponds to a complete suppression of the capacitive coupling. This allows to conclude that the resistance change induced by a back-gate voltage mainly stems from a variation of the lower surface. Naturally, the capacitive coupling from the BG to the top surface is largest, when the lower surface has a minimal conductance due the accompanying minimization of screening effects [149]. The correspondence of capacitive coupling and $R_s(V_{BG})$ observed in Fig. 7.7 hence suggests that the sheet resistance curve of the lower panel mainly describes the variation of the lower surface.

On the other hand, the fact that the capacitive coupling is not zero for the complete back-gate range shows that the $R_s(V_{BG})$ curve should still contain some contribution from the top surface state. A hint to this could be the observation of an incipient second peak in the three samples of the 1+x series, manifesting in a shallow broadening of the curve next to the main maximum. In Fig. 7.8 a) the $R_s(V_{BG})$ measurements of samples 1+12, 1+20, and 1+40 are plotted separately with arbitrary units to compare their qualitative behavior.[6] While the most noticeable second peak, highlighted by the respective arrows,

---

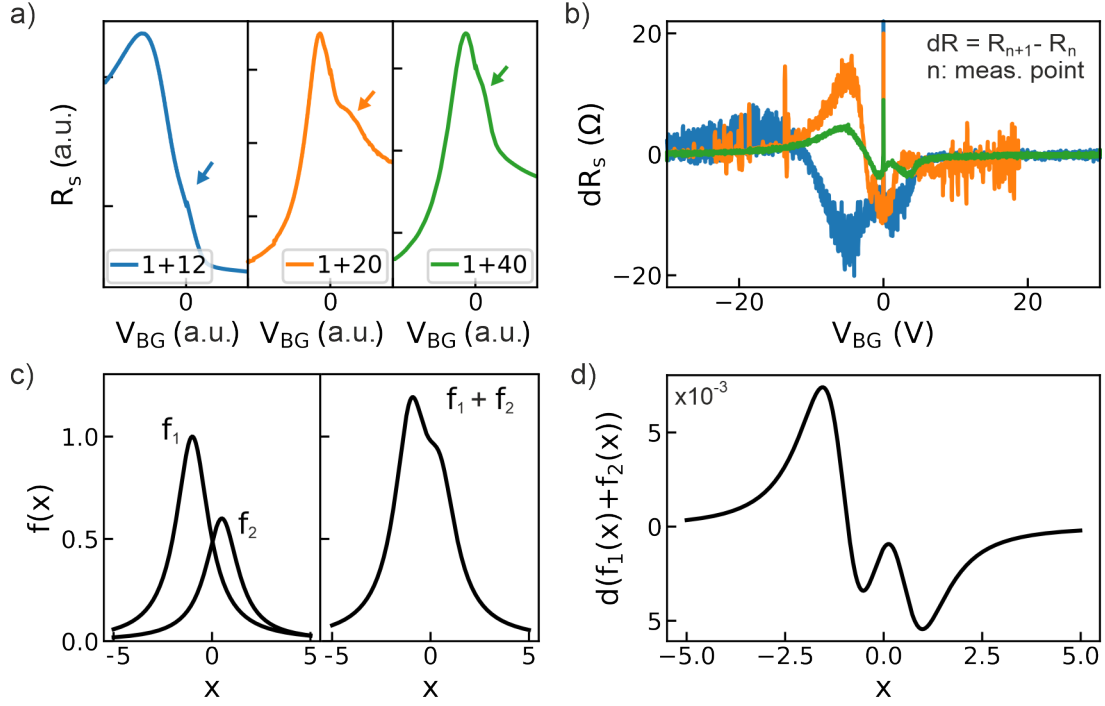[6]These measurements were plotted with units in Fig. 7.5 b).

Figure 7.8: Evaluation of of the signature of a second peak in the $R_s(V_{BG})$ measurements. a) Separate depiction of $R_s(V_{BG})$ for samples 1+12, 1+20, and 1+40 using arbitrary units to compare the qualitative behavior. A clear onset of a second peak can be observed for sample 1+20 as highlighted by the arrow. This second peak signature is less obvious for samples 1+12 and 1+40. b) Plot of dR_s obtained by subtracting R_s at every measurement point by the preceding value: $dR = R_{n+1} - R_n$, where n are the measurement points. The behaviors observed in a) and b) are characteristic for the superposition of two peak-like functions. c), d) Illustration of this behavior by using two arbitrary Lorentzians: $f_1 = 1/(x+1)^2 + 1$, $f_2 = 0.6/(x-0.5)^2 + 1$.

is observed in sample 1+20, it is still clearly observable in 1+40. On the contrary, this is much less obvious for sample 1+12, where the signature of a second maximum could get lost in the large change of R_s for negative voltages due to the depletion of the remaining m-bulk channel. Still, a slight broadening might be visible around zero voltage. This can be more clearly revealed by plotting the difference dR_s obtained by subtracting R_s at every measurement point by the preceding value. This is displayed in panel b). All three curves follow a qualitatively similar behavior showing a large maximum for positive and two smaller minima with negative dR_s. Using two arbitrary Lorentzians f_1 and f_2, sub-figures c) and d) illustrate that the observations from a) and b) are indeed characteristic for the superposition of two peak-like functions. A separate depiction of f_1 and f_2 and the sum of both are depicted in the left and right panel of c), respectively. Due to the close proximity in x, the smaller peak of f_2 gets absorbed into f_1 when the functions are added, yielding the same qualitative behavior as observed in the measurements. Subsequently, the difference function $d(f_1(x) + f_2(x))$ plotted in d) as well reflects the observations obtained from the measured curves. The fact that this second peak signature is reproducibly observed in three individual samples clearly indicates that it corresponds to a maximum resistance of one of the contributing transport channels. Since, as stated above, the main maximum is determined by the bottom surface, this second peak might reflect the behavior of the top TSS. In this sense, it would be reasonable, especially for the thicker 1+20 and 1+40 samples, to expect one peak at negative and the other at positive voltages due to the n-type character of BS and the p-type doping of BSTS. However, additional measurements would be useful to provide a more direct evaluation. By back-gated ARPES, for example, the effect of the back-gate on the top surface band structure could be directly imaged.

7.3.3 Back-gated Hall measurements

The back-gate dependent measurements presented so far have discussed the transport behavior in the absence of a magnetic field. Additionally, all samples presented in this chapter have also been investigated in terms of the BG influence on the Hall resistance that is induced by a perpendicular magnetic field. Here, V_{BG} was kept constant at the targeted value, while the magnetic field was swept between $\pm 5\,\mathrm{T}$ at $T = 4.2\,\mathrm{K}$. In Fig. 7.5 a) an oversimplified model was introduced to illustrate the change of the longitudinal resistance with respect to a variation of the gate voltage, when only the bulk bands and one set of TSS contribute to the transport. In such a system, R_{peak} would be observed when the chemical potential crosses the Dirac point. Considering the Hall resistance, the slope of the curve should then reverse its sign due to the change of charge carrier type from electrons to holes, or vice versa. In our measurements, we indeed observed a back-gate induced ambipolar transport for all samples, where the $R_s(V_{BG})$ showed a maximum for a specific back-gate voltage. In samples 4+2, 4+6, and 4+12 no such R_{peak} was reached even for BG voltages up to $-100\,\mathrm{V}$ due to the screening of the field effect by a large m-bulk channel. Accordingly, we observed a dominant n-type Hall behavior independently of the applied back-gate voltage. Only when the BSTS thickness is increased to 20 QL in the 4+x series, the sign of the Hall coefficient can be switched by means of back-gating. In figures 7.9 -

7.11 this sample 4+20 is compared to samples 1+12 and 1+40, respectively. In each, panel a) shows the Hall resistance R_{xy} versus magnetic field B for different back-gate voltages as given in the legend, with a positive slope corresponding to n-type and a negative slope to a p-type dominated transport. The gray curves in panels b) show the R_{xy} value at $B = 5$ T with respect to V_{BG}, where the dashed line marks $R_{xy} = 0$ and the red curve shows the $R_s(V_{BG})$ curves at zero magnetic field.[7] The colored backgrounds provide a guide to the eye and have a width of 20 V on the V_{BG} scale in all three figures.

Sample 4+20:

Sample 4+20 (Fig. 7.9) has been investigated in a back-gate range of ±150 V. For all voltages ≥ 0 V, the Hall curves displayed in a) show a n-type character with identical slope. This again shows the effective screening of the induced field-effect by the large electron doped m-bulk channel that we have demonstrated to be especially relevant when the BS layer has a thickness of 4 QL and that prevents a modulation of the sample's electronic bands by positive voltages. On the other hand, when negative voltages are applied, the Hall coefficient is modified and changes sign in the vicinity of −15 V, accompanied by the observation of non-linear Hall curves, before obtaining a clear p-type character at larger negative back-gate values. The $R_{xy}|_{B=5T}$ curve of panel b) (gray) nicely visualizes this behavior and furthermore allows a direct comparison to the simultaneous modification of the zero-field longitudinal resistance R_s (red). Intriguingly, while R_{xy} remains constant for +150 V ≤ V_{BG} ≤ −5 V , a steep increase of R_s already sets in at +20 V changing from 1825 Ω/□ to 2690 Ω/□ at −5 V. In the back-gate range between -5 V and -25 V, highlighted by the colored background, the sharp apex of the sheet resistance is accompanied by an abrupt, approximately linear decrease of R_{xy}. Furthermore, the zero crossing of the Hall coefficient, marked by the dashed line, precisely agrees with R_{peak} at a voltage of −15 V. For smaller voltages outside of the colored region, both curves reapproach a flat behavior.

Sample 1+12:

Sample 1+12 (Fig. 7.10) behaves similarly to 4+20 in many ways. The sign change of the Hall coefficient, again accompanied by non-linear curves in the vicinity, is observed for slightly smaller negative voltages between −5 V and −9 V, but as for sample 4+20, it shows n-type character at zero bias and is not modified for positive gate voltages (see panel a)). This manifests in sub-figure b) in a constant behavior of $R_{xy}|_{B=5T}$ for all $V_{BG} > 0$. The sheet resistance, on the other hand, again already shows a significant increase within this gate region. Even the relative variation is similar to sample 4+20 as it changes from 5228 Ω/□ at 8 V to 7100 Ω/□ at 0 V. As above, the steep decrease of R_{xy} coincides well with the apex of the R_s curve and occurs within a back-gate range of approximately 20 V (colored background). However, some noticeable differences to sample 4+20 are also observable. First, the zero crossing of R_{xy} occurs at −7 V and does

---

[7]The Hall curves in a) have been digitally symmetrized (see appendix C). The $R_s(V_{BG})$ curves are equivalent to the ones presented in Fig. 7.5. Instead of the BG being swept continuously, the value is obtained here from the zero crossing of the magnetic field sweeps at discrete voltages.
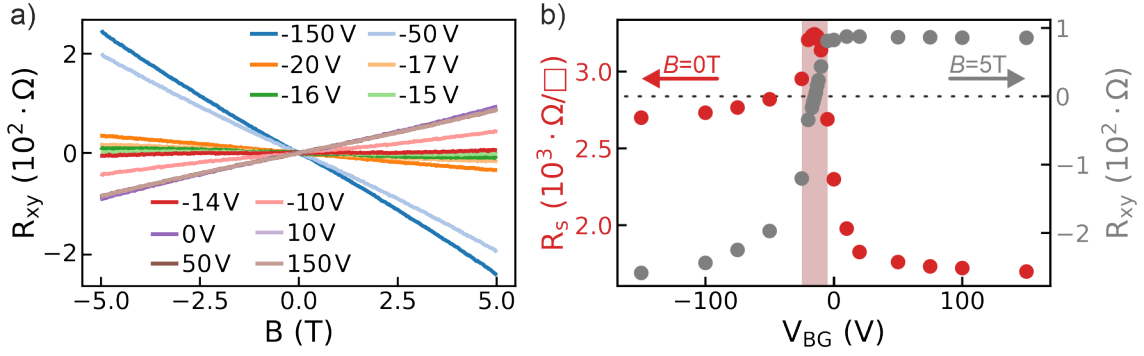
Figure 7.9: Sample 4+20 measured at $T = 4.2$ K. a) Hall resistance R_{xy} with respect to perpendicular magnetic field B. b) R_s at $B = 0$ T (red) and R_{xy} at $B = 5$ T (gray) versus back-gate voltage V_{BG}.

Figure 7.10: Sample 1+12 measured at $T = 4.2$ K. a) Hall resistance R_{xy} with respect to perpendicular magnetic field B. b) R_s at $B = 0$ T (red) and R_{xy} at $B = 5$ T (gray) versus back-gate voltage V_{BG}.

Figure 7.11: Sample 1+40 measured at $T = 4.2$ K. a) Hall resistance R_{xy} with respect to perpendicular magnetic field B. b) R_s at $B = 0$ T (red) and R_{xy} at $B = 5$ T (gray) versus back-gate voltage V_{BG}.
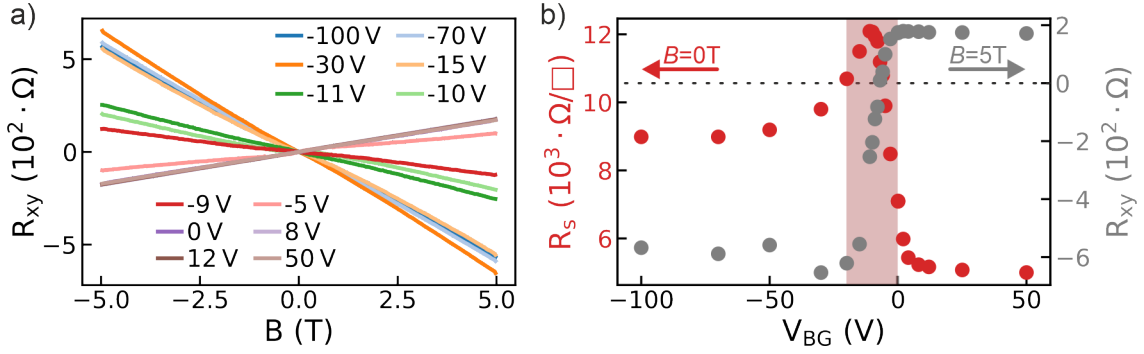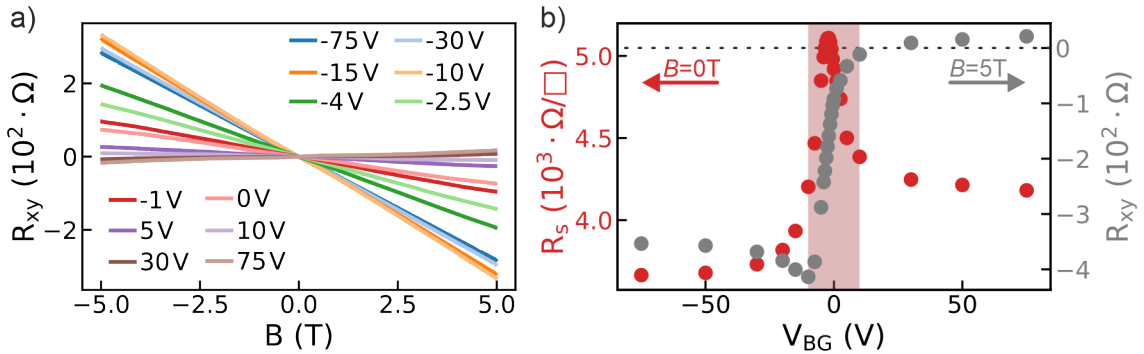
not coincide precisely with R_{peak} at -11 V. After the decrease, R_{xy} furthermore shows a distinct minimum in the vicinity of -30 V, before a horizontal behavior is approached. Considering the sheet resistance, while the qualitative behavior is very similar, its absolute values are significantly higher in 1+12 within all gate regions.

Sample 1+40:

The discussions of preceding sections suggested that the m-bulk channel is completely depleted as-grown for sample 1+40 and thus differences to samples 4+20 and 1+12 in the back-gated magnetotransport measurements are expected. Importantly, the Hall resistance of the unbiased measurement shown in panel a) of Fig. 7.11 shows a negative slope and hence a p-type behavior. A switch to n-type dominant electronic transport is achieved for positive gate voltages with $V_{\text{BG}} > 10$ V. For larger back-gate values R_{xy} approaches saturation, but still a slight variation can be observed even from $+30$ V to $+70$ V. This becomes more obvious in sub-figure b). Within $+10$ V $\leq V_{\text{BG}} \leq +75$ V $R_{\text{xy}}|_{B=5\text{T}}$ shows a small, but non-vanishing decrease. As a further contrast to samples 4+20 and 1+12, this is accompanied by an also only small variation of R_{s}. The strong modification of both curves sets in simultaneously below $V_{\text{BG}} = 10$ V. A striking resemblance of all three presented samples is the observation that, for 1+40 as well, the abrupt decrease of R_{xy} not only coincides with the apex of R_{s}, but also encloses a back-gate range of about 20 V (colored background). Similar to 1+12, R_{xy} shows a dip at -10 V, before again a horizontal behavior is approached for larger negative voltages. Interestingly, the zero crossing of R_{xy} does not coincide with R_{peak} in this sample and their respective back-gate voltage values do not agree in sign.

Discussion

As stated in the beginning of this section, in an idealized system with one Dirac-like transport channel the maximum of the sheet- and the zero crossing of the Hall resistance are simultaneously observed, when the gate has tuned the chemical potential to the Dirac point, as for example observed in graphene that is essentially described by this model [152, 153]. When a second transport channel of different charge carrier mobility is present, or the two channels are not equally modified by the applied voltage, the situation becomes more complex. Disregarding possible quantum corrections to both Hall and sheet resistance, the maximal generality is retained within a semi-classical discussion of the presented data in the diffusive transport regime by underlying a Drude model for an arbitrary number of contributing channels N. The relevant equations (see Sec. 3.1) are[8]:

---

[8]The minus sign in σ_{xy} is introduced to adapt the equation to the definition chosen in the measurements. R_{S} is proportional to the given expression as it has to be normalized by a constant that reflects the Hall-bar geometry.

$$\sigma_{xx} = \sum_i^N \frac{|q_i \cdot n_i \cdot \mu_i|}{1 + (\mu_i \cdot B)^2}, \qquad\qquad \sigma_{xy} = -\sum_i^N \frac{q_i \cdot n_i \cdot \mu_i^2 \cdot B}{1 + (\mu_i \cdot B)^2},$$

$$R_s \sim \frac{\sigma_{xx}}{\sigma_{xx}^2 + \sigma_{xy}^2}, \qquad\qquad R_{xy} = \frac{\sigma_{xy}}{\sigma_{xx}^2 + \sigma_{xy}^2}.$$

The longitudinal (σ_{xx}) and Hall conductivity (σ_{xy}) depend on the magnetic field B and the summation over the charge carrier density n_i, mobility μ_i, and charge q_i of the i-th channel. Here, the value of q_i is the elementary charge, being positive for holes and negative for electrons. Since the induction of a field effect to the sample tunes the respective charge carrier density n_i of channel i, these equations essentially become functions of the applied gate voltage and can be used to explain the expected observations for R_{xy} and R_s for a graphene-like sample. To replicate the typical data depiction used in the literature as well as in our studies within the panels b) of Figs. 7.9 - 7.11, the following will assume $B = 0$ for the longitudinal σ_{xx} and a constant $B \neq 0$ for the transversal σ_{xy}. In graphene, only one conduction channel is present in the system and the charge carrier density n goes to zero, when E_F is tuned to the Dirac point. This would yield $\sigma_{xx}(B = 0) = \sigma_{xy}(B \neq 0) = 0$ and the according R_s and R_{xy} would diverge. In a real measurement at non-zero temperature, however, the charge carrier density is not exactly zero, when the Fermi level lies at the DP, but an equal, finite amount of conduction electrons and holes of the same mobility and opposite charge will be present. Hence, the n- and p-channels cancel to zero in σ_{xy} and accordingly $R_{xy} = 0$. The longitudinal conductivity, on the other hand, can not go to zero if n does not vanish, since it is proportional to $\sum_i^N |q_i \cdot n_i \cdot \mu_i|$. It is, however, minimized when the Fermi level is tuned to the Dirac point since the carrier density is minimized and therefore yields a maximum in R_s. From this consideration it is conclusive, why a simultaneous zero crossing of R_{xy} and peak of R_s is not generally expected, when more than one channel contributes to the electronic transport: $R_{xy}(B \neq 0)$ goes to zero, when the $\sum_i^N q_i \cdot n_i \cdot \mu_i^2$ within $\sigma_{xy}(B \neq 0)$ vanishes. Therefore, the single terms of the sum and hence the single charge carrier densities n_i can be arbitrarily large, as long as they cancel to zero in the sum over all channels due to a varying sign of q_i. On the other hand, $R_s(B = 0)$ shows a peak, when $\sum_i^N |q_i \cdot n_i \cdot \mu_i|$ and subsequently the total charge carrier density is minimized. Hence, as soon as the number of contributing channels N with a gate-induced modulation of the carrier density n_i and varying charge carrier type q_i exceeds 1, the zero crossing of R_{xy} and the maximum of R_s are not necessarily expected to be observed at the same gate voltage.

In investigations on topological insulators both scenarios have been observed, where the zero crossing of R_{xy} and the maximum of R_s are positioned at the same [84, 151, 154–156] or at different [81, 148] gate voltage values. Due to the asymmetric design, we in general expect the latter case to be observed in our p-n heterostructures. The simultaneous appearance of R_{peak} and $R_{xy} = 0$ in sample 4+20 might be coincidental, as it also was the only one where this was observed. In this sample, equivalently to 1+12,

the non-depleted m-bulk channel leads to dominant electron conduction at $V_{BG} = 0$ V and the screening of the field effect for positive voltages. Interestingly, in a gate region, where R_{xy} stays completely constant, the sheet resistance still changes in both samples by approximately 30 %. This is surprising, since the formulas given above show that the values of σ_{xx} and σ_{xy} and accordingly R_s and R_{xy} are both modified by changes in density and mobility of the contributing transport channels. However, in contrast to σ_{xx}, σ_{xy} is proportional to μ^2, meaning it is more susceptible to changes in channels of higher mobility. This suggests that R_{xy} might be a more sensitive indicator for back-gate-induced variations of the topological surface states, assuming a higher mobility of the TSS than of bulk carriers. The variation of R_s and R_{xy} within the highlighted regions in the b) panels of Figs. 7.9 - 7.11 could hence be interpreted as the tuning of the Fermi level through the bottom TSS, whereas the changes in R_s for higher voltages, where R_{xy} remains constant, could be caused by a reduction of m-bulk carriers. This would explain, why the steepest decrease of R_{xy} occurs on a very similar back-gate range for all three samples and is accompanied by the apex of R_s.

Furthermore, combining these observations with the large differences observed in the absolute sheet resistance values between the three presented samples allows important conclusions on the effect of intrinsic compensation processes by the n- and p-type layer within the heterostructures: in contrast to samples 4+2, 4+6, and 4+12, sample 4+20 shows a back-gate-induced tuning through the bottom TSS, proving an as-grown depletion of the m-bulk channel and a subsequent reduction of screening effects. On the other hand, if applying a back-gate voltage to this sample would completely deplete the m-bulk channel before E_F is tuned through the b-TSS, the observed sheet resistance in Fig. 7.9 b) should not be almost four times lower than for sample 1+12 (Fig. 7.10 b). A possible explanation is sketched in Fig. 7.12. Let a), for example, represent sample 4+12 in an unbiased, as-grown scenario. Due to the comparatively large BS and low BSTS thickness the sample possess a very pronounced m-bulk channel, where E_f lies deep above the conduction band minimum (CBM). When the BSTS thickness is increased to e.g. 4+20, as sketched in sub-figure b), still a m-bulk contribution remains, but the Fermi level is shifted closer to the CBM throughout its whole thickness. Applying now a negative back-gate voltage results in an upward bending of the bands sketched in Figs. 7.12 c) and d). Subsequently, the m-bulk channel is reduced and the sheet resistance increases. For the sample sketched in c), the Fermi level still completely stays above the CBM and no R_{peak} is observed like for sample 4+12 in our measurements (see Fig. 7.5 c)). On the other hand, in the case of panel d), representing our picture of sample 4+20, the band bending is sufficient to pull E_F below the CBM at the STO/BS interface and due to the small density of states of the TSS, it is easily tuned through the bulk energy gap. However, there remains a sizeable area, where E_F remains above the CBM that leads to a large bulk contribution to conduction and the observation of an overall small sheet resistance in this sample, compared to e.g. sample 1+12, where we expect the Fermi level to be tuned by the back-gate into the energy gap throughout the whole sample thickness.
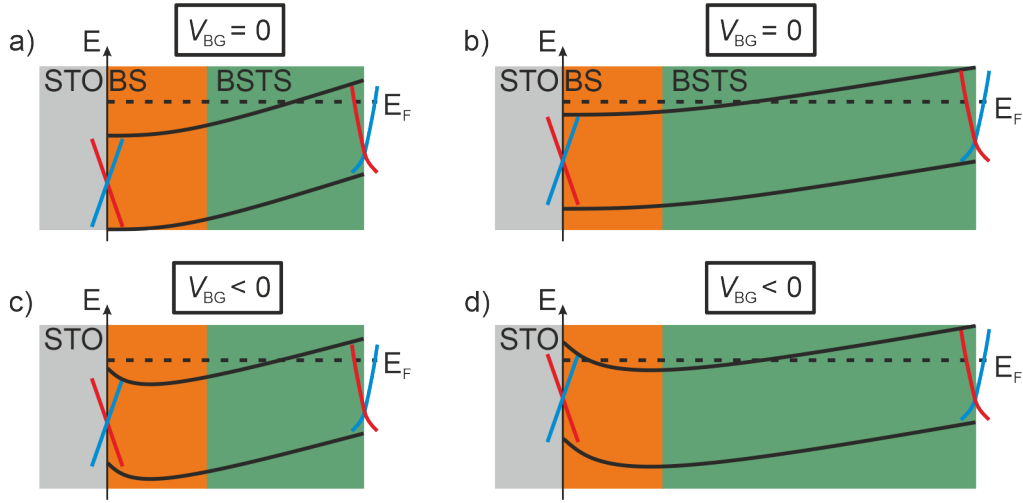
Figure 7.12: Sketches of band edge behavior in samples with large BS thickness. a), b) With increasing BSTS thickness (b) the Fermi level is shifted closer to the conduction band minimum at the STO/BS interface in comparison to a sample with smaller BSTS thickness (a). c), d) Applying a back-gate voltage $V_{BG} < 0$ to the thin sample (c) does not shift E_F below the CBM. In the thicker sample (d), it is shifted below the CBM at the STO/BS interface, such that it can be tuned through the b-TSS. In our exemplary case there remains, however, an area, where E_F lies above the CBM that leads to a small measured sheet resistance.

7.4 Summary and discussion

This chapter presented some of the key results of this thesis. After the preceding Ch. 6 had discussed the challenging MBE preparation of quaternary $(Bi_{1-x}Sb_x)_2(Te_{1-y}Se_y)_3$ ($x, y \neq 0$) alloys and highlighted the significant benefits for sample growth provided by the implementation of a Bi_2Se_3 seed layer, the investigations we discussed here considered the electronic properties of such BS/BSTS bilayers. To counteract the contribution to the bulk conduction introduced by the large unintentional n-type doping of BS, we created vertical p-n-type heterostructures in tuning the BSTS layer into a slight acceptor surplus via its stoichiometry, aiming to reduce the amount of parasitic bulk dopants via intrinsic compensation processes. In section 7.1 we presented our concept of the expected thickness dependent band bending within a p-n device, which was evidenced by an imaging of the surface band structure via ARPES. The proposed concept furthermore predicted the emergence of two types of bulk transport channels additional to the expected contribution of the surface states: a metal-like channel appearing when the Fermi level intersects one of the bulk bands and a semiconductor-like channel, when E_F lies within the energy gap. Their respective contributions to the overall conductance of the sample is expected to be largely dependent on the thicknesses of the BS and BSTS layers. To evaluate this prediction, a study of three sample series was presented in Sec 7.2, where the BS thickness was kept constant at 1 QL, 2 QL, or 4 QL, respectively, whereas the BSTS thickness was varied between 2 QL and 43 QL. Within this investigation the electronic behavior of the heterostructure was probed via a standardized characterization procedure (see appendix C) utilizing temperature-, magnetic field-, and back-gate-dependent transport measurements. Whereas the temperature dependence of the longitudinal sheet resistances showed signatures of all three channels varying with the respective layer thicknesses, the cusp-shaped magnetoresistance was ascribed to dominantly stem from the TSS. At least for small fields it is expected to be caused by weak anti-localization, allowing an analysis applying the Hikami-Larkin-Nagaoka theory. By tracking the prefactor α with respect to BSTS thickness, a continuous evolution from -0.5 to -1 was observed that corresponds to one or respectively two contributing conduction channels. For all three series, increasing the BSTS thickness lead to an increase of the semiC-bulk channel that is insulating enough at $T = 4.2\,K$ to cause an effective separation of conduction channels on top and bottom surfaces. Investigating the behavior of the sheet resistance with respect to back-gate voltage, on the other hand, allowed to gain important insight on the as-grown band bending effects within the p-n heterostructure. It not only showed the increasing compensation of excess charge carriers for larger BSTS thicknesses in the 4+x series, but, most importantly, also the approach of complete depletion of the m-bulk channel for 1 QL of BS and BSTS thicknesses above 20 QL.

A deeper evaluation of the back-gate-induced tuning of the electronic properties was provided in Sec. 7.3. Although the different responses of the contributing transport channels to the induced field effect render the measurements difficult to interpret and some observations suggest that the main modulation of the transport properties is connected to a Fermi level tuning mostly of the bottom surface, clear evidence was also provided

that the back-gate can indeed capacitively couple to the front surface by utilization of a dual-gated sample design. A key requirement for effective back-gating of the samples was identified to be the minimization of the m-bulk channel, as a large amount of mobile charge carriers at the STO/BS interface can easily screen the induced field effect. Connecting the observations presented in this chapter allows to provide a clear picture of the electronic characteristics of the investigated heterostructures. As predicted by the band bending concept displayed in Fig. 7.2, the transport of the p-n bilayers is largely governed by the precisely tunable thicknesses of the BS and BSTS layers. When 4 QL of BS seed layer are used, the electronic properties are dominated by the m-bulk channel. Increasing the BSTS thickness in such a sample does lead to a enhanced depletion of bulk carriers, but does not lead to a complete vanishing of the m-bulk channel in the investigated BSTS thickness range. For 1 QL of BS seed layer, on the other hand, this is achieved once the BSTS thickness reaches 20 QL. This leads to the important conclusion that the BS seed layer, which is crucial for high quality thin film epitaxy, can be implemented while its contribution to the unintentional bulk conductance of the sample can indeed be largely suppressed within a p-n bilayer device. Moreover, the presented measurements also provide valuable information about the parasitic bulk conductance of the semiconductor-like channel. In Sec. 7.2.1 we obtained a non-vanishing conductivity of this channel even at a temperature of $T = 4.2$ K. Such a behavior is often observed in literature even for nominally compensated TI materials and is usually ascribed to charge puddles. However, in our samples, this conductivity stemming from the BSTS bulk is small enough to observe a separation into two parallel, uncoupled conduction channels within the HLN analysis and to allow an un-screened capacitive coupling from the back-gate to the top surface in a dual-gated device even for a sample thickness of 41 QL. Nevertheless, we expect the largest TSS-to-bulk transport ratio for sample 1+20, as it is the thinnest heterostructure within our study, where a depletion of the m-bulk channel is achieved. Indeed, this sample showed the highest absolute magnetoresistance in Fig. 7.4 providing an indication confirming this claim. From this reasoning a straightforward starting point towards a further optimization of our p-n bilayer design follows: ideally, by modifying or varying the constituents of the sample stack, a complete depletion of the m-bulk channel should be achievable in even thinner films. Samples of a maximal thickness of about 10 QL should not only suffer from less parasitic bulk conduction, but moreover also offer a more effective back-gate-induced tuning of the electronic bands throughout the whole sample thickness. A first approach to achieve such an optimized second generation of heterostructure samples will be discussed in Ch. 9.

An important note considering the first sample generation that was presented in this chapter is the absence of Landau quantization effects, like e.g. Shubnikov-de Haas oscillations, in our magnetotransport studies, which might be expected in the case of dominant two-dimensional surface state transport. While the comparatively low magnetic fields of maximal ± 5 T and the high measurement temperature of $T = 4.2$ K utilized for the experiments of this chapter might not allow such effects to manifest, Landau quantization was also not observed in few selected samples that were measured up to $B = 12$ T or even $B = 16$ T with $T \ll 1$ K. Various mechanisms are conceivable to lie

at the origin of this circumstance. On the one hand, the most obvious causes could be the non-vanishing bulk conductivity and the rather rough surface topography decreasing the TSS mobility (see Fig. 6.7 for an AFM scan). There are, however, several more intricate effects that could further contribute to a decrease of the surface state mobility. Due to the variable x and y, the quaternary alloy $(Bi_{1-x}Sb_x)_2(Te_{1-y}Se_y)_3$ is susceptible to local disorder and chemical inhomogeneity. This leads to potential fluctuations that can ultimately cause the formation of the randomly distributed charge puddles. In this case, surface electrons can scatter in the subsequently present bulk states at the Fermi level [103], which reduces the TSS mobility. Furthermore, even in almost perfectly compensated BSTS materials, the formation of *surface* charge puddles has been reported to influence the TSS' electronic properties [135]. While for such puddles to form in the bulk the potential fluctuations have to exceed $\Delta/2$, with Δ being the energy gap size, the gap-less nature of the surface states leads to the appearance of surface puddles for any non-zero variation of the surface potential. In other words, surface disorder can yield a local modulation of the TSS' electronic structure on a nanometer scale that leads to a significant "blurring" of the surface state bands, when integrating over a mesoscopic area like in our magnetotransport experiments. This kind of surface disorder may not only have a negative impact on the formation of sharp Landau levels to observe effects like Shubnikov-de Haas oscillations, but might possibly also play an important role for an increased localization of surface electrons by means of strong interelectron correlations. This will be discussed in detail in the following chapter.

8

Analysis of magnetoresistive effects

The previous chapter presented a systematic transport characterization to investigate the electronic properties of the p-n heterostructures with respect to the thicknesses of the BS and BSTS layers. There, the cusp-shaped magnetoresistance was briefly discussed and ascribed to mainly stem from the topological surface states. At least at low temperatures and for small, perpendicular magnetic fields it was assumed to be caused by weak anti-localization, allowing an analysis by applying the Hikami-Larkin-Nagaoka formalism and the obtained results corresponded well with observations from e.g. the temperature dependence of the sheet resistance. However, beyond the measurements presented in the previous chapter, applying higher magnetic fields, increasing the temperature, or changing the field angle revealed a rich magnetoresistive behavior that motivates a deeper investigation, not only concerning the applicability of the HLN theory, but also to gain deeper insight into the mechanisms of electronic transport in our samples. For this purpose, four samples from the heterostructure study were chosen: 1+12, 1+40, 4+12, and 4+40. Additionally, a Bi_2Se_3 film with a thickness of 60 QL, in the following termed sample 60BS, was measured as a reference. Due to the large n-type doping in BS, the electronic transport in this sample is expected to be largely dominated by bulk carriers. The measurements discussed in this chapter utilized the *Spektromag SM-4000* cryostat described in section 5.1.4 that enables the application of magnetic fields up to ± 7 T for variable temperatures between 1.4 K and 300 K and adjustable penetration angles from the perpendicular out-of-plane- (OOP) to the in-plane (IP) configuration. Figure 8.1 shows the absolute magnetoresistances $MR^{abs} = R_s(B) - R_s(0\,T)$ at $T = 1.4$ K in the OOP configuration of the heterostructures in a) and 60BS in b). By means of the curves displayed in a), the reasoning for the TSS being the main cause of MR for the heterostructure samples provided in section 7.2.2 shall be briefly repeated: in simplified terms, the m-bulk and the semiC-bulk conduction contributions should increase with increasing BS or, respectively, BSTS thickness, but no correlation to an increase of magnetoresistance is observed in the measurements, leaving the TSS as the main origin.
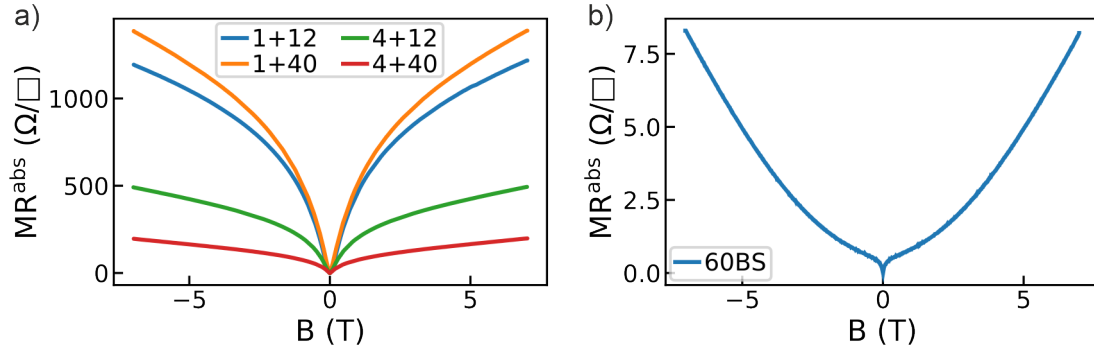
Figure 8.1: Absolute magnetoresistance $MR^{\text{abs}} = R_{\text{s}}(B) - R_{\text{s}}(0\,\text{T})$ at $T = 1.4\,\text{K}$ in the OOP configuration of the samples investigated in this chapter. a) 1+12, 1+40, 4+12, and 4+40. b) 60BS.

As apparent from Fig. 8.1 b), the completely bulk dominated transport in sample 60BS not only yields much smaller magnetoresistance values, but also a qualitatively different behavior. While a small cusp-like feature is still observable around zero magnetic field, the MR^{abs} curve follows a power-law behavior for $B \gtrsim 0.5\,\text{T}$. Such a magnetoresistance is typical for TIs with dominant bulk conduction and the high-field response is usually interpreted to stem from the Lorentz deflection of bulk carriers, where Kohler's rule (see Sec 3.1.2) yields $MR \sim B^2$ [137, 157–161]. This sample is hence the ideal reference to identify possible bulk contributions to the magnetoresistance of the heterostructures within the following investigations. First, the temperature dependence of the MR in the OOP configuration will be studied, including a particular interest on the high temperature behavior. In section 8.2, several observations will be presented that clearly demonstrate the presence of low-temperature effects additional to weak anti-localization from the TSS and signatures of electron-electron interactions will be discussed. Possible indications of bulk contributions to the MR at high fields will be investigated in Sec. 8.3. Finally, section 8.4 will summarize and discuss the main results, with a particular emphasize on the applicability and accuracy of the HLN analysis for OOP magnetic fields in the presence of additional magnetoresistive effects.

Note that in the experiments presented in the following, the p-n heterostructures mostly showed a qualitatively identical behavior and hence usually only the data from selected samples will be presented.

8.1 Temperature dependence of the magnetoresistance

In Figure 8.2 the temperature dependence of the OOP-MR of samples 1+12 (a, b), 1+40 (c, d), and 60BS (e, f) is displayed.

The magnetic field sweeps at constant temperature, shown in a), c), and e), reveal a cusp
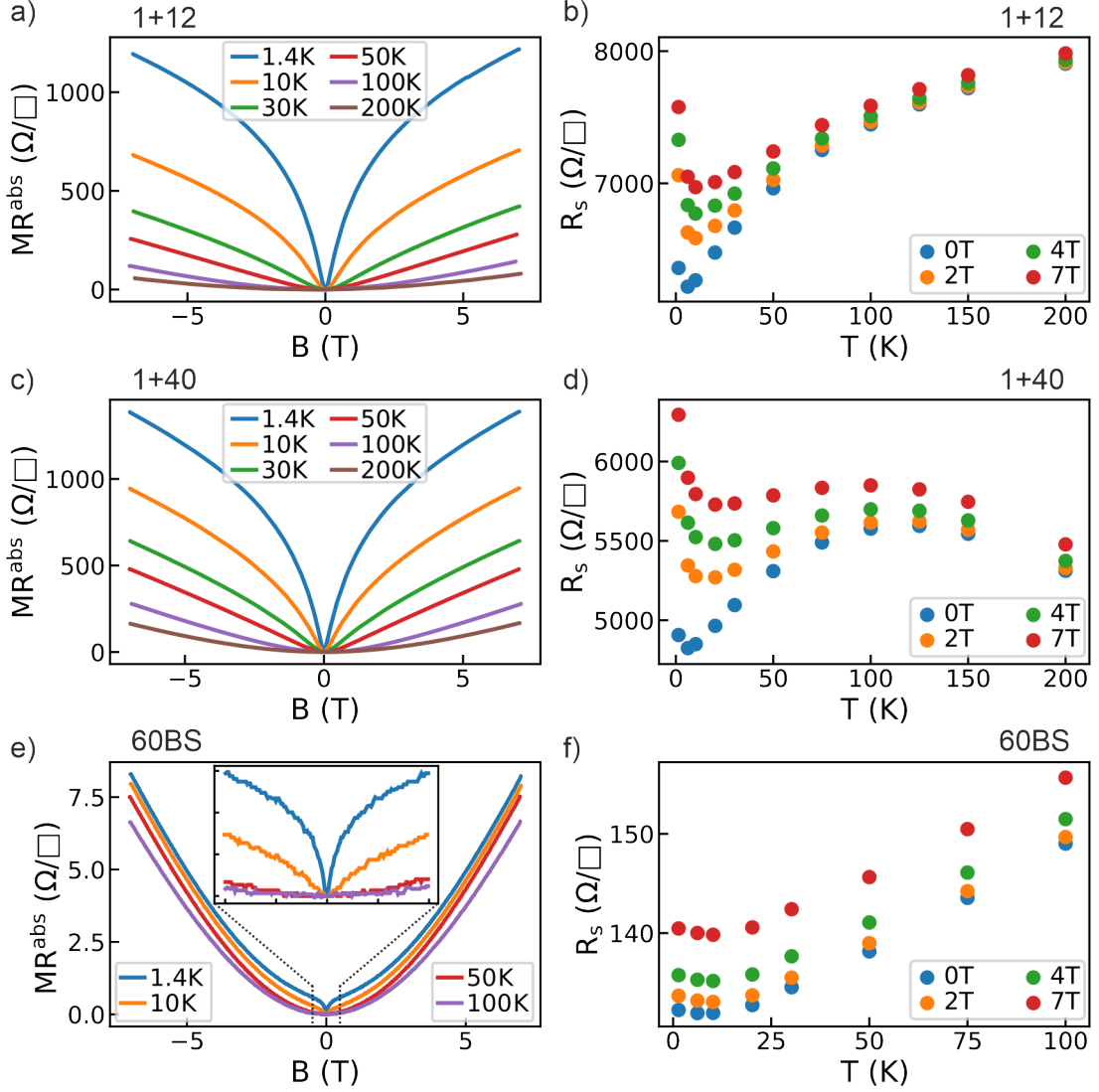
Figure 8.2: Temperature dependence of the magnetoresistance of samples 1+12 (a, b), 1+40 (c, d) and 60BS (e, f). a), c), d) Absolute magnetoresistance versus magnetic field at fixed temperatures of the respective samples. The inset in e) shows a magnification of $B = \pm 0.5$ T. b), d), f) Sheet resistance R_s versus temperature and fixed magnetic fields of the respective samples.

shape for all three samples at $T = 1.4$ K. However, while this cusp spans the complete range of ± 7 T for the heterostructures, it only manifests within $\approx \pm 0.5$ T in sample 60BS, which is magnified in the inset of panel e). As a fingerprint of quantum interference effects, the cusp-shaped MR becomes broader and gradually diminishes in amplitude, when the temperature is increased due to the decrease of the phase coherence length l_φ [50]. For sample 60BS, it already vanished entirely at 50 K. The MR then only follows the power-law behavior that is almost unchanged within the presented temperature range, which clearly suggests classical effects as its origin. In both heterostructure samples, the MR still shows cusp-like contributions at $T = 50$ K that completely vanish, however, on further increase of the temperature, where a power-law regime similar to sample 60BS is reached. These observations can be further clarified by investigating the modulation of the temperature dependent sheet resistance $R_s(T)$ by the applied field as plotted in panels b), d), and f). The temperature dependent freeze-out of bulk carriers has been discussed in Sec. 7.2.1 and can be retraced in Fig. 8.2 d) by means of the zero-field curve. There, the increase of R_s with decreasing temperature between 200 K and 125 K discloses dominant electronic transport by thermally activated bulk carriers. Below 100 K all three samples show a metal-like behavior at $B = 0$. However, the response of R_s to the application of a perpendicular magnetic field is drastically different in the heterostructures compared to sample 60BS, suggesting that indeed two different types of metal-like conduction channels might be present in the TI samples. For sample 60BS, where the large n-type doping is expected to shift the Fermi level into the conduction band, the metallic temperature dependence of R_s stems from trivial bulk states throughout the whole temperature range and applying a perpendicular magnetic field increases R_s only slightly and essentially independent of temperature. On the other hand, the behavior of the heterostructures can be roughly divided into two regimes. Above $T \approx 100$ K, the transport is dominated by bulk carriers, with a semiconductor-like temperature behavior in sample 1+40, a metal-like response in sample 1+12 originating from trivial carriers of the m-bulk channel and a small, approximately parabolic magnetoresistance in both samples as observed in BS. Below $T \approx 100$ K, the magnetoresistance increases in value and gradually evolves into the cusp-shaped form typical for quantum interference effects. This strongly suggests a drastically increasing contribution of the TSS to the electronic transport below this threshold temperature. Further indications for the power-law behavior stemming from trivial bulk states can be found in literature. For example, in Refs. [159, 160] an evolution from a cusp-shaped to a parabolic MR is observed by increasing the sample thickness and hence increasing the relative bulk contribution to the transport. In Refs. [157, 162], moreover, it is shown how the deposition of a thin, magnetic layer as well changes the MR from a cusp shape to a parabolic behavior, which is ascribed to the introduction of magnetic scattering of the TSS or the opening of a band gap due time-reversal symmetry breaking.

Figure 8.3 shows a further evaluation of the high temperature response of the heterostructures' resistances to a perpendicular magnetic field, where panel a) depicts the field sweeps for the p-n samples at $T = 200$ K. Whereas the measurements at $T = 1.4$ K shown in Fig. 8.1 a) revealed a large difference between the samples of the 1+x and 4+x series, the
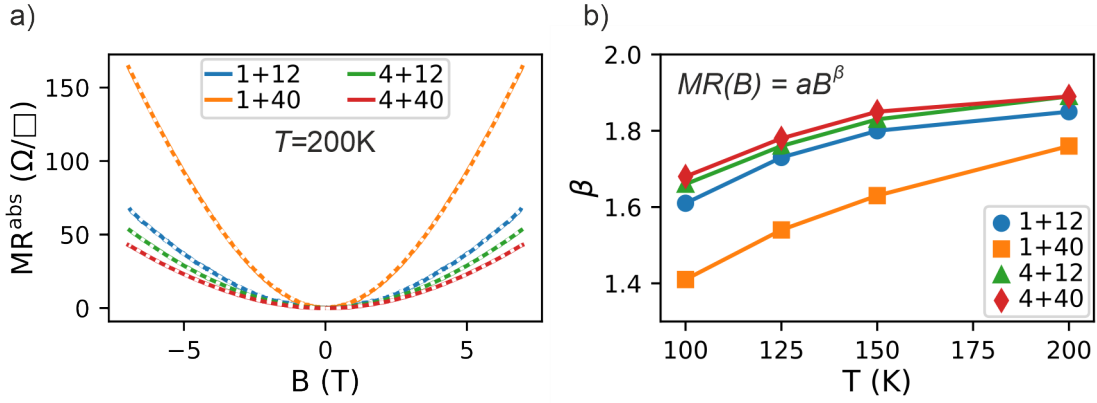
Figure 8.3: High temperature behavior of the magnetoresistance. a) Absolute magnetoresistance versus magnetic field at $T = 200\,\text{K}$ of the heterostructure samples. The white dotted lines fit the curves to a power-law behavior: $MR^{\text{abs}} = aB^{\beta}$. b) Temperature dependence of the exponent β between $100\,\text{K}$ and $200\,\text{K}$. All samples show an increase of β with increasing temperature T, but do not reach the classically predicted $\beta = 2$ within the investigated range.

values at 200 K at least for samples 1+12, 4+12, and 4+40 are similar. Only sample 1+40 shows a higher absolute MR, which could be connected to the lowest m-bulk conduction contribution in this sample, or, alternatively, a remaining influence of the TSS on the magnetoresistance. Such a residual TSS contribution might also be responsible for the observed deviation from the theoretically expected $MR \sim B^2$ behavior predicted by Kohler's rule for a classical magnetoresistance. The white dotted lines in Fig. 8.3 a) show a fit to the data using the equation $MR^{\text{abs}}(B) = aB^{\beta}$. The temperature dependence of the exponent β between 100 K and 200 K is displayed in sub-figure b). The Samples 1+12, 4+12, and 4+40 not only show a very similar MR at 200 K, but also an almost identical behavior of β with respect to temperature. Again, sample 1+40 poses an outlier, but its β values approach the other samples more closely at higher temperature. All samples show an increase of β with increasing temperature, but fall short of the classically predicted $\beta = 2$, possibly hinting towards a remaining presence of non-classical effects that could further diminish with higher temperature.

8.2 Signatures of electron-electron interactions

In the previous section the high temperature ($T > 100$ K) magnetoresistance was argued to dominantly stem from the electronic transport of trivial bulk carriers for the investigated samples. For the p-n-type heterostructures, the MR drastically increases in value and gradually evolves to the typical cusp shape, when the temperature is decreased. We ascribed this observation to an increasing contribution of the TSS to electronic transport. So far, the discussion of the origin of this low temperature MR was limited to weak anti-localization. The investigations presented in this chapter, however, clearly suggest the presence of low-temperature (magneto-) resistive effects additional to WAL stemming from the two-dimensional surface states. In the following, the key observations will be briefly presented, before they are discussed in more depth in the subsequent sections showing that effects of strong electron-electron interactions are a possible common origin.

Zero field, low temperature resistance behavior

The first relevant observation was already contained in the measurements of the *zero field* temperature dependence of the sheet resistance presented in Fig. 8.2 b) and d). There, the main behavior of the curves of samples 1+12 and 1+40 was ascribed to semiconductor- and metal-like bulk contributions, as well as, especially at low temperatures, the metallic TSS. However, even in the absence of a magnetic field, the $R_s(T)$ measurements showed a small increase for $T \lesssim 10$ K that was disregarded in the discussion above. This upturn can only be very slightly observed in sample 60BS (see Fig. 8.2 f), but is clearly present in all four investigated p-n heterostructures. This is shown in Fig. 8.4, where R_s is normalized by R_{min}, which corresponds to the minimum resistance at the temperature T_{min}, before the increase in R_s occurs. In the context of quantum corrections to the electronic transport at low temperatures this observation is surprising, since the expected weak anti-localization should *decrease* the resistance at $B = 0$. An increase of R_s could, in principle, stem from weak localization, but this effect should yield a negative magnetoresistance that is not observed in the measurements. Hence, an additional effect must be present that modifies the electronic transport in our heterostructure samples at low temperatures. This will be discussed in Sec. 8.2.1.

Figure 8.4: Sheet resistance R_s normalized by the resistance R_{min} at the minimum temperature T_{min} for $1.4\,\text{K} < T < 20\,\text{K}$. In this relative depiction, the resistance upturn for $T < T_{min}$ is very similar for all four samples.
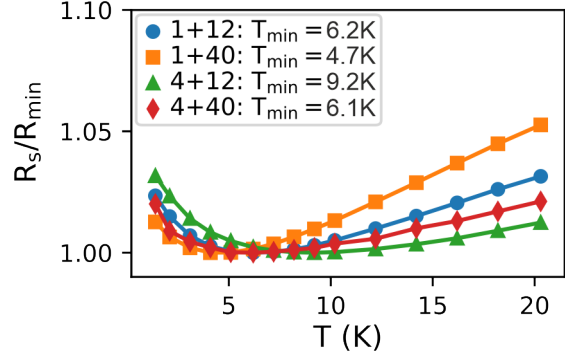
Figure 8.5: Absolute magnetoresistance MR^{abs} of sample 1+12 at $T = 1.4\,\text{K}$ for different angles between B and the sample surface from OOP ($0°$) to IP ($90°$). The MR does clearly not vanish in the IP configuration as it would be expected from weak anti-localization of the TSS.
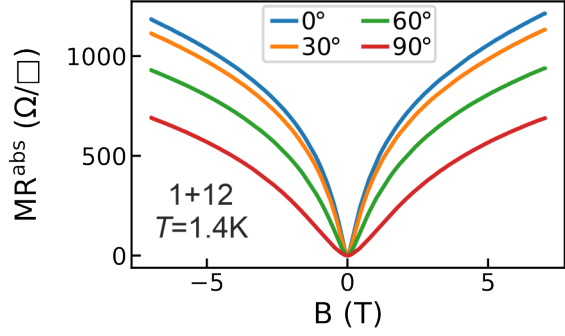
Figure 8.6: Absolute magnetoresistance MR^{abs} (upper panel) of sample 1+12 versus a magnetic field B at $T = 1.4\,\text{K}$. No saturation of the cusp-shaped MR is observed within the investigated field range. The lower panel shows the HLN fit (red dashed line) to the corresponding magnetoconductance (blue solid line), where a very good agreement is observed yielding the fit parameters $\alpha = -0.66$ and $l_\varphi = 58.6\,\text{nm}$.

113
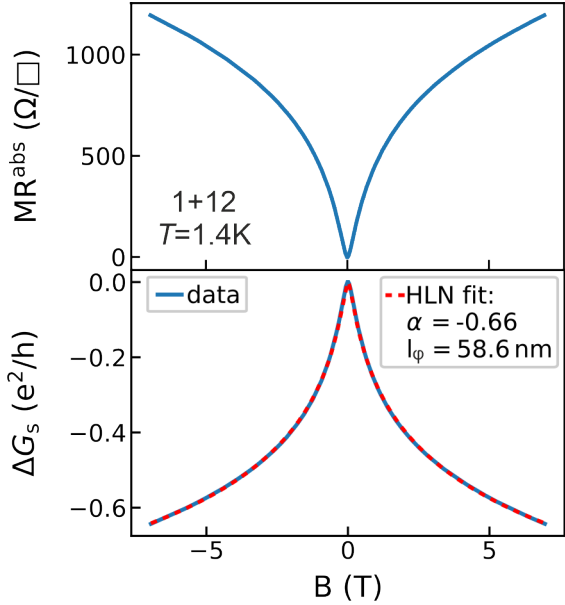
In-plane magnetoresistance

A second observation that can not be explained by WAL from the two-dimensional topological surface states is revealed by tilting the angle of the applied magnetic field with respect to the sample surface. As explained in Sec. 3.2.2, the positive correction to the conductivity by WAL stems from the destructive quantum interference of phase-coherent, time-reversed loops of a single electron wave function. Applying a magnetic field perpendicular to the loops dephases the partial waves and hence destroys the effect, leading to a positive magnetoresistance. Since the TSS are confined to the sample surface, only the component of the magnetic field perpendicular to the surface plane should contribute to the magnetoresistance. Figure 8.5 exemplarily shows a MR measurement of sample 1+12, where the angle between B and the sample surface is tilted from the OOP-($0°$) to the IP configuration ($90°$).[1] While the magnetoresistance shows a decreased value in the IP case and a more rounded shape around $B = 0$, it does clearly not vanish as would be expected if it originated solely from weak anti-localization of the TSS. Hence, like the sheet resistance increase at low temperatures, this requires a deeper evaluation of the underlying phenomena that will be given in Sec. 8.2.2.

Non-saturating out-of-plane magnetoresistance

So far, weak anti-localization has been the only effect discussed in the context of the observed cusp-shaped magnetoresistance. The upper panel of Fig. 8.6 shows an OOP-MR measurement of sample 1+12 performed at $T = 1.4\,\text{K}$, where no saturation is observed in the applied field range of $\pm 7\,\text{T}$. Applying the HLN formalism that theoretically describes the WAL effect in a magnetic field to the corresponding magnetoconductance ΔG_{s}, as displayed in the lower panel, shows nearly perfect agreement between theory and data, yielding realistic values with respect to literature for the fit parameters $\alpha = -0.66$ and $l_\varphi = 58.6\,\text{nm}$. While this observation not necessarily requires an explanation that goes beyond weak anti-localization, it is still worth to be discussed in more detail. In the theoretical introduction given in Sec. 3.2.2 it was shown that the magnetic field necessary to dephase two time-reversed partial waves depends on the surface area S enclosed by the respective loops, requiring larger B for smaller S. In order to travel a closed loop an electron has to be scattered multiple times. Hence, a lower limit of the enclosed area S and subsequently an upper limit of B exists, above that no further contribution to the magnetoresistance should be caused by WAL. As discussed in Sec. 3.2.2, the smallest possible surface area depends on the mean-free path ℓ and is of the order of ℓ^2. The corresponding upper magnetic field limit for the WAL contribution is then given by $B \approx h/(4e\ell^2)$. In many material systems that show signatures of weak anti-localization, like semiconductor-based two-dimensional electron gases, the effect manifests on magnetic field scales of $B \ll 1\,\text{T}$ due to large mean-free paths [163–166]. If the anti-localization in our samples is still present at $B = \pm 7\,\text{T}$, this would then yield an upper boundary of the mean-free path $\ell = \sqrt{h/(4eB)} \approx 12\,\text{nm}$. Of course, the investigated TIs are not strictly comparable to very clean semiconductor quantum wells, but on the other hand, the used

---

[1]In the IP configuration, the magnetic field is oriented perpendicular to the current applied through the Hall-bar. The three other p-n samples qualitatively show the same behavior.

magnetic field range of $B = \pm 7\,\text{T}$ was merely limited by the experimental conditions and no real prediction for the behavior beyond this field regime can be made. This raises the question, whether the high field MR of the heterostructure samples is still dominated by WAL or other effects are present that might be easily misinterpreted when the HLN formalism is applied. This will be evaluated in Sec. 8.2.3.

8.2.1 Zero field, low temperature resistance behavior

For the increase of the resistance below $10\,\text{K}$ several processes are conceivable. As stated above, a quantum correction originating from weak localization can be excluded, since this is expected to be accompanied by a negative magnetoresistance, which is not observed in the measurements. It could furthermore be ascribed to the freeze-out of bulk carriers, for example from an impurity band [167]. Then, the resistance in this temperature regime should follow an activation law as [50, 127]

$$R_{\text{S}} = R_0 \exp\left(\frac{\Delta}{k_{\text{B}}T}\right),$$

where R_0 is a constant, Δ is the activation and $k_{\text{B}}T$ the thermal energy. In Fig. 8.7 a) and b) the sheet resistance measurement of sample 4+12 is plotted between $T = 1.4\,\text{K}$ and $T = T_{\text{min}} = 9.2\,\text{K}$. To provide a dimensionless representation, the values of the sheet resistance and the temperature are normalized to R_{min} and T_{min}, respectively. In panel a), both axes are rescaled such that the curve should approach a linear behavior for decreasing temperature, if the resistance indeed followed an activation law behavior. As can be seen in the plot, no good agreement with a straight line is observed.

Another effect that is expected to cause an increase of resistance at low temperatures is strong electron-electron interaction (EEI). In literature, EEI has been discussed extensively in the context of topological insulators from an experimental [57, 80, 140–142, 161, 168] as well as a theoretical [59, 139] perspective and moreover also for other Dirac systems such as Weyl semimetals [143, 169–171] or graphene [172, 173]. This sometimes termed Altshuler-Aronov effect was theoretically described for disordered metals long before the discovery of TIs and predicts a $R_{\text{s}} \sim \ln(T)$ behavior for two-dimensional systems as introduced in Sec. 3.2.3 [54, 61, 63, 174]. Panel b) of Fig. 8.7 plots the same measurement as sub-figure a), but here the normalized sheet resistance $R_{\text{s}}/R_{\text{min}}$ of sample 4+12 is depicted versus $\ln(T/T_{\text{min}})$, such that a linear behavior is expected for an underlying electron-electron interaction mechanism. Indeed, below $T \approx 5\,\text{K}$ the presented data approaches a straight line. However, the discussion is further complicated when the additional effect of weak anti-localization is taken into account that should yield a contribution that reduces the resistance for decreasing temperature at zero magnetic field. While this could explain the deviation from a straight line for the activation law consideration given in Fig. 8.7 a), it was shown in Sec. 3.2.2 that for WAL as well a logarithmic temperature dependence is predicted. Hence, assuming that the two
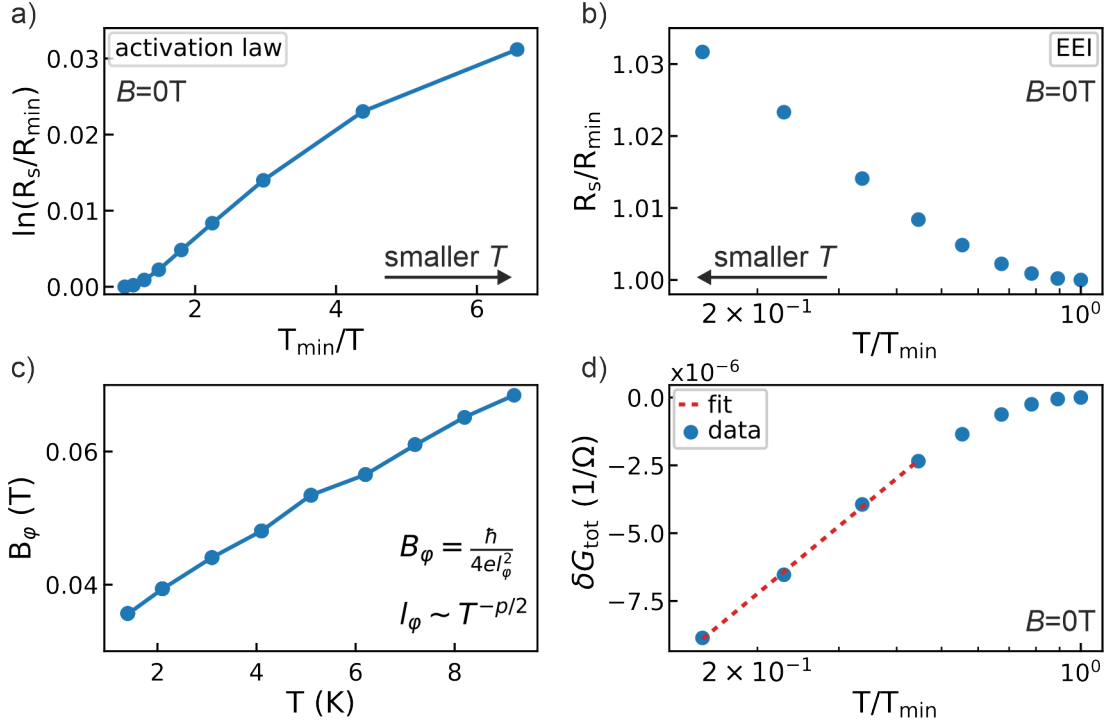
Figure 8.7: a), b) Sheet resistance of sample 4+12 normalized to the resistance R_{min} obtained at temperature $T_{min} = 9.2\,\text{K}$ plotted for a temperature range between 1.4 K and T_{min}. The axes of the plots are respectively adjusted such that a linear dependence would be expected, if the data followed an activation law (a) or an electron-electron interaction (b) behavior for the lowest temperatures. The black arrows indicate the direction of decreasing T. c) $B_\varphi = \hbar/(4el_\varphi^2)$ versus temperature obtained from the HLN fit to the magnetoconductance. The observed linear behavior corresponds to $l_\varphi \sim T^{-1/2}$ indicating dephasing mediated by quasi-elastic electron-electron interactions. d) Measured total correction of the conductance δG_{tot} (blue circles) plotted versus $\ln(T/T_{min})$. From the linear fit (red dashed line) the Coulomb screening factor $\tilde{F}_\sigma$ can be obtained.

corrections to the conductance δG_{WAL} and δG_{EEI} are approximately additive [141], the total correction δG_{tot} would still be expected to show a logarithmic behavior in temperature and be given by[2] [57, 141, 143]

$$\delta G_{\text{tot}} = \underbrace{(1 - \frac{3}{4}\tilde{F}_{\sigma})\frac{e^2}{\pi h}\ln\left(\frac{T}{T_{\text{EEI}}}\right)}_{\delta G_{\text{EEI}}} + \underbrace{\alpha p \frac{e^2}{\pi h}\ln\left(\frac{T}{T_{\text{WAL}}}\right)}_{\delta G_{\text{WAL}}}. \tag{8.1}$$

Here, $\tilde{F}_{\sigma}$ is the Coulomb screening factor of the electron-electron interaction, α is the pre-factor of the HLN formula (see Eq. 3.39) accounting for the strength of spin-orbit coupling and the number of channels contributing to electronic transport and p is determined by the dominant dephasing mechanism and is connected to the phase coherence length via $l_{\varphi} \sim T^{-p/2}$ (see Sec. 3.2.1). The parameters T_{EEI} and T_{WAL} are the critical temperatures, below which the quantum corrections are expected to dominate the $G_{\text{s}}(T)$ behavior. Following the approach of Refs. [57, 141, 143], the EEI screening factor $\tilde{F}_{\sigma}$ can be obtained, when $T_{\text{EEI}} = T_{\text{WAL}} = T_{\min}$ is assumed and the parameters α and p are determined from the magnetoconductance measurements. To obtain a value for p, Fig. 8.7 c) plots $B_{\varphi} = \hbar/(4el_{\varphi}^2)$ of sample 4+12 for $1.4\,\text{K} < T < 9.2\,\text{K}$. The values are obtained by fitting the HLN formula to the magnetoconductance measurements at the respective temperature within a magnetic field range of $\pm 1\,\text{T}$.[3] Since the phase coherence length is proportional to $T^{-p/2}$ and $B_{\varphi} = \hbar/(4el_{\varphi}^2)$, the observed linear behavior of B_{φ} yields $p = 1$, which corresponds to dominant dephasing by quasi-elastic electron-electron interactions in a two-dimensional system [56] that has similarly been reported for other TI systems [57, 175, 176]. From the same HLN fit to the magnetoconductance $\alpha \approx -0.77$ is obtained and after converting the resistance measurement to the conductance correction by [161, 167, 177]

$$\delta G_{\text{tot}}(T) = \frac{R_{\text{s}}(T) - R_{\text{s}}(T_{\min})}{R_{\text{s}}^2(T_{\min})}, \tag{8.2}$$

the data can be fitted to Eq. (8.1) for $T \leq 4.2\,\text{K}$ as shown in Fig. 8.7 d). The slope of the linear fit yields $\tilde{F}_{\sigma} \approx 0.86$, which is in good agreement with the theoretically expected range $0 < \tilde{F}_{\sigma} < 1$ [61], where $\tilde{F}_{\sigma} \to 1$ indicates complete screening [143]. While this value certainly contains significant uncertainty due to the large amount of influencing parameters and the narrow temperature window it was obtained from, the fact that it lies within the theoretically predicted regime provides a further indication that electron-electron interaction is indeed the origin of the resistance increase at low temperature.

---

[2]Both δG_{WAL} and δG_{EEI} describe conductances, while the formulas were theoretically introduced for conductivities in the corresponding sub-sections of Sec. 3.2. Like for the HLN formula describing the WAL magnetoresistance, this discrepancy stems from the fact that the original formulas were theoretically derived for purely (quasi-) 2D systems.

[3]Note that, as introduced in the beginning of section 8.2, a key question of this chapter is the accuracy of the HLN fit procedure in the presence of magnetoresistive effects additional to WAL. This will be discussed in Sec. 8.4.

Besides the physical origin of this anomaly, also the question about the responsible conduction channel has to be discussed. In the previous chapter, the presence of metal-like and semiconductor-like bulk contributions to the electronic transport additional to the TSS has been presented. The linear increase of the sheet resistance in $ln(T)$ at low temperatures shown in Fig. 8.7 b) specifically indicates electron-electron interactions within a *two-dimensional* system. However, a thin film can be considered (quasi-) two-dimensional in the context of EEI, already if the Thouless length $L_{\mathrm{Th}} = \sqrt{D/k_{\mathrm{B}}T}$ is larger than the film thickness t [61, 178]. While the diffusion constant D is unknown for our systems and thus no quantitative value for L_{Th} can be provided, it is conceivable that the thin films discussed in this chapter with a maximal thickness of $t \approx 44\,\mathrm{nm}$ lie below this quasi-2D threshold and all present transport channels could in principle be the origin of the two-dimensional EEI signature in the measurement. On the other hand, the fact that the manifestation of the resistance anomaly was shown to be very comparable within all four investigated samples, despite the variation of the layer thicknesses (see Fig. 8.4), and that very similar observations have been reported in literature for different topological insulators and other Dirac materials lend credence to the assumption that the topological surface states are the origin. A possible way to gain deeper insight to this questions is the investigation of magnetic field effects presented in the following.

8.2.2 In-plane magnetoresistance

In the previous section we ascribed the peculiar behavior of the sheet resistance at low temperatures to strong electron-electron interactions. The presence of this effect is intriguing, since it could also lie at the origin of the observed in-plane magnetoresistance that was exemplarily shown for sample 1+12 in Fig. 8.5.

In figure 8.8 a) the IP-MR of the four investigated heterostructure samples at $T = 1.4\,\mathrm{K}$ is presented. Compared to the OOP measurements the IP values of MR^{abs} are smaller, but the respective decrease for each of the four samples is almost identical with $MR_{\mathrm{IP}}^{\mathrm{abs}}/MR_{\mathrm{OOP}}^{\mathrm{abs}} \approx 55\%$. Hence, as in Fig. 8.1 for the OOP configuration, also in the IP case a significantly higher MR is observed for the 1+x compared to the 4+x samples. Applying the same argumentation as above for perpendicular fields thus suggests that the IP MR at $T = 1.4\,\mathrm{K}$ as well stems from the TSS. To further emphasize the presence of a magnetoresistive effect that does not solely depend on the perpendicular component of the applied magnetic field, figure 8.8 b) exemplarily shows the MR^{abs} of sample 4+40 at 1.4 K for different angles θ versus $B\cos(\theta)$. The inset shows the corresponding geometry. The current I_{x} is applied through the Hall-bar along the x-axis. In the OOP configuration ($\theta = 0°$), the magnetic field is parallel to the z-axis and it is tilted in the z-y plane for increasing θ. Thus, B is still perpendicular to I_{x} in the IP configuration and the value $B\cos(\theta)$ equals the component of the magnetic field normal to the sample surface. If MR^{abs} was only proportional to $B\cos(\theta)$, all measurements displayed in 8.8 b) would collapse on the $\theta = 0°$ curve. However, while the measurements for $0°$ and $30°$ coincide well, a clear deviation is observed for larger angles. A variety of candidates have been discussed to possibly cause such a non-vanishing IP magnetoresistance in topological insulators, reaching from WAL
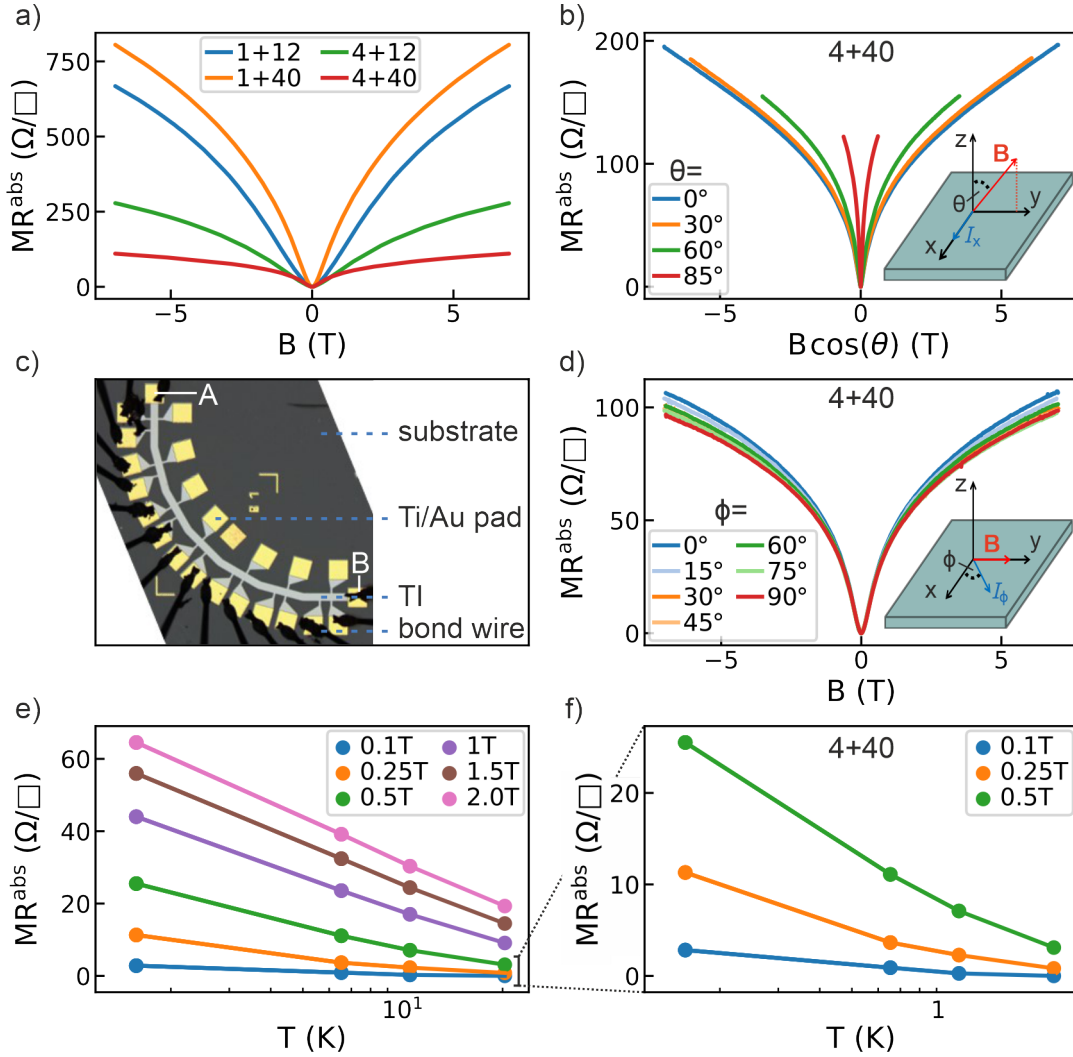
Figure 8.8: Investigation of the absolute magnetoresistance in the in-plane geometry at $T = 1.4\,\text{K}$. a) IP MR of the four heterostructure samples. Similar to the OOP configuration, the 1+x samples show significantly higher values. b) MR^{abs} for an out-of-plane to in-plane rotation of sample 4+40 plotted against the the magnetic field component perpendicular to the sample surface $B\cos(\theta)$. The measurement geometry is sketched in the inset. For large angles θ a clear deviation from the 0° curve is observed, indicating the presence of magnetoresistive effects that are not solely dependent on the perpendicular field component. c) Modified Hall-bar layout that allows MR^{abs} measurements with respect to the IP angle ϕ. The current is driven between contacts A and B, the longitudinal voltage is measured between two adjacent contacts, where each pair is tilted with respect to the previous by $\Delta\phi = 15°$. d) Dependence of MR^{abs} on the in-plane angle ϕ of sample 4+40 obtained by utilizing the Hall-bar shown in c) and the measurement geometry shown in the inset. e) MR^{abs} versus $\ln(T)$ of sample 4+40. Above $B \approx 1.5\,\text{T}$ a linear behavior is observed as predicted by theory for EEI. f) Magnified plot of the small field curves shown in e).

119

effects stemming from the sample bulk [157, 179], the sample sidewalls [180], or the non-zero extension of the TSS into the bulk [181], to coupling effects between parallel conductors [182], hexagonal warping of the surface states [183, 184], or a tilt of the Dirac cone by the magnetic field [185]. A measurement that excludes most of these effects to be the origin of the in-plane MR in our samples is presented in Figs. 8.8 c) and d), where the MR dependence on the in-plane angle ϕ is shown for sample 4+40 at $T = 1.4\,\mathrm{K}$. The measurement geometry is shown in the inset of panel d). The direction of the magnetic field is kept constant parallel to the y-axis, while ϕ is varied by changing the direction of the applied current I_ϕ. For this, a modified Hall-bar layout is utilized that is shown in an optical image in c). The current is driven between A and B and the four-point voltage is measured between two adjacent contacts, where each pair is tilted with respect to the previous one by 15°. The measurement displayed in d) reveals an almost isotropic MR between $\phi = 0°$ and $\phi = 90°$, where we ascribe the small deviations at large fields to minute local variations of the sample. As discussed in the theoretical introduction of Sec. 3.2.3, Lee and Ramakrishnan predict an *isotropic* magnetoresistance in disordered metals originating from the influence of field-induced spin splitting on the electron-electron interactions in Ref. [61]. While the observed anisotropy of the OOP-to-IP measurements is expected to stem from a WAL contribution that solely depends on perpendicular fields, the isotropy in the IP geometry, where WAL from the surface states is absent, provides a strong indication for the presence of such a magnetoresistive effect caused by isotropic spin-splitting. The functional dependence of the magnetoconductance corresponding to EEI was provided in Eq. (3.46) and from this the MR caused by electron-electron interaction is expected to be proportional to $\ln(h)$ with $h = g\mu_B B/k_B T \gg 1$. To test this prediction, Fig. 8.8 e) plots MR^{abs} of sample 4+40 at fixed magnetic fields in the IP configuration, where no additional effects from WAL should be present, against $\ln(T)$ for T between 1.4 K and 20 K. In this plot the data should approach a straight line, if $h \gg 1$ is fulfilled. According to expectation, the measurements for $0.1\,\mathrm{T} < B < 0.5\,\mathrm{T}$, that are magnified in Fig. 8.8 f), do not show a straight line behavior. For $B \gtrsim 1.5\,\mathrm{T}$ the regime of $h \gg 1$ already seems to be approached and the presented data thus qualitatively agrees with the prediction. To conclude, additional to the presented fingerprint of strong electron-electron interactions in the context of the $R_s(T)$ measurements presented in the previous sub-section, also the observed IP magnetoresistive effects agree well with the theoretical predictions for EEI. The in-plane geometry is ideal for studying the effects of a magnetic field on interelectron correlations, since no additional contributions by weak anti-localization from the TSS should be present. However, since the theory of EEI in principle predicts a completely isotropic magnetoresistance, its influence on the obtained *out-of-plane* MR has in turn to be investigated. This will be discussed in the following.

8.2.3 Non-saturating out-of-plane magnetoresistance

Next to the $R_s(T)$ anomaly and the in-plane magnetoresistance, the third observation presented in the introduction of this section was the non-saturating cusp-shaped mag-
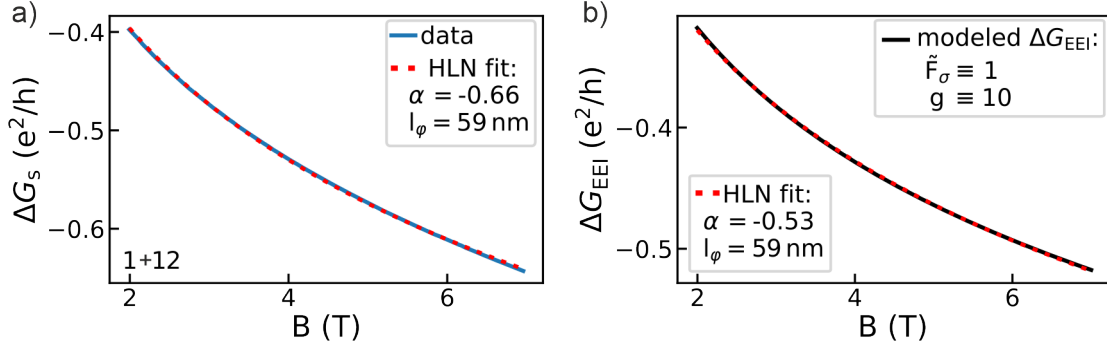
Figure 8.9: Comparison of HLN fitting of measured and modelled data artificially generated by the equation for $\Delta G_{\mathrm{EEI}}(B)$. a) Measurement of the sheet magnetoconductance ΔG_{s} of sample 1+12 for $2\,\mathrm{T} < B < 7\,\mathrm{T}$ at $T = 1.4\,\mathrm{K}$ (blue solid line) and according HLN fit (red dashed line) showing good agreement. b) Data generated using the equation for $\Delta G_{\mathrm{EEI}}(B)$ for the same B-range using the parameters $g \equiv 10$ and $\tilde{F}_\sigma \equiv 1$ (black solid line). The HLN fit (red dashed line) as well shows good agreement demonstrating the close functional similarity between ΔG_{EEI} and ΔG_{HLN}

netoresistance in the OOP geometry displayed for sample 1+12 in Fig. 8.6, where the corresponding magnetoconductance was shown to exhibit nearly perfect agreement with the applied HLN fit within the complete investigated field range of $\pm 7\,\mathrm{T}$. This measurement is shown again for $2\,\mathrm{T} \leq B \leq 7\,\mathrm{T}$ in Fig. 8.9 a).

In literature, the HLN formalism is usually applied for small magnetic fields ($B \lesssim 1\,\mathrm{T}$), since for larger B the magnetoconductance often deviates from the WAL-type cusp shape and adopts a linear or parabolic behavior. The latter was e.g. observed in our studies for sample 60BS (see Fig. 8.1 b)), where we expect the transport to be largely dominated by trivial bulk carriers. In some publications [186–188], the magnetoconductance is analyzed within the HLN framework for much larger magnetic fields, even up to $60\,\mathrm{T}$ in Ref. [188]. However, the underlying physical meaning is unclear. While the magnetic field range relevant for the WAL effect is inversely proportional to the mean-free path and hence increases with disorder, at some B even the smallest possible pairs of time-reversed loops should be dephased and the contribution of WAL to the magnetoconductance should vanish. In the context of the observed signatures of a magnetoresistance stemming from the modulation of electron-electron interactions in the in-plane geometry, presented in the previous sub-section, a new aspect is added to this discussion, as the theory provided by Lee and Ramakrishnan in Ref. [61] predicts the effect to be *non-saturating* and, in principle, *isotropic*. The close functional similarity for the respective magnetoconductances ΔG_{HLN} and ΔG_{EEI} raises the question, whether contributions of EEI are present or even dominate the MR in the OOP geometry for large B, while being easily misinterpreted for WAL. The equations for ΔG_{HLN} and ΔG_{EEI} were theoretically introduced in section 3.2 and are given by

$$\Delta G_{\text{HLN}}(B) = \alpha \frac{e^2}{2\pi^2\hbar} \left[\psi\left(\frac{1}{2} + \frac{\hbar}{4eBl_\varphi^2}\right) - \ln\left(\frac{\hbar}{4eBl_\varphi^2}\right) \right] \sim \alpha \begin{cases} \sim B^2, & (4el_\varphi^2 B)/\hbar \ll 1 \\ \sim \ln(B), & (4el_\varphi^2 B)/\hbar \gg 1, \end{cases}$$

$$\Delta G_{\text{EEI}}(B) = -\frac{e^2}{4\pi^2\hbar} \tilde{F}_\sigma g_2(h) = -\frac{e^2}{4\pi^2\hbar} \tilde{F}_\sigma \begin{cases} 0.084h^2, & h = (g\mu_{\text{B}}B)/(k_{\text{B}}T) \ll 1 \\ \ln(h/1.3), & h = (g\mu_{\text{B}}B)/(k_{\text{B}}T) \gg 1. \end{cases}$$

Importantly, both equation predict a magnetoconductance proportional to B^2 for small and to $\ln(B)$ for large magnetic fields. The close similarity is visualized in Fig. 8.9 b). There, the black solid line shows model data artificially generated using the theoretical formula for $\Delta G_{\text{EEI}}(B)$ inserting $T = 1.4\,\text{K}$, $2\,\text{T} \leq B \leq 7\,\text{T}$ and the arbitrarily chosen $\tilde{F}_\sigma = 1$ and $g = 10$, whereas the red dashed line represents a fit to this artificial data using ΔG_{HLN} with the free parameters α and l_φ. The fitted curve not only exhibits very good agreement with the generated data, but also yields realistic values for $\alpha = -0.53$ and $l_\varphi = 59\,\text{nm}$ that even lie in the vicinity to those obtained in our measurements. Testing the HLN fitting of artificial ΔG_{EEI} curves for different sets of parameters revealed that the functional agreement increases with increasing g-factor, since for large g and the chosen field range the functions for both ΔG_{HLN} and ΔG_{EEI} lie in the $\sim \ln(B)$ regime. The amplitude of both conduction corrections is then mainly determined by the prefactors that are identical if $\tilde{F}_\sigma = 1$ and $\alpha = -0.5$, which are realistic values within the respective theories. For the WAL effect the condition for $\Delta G_{\text{HLN}}(B)$ to enter the $\sim \ln(B)$ domain is already reached for fields of the order of a few tens of millitesla for typical phase coherence lengths. At a temperature of $T = 1.4\,\text{K}$ the requirement to enter this regime in the case of EEI is met if $gB \gg 2$. Considering the usually reported large g-factors for Bi-based TIs[4] [141, 189, 190], this condition should as well be fulfilled for the presented magnetic field range of $B \geq 2\,\text{T}$. Thus, from a functional point of view, the two effects can be easily misinterpreted, especially when considering comparably large magnetic fields. However, the actual physical interpretation of the measured data is more complex. In sub-section 8.2.1 the simultaneous presence of weak anti-localization and electron-electron interaction effects on the low temperature conductance at *zero magnetic field* was discussed. For $B = 0$, the corresponding quantum corrections to the conductivity were shown to have opposite sign, while both exhibit a $\sim \ln(T)$ behavior in temperature. We observed the effect of EEI to be stronger, such that the measured total conductance correction $\delta G_{\text{tot}}(T)$ was negative and obtained a linear behavior in $\ln(T)$ for $T < 5\,\text{K}$. In

---

[4]Experimentally obtaining reliable g-factor values relevant for this discussion by fitting the equation for ΔG_{EEI} to the obtained magnetoconductance data is not straight forward. On the one hand, fitting to the OOP data is questionable, since it is unclear, if EEI effects play a role in the OOP magnetoconductivity (see discussion below). On the other hand, fitting the IP data, where we ascribe the magnetoconductance to dominantly stem from EEI, yields values of $3 \lesssim g \lesssim 10$, but using these values in a discussion of OOP data would disregard a possible large IP-to-OOP anisotropy of the g-factor [141, 189]. Hence, providing distinct values is omitted at this point.

Ref. [139] it is theoretically proposed to use the measured sheet conductance G_s with respect to temperature under constant, non-zero magnetic fields to obtain a threshold for B, above which the WAL effect is expected to be completely quenched. For this, the slope of G_s in the linear regime is parameterized as κ given by

$$\kappa = \frac{\pi h}{e^2} \frac{\partial G_s}{\partial \ln(T)}.$$ (8.3)

For $B = 0$ both WAL and EEI contribute to κ in full extend. However, when applying non-zero, out-of-plane magnetic fields in increasing discrete steps, κ is predicted to be modified, until B is large enough to completely suppress the WAL effect. This approach has been applied experimentally in Refs. [57, 140, 141, 161, 168] and is shown for our samples in Fig. 8.10 a) and b). Panel a) exemplarily displays the sheet conductance G_s plotted versus the logarithmic temperature at distinct OOP magnetic fields between 0 T and 2 T for sample 1+12. The respective dashed lines represent linear fits to the data for $T \leq 4$ K. Applying small magnetic fields yields a variation of the linear slope in comparison to the $B = 0$ T curve. Approximately above $B = 1$ T, however, almost no additional modulation is observed. This manifests in the extracted values for κ that are shown as function of B for all four heterostructure in sub-figure b). All samples exhibit a very similar behavior with respect to magnetic field, showing an increase of κ for small B before saturation is approached above $B \approx 1$ T. The results we obtain for $\kappa(B)$ are in good agreement with literature. For example, in Ref. [191] the effect of interelectron correlations is systematically studied using Bi_2Te_3 antidot arrays and comparable values for κ with a very similar field dependence are reported. This result would suggest a quenching of the WAL effect on the magnetoresistance already for magnetic fields $B \gtrsim 1$ T and hence reinforces the question raised above about the physical origin of the logarithmic OOP MR for larger fields that was, for example, observed in sample 1+12, which is displayed again in Fig. 8.10 c) ($\theta = 0°$). As discussed above, comparing this curve qualitatively with the corresponding in-plane measurement ($\theta = 90°$) does reveal that in the presence of WAL in the OOP geometry the MR retains a logarithmic behavior to almost zero field, while the EEI originated IP curve adopts a clear parabolic shape around $B = 0$ T. For large fields, both measurements are logarithmic in B with similar slopes. If the magnetoresistance stemming from interelectron correlations observed for in-plane magnetic fields was completely isotropic, as predicted by the theory of Lee and Ramakrishnan, to a first approximation the curve for $\theta = 90°$ should be identically contained in the OOP measurement. Thus, calculating the difference to obtain $\Delta MR^{abs}(B) = MR^{abs}(\theta = 0°) - MR^{abs}(\theta = 90°)$ would yield the magnetoresistance that solely depends on the OOP field component. This is shown for sample 1+12 in Fig. 8.10 d). Intriguingly, the field dependence of the resulting curve agrees well with the results obtained from the investigation of κ extracted from the temperature dependencies of the conductance in constant magnetic fields shown in panel b). Around $B = 0$ T, a sharp WAL-type cusp is observed that starts to vanish for $|B| \gtrsim 1$ T and evolves into an approximately linear behavior for $|B| \gtrsim 2$ T. The vertical dashed lines
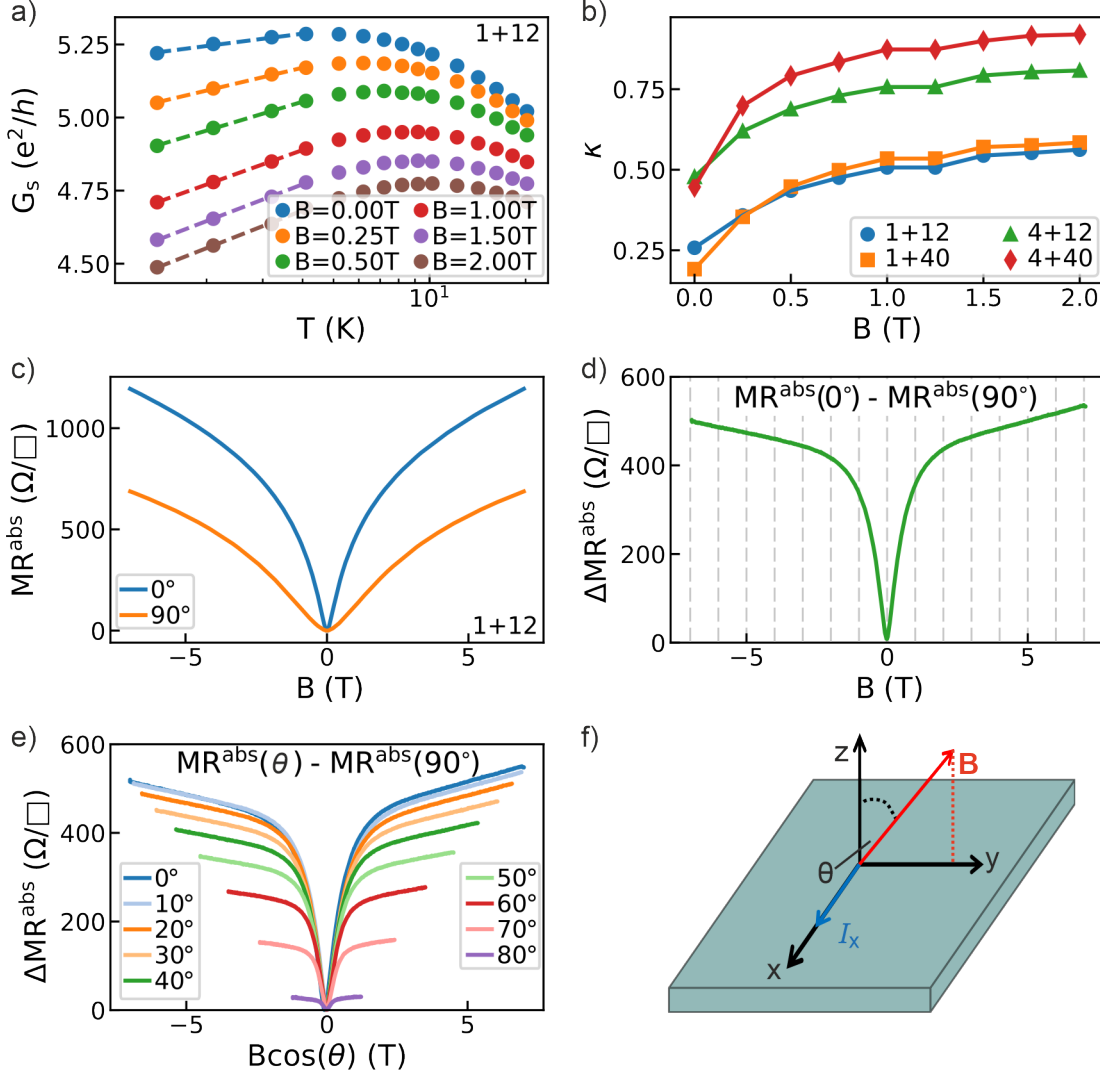
Figure 8.10: a) Measured sheet conductance G_s with respect to temperature of sample 1+12 and under static magnetic fields B. Independent of B, the curves exhibit a linear behavior below $T \leq 4\,\mathrm{K}$ and the dashed lines represent the respective linear fits. b) κ versus B extracted from the linear fits for all four heterostructure samples. c) OOP ($\theta = 0°$) and IP ($\theta = 90°$) MR of sample 1+12 at $T = 1.4\,\mathrm{K}$. d) Difference ΔMR^{abs} of the two curves shown in c). e) ΔMR^{abs} at different angles θ between the OOP and IP geometry. f) Used coordinate system.

in Fig. 8.10 d) mark the integer field values as a guide to the eye and we ascribe the slight asymmetry with respect to $B = 0\,\mathrm{T}$ in the displayed curve to an artefact of the measurement. At first sight, the agreeing observations for κ and $\Delta MR^{\mathrm{abs}}(B)$ would clearly suggest that WAL is indeed only relevant for $|B| \lesssim 2\,\mathrm{T}$ in the OOP geometry and suggest the conclusion that the logarithmic MR for larger fields might be largely determined by an effect of electron-electron interactions. However, while the evaluation of κ should actually be valid within the theoretical approach proposed in Ref. [139], the justification to calculate $\Delta MR^{\mathrm{abs}}(B) = MR^{\mathrm{abs}}(\theta = 0°) - MR^{\mathrm{abs}}(\theta = 90°)$ relies on the assumption of complete isotropy of the magnetoresistive EEI effect. In principle, the theory indeed does predict an isotropic behavior and the IP angle dependence presented in Fig. 8.8 d) of the previous sub-section experimentally confirmed this for the x-y-plane (see Fig. 8.10 f) for the coordinate system). However, an "indirect" IP-to-OOP anisotropy within the y-z-plane could arise via two different mechanisms. On the one hand, large anisotropies of the g-factor between IP and OOP magnetic fields have been reported for example for Bi_2Se_3 [141, 189], which would in turn modulate the EEI effect, when the angle θ is varied. Moreover, the theory of Lee and Ramakrishnan and hence the equation for $\Delta G_{\mathrm{EEI}}(B)$ given above, was derived disregarding spin-orbit scattering. If spin scattering is non-negligible, the spin-up and spin-down channels are mixed and the effect of spin-splitting and subsequently the magnetoconductivity is attenuated. For this case, Lee and Ramakrishnan propose in Ref. [61] that the additional condition $g\mu_B B \gg \hbar/\tau_{\mathrm{so}}^{\mathrm{i}}$ has to be fulfilled, before the Zeeman term causes a modulation of the EEI conductance correction. Here, $\tau_{\mathrm{so}}^{\mathrm{i}}$ is the characteristic spin scattering time, where the superscript i specifies the geometric axis with i=(x,y,z). This presents the second possible mechanism to induce an anisotropy to the EEI magnetoresistance, since, while usually $\tau_{\mathrm{so}}^{\mathrm{x}} = \tau_{\mathrm{so}}^{\mathrm{y}}$ within the sample plane is assumed, the value of $\tau_{\mathrm{so}}^{\mathrm{z}}$ can differ widely. The influence of spin-orbit coupling on the interelectron correlations has been under debate for trivial, disordered metallic systems [192–199] and also has received some attention in the context of topologically non-trivial materials [139, 140, 143, 186]. For the latter, the publications unambiguously report a *suppression* of the EEI induced magnetoresistive effects in OOP fields, which is qualitatively ascribed to a very small $\tau_{\mathrm{SO}}^{\mathrm{z}}$ due to strong spin-orbit coupling and the subsequently non-valid condition $g\mu_B B \gg \hbar/\tau_{\mathrm{so}}^{\mathrm{z}}$ for the available field ranges. In Ref. [186] quantitative values for $\tau_{\mathrm{SO}}^{\mathrm{x}}$ and $\tau_{\mathrm{SO}}^{\mathrm{z}}$ of thin Bi_2Te_3 films are obtained by fitting the OOP magnetoconductance to the non-approximated HLN formula introduced in Eq.

(8.2.3) of section 3.2 that is given by

$$\Delta G_{\mathrm{HLN}}(B) = \frac{e^2}{2\pi^2\hbar}\left[\ln\left(\frac{1}{b\tau_{\mathrm{e}}}\right) - \psi\left(\frac{1}{2} + \frac{1}{b\tau_{\mathrm{e}}}\right)\right.$$

$$-\ln\left(\frac{1}{b\tau_1}\right) + \psi\left(\frac{1}{2} + \frac{1}{b\tau_1}\right)$$

$$+\frac{1}{2}\ln\left(\frac{1}{b\tau_2}\right) - \frac{1}{2}\psi\left(\frac{1}{2} + \frac{1}{b\tau_2}\right)$$

$$\left.-\frac{1}{2}\ln\left(\frac{1}{b\tau_3}\right) + \frac{1}{2}\psi\left(\frac{1}{2} + \frac{1}{b\tau_3}\right)\right],$$

where $b = 4eDB/\hbar$ and the parameters $\tau_{\mathrm{SO}}^{\mathrm{x}}$ and $\tau_{\mathrm{SO}}^{\mathrm{z}}$ together with the characteristic times τ and τ_φ are contained in τ_{e}, τ_1, τ_2, and τ_3 as shown in Eqs. (3.36). The authors of Ref. [186] report $\tau_{\mathrm{SO}}^{\mathrm{x}} \gg \tau_{\mathrm{SO}}^{\mathrm{z}}$. Subsequently, they ascribe the observed IP magnetoresistance to EEI and claim a suppression of this effect in the OOP geometry, where the MR is solely ascribed to weak anti-localization. However, we were unable to apply this approach, since the fitting to our data with the extended HLN equation did not yield reliable results. We attribute this to the large amount of unknown parameters contained in the theory. Hence, we can not provide a quantitative investigation of the magnetic field range for which the condition $g\mu_{\mathrm{B}}B \gg \hbar/\tau_{\mathrm{so}}^{\mathrm{i}}$ is fulfilled in our samples. We do, however, have experimental evidence of an IP-to-OOP anisotropy of the magnetoresistance in our heterostructures, which is shown in Fig. 8.10 e). There, $\Delta MR^{\mathrm{abs}} = MR^{\mathrm{abs}}(\theta) - MR^{\mathrm{abs}}(\theta = 90°)$ is plotted for different angles θ versus the perpendicular component of the magnetic field $B\cos(\theta)$, according to the geometry sketched in panel f). The displayed curves are obtained by measuring the magnetoresistance up to $B = \pm7$ T at constant angles θ and subtracting the in-plane MR ($\theta = 90°$). As explained above in the context of Fig. 8.10 d), subtracting the $\theta = 90°$ should yield the contribution to the magnetoresistance that only depends on the OOP field component, if the in-plane MR was indeed stemming from a completely isotropic effect. Hence, plotting the curves against $B\cos(\theta)$ should make all measurements collapse onto one curve, which is clearly not observed in the presented figure.

To conclude, the origin of the logarithmic OOP magnetoresistance observed, for example, in sample 1+12 remains puzzling. On the one hand, especially the investigation of κ for increasing magnetic fields displayed in Figs. 8.10 a) and b) provides a clear hint that the influence of weak anti-localization on the sample conductance already starts to vanish for $B \gtrsim 1$ T. The magnetoresistive effect of EEI described by Lee and Ramakrishnan is the most obvious candidate to induce the logarithmic behavior above this threshold, since we not only experimentally observed it for in-plane magnetic fields, but the theoretically derived B-dependence of the conductance corrections stemming from WAL and EEI also show a close similarity. However, the predicted isotropy and hence the contribution to

the OOP MR is questionable, as shown within the discussion of Fig. 8.10 e). While the origin of the observed IP-to-OOP anisotropy could be the dependence of the g-factor on the field angle θ, an aspect more widely discussed in literature is the influence of spin-orbit coupling on the EEI induced magnetoresistance. A quantitative investigation of the condition $g\mu_\text{B}B \gg \hbar/\tau_\text{so}^\text{i}$ would allow to create a clearer picture of the presence of EEI contributions to the magnetoresistance with respect to magnetic field magnitude and angle. A possible framework to access values for τ_so^x and τ_so^z is provided by the extended HLN equation. If some of the material parameters contained in this theory, like the diffusion constant D or the mean-free time τ could be accurately obtained by means of additional measurement methods, a reliable determination of the spin-orbit scattering times would be conceivable.

8.3 Linear magnetoresistive regime: classical bulk effects at low temperatures

In the previous two sections of this chapter the magnetoresistance was discussed for two distinct temperature regimes. In Sec. 8.1 it was shown that the MR in OOP fields at high temperatures ($T \gtrsim 100\,\text{K}$) shows a power-law behavior that was ascribed to classical effects of bulk electrons. Decreasing the temperature revealed an increasing emergence of quantum mechanical interference contributions that largely dominate the MR and mostly show a logarithmic B-dependence in the heterostructure samples. On the other hand, for sample 60BS, where we expect the electronic conduction to be largely dominated by trivial bulk states at all temperatures, the subsequent characteristic cusp shape of the magnetoresistance was only observed within $|B| \lesssim 0.5\,\text{T}$. For larger fields the observed power-law behavior proved to be largely independent of temperature. The magnetoresistance of the heterostructure samples at the lowest available temperature was so far only discussed in the context of the quantum mechanical interference effects, i.e. the interplay of weak anti-localization and electron-electron interactions presented in Sec. 8.2. In figure 8.6 the dominance of the interference terms was illustrated by displaying how sample 1+12 exhibited a logarithmic dependence in B within the whole investigated field range of $\pm 7\,\text{T}$. While the same behavior was obtained in our measurements for sample 1+40, the samples 4+12 and 4+40 revealed a contrasting observation.
This is exemplarily shown in Fig. 8.11 a) for sample 4+40, where in accordance to figure 8.6 the HLN fit is applied for $B \pm 7\,\text{T}$. In contrast to sample 1+12, sample 4+40 shows a clear deviation from the logarithmic behavior of the fit. The corresponding OOP magnetoresistance ($\theta = 0°$) is displayed in 8.11 b), which approaches an approximately linear field dependence for large B. The observation of linear magnetoresistive regimes has been reported before for topological insulator systems [82, 106, 137, 187, 200–208] and different responsible mechanisms have been identified. In Refs. [204, 206] the linear magnetoresistance (LMR) is associated to disorder induced inhomogeneities of the carrier distribution and mobility [209]. Since we expect such inhomogeneities to be present in
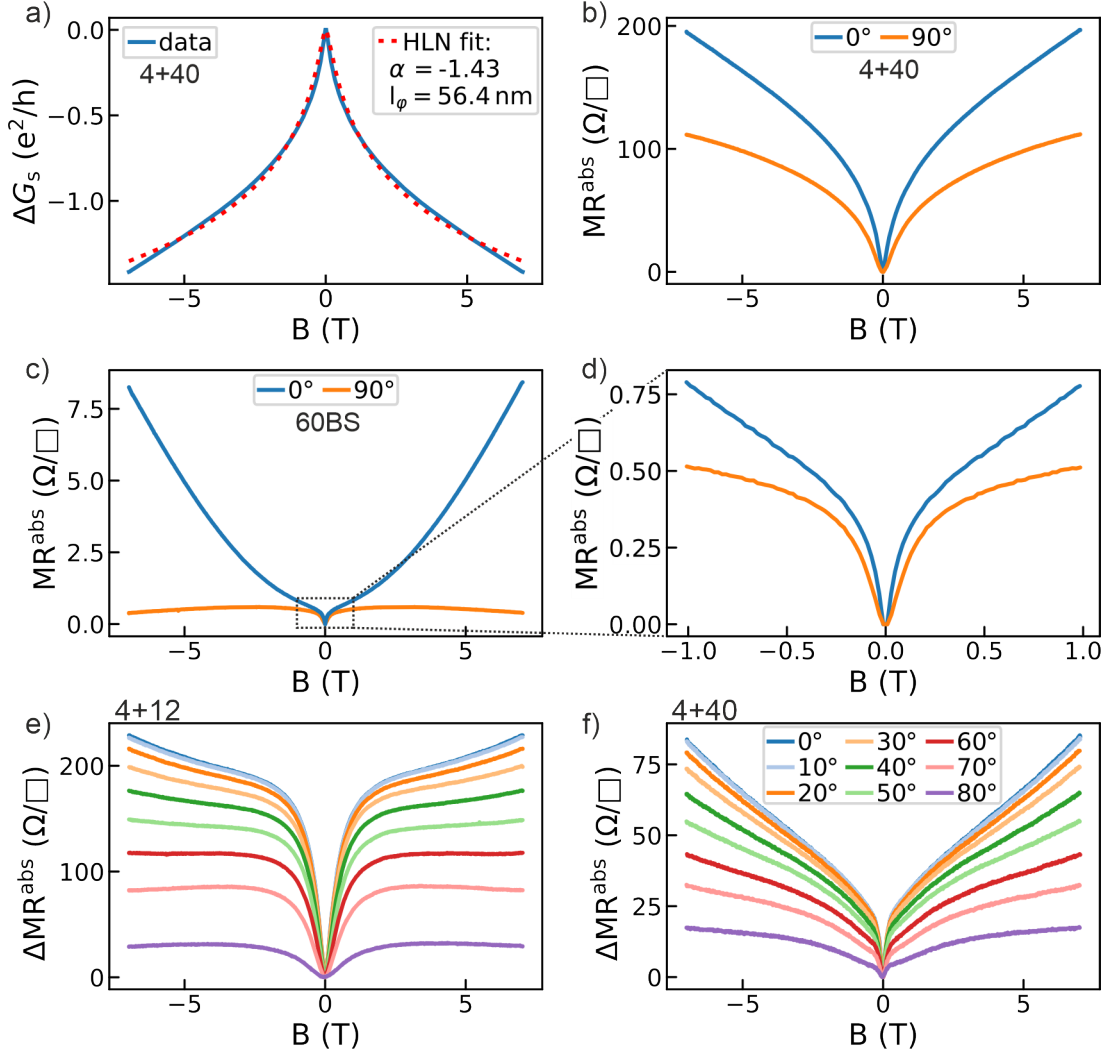
Figure 8.11: Investigation of linear magnetoresistive regime at $T = 1.4\,\mathrm{K}$. a) Magnetoconductivity ΔG_s of sample 4+40 and HLN fit for $B = \pm 7\,\mathrm{T}$. In contrast to sample 1+12, the fit shows a clear deviation for sample 4+40. b) Absolute magnetoresistance MR^{abs} of sample 4+40 in the out-of-plane ($\theta = 0°$) and in-plane ($\theta = 90°$) geometry. For OOP fields, the MR approaches a linear behavior for large fields, which is absent in the IP case. c) OOP and IP MR^{abs} for sample 60BS. The parabolic B-dependence for $B \gtrsim 1\,\mathrm{T}$ vanishes, when the field is tilted to the in-plane orientation. d) Magnification of the cusp-like feature around zero field of sample 60BS. The behavior for $-1\,\mathrm{T} \leq B \leq 1\,\mathrm{T}$ closely mirrors the B-dependence of sample 4+40 for $B = \pm 7\,\mathrm{T}$. e), f) ΔMR^{abs} obtained by subtracting the IP MR from the measurements obtained at angle θ for samples 4+12 (e) and 4+40 (f). Both plots share the legend provided in f). By subtracting the mostly logarithmic IP MR, the two samples reveal an evolution into an approximately power-law behavior for fields beyond the cusp around $B = 0\,\mathrm{T}$, which behaves like the parabolic B-dependence in sample 60BS, when θ is increased.

our samples, these effects are intriguing candidates. However, disorder effects should be equally relevant for all four heterostructures, but the linear MR regime is only clearly observed for samples 4+12 and 4+40. Moreover, in Ref. [204], the slope of the LMR is reported to be directly proportional to the sheet resistance of the samples in a gate-dependent study. This is not observed in our measurements (not shown). The fact that the LMR regime in our investigations is only clearly obtained in the heterostructures of the 4+x series suggests a connection to the significantly larger contribution of the m-bulk channel in these samples (see Ch. 7.2). This would furthermore exclude the quantum mechanical model proposed by Abrikosov [210], which links a linear magnetoresistance to linearly dispersive states and is hence discussed as an LMR origin in the context of topological surface states [118, 207, 208]. On the other hand, Parish and Littlewood suggest in a classical model the emergence of a LMR in trivial two-dimensional disordered conductors [211, 212], which could be applicable to describe the sizeable contribution to electronic transport by the m-bulk channels in the samples of the 4+x series. Another explanation conceivable for our samples is provided in Ref. [187], where the superposition of a parabolic and a logarithmic term within the extended HLN model (Eq. (3.35)) is suggested to yield an approximately linear overall behavior. The authors thus ascribe both types of field dependencies to stem from the anti-localizing quantum interference mechanism. In our measurements, we observe an approximately quadratic MR in sample 60BS (see Fig. 8.11 c)). Due to the weak temperature dependence of this parabolic behavior, we described this observation to be caused by classical effects. A very similar power-law field dependence of the MR was revealed for the heterostructures at high temperatures, where the quantum interference effects are suppressed. Assuming the same physical origin as for sample 60BS, it would follow from the weak temperature dependence that the power-law MR contribution is as well present for all heterostructures at low temperatures, but is largely masked by the logarithmic quantum effects, especially for the investigated 1+x samples due to the thin BS layer. Since the m-bulk channel and subsequently trivial bulk electrons provide a large contribution to the electronic transport in the 4+x samples, a possibly associated quadratic MR would naturally be more pronounced and could in turn yield an approximately linear behavior in a superposition with logarithmic quantum effects. This motivates a close comparison between the magnetoresistances of sample 60BS and the 4+x heterostructures. In Figs. 8.11 b) and c) the absolute magnetoresistance MR^{abs} at $T = 1.4\,\mathrm{K}$ and within $B = \pm 7\,\mathrm{T}$ measured in the OOP ($\theta = 0°$) and IP ($\theta = 90°$) geometry is displayed for samples 4+40 and 60BS, respectively. As can be seen in panel b), the LMR vanishes, when the magnetic field is tilted from the perpendicular to the in-plane orientation and the remaining MR exhibits a logarithmic behavior. Comparing this to the same measurements in c) reveals that the quadratic component of the MR indeed goes to zero and even adopts a slightly negative slope in the IP geometry for sample 60BS, which corresponds to a (quasi-) 2D behavior in the picture of classical Lorentz deflection of charge carriers [213–215]. The low-field MR for $B = \pm 1\,\mathrm{T}$, which is shown magnified in Fig. 8.11 d), almost mirrors the behavior exhibited by sample 4+40 within the whole available field range. After a sharp cusp around $B = 0$, the MR adopts an almost linear dependence up to $\approx 1\,\mathrm{T}$ in OOP orientation, where it begins to evolve into the parabolic

shape observed for larger fields in panel c). In the IP geometry the cusp is slightly broader in B and the linear regime has vanished. This directly projects how the superposition of logarithmic quantum- and quadratic bulk effects can yield a linear MR. The origin of the logarithmic MR for in-plane magnetic fields of the heterostructure samples and the question about its predicted isotropy have been discussed in-depth in sections 8.2.2 and 8.2.3. As stated in the latter, subtracting the measured IP magnetoresistance from the curve obtained for fields with $\theta \neq 90°$ is only completely justified, if the IP effect is perfectly isotropic. While this is not necessarily the case, subtracting the two curves to obtain ΔMR^{abs} does eliminate a logarithmic component from the OOP data. The residual curves for samples 4+12 and 4+40 are shown in Figs. 8.11 e) and f), respectively, where both panels share the legend given in f). For $\theta = 0°$, both samples show a sharp cusp around $B = 0$, but evolve into a parabolic shape for lager fields. When θ is increased, like for sample 60BS, this parabolic part bends downwards and even adopts a slight negative slope in sample 4+12. In combination, the presented observations thus indicate that the approximately linear MR obtained in our investigation for samples 4+12 and 4+40 at low temperatures originates from the superposition of quantum and classical effects that are logarithmic and parabolic in B, respectively.

8.4 Summary and discussion

In summary, this chapter provided an in-depth analysis of the influence of magnetic fields on the longitudinal sample resistance. By comparing the samples 1+12, 1+40, 4+12, and 4+40 from the p-n heterostructure series with a pure 60 QL thick Bi_2Se_3 film in temperature and field angle dependent investigations, different aspects and contributions to the magnetoresistance have been discussed, yielding valuable information to gain a deeper understanding of electronic transport processes relevant in our topological insulator samples. Especially nearing liquid helium temperatures a rich MR behavior emerges, combining classical with different kinds of quantum interference effects. The first section of this chapter (Sec. 8.1) presented the temperature dependence between 1.4 K and 200 K for out-of-plane magnetic fields. For $T \gtrsim 100$ K all samples showed a power-law behavior approaching a parabolic B-dependence. The weak temperature dependence of this parabolic MR, especially observed in sample 60BS, lets us ascribe this term to stem from a classical Lorentz deflection of charge carriers described by Kohler's rule. When the samples are cooled down below the $T \approx 100$ K threshold, an increasing manifestation of a cusp-shaped magnetoresistance is observed. In sample 60BS this cusp is observed for $B \approx \pm 1$ T, whereas for larger fields the parabolic MR behavior preserves. On the other hand, for the heterostructures the cusp-shaped MR almost spans the complete available field range of ± 7 T, especially in samples 1+12 and 1+40. The cusp shape is a characteristic fingerprint of quantum interference effects, with weak anti-localization being most prominently discussed in literature in the context of topological insulators. However, section 8.2 of this chapter presented observations that require additional contributions beyond WAL of the topological surface states to be present.

First, in sub-section 8.2.1 the temperature dependence of the zero field sheet resistance showed a distinct increase for $T \lesssim 10\,$K, contrary to the expectation considering anti-localization effects, which should decrease the resistance. The logarithmic temperature dependence of this upturn of $R_s(T)$ is typically explained in literature by localizing effects stemming from electron-electron interactions. This interpretation is supported in our investigations by the second observation presented in sub-section 8.2.2, where strong interelectron correlations as well serve as a viable explanation. Tilting the magnetic field at $T = 1.4\,$K into an orientation parallel to the sample plane, revealed a sizeable positive magnetoresistance, which can as well not be explained by two-dimensional WAL. The observed B-dependence and the in-plane anisotropy of this IP magnetoresistance agree well with the theory of Lee and Ramakrishnan provided in Ref. [61] describing the influence of magnetic fields on strong electron-electron interactions in disordered metals and the subsequent modulation of the conductance. In the context of the observed logarithmic magnetoresistance spanning the whole investigated field range of $\pm 7\,$T, sub-section 8.2.3 discussed possible EEI influences on the OOP magnetoresistance and demonstrated the close functional similarity between EEI and WAL effects under magnetic fields. While theory predicts the MR from electron-electron interaction to be isotropic, literature consensually reports its suppression in perpendicular magnetic fields due to large spin-orbit coupling in topological insulators. Within our investigations no clear conclusion could be drawn. On the one hand, the magnetoresistance of sample 1+12 was shown to exhibit good agreement with the HLN theory for fields up to $\pm 7\,$T. However, especially the presented study of κ, which parameterizes the slope of the logarithmic temperature dependence of the conductance under static magnetic fields, provides direct hints towards a vanishing of the WAL contribution to the magnetoresistance already for $B \gtrsim 1\,$T. For a quantitative evaluation of the EEI effect in perpendicular magnetic fields values for the spin-orbit scattering times of the system would be essential. A further possible additional contribution to the OOP magnetoresistance at low temperatures was discussed in Sec. 8.3, where the observation of a linear magnetoresistive regime for large fields observed in samples 4+12 and 4+40 was presented. While multiple mechanisms could be the origin of a linear magnetoresistance and have been discussed in literature, the data displayed in section 8.3 suggest classical effects from the large m-bulk transport contribution to be the origin in these samples. Like more dominantly observed in sample 60BS, these classical effects are expected to exhibit a power-law behavior in B. The subsequent superposition of this approximately parabolic field dependence with logarithmic contribution from the quantum interference effects can subsequently lead to the observation of an apparent linear magnetoresistance for large fields within the investigated range.

The magnetoresistance is one of the key observables in electronic transport experiments on topological insulator systems. Especially for OOP magnetic fields the usually observed cusp-shaped MR around $B = 0$ is mostly associated solely to WAL and analyzed within the HLN formalism. While the application of the HLN fitting to TI transport experiments has received some general theoretical criticism, since the theory was originally derived for (quasi-) two-dimensional systems with parabolic dispersion [216, 217], our data presented in this chapter furthermore raises the question of the accuracy of the HLN

evaluation in the potential presence of additional MR contributions from bulk effects or electron-electron interactions. For our heterostructure samples, the bulk effects are observed to be small at low temperatures, especially for small fields due to the parabolic B-dependence. Furthermore, we would expect a sizeable contribution of such effects to lead to a clear deviation of the HLN fit from the obtained data. This is observed for sample 4+40 in Sec. 8.3 within $B = \pm 7$ T, but not the case, if the fitting range is limited to fields of $B \leq 1$ T as performed in Sec. 7.2.2 of the previous chapter. On the other hand, possible contributions of EEI could more subtly hamper the accuracy of the HLN fitting, because of the theoretically predicted similarity of the field behavior to that of WAL. Even in the presence of a sizeable EEI contribution to the MR, the overall measured response could thus preserve a B-dependence that can be fitted well by the HLN equation. However, the investigations we presented in Sec. 8.2.3 suggest that WAL indeed is the dominant magnetoresistive effect in perpendicular magnetic fields within the heterostructure samples, at least for $B \lesssim 1$ T. This is supported by the HLN study of the three heterostructure thickness series presented in Sec. 7.2.2 of the preceding chapter, where the fitting range was limited to $B \leq \pm 1$ T and particularly the obtained values for the prefactor α showed a very predictable behavior and good agreement with expectation as well as with observations drawn from separate measurements.

In the temperature dependence of the zero field sheet resistance discussed in Sec. 8.2.1 the EEI effects clearly dominate over the anti-localization for $T \lesssim 10$ K. Considering the sample thickness dependence of the EEI-induced in-plane MR displayed in Fig. 8.8 a), the very similar observations reported in literature for different topologically non-trivial materials, and the theoretical prediction of an increased EEI relevance in low-dimensional systems [61], it is plausible that interelectron correlations in the transport conducted by TSS electrons are the origin of the EEI manifestations in our measurements. Moreover, as discussed in the theoretical introduction provided in Sec. 3.2.3, for electron-electron interactions to be non-negligible, sizeable disorder of the system is required. Structural and atomic surface disorder was already identified in the conclusion of the previous chapter as a possible cause of the absence of observable Landau quantization in our magnetotransport studies (see Sec. 7.4). Since we expect the observed strong interelectron interaction signatures in our measurements to be as well correlated to this type of disorder, the EEI effects could be used as a sensor in future efforts to improve the surface quality, e.g. by optimizing the growth conditions and post-growth treatment, changing the alloy composition or varying the heterostructure components. Additionally to the mapping of the surface topography via AFM, especially the temperature dependence of the longitudinal sheet resistance at zero field, where the EEI show the largest influence on the electronic transport, would thus provide a quick and easy method to test the influence of surface disorder on the electronic behavior of the samples. For this, not even a Hall-bar sample geometry would be necessary and the patterning process could be omitted by utilizing a *van der Pauw*-like measurement geometry [218].

9

Optimizing the p-n heterostructure sample design

From the conclusions of the previous two chapters, two main challenges towards a further optimization of the p-n sample concept can be identified. Chapter 7 introduced the BS/BSTS heterostructure design and showed how the implementation of the Bi_2Se_3 seed layer significantly contributed to the improvement of sample growth quality, whereas its sizeable n-type impact to the parasitic bulk conduction can be suppressed by creating intrinsic compensation of excess bulk carriers when using a p-type BSTS layer. This electronic depletion of the metal-like bulk (m-bulk) conduction channel caused by the strongly n-type BS layer was achieved by limiting the BS thickness to 1 QL, while the thickness of the slightly p-type BSTS layer needed to be increased to at least 20 QL. Reaching a completely depleted m-bulk channel with minimized BSTS thickness poses the first challenge for the concept optimization, since this would provide two crucial advantages: first, it was presented in Ch. 7 that despite the Fermi level being nominally tuned into the bulk band gap for the used $(Bi_{1-x}Sb_x)_2(Te_{1-y}Se_y)_3$ stoichiometry, still a not completely vanishing bulk conductance is obtained, which could be caused by remaining charge puddles. A reduction of the overall sample thickness is thus favorable in terms of parasitic contributions to the electronic transport stemming from the BSTS layer. The second advantage of a minimized BSTS thickness concerns the electrostatic tunability of the electronic properties by back-gating. While the BG was shown in section 7.3 to be capable of creating a capacitive coupling to the top surface of the sample even for a total device thickness of 41 QL, we expect a still enhanced field effect induced variation of the Fermi level throughout the sample thickness in thinner films. Besides the reduction of the sample thickness, the second major challenge for optimizing the heterostructure concept is the minimization of surface disorder. This disorder was not only identified in the conclusion of chapter 7 as one of the main possible reasons for the absence of Landau quantization in the magnetotransport studies of our samples, but also discussed in chapter 8 as the root of strong interelectron correlations that contribute to a localization of TSS electrons.

These two challenges motivate the investigations presented in this chapter. Addressing the goal of minimizing the sample thickness, we aim to achieve electronic depletion of the m-bulk channel in samples consisting of 1 QL BS and 10 QL of BSTS (1+10). We approach this by continuously increasing the antimony concentration of the BSTS layer, which enhances the amount of present excess acceptors, with the goal of optimizing the compensation between n- and p-type bulk carriers for the targeted thickness. Concerning the issue of disorder, the samples discussed in this chapter underwent a slightly modified growth procedure. While all growth parameters were applied identically to the previously presented heterostructure samples, an additional heating was supplied to the front of the sample, which will be termed *front-heating* in the following. In the usual epitaxial growth procedure, the only heating is applied to the sample through the substrate by the manipulator heating station. By running an additional evaporation cell at $1030°C$[1], we provide more heat to the sample surface by radiation and hence to every newly impinging atom during the growth process, aiming to reduce the atomic disorder.

To investigate these approaches towards an optimization of our p-n heterostructure concept, this chapter is structured as follows. First, Sec. 9.1 will present a series of 1+10 samples with varying Sb concentration x, covering a range of $0\% \leq x \lesssim 89\%$, where especially beyond $x \gtrsim 0.7$ an intriguing electronic behavior was observed. To provide a deeper understanding of the phenomena obtained for high x, Sec. 9.2 will discuss a thickness series at a constant Sb concentration of $x \approx 0.9$. The thinnest sample of this series (1+10) will be more deeply discussed in Sec. 9.2.1, before Sec. 9.3 will provide a brief summary and discussion of this chapter. Note that a detailed evaluation of the influence of front-heating on the sample *topography* can be found in Ref. [219]. The following investigations focus on the electronic properties of the samples and all magnetotransport measurements were performed utilizing the ^{4}He dewar introduced in Sec. 5.1.4.

9.1 Antimony concentration series

As stated in the introduction to this chapter, a main goal for the optimization of the p-n heterostructure sample design is to obtain a completely depleted m-bulk channel for very thin BSTS films. This way, the sizeable contribution to the parasitic bulk conduction introduced by the BS seed layer would be suppressed, whereas the small BSTS thickness not only minimizes possible further conduction contributions by the BSTS bulk, but would also be expected to facilitate an improved capacitive coupling of the back-gate throughout the whole sample thickness. For the samples discussed in this section we chose a 1+10 structure, i.e. 1 QL Bi_2Se_3 and 10 QL of $(Bi_{1-x}Sb_x)_2(Te_{1-y}Se_y)_3$. While even thinner films can easily be prepared by means of MBE, this thickness is used to certainly stay above the threshold, where the TSS of top and bottom sample surface are predicted to hybridize accompanied by a gap opening [220, 221]. Figure 9.1 provides an overview of the investigated samples with a fixed Se ($y \approx 0.9$) and varying Sb concentration, that are

---
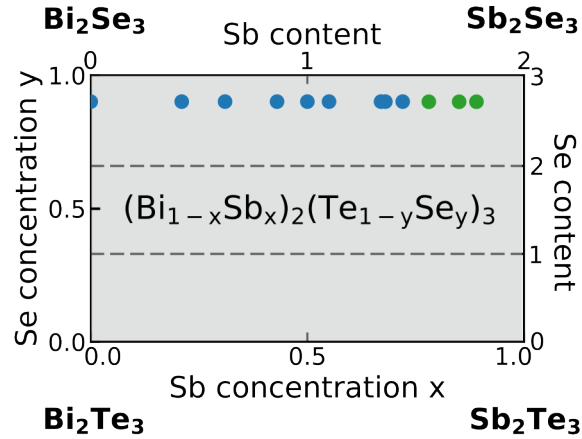
[1]Without evaporating any material.

Figure 9.1: Overview of investigated $(Bi_{1-x}Sb_x)_2(Te_{1-y}Se_y)_3$ samples with fixed $y \approx 0.9$ and varying x. The samples are subdivided into two groups. The first group (blue circles) contains all samples of the series with an Sb concentration up to $x \approx 0.72$, which corresponds to the value used in Ch. 7. Samples of the second group (green circles) were grown with $x > 0.72$. The values of x and y were targeted during growth by adjusting the beam fluxes and verified post growth by XPS.

subdivided into two groups.

The first group (blue circles) contains all samples with an Sb concentration up to $x \approx 0.72$, which corresponds to the value used for all heterostructures discussed in Ch. 7. These samples will be used here to verify the results of chapter 7 and to possibly identify any significant influences of the front-heating procedure on the electronic properties. From the findings of Ch. 7 clear expectations for the behavior of the group 1 samples in these studies can be formulated. For low x, we expect the Fermi level of the BSTS layer to lie in the conduction band and hence the complete sample stack should exhibit a metal-like behavior in electronic transport experiments. When the BSTS Fermi level is tuned into the band gap by increasing x, less bulk conduction and semiconductor-like signatures should be observed. Once the BSTS enters a p-type regime, we expect a compensation of bulk carriers with the n-type BS and hence an additional reduction of bulk conduction. However, since no complete depletion of the m-bulk channel was observed in Ch. 7 on a 1+12 sample, where the BSTS layer was grown with a Sb concentration of $x \approx 0.7$, a sizeable metal-like contribution stemming from BS-induced trivial bulk carriers should remain for all group 1 samples of this series. Only for the samples of the second group (green circles in Fig. 9.1), where the Sb concentration is increased beyond $x \approx 0.72$, a modified transport behavior is expected. Both groups will be investigated and compared below by means of temperature, magnetic field, and back-gate dependent magnetotransport measurements. Note that the desired values for x have been targeted during MBE growth by adjusting the beam fluxes. The values provided in the following investigations have been obtained post growth by means of XPS and have to be considered with an error of

about $\pm 3\%$. For details see Ch. 4.

9.1.1 Temperature dependence of the sheet resistance

The temperature dependence between room temperature and 4.2 K of the longitudinal sheet resistance R_s of the complete series is shown in Fig. 9.2 a), where the respective blue and green colors represent the two sample groups as introduced in Fig. 9.1.
The samples of group 1 precisely meet the expectations formulated above based on the results of Ch. 7. For small x, a low sheet resistance with a strictly metallic temperature dependence is observed, which we ascribe to the BSTS Fermi level lying inside the bulk conduction band and hence the whole sample stack essentially behaves like a metal. From $x = 0.5$ to $x = 0.55$ the sheet resistance at $T = 4.2$ K almost doubles, accompanied by the appearance of a semiconductor-like signature in the temperature dependence that becomes more pronounced when increasing x towards 0.72. This is highlighted in Fig. 9.2 b), where the temperature dependence of the sheet resistance normalized to its value at room temperature R_s^{norm} is shown to exemplarily compare the qualitative temperature behavior of the samples with $x = 0.21$ and $x = 0.67$. In contrast to the strict metal-like trend observed for $x = 0.21$, the sample with $x = 0.67$ exhibits an upwards bending of the curve for temperatures of $T \gtrsim 150$ K, which is a clear sign of a freeze-out of bulk carriers. In chapter 7 we connected such a behavior to a semiconductor-like conduction channel within the heterostructure, where the Fermi level is located in the bulk band gap. From the observations of Fig. 9.2 a) we thus conclude E_F to lie within the energy gap for the samples with $0.55 \leq x \leq 0.72$ at least partially within the sample stack. In this concentration regime we also observe a small increase of R_s, when the sample is cooled down towards the lowest available temperatures. In section 8.2.1 such an upturn was interpreted as a manifestation of disorder-induced quantum mechanical electron-electron interactions in transport mediated by the TSS. While this is a further hint for an increased surface contribution at low T for $x \geq 0.55$, this also suggests that the slightly modified growth procedure, which all samples of this chapter underwent, does not decisively solve the issue of surface disorder. The highest observed resistance within group 1 is observed for $x = 0.72$. For a very similar Sb concentration ($x \approx 0.7$), we have shown in Ch. 7 that the BSTS layer possesses a slight surplus of acceptor-type donors and the subsequent compensation of p-type BSTS with n-type BS carriers leads to an overall reduction of parasitic bulk conduction. On further increase of x it could be expected that after a maximum of R_s, obtained where the optimum intrinsic bulk charge carrier compensation is reached, the acceptors within the BSTS become dominant until the Fermi level is pushed into the bulk valence band, accompanied by a stark decrease of the sample resistance and the recovering of a completely metal-like temperature dependence. However, the measurements presented in Fig. 9.2 a) show a completely different picture. For the samples of group 2 (green), where the Sb concentration is increased beyond $x = 0.72$, the sheet resistance shows a drastic increase with x, reaching a value of 37.5 k$\Omega/\square$ at $T = 4.2$ K for $x = 0.89$. For a sample with an Sb concentration of $x = 0.94$ the resistance became so high that no electrical measurement was possible by the applied
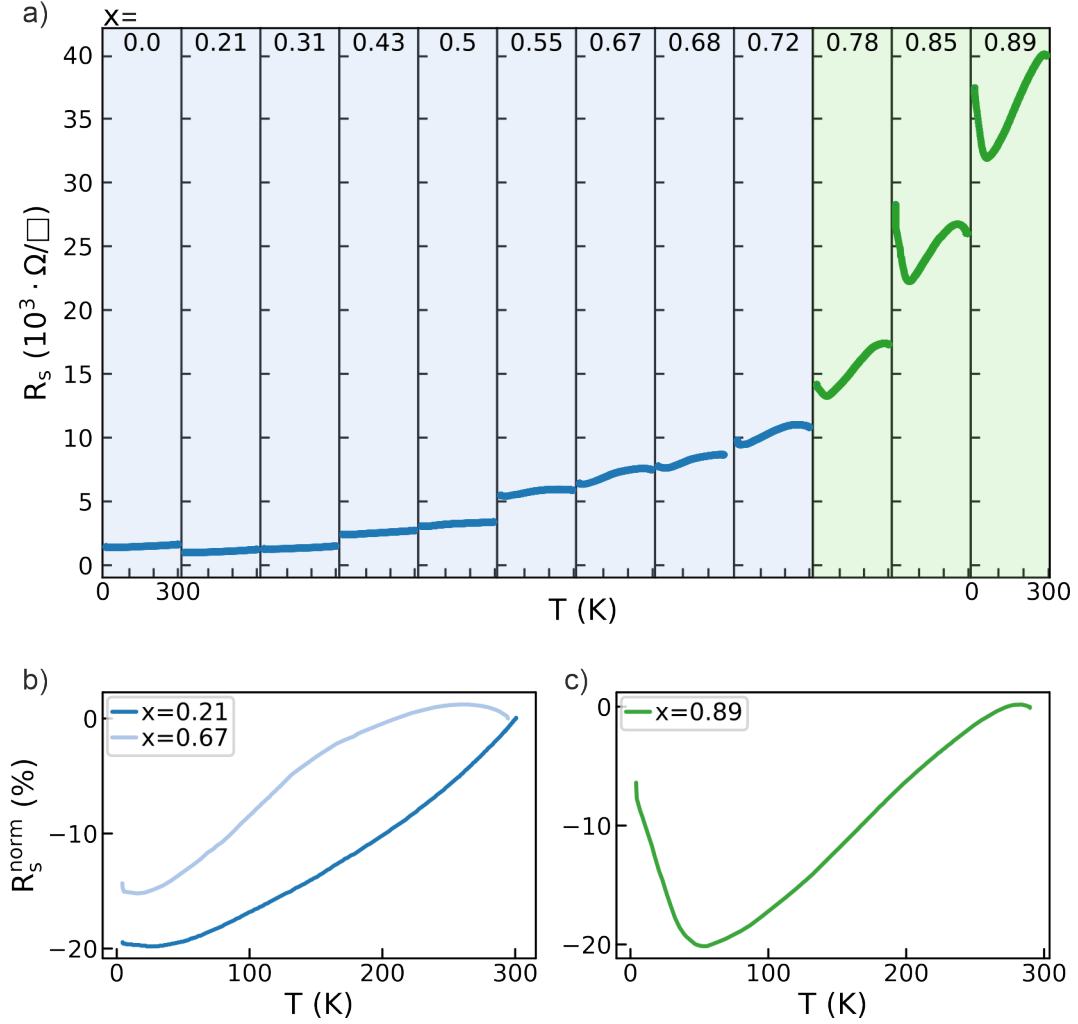
Figure 9.2: Temperature dependence of the longitudinal sheet resistance R_s between room temperature and 4.2 K. a) Overview of all samples from the Sb concentration series, with the respective value of x being given at the top of each column. The samples are subdivided into two groups as introduced in Fig. 9.1. The first group (blue) contains samples with $x \leq 0.72$, which approximately represents the value used in Ch. 7. The second group (green) contains samples with a higher Sb concentration, where a different transport regime is reached. b) Comparison of $R_s^{\mathrm{norm}}(T) = R_s(T)/R_s(300K) - 1$ for two samples from group 1, showing a strictly metallic behavior ($x = 0.21$) and signatures of semiconductor-like carrier freeze-out ($x = 0.67$), respectively. c) $R_s^{\mathrm{norm}}(T)$ for $x = 0.89$, exhibiting a similar behavior to $x = 0.67$ shown in b) for high temperatures, but a steep increase of the resistance for $T \lesssim 60$ K.

low frequency lock-in technique for all available temperatures. The behavior of the normalized sheet resistance R_s^norm versus temperature for $x = 0.89$ is shown in Fig. 9.2 c). For high temperatures the curve is similar to that of $x = 0.67$ displayed in b), exhibiting an overall metal-like dependence with slight semiconductor-like freeze-out signatures. Below $T \approx 60\,\text{K}$, on the other hand, a steep increase of R_s^norm is observed. Section 9.2.1 will show that this very pronounced resistance upturn is not solely explainable by an effect of EEI.

From these observation it is clear that the group 2 samples with $x \geq 0.78$ enter a different transport regime. Due to the used high Se concentration ($y = 0.9$) the stoichiometry approaches the binary Sb_2Se_3 for $x \rightarrow 1$, which is predicted to display properties drastically contrasting to the other binary compounds of the BSTS family. While the topologically non-trivial Bi_2Te_3, Sb_2Te_3, and Bi_2Se_3 show a rhombohedral crystal structure [27], Sb_2Se_3 is mostly been described in literature to crystallize in an orthorhombic pattern, which is accompanied by a topological phase transition to a trivial insulator [222–228]. Considering the Sb_2Se_3 bulk band gap, a variety of values have been reported experimentally and theoretically that usually exceed 1 eV and are hence considerably larger than that for the three other binary BSTS compounds [224, 229–233]. An extensive overview over the range of proposed band gap sizes including the respective determination method is provided in Ref. [226]. In our transport investigations we did observe a completely insulating behavior of a sample with $x = 0.94$ and $y = 0.90$, which indeed suggests the transition towards a trivial insulator. On the other hand, this also means that no electrical transport is mediated through the bulk of the system. For the three measured samples of group 2 shown in green in Fig. 9.2 a), where x and y are large, but smaller than 1, this opens interesting perspectives. Especially considering MBE grown samples, this stoichiometry regime has received little experimental attention so far. In Ref. [234] $(Bi_{1-x}Sb_x)_2Se_3$ (i.e. $y = 1$) nanosheets prepared in a tube furnace have been investigated and a similar evolution towards an insulating behavior was observed, however already for $x > 0.2$. By performing first-principles calculations, Ref. [235] theoretically predicts a transition of $(Bi_{1-x}Sb_x)_2Se_3$ from a non-trivial to a trivial $\mathbb{Z}_2$ topology for $0.78 \lesssim x \lesssim 0.83$. Crystallographically, a mixed phase of rhombohedral and orthorhombic crystal structure is reported in Ref. [228] for high values of x and y smaller than 1. These considerations suggest that the electronic transport for our group 2 samples with high x becomes even more complex. On the one hand, the drastic increase of the observed sheet resistance hints towards a strong suppression of parasitic bulk conduction, including a depletion of the metal-like bulk channel induced by the BS seed layer, which was one of the main goals of this sample series. On the other hand, the impact of the high Sb concentration on the topological surface states is unclear. Even for the binary Sb_2Se_3 the underlying topology is under some debate in literature. While orthorhombic Sb_2Se_3 is predicted to be in principle $\mathbb{Z}_2$ trivial as stated above, some publications suggest a transition to a non-trivial topology under pressure or strain [236–240]. In Ref. [241] a non-trivial Sb_2Se_3 topology is theoretically reported even for ambient conditions, when the van-der-Waals bonding between the quintuplelayers is taken into account and a *rhombohedral* crystal structure is assumed. While strain could

play a role in our samples, especially the latter prediction of a non-trivial band structure for rhombohedric Sb_2Se_3 is intriguing, because in our studies such a crystal structure could be maintained for very high values of x, as the thin BSTS film is grown onto a rhombohedral layer of Bi_2Se_3 [242]. However, if the BSTS layer crystallizes in a mixed phase, local changes between trivial and non-trivial topology are conceivable, which should manifest in magnetotransport investigations.

From these complex prerequisites the central question for the following experimental investigation is the presence of electrical transport mediated by topological surface states in the group 2 samples. The previous two chapters have shown that gate and magnetic field dependent transport experiments provide valuable insights on bulk and TSS contributions to conduction. These studies are presented in the following.

9.1.2 Back-gate dependence of the sheet resistance

We have shown in Chapter 7 that the response of the longitudinal sheet resistance to an applied back-gate voltage by using the $SrTiO_3$ substrate as the dielectric allows to gain valuable information especially concerning bulk contributions to the electronic transport. An idealized behavior was illustrated in Fig. 7.5 a) showing a symmetric $R_s(V_{BG})$ reaching a maximum value R_{peak} for a certain applied voltage. In this context it was explained, however, how our asymmetric p-n sample structure and the possible presence of bulk conduction channels can largely complicate the matter. In particular, a large metallic bulk contribution induced by the highly doped BS seed layer at the interface to the STO substrate can completely screen the field effect, preventing the observation of a maximum in the resistance.

Figure 9.3 exemplarily shows the dependence of the longitudinal sheet resistance R_s on the applied back-gate voltage measured at a temperature of $T = 4.2$ K for four samples of group 1 (blue, a) - d)) and two samples of group 2 (green, e) - f)) of the Sb concentration series. The respective values for x are given within each plot. In the investigations of the temperature dependent sheet resistance presented in the previous subsection, the samples of group 1 were shown to fully confirm the expectations formed from the introduction of the heterostructure concept in Ch. 7. The two different kinds of temperature behaviors observed within this regime were highlighted in Fig. 9.2 b) and connected to a tuning of the BSTS Fermi level from the conduction band towards the bulk energy gap starting above a Sb concentration of 0.55. This trend is reproduced in the gating response. For $x = 0.31$ displayed in Fig. 9.3 a) the bulk conduction is large enough that no R_{peak} can be observed even when applying voltages up to -150 V. We obtained such a gate dependence for all samples with $x \leq 0.5$. As for the temperature investigations, the behavior starts to change from a Sb concentration of $x = 0.55$, which is depicted in Fig. 9.3 b), where the onset of a very shallow maximum of R_s can be observed for a gate voltage of approximately -28 V. On further increase of x to 0.68 and 0.72, displayed in panels c) and d) of Fig. 9.3, this maximum becomes continuously more pronounced and shifts towards smaller back-gate voltages. We ascribe this trend to an enhanced as-grown depletion of the m-bulk channel at the STO/TI interface by intrinsic compensation of opposite charge carriers,
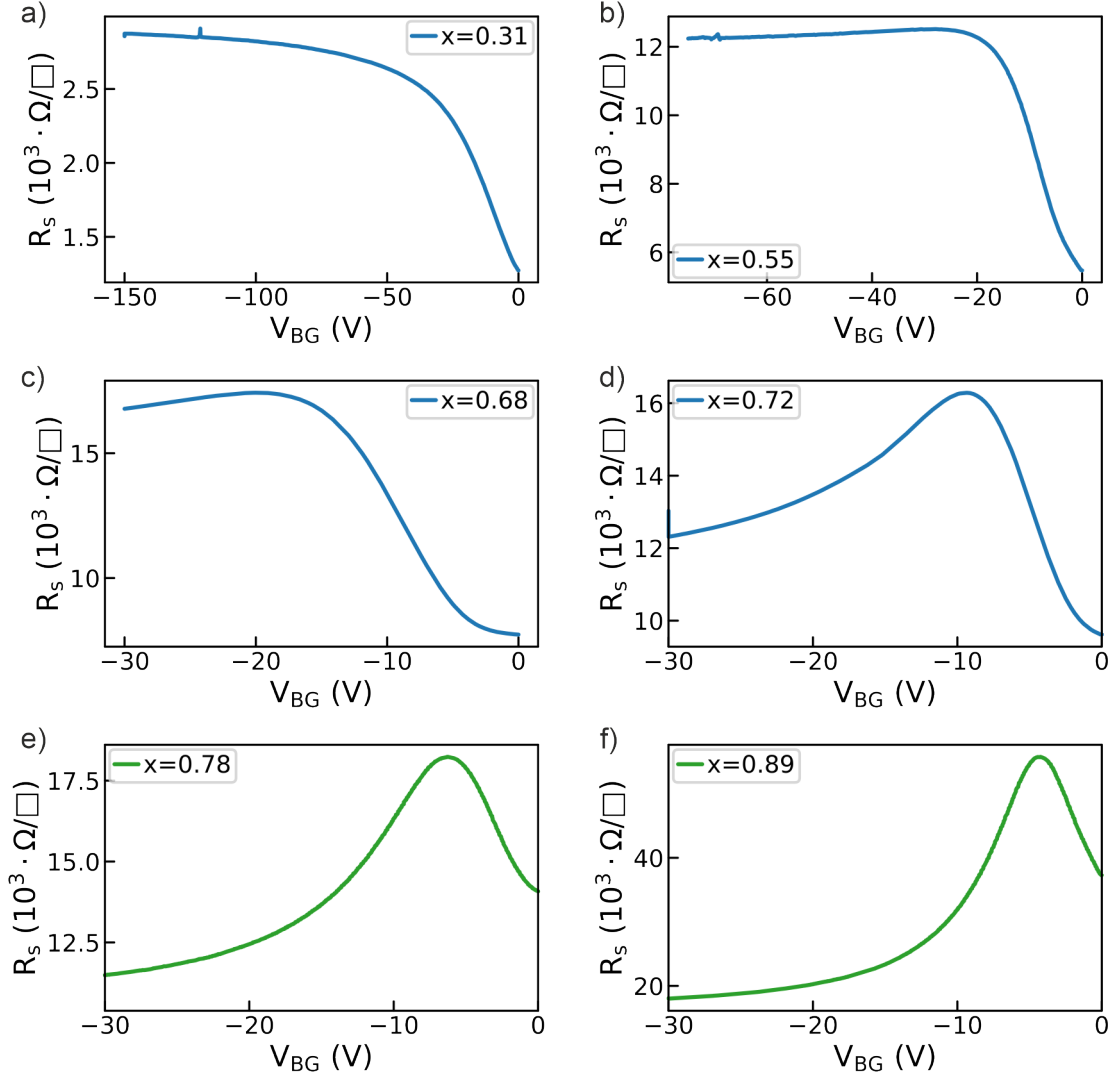
Figure 9.3: Dependence of the longitudinal sheet resistance R_s on the back-gate voltage measured at $T = 4.2\,\text{K}$ and at a gate sweeping rate of $\sim 50\,\text{mV/s}$ for selected samples from the Sb concentration series. The value for x is given in each respective panel. a)-d) Exemplary measurements of samples from group 1. While no R_{peak} is reached for $x = 0.31$, a shallow maximum can be observed for $x = 0.55$ that becomes increasingly more pronounced with increasing x. e), f) Measurement for samples of group 2 with $x = 0.78$ and $x = 0.89$. Accompanied by a drastic increase of the sheet resistance, especially for $x = 0.89$, the qualitative trend continuous and an increasingly more pronounced R_{peak} showing a increasingly more symmetric curve is observed.

when x is sufficiently large to tune the BSTS into a slight p-type regime. At $x = 0.72$ the obtained qualitative gate dependence almost identically reproduces the curve obtained for sample 1+12 with $x = 0.7$ presented in Ch. 7 (see Fig. 7.5 b)). Intriguingly, when the Sb concentration enters the range of group 2 with $x \geq 0.78$, where a possible transition to a different transport regime has been discussed above, the qualitative trend of the series continues. Figures 9.3 e) and f) show the obtained results for $x = 0.78$ and $x = 0.89$. Especially for the latter, the absolute sheet resistance value has drastically increased, but still a curve with a pronounced R_{peak} is observed, exhibiting an almost symmetric gate dependence. This observation closely resembles the expected behavior for an idealized TI sample. The high sheet resistance and the symmetric gate dependence provide a hint that parasitic bulk conduction is largely suppressed in this sample. Considering electronic transport mediated by topological surface states, more insight can be gained by investigating the behavior under the influence of a perpendicular magnetic field, which will be discussed in the following.

9.1.3 Magnetotransport in out-of-plane magnetic fields

The presented back-gate study provided promising results, especially concerning the bulk conduction in the range of high Sb concentration. Applying an out-of-plane magnetic field, on the other hand, was discussed in the previous two chapters to be a valuable tool to gain indications for the contribution of the topological surface states to transport. In simplified terms, we argued that increasing the TSS-to-bulk transport ratio is accompanied by an increase in magnetoresistance, due to the surface states being subject to strong quantum interference effects at low temperature. Previously, we plotted the absolute magnetoresistance defined as $MR^{\text{abs}} = R_{\text{s}}(B) - R_{\text{s}}(0\text{T})$. This is shown in gray in Fig. 9.4 a) for constant $B = 5\,\text{T}$ and measured at $T = 4.2\,\text{K}$ with respect to the antimony concentration x.

The obtained results again confirm the assumption that a high MR is connected to a high TSS-to-bulk transport ratio: within group 1 we have shown above by temperature and gate-dependent measurements of the Sb concentration series that the transport is dominated by trivial bulk states for $x \leq 0.5$. This is accompanied with a comparatively almost vanishing MR^{abs}. Above $x = 0.5$, where we expect the bulk conduction to be increasingly reduced, also the value of the absolute magnetoresistance starts to drastically increase up to $x = 0.89$. However, when MR^{abs} is additionally normalized to yield the *relative* field induced increase of the resistance MR^{rel}, i.e. $MR^{\text{rel}} = MR^{\text{abs}}/R_{\text{s}}(0\text{T})$, a different behavior for the samples of group 2 (green background) can be observed, as MR^{rel} decreases after a maximum is reached at $x = 0.78$. This means that in this concentration regime the enhancement of MR^{abs} is smaller than that of the zero field resistance $R_{\text{s}}(0\text{T})$.[2] The dependence on the applied OOP magnetic fields of three exemplary samples are displayed in Fig. 9.4 b) - d) for B up to $\pm 5\,\text{T}$ obtained at $T = 4.2\,\text{K}$. While the amplitude

---

[2]Note that this is the only measurement within all of our studies, where a significant qualitative difference between MR^{abs} and MR^{rel} was observed.
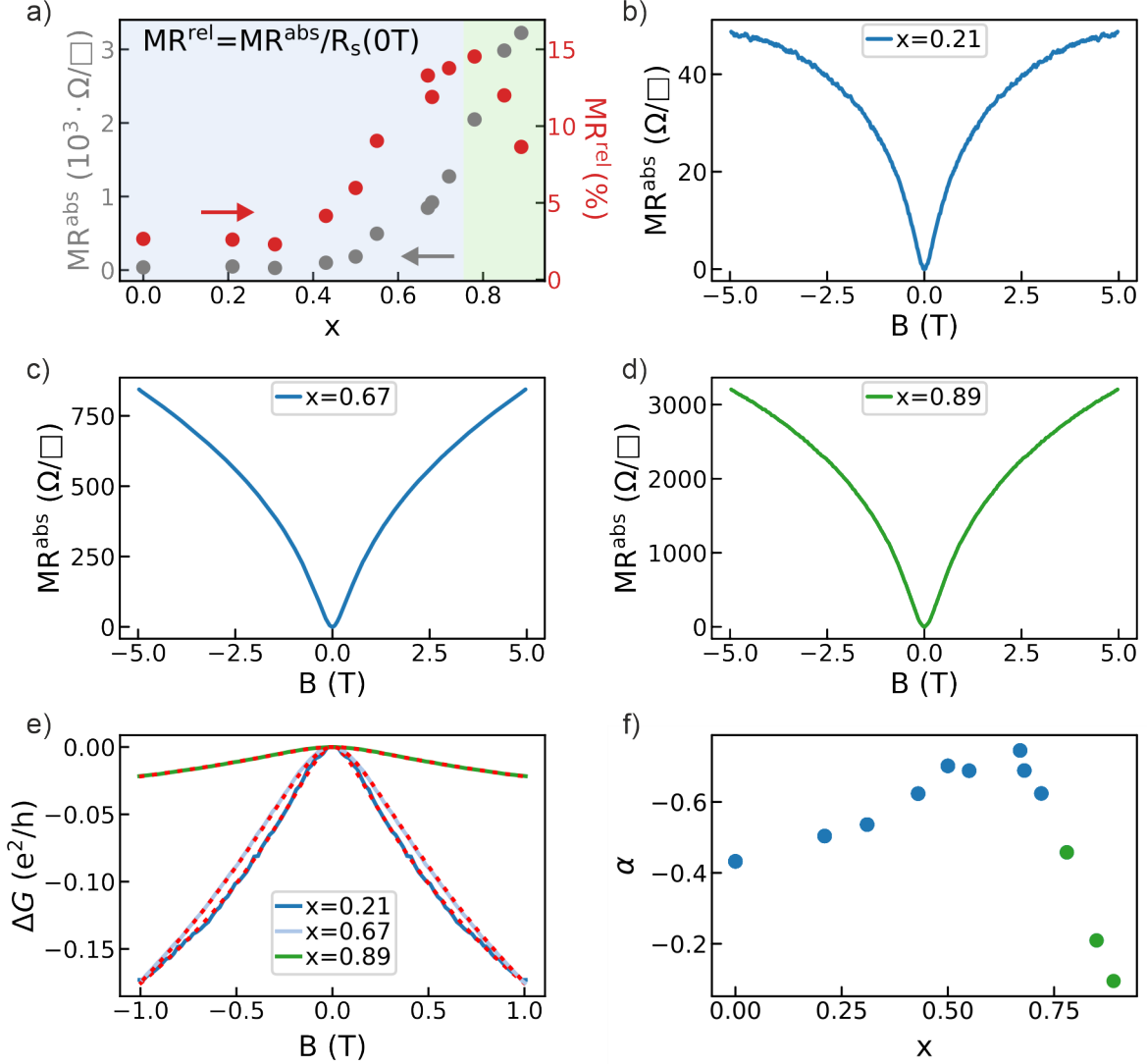
Figure 9.4: Investigation of transport properties under an OOP magnetic field up to ±5 T and measured at $T = 4.2$ K. a) Absolute (MR^{abs}, gray) and relative magnetoresistance (MR^{rel}, red) at $B = 5$ T. Both values show a drastic increase for $x \gtrsim 0.5$, but while MR^{abs} keeps increasing for all x, MR^{rel} starts to decrease for $x > 0.78$. b)-d) Exemplary measurements of MR^{abs} versus magnetic field for different x as given in the respective panel. Independent of the Sb concentration all samples qualitatively exhibit a cusp-shaped behavior. e) HLN fits (red dashed lines) to the magnetoconductance for samples $x = 0.21$, $x = 0.67$, and $x = 0.89$ attesting good agreement between theory and measurement. f) Obtained values for α from the HLN fits with respect to x. After a slight increase of $|\alpha|$ for $0 \leq x < 0.5$ and a plateaus-like behavior for $0.5 \leq x \leq 0.68$, $|\alpha|$ exhibits a steep decrease towards zero.

of the displayed MR^{abs} drastically depends on the respective antimony concentration, the qualitative field dependence is very similar, exhibiting the cusp-shaped form typical for quantum interference effects. The qualitative behavior for $x = 0.67$ (Fig. 9.4 c)) and $x = 0.89$ (Fig. 9.4 d)) is almost identical. Hence, under the assumption that this type of MR is a fingerprint of TSS conduction, this would suggest that even for an Sb concentration of 0.89 sizeable surface transport is still present and at least no complete transition towards a trivial insulator has occurred. Interpreting the origin of this magnetoresistance to stem from weak anti-localization at least for small fields, as discussed in detail in Ch. 8, the HLN formalism can be applied to provide a deeper evaluation. The relevant equation was introduced in Sec. 3.2.2 and is given by

$$\Delta G_{\text{HLN}}(B) = \alpha \frac{e^2}{2\pi^2 \hbar} \left[\psi \left(\frac{1}{2} + \frac{\hbar}{4eBl_\varphi^2} \right) - \ln \left(\frac{\hbar}{4eBl_\varphi^2} \right) \right],$$

with the free fit parameters α and l_φ and the digamma function ψ. Figure 9.4 e) shows the HLN fits (red dashed lines) to the magnetoconductance corresponding to the three samples shown in panels b) to d) and a very good agreement between theory and data is observed independent of the Sb concentration. A key role within this framework is played by the prefactor α, as it is predicted by theory to "count" the number of uncoupled channels contributing to conduction in units of -0.5 in the case of topological insulator systems. The obtained values of α for all samples of the Sb concentration series are plotted in Fig. 9.4 f).[3] Due to the strong bulk conduction, which effectively couples all possible conduction channels within the sample, α indeed lies around the expected value of -0.5 for the lowest values of x. However, already a slight absolute increase is observed for Sb concentrations larger than zero, what we ascribe to a reduction of bulk conductivity. At $x = 0.5$ a plateau is reached with $\alpha \approx -0.7$ that holds up to a Sb concentration of 0.68. Despite our expectation formed from the above considerations that the Fermi level within this regime is tuned into the bulk band gap at least partially within the sample thickness, the value of -1 for two completely decoupled channels is not reached. We observed the same behavior for similarly thin films in Sec. 7.2.2 and ascribed this to a remaining coupling between conduction channels at top and bottom surfaces due to the small sample thickness as suggested in Ref. [146]. Indeed, when increasing the BSTS thickness at $x = 0.65$ to 25 QL we again obtained a value of $\alpha \to -1$ as in Sec. 7.3, which remained constant on a further thickness increase to 50 QL. After this plateau-like behavior for $0.5 \leq x \leq 0.68$, α starts to fall towards 0, which is particularly pronounced for the samples of group 2 shown in green, reaching a value of $\alpha = -0.1$ for $x = 0.89$. Such a behavior is puzzling, since it is unaccounted for by the underlying theory. It has, nonetheless, been similarly observed before in the context of topological insulators in Refs. [159, 243] for Bi_2Se_3 samples. However, in both publications the transition of $\alpha \to 0$ occurred in a thickness dependent study only for samples thinner

---

[3]For the second free fit parameter, l_φ, no systematic behavior with respect to the Sb concentration was observed. The values scattered between $\sim 35\,\text{nm}$ and $\sim 55\,\text{nm}$

than 5 QL. In Ref. [243] a gap opening caused by the hybridization of top and bottom surface state was proposed as a possible explanation. In our samples, on the other hand, such a hybridization should not play a sizeable role due to a total sample thickness of 11 QL and it should moreover not depend on the Sb concentration. In Ref. [133] large disorder and surface scattering are suggested to be a further mechanism possibly causing α to go to zero. Especially considering possible changes of the crystallographic structure that might even be accompanied by a topological phase transition, a further increase of surface scattering in the Sb concentration regime of group 2 is conceivable.

In combination, these observations in the Sb concentration dependent study of the OOP magnetoresistance could indeed hint towards the formation of a crystallographic mixed-phase of rhombohedric and orthorhombic structure as discussed above and shown in Ref. [228]. The quantum interference fingerprint we obtained independent of the Sb concentration as displayed in Fig. 9.4 b) to d) does suggest some contribution of surface states to electronic transport independent of x. An enhancing decay of the crystal with increasing x in the regime of group 2 towards a completely orthorhombic structure could significantly enhance the surface scattering potential and hence explain the decreasing relative magnetoresistance MR^{rel} observed in Fig. 9.4 a), as well as the evolution of α towards zero shown in Fig. 9.4 f). Importantly, even the topology of such a mixed crystal structure is uncertain, since the material could enter a topologically trivial phase when taking an orthorhombic form. To our knowledge, such a possible crystallographic mixed phase of BSTS has not been investigated in detail so far, but would be intriguing especially concerning the electronic and topological properties and will thus be subject of our future studies. MBE TI growth, where samples with precisely tuned thickness and stoichiometry can be quickly prepared, in combination with our BS seed layer sample design that allows high quality BSTS epitaxy independent of the alloy composition, is the ideal basis for such an investigation. The following section will already provide a first step in presenting magnetotransport experiments on a sample thickness series at $x = 0.9$.

9.2 Thickness dependence at x=0.9

Chapter 7 introduced the heterostructure concept with a $(\mathrm{Bi}_{1-x}\mathrm{Sb}_x)_2(\mathrm{Te}_{1-y}\mathrm{Se}_y)_3$ stoichiometry of $x \approx 0.7$ and $y \approx 0.9$. The idea to go beyond this Sb concentration that is discussed in this chapter was based on the desire to increase the amount of excess acceptor BSTS dopants to achieve a maximum compensation with the n-type carriers induced by the BS seed in very thin films. As discussed above, the situation for $x \rightarrow 1$ does further complicate due to possible crystallographic changes that might even have impact on the underlying topology of the system. What was not subject of discussion in the Sb concentration series of Sec. 9.1, was the evolution of the horizontal Hall resistance R_{xy} with respect to x obtained from the OOP magnetic field dependence and from which the dominant charge carrier type of the electronic transport can be determined. Along with the expectations, we did observe a clear n-type conduction for all samples of group 1 ($x \leq 0.72$) corresponding to an overall donor surplus within the heterostructure. On the

other hand, by further increasing the Sb concentration, the dominant behavior did shift to a p-type conduction for $x \geq 0.78$. Hence, this indicates that the principle idea of increasing the amount of acceptor-type dopants within the BSTS layer by tuning x did fulfill the expectation. For $x = 0.89$ we observed a vastly enhanced longitudinal sheet resistance in Fig. 9.2 a). Disregarding possible implication of such a high x for the TSS at this point, this means that also bulk conduction should be highly suppressed. In our interpretation, two mechanisms are conceivable leading to this suppression of bulk conductance. First, it could indeed be caused by the desired compensation of opposite excess carriers. Second, the observed behavior could be connected to a drastic enhancement of the band gap when the BSTS stoichiometry approaches the binary Sb_2Se_3, which can considerably exceed 1 eV as mentioned above [226].

A tool to investigate this question is the variation of the BSTS thickness in this stoichiometry regime, as this should largely influence the transport properties in case of the first proposed mechanism and not or little in case of the second. For this, we kept the stoichiometry constant at $x = y = 0.9$ and investigated three samples utilizing 1 QL of BS seed layer and varying the BSTS thickness from 10 QL to 25 QL and 50 QL. The main results of this study are shown in Fig. 9.5. Panel a) compares the temperature dependence of the three samples with increasing BSTS thickness from left to right as given at the top of each column. Sample 1+10 shows a very similar behavior to the heterostructure given with a value of $x = 0.89$ in Fig. 9.2 a), exhibiting a slight freeze-out signature at high temperatures, a decrease of R_s cooling down from $T \approx 250$ K to $T \approx 100$ K (see inset for 100 K $\leq T \leq$ 300 K) and a steep increase for lower temperatures.[4] The upturn of R_s below 100 is even more pronounced and the sheet resistance reaches a value above 60 kΩ/$\square$ at $T = 4.2$ K. When the BSTS thickness is increased to 25 QL, however, the behavior completely changes. Not only does the sheet resistance decrease to around 10 kΩ/$\square$, but especially the qualitative temperature dependence adopts a strictly metal-like behavior. This is also observed for sample 1+50, where the sheet resistance further decreases to $R_s \approx 1$ kΩ/$\square$ at $T = 4.2$ K. This clearly suggests that the electronic transport is completely dominated by bulk carriers for the samples with a thickness larger than 10 QL. Since a p-type Hall resistance is observed in magnetic field dependent measurements (not shown), we expect this to be caused by the Fermi level residing in the bulk valence band for samples 1+25 and 1+50. This is confirmed by evaluating the response of the longitudinal resistance to the application of a back-gate voltage, which is presented for samples 1+10 and 1+50 in Fig. 9.5 b) and c), respectively. For sample 1+50 no maximum of R_s is obtained for voltages up to 250 V, which was previously argued in this thesis to be caused by a screening of the gate induced field effect by a high density of mobile bulk carriers. The gate dependence of sample 1+10, on the other hand, closely resembles the behavior expected for an idealized TI system (see Sec. 7.5 for a discussion). A very pronounced and symmetric peak is obtained close to $V_{BG} = 0$ and the

---

[4]Of course, the XPS obtained values for x of the respective samples specified with $x = 0.89$ in Fig. 9.2 a) and $x = 0.90$ in Fig. 9.5 a) are identical within the error of the measurement and a very similar behavior is expected.
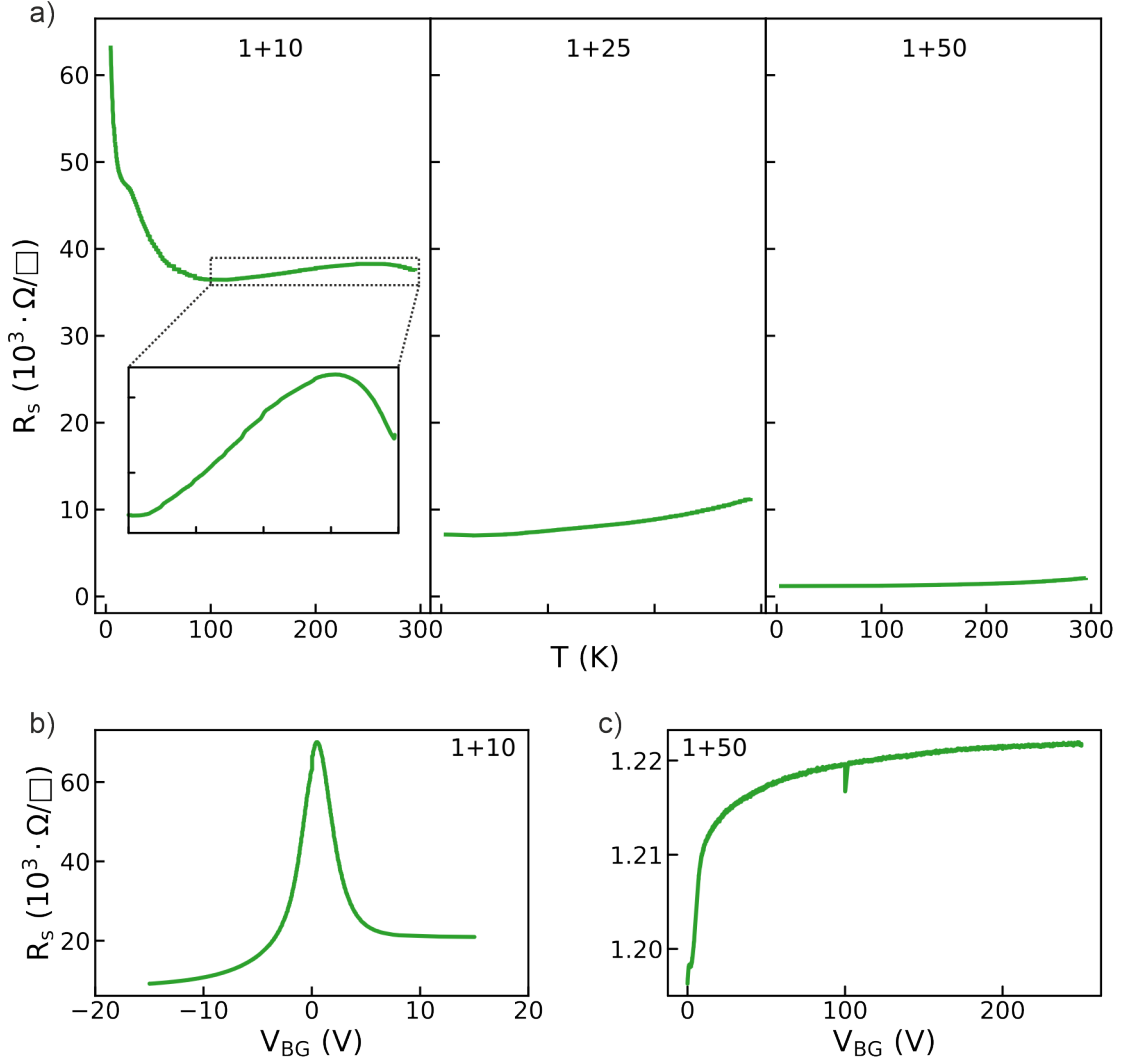
Figure 9.5: a) Temperature dependence of the longitudinal sheet resistance R_s for the three investigated samples. All samples use 1 QL of BS seed layer and the BSTS thicknesses are chosen to be 10 QL, 25 QL, and 50 QL as given at the top of each column. While sample 1+10 shows a very high R_s exhibiting a steep increase for $T \lesssim 100\,\mathrm{K}$, the two other samples follow a strictly metal-like dependence with a reduced R_s. b), c) R_s versus applied back-gate voltage measured at $T = 4.2\,\mathrm{K}$ for sample 1+10 (b) and 1+50 (c). The resistance of sample 1+10 exhibits a strong response to the applied voltage and shows a pronounced peak at $V_{BG} \approx 0.45\,\mathrm{V}$. Due to large bulk conductivity, the field effect is screened in sample 1+50 and no peak of R_s is observed for voltages applied up to 250 V. Back-gating of sample 1+25 did not work due to technical reasons.

value of R_s can be strongly modulated for negative as well as positive voltages. While, as discussed above, the topological state of a sample with such a high Sb concentration is inconclusive, this observation at least indicates that we indeed achieved a significant suppression of bulk carriers in this sample. Most importantly, due to the evolution to a metal-like bulk conduction by merely increasing the BSTS thickness, we interpret this bulk depletion to stem from compensation effects within the p-n heterostructure and not from a drastic opening of the band gap. Furthermore, this sample with a 1+10 stack and $x = 0.9$ stands out due to a very strong influence of temperature and back-gate voltage on the longitudinal sheet resistance. These signatures will be more closely discussed in the following section.

9.2.1 Sample 1+10 at x=0.9

The temperature dependence of the sheet resistance of sample 1+10 with an Sb concentration of $x = 0.9$ was already plotted in Fig. 9.5 a) and is shown again in Fig. 9.6 a) (green, 0 V) normalized to the value at room temperature, i.e. $R_s^{norm} = R_s(T)/R_s(300\,\text{K}) - 1$.
Most prominently, the behavior with decreasing temperature shows a drastic increase of R_s below $T \approx 100\,\text{K}$. In section 8.2.1, small upturns of the sheet resistance were presented for samples with $x = 0.7$ and discussed in the context of electron-electron interactions. There, however, the increase was observed only for temperatures below $10\,\text{K}$ and with values less than 5% relative to the minimum resistance. For the sample presented here, the evolution into an increasing resistance behavior with decreasing temperature not only already starts at much higher temperatures, but also exceeds a value of 50% with respect to the minimum. Figure 9.6 b) shows the corresponding sheet conductance G_s versus temperatures of $4.2\,\text{K} < T < 20\,\text{K}$ in a logarithmic scale. As a fingerprint of EEI, the conductance indeed exhibits a linear behavior in $\ln(T)$, but only for $T \lesssim 7\,\text{K}$. Hence, while EEI still seems to be present within the lowest available temperature range, we expect the majority of the observed resistance increase for higher temperatures to stem from different mechanisms, such as an activation law behavior or a variable range hopping process. As discussed in Ch. 8, a manifestation of EEI does on the one hand suggest the presence of sizeable surface disorder, but could in turn also be a hint to a surface contribution to electronic transport. A clear indication that the unique temperature dependence of the sheet resistance of this sample is connected to the Fermi level residing within the band gap can be seen from the biased cool-down measurements shown in Fig. 9.6 a). The drastic response of R_s to the application of a back-gate voltage V_{BG} at constant temperature $T = 4.2\,\text{K}$ was already plotted in Fig. 9.5 b). In the as-grown state at $V_{BG} = 0\,\text{V}$ the resistance lies close to the observed peak value and a steep decrease of R_s is obtained, when applying positive or negative voltages, before saturation is approached for $V_{BG} = \pm 15\,\text{V}$. Next to the as-grown temperature curve, Fig. 9.6 a) shows measurements, where a constant back-gate voltage of $+15\,\text{V}$ (orange) or $-15\,\text{V}$ (red) is applied at room temperature at the beginning of the gradual cool down of the sample towards $T = 4.2\,\text{K}$. Intriguingly, these comparatively small voltages are sufficient to change the temperature curve from the insulating behavior observed at $V_{BG} = 0\,\text{V}$ to a metal-like dependence
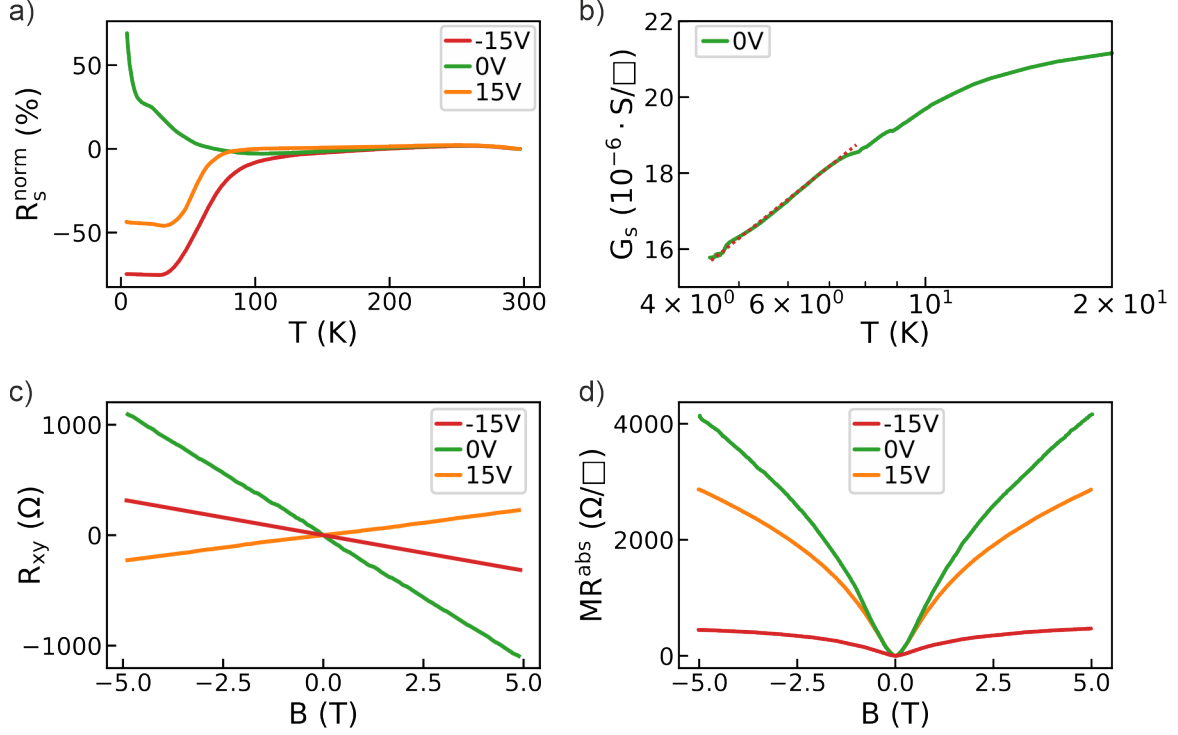
Figure 9.6: Transport properties of sample 1+10 with $x = 0.9$. a) Temperature dependence of the normalized sheet resistance $R_\mathrm{s}^\mathrm{norm}(T) = R_\mathrm{s}(T)/R_\mathrm{s}(300\,\mathrm{K}) - 1$ in the as-grown case (green, $0\,\mathrm{V}$) and under constant back-gate voltages of $\pm 15\,\mathrm{V}$ (orange and red). While $R_\mathrm{s}^\mathrm{norm}(T)$ shows a stark increase for low temperatures in the as-grown case, a metal-like behavior is adopted for applied voltages. b) Conductance versus temperature in a logarithmic scale for the unbiased measurement. The curve shows indications of strong electron-electron-interactions as it exhibits a linear behavior, but only for $T \lesssim 7\,\mathrm{K}$. The observed steep resistance increase in a) for larger temperatures is thus expected to stem from different mechanisms. The red dashed line provides a guide to the eye. c) Transversal Hall resistance R_xy versus magnetic field measured at $T = 4.2\,\mathrm{K}$ for different gate voltages. The curve shows dominant p-type transport for $V_\mathrm{BG} = 0\,\mathrm{V}$ and $V_\mathrm{BG} = -15\,\mathrm{V}$ and a switch to n-type for $V_\mathrm{BG} = +15\,\mathrm{V}$. d) Absolute magnetoresistance at $T = 4.2\,\mathrm{K}$. Especially for $V_\mathrm{BG} = -15\,\mathrm{V}$ MR^abs drastically decreases compared to the unbiased measurement, showing the strong influence of the back-gate on the electronic properties of the sample.

that is qualitatively independent of the sign of the applied voltage.[5] We interpret this behavior to stem from a gate-induced shift of the Fermi level from the energy gap towards the bulk bands, creating a metal-like channel that dominates the electronic transport. This is supported by determining the dominant charge carrier type from the slope of the transversal Hall resistance $R_{xy}(B)$ that is shown in Fig. 9.6 c) for the applied voltages. In the unbiased measurement (green), a p-type behavior is observed indicated by a negative slope in our measurement geometry. Applying a negative gate voltage shifts the Fermi level downwards in energy and, subsequently, transport stays p-dominated at $V_{BG} = -15$ V. From the smaller slope of the Hall curve, an increased carrier density can be concluded, which we ascribe to an increased participation of valence band states in comparison to $V_{BG} = 0$ V. For $V_{BG} = +15$ V, on the other hand, E_F is shifted towards the bulk conduction band and the transport becomes n-type dominant. The strong influence of the back-gate on the electronic sample properties, furthermore, manifests in the absolute magnetoresistance displayed in Fig. 9.6 d). While, as discussed above, this quantity becomes more difficult to interpret in the regime of high Sb concentration, the presented measurements further confirm the large back-gate tunability of the electronic properties, as MR^{abs} is almost decreased by an order of magnitude going from $V_{BG} = 0$ to $V_{BG} = -15$ V. In conclusion, these observations suggest that the as-grown Fermi level of this sample resides mainly within the bulk energy gap and that the back-gate is capable to induce a very effective tuning of the electronic properties.

9.3 Summary and discussion

In the beginning of this chapter, two main objectives were formulated for the optimization of the p-n heterostructure concept. First, to address the issue of large surface disorder, all samples discussed in this chapter underwent a slightly modified growth procedure, where additional heat was provided from the front side during epitaxy. However, while we observed some positive effects in terms of sample topography [219], a possible beneficial influence on the electronic properties remains inconclusive. Within the Sb concentration series introduced in Sec. 9.1 we obtained indications of a sizeable surface state contribution in magnetotransport for $x \gtrsim 0.55$. In all of these samples, we still observed signatures of strong electron-electron interactions in the $R_s(T)$ measurements, which was identified in Ch. 8 as a potential electronic indicator for large surface disorder. Due to a possible crystallographic evolution from a rhombohedric to an orthorhombic structure, accompanied by a mixed-phase in the transition regime, the disorder could

---

[5]The almost identical temperature dependence of all three curves in Fig. 9.6 a) for $T \gtrsim 120$ K can be explained by the temperature behavior of the dielectric constant ϵ of the STO substrate shown in Fig. 6.1 e), which causes a strong temperature dependence of the effective field effect induced by a constant back-gate voltage. Since ϵ is significantly decreased at high T, the applied voltages of ± 15 V only induce a negligible tuning to the electronic bands of the sample in this range. When T falls below ≈ 120 K, ϵ steeply increases and the applied voltage manifests in a sizeable field effect that tunes the position of the Fermi level within the sample and subsequently influences the temperature dependence of R_s.

further increase for an Sb concentration of $x > 0.72$. Experimental hints to this claim were provided in Fig. 9.4 of section 9.1, where we observed a decrease of the relative magnetoresistance and the approach of $\alpha \to 0$ obtained from the HLN fits. However, the front-heating procedure still provides an important starting point for the optimization of the growth procedure for future efforts to further improve the sample quality.

The second objective was to achieve a depletion of the excess n-type bulk carriers induced by the Bi_2Se_3 seed layer as already realized in chapter 7, but by employing a thinner p-type BSTS layer aiming for a further reduced total parasitic bulk conduction and for an enhanced tunability of the electronic properties by means of back-gating. Utilizing two of the main advantages of MBE, the precise thin film growth and the comparatively quick preparation of samples with varying stoichiometries, we approached this in section 9.1 by fixing the heterostructure to 1 QL of Bi_2Se_3 and 10 QL of $(Bi_{1-x}Sb_x)_2(Te_{1-y}Se_y)_3$ and tuned the Sb concentration x with a constant $y = 0.9$. The samples of this series with $x \leq 0.72$ (group 1) were used to test the expectations gained from the investigations of Ch. 7 and all transport measurements confirmed the previous results. By increasing x beyond 0.72 (group 2), we aimed to increase the amount of excess BSTS acceptors and thus enhance the compensation with the donor-type dopants present within the BS layer. From the observed drastic enhancement of the sheet resistance and the evolution of the back-gate response, we concluded that indeed a strong suppression of bulk conduction is achieved in this Sb concentration regime. However, especially considering the investigations of the magnetoresistance in OOP fields (Fig. 9.4) and the observed approach of a completely insulating state for $x = 0.94$, also questions concerning possible transport mediated by the TSS were raised. Deeper insight to the transport properties in the high Sb regime was gained in Sec. 9.2, where x was fixed to 0.9 and the BSTS thickness was increased from 10 QL to 25 QL and 50 QL, still using 1 QL of BS seed layer. While the thinnest sample again showed an extremely enhanced sheet resistance, exhibiting a unique temperature dependence and a very large back-gate induced modulation at $T = 4.2$ K, a metal-like behavior was adopted for samples 1+25 and 1+50. We thus concluded that the transport properties of sample 1+10 originated from an intrinsic compensation of charge carriers and not a complete transition to a trivial insulator with a largely increased band gap. Especially concerning the back-gate tunability of the electronic characteristics, sample 1+10 seemed to approach the expected behavior for an idealized TI system. We not only observed a very pronounced and symmetric peak in the R_s versus V_{BG} measurement, but Fig. 9.6 also illustrated the strong back-gate influence on other magnetotransport observables. Particularly, we presented a modulation of the as-grown insulator-like temperature dependence of R_s to a metal-like behavior for V_{BG} and the tuning between dominant p-type and n-type conduction at $T = 4.2$ K for $V_{BG} = \pm 15$ V.

While some uncertainties concerning electronic transport of the TSS arise when increasing the Sb concentration to $x \to 1$, the presented results of this chapter open two intriguing perspectives. On the one hand, the BSTS regime with high Se and high Sb concentration has to our knowledge received little to no attention so far in literature, especially concerning magnetotransport of samples prepared by MBE. The predicted crystallographic transition from rhombohedric to orthorhombic, accompanied by an intermediate mixed-phase, not

only poses interesting questions in terms of basic electronic properties such as the size of the energy gap, but also about the topology of the system, as the orthorhombic crystal structure is often associated in literature to possess a trivial insulator topology. Further studies are necessary, ideally employing methods like AFM, STS, or ARPES with high local resolution, to create a clearer picture of this stoichiometric BSTS regime. The second intriguing result is the prove of concept of our approach to optimize the p-n heterostructure sample design. The enhanced amount of acceptor-type BSTS dopants by increasing the Sb concentration did indeed lead to a stronger suppression of parasitic bulk conduction and, in combination with the small film thickness, yielded a very strong back-gate tunability of the electronic characteristics of the samples. We expect this principle approach, i.e. creating a maximal intrinsic compensation in very thin p-n-type heterostructures, to be highly favorable for the desired transport properties of the system and furthermore applicable to many different combinations of p- and n-type TIs. Varying the heterostructures' constituents, employing the same underlying approach, could furthermore avoid possible crystallographic changes and be moreover beneficial for the issue of surface disorder. This will be one of the main objectives for future studies.

10

Conclusion and Outlook

The main focus of this thesis was the development and investigation of reliable and high quality MBE grown quaternary $(Bi_{1-x}Sb_x)_2(Te_{1-y}Se_y)_3$ samples. The promise of this topological insulator alloy is twofold: on the one hand, effective suppression of parasitic bulk conductivity along with high mobility surface transport has already been reported for certain alloy ratios [150]. Secondly, the possibility to engineer the electronic characteristics simply by means of varying the material stoichiometry opens perspectives to design TI samples with band structures custom-tailored to the respective application. Efforts to exploit both of these desirable properties, however, face the challenge of a suitable crystal growth method. While the high mobility surface transport was realized in exfoliated flakes from macroscopic Bridgman crystals, the band structure engineering aspect is only practically applicable by means of epitaxy. Moreover, epitaxial growth provides a variety of additional benefits that are indispensable for many types of use scenarios, with several of them playing a key role in this thesis, where we employed molecular beam epitaxy.

Chapter 6 provided an introduction to the field of band structure engineering in the family of Bi-based topological insulators. It presented first results of our MBE grown samples, evidencing the presence of topological surface states and demonstrating the influence of the alloy stoichiometries on the electronic characteristics of the material. Moreover, it also discussed issues of the epitaxy especially of the quaternary BSTS alloys and presented the benefits of the implementation of a Bi_2Se_3 seed layer as a milestone for the sample quality and the reproducibility of their electronic properties.

One of the central results of this thesis was reported in **chapter 7**. Therein, we have shown that interfacing the n-type BS seed with a BSTS layer that is tuned into a slight p-type regime via its stoichiometry creates an intrinsic band bending within the heterostructure. This vertical p-n-type sample concept provides an additional tool for band structure engineering, as the electronic properties of the bilayer can now be largely tuned by the

respective thicknesses of its constituents. Depending on the heterostructure stack, two types of bulk contributions to transport additionally to the surface states can be identified: a metal-like and a semiconductor-like channel. In a systematic magnetotransport study we were not only able to disentangle the different contributions, but, most importantly, also showed that the metal-like channel introduced by the BS seed layer can be completely suppressed by compensation of opposite charge carriers within the heterostructures. Hence, the BS seed layer approach can be employed for its benefits regarding the sample growth, while its detrimental influence on the parasitic bulk conductivity can be inhibited. Moreover, already in this first generation of these heterostructure samples we demonstrated in Ch. 7 the capability to tune the electronic bands at the Fermi level throughout the whole sample thickness via electrostatic back-gating by utilizing the SrTiO$_3$ substrate as the dielectric. In combination with the precise as-grown band engineering by varying the layer thicknesses or the BSTS stoichiometry, this sample design opens a multitude of perspectives. The dispensability of a front-gate leaves the sample surface vacant, allowing, for example, optical experiments or a clean interfacing of the TI with a ferromagnetic layer for spin-pumping investigations. Employing our TI heterostructure concept, we are able to realize samples for such experiments with precisely tailored and well understood as-grown electronic properties that are, moreover, externally tunable during the measurements by means of back-gating. Beyond these investigations, the p-n heterostructure concept presented in Ch. 7 also laid the ground work for the deeper studies on electronic transport discussed in this thesis.

The ability to deliberately tune the respective transport contributions of the two bulk channels by varying the BS and BSTS thicknesses, enabled us to disentangle different magnetoresistive effects in **chapter 8**. Moreover, a strong focus of this chapter was the interplay of two types of quantum interference effects that largely dominate the magnetoresistance of the heterostructures at low temperatures: weak anti-localization and electron-electron interactions. Analyzing these two effects together with bulk contributions and comparing the results between different heterostructure stacks in addition to a pure Bi$_2$Se$_3$ film not only allowed us to generate a deeper understanding of the transport processes relevant in our samples, but also highlighted potential challenges in the interpretation of magnetoresistive effects of TIs, which is one of the most employed tools for sample characterization in literature.

The p-n heterostructure sample design furthermore opens a myriad of concepts towards a further optimization of the TI characteristics. A first approach was presented in **chapter 9**. Aiming to realize a depleted metal-like bulk transport channel in even thinner films as achieved in Ch. 7, we continuously increased the antimony concentration of the BSTS layer to enhance the inherent amount of excess acceptors and hence facilitate a compensation of the n-type BS dopants in thinner samples. The findings of Ch. 9 clearly highlighted the benefits of a reduced film thickness for the suppression of bulk conductivity and the ability to tune the samples' electronic properties by means of back-gating. While a high Sb ratio was shown to provide indications to enhance the sample disorder and even affect the topological properties, which calls for a deeper evaluation, the results already provide a proof of concept paving the way for a further development of the MBE grown

topological insulator samples.

The work presented in this thesis not only introduced and investigated the p-n heterostructure concept, but also clearly identified two major challenges going forward towards the goal of realizing MBE grown TIs with completely suppressed bulk conductivity and high mobility surface transport. While the results presented in Ch. 9 already showed how compensation in very thin films can lead to a strongly reduced parasitic bulk conduction, a clear future task is to combine this property with a reduction of the structural disorder of the samples. This could, for example, be directly achieved by further optimizing the pre-growth substrate treatment, the growth conditions, and the post-growth annealing procedures. On the other hand, the underlying concept of the p-n sample design can also be extended or modified. For example, a *virtual substrate* could be realized, where the n-type BS seed layer is interfaced with a thin, strongly p-type TI layer to account for the desired compensation of the excess bulk dopants. This bilayer could then be used as a substrate for the subsequent growth of the *active layer*, that can be arbitrarily chosen, since it does not need to provide excess acceptors to create a band bending and can hence be freely optimized to minimize bulk conduction and structural disorder. Within such a trilayer or even multilayer design, it is furthermore conceivable to exchange the quaternary BSTS film with ternary or even binary TI materials. While this would, of course, decrease the band structure engineering capabilities of such samples, the flexibility in tailoring the electronic properties could at least be partially replaced by the variation of the respective thicknesses of the stacks' constituents. Such a design could allow a band structure tunability sufficient for many applications, while simultaneously be less prone to disorder in comparison to devices utilizing a quaternary BSTS film.
Beyond the material optimization, the developed sample concept provides a multitude of intriguing experimental perspectives. In magnetotransport, for example, the utilization of local front-gating in addition to the global back-gating provided through the $SrTiO_3$ substrate could allow the creation and precise control of lateral p-n junctions, where unique signatures in the transport of Dirac electrons across an implemented lateral p-n potential step are expected [151, 244–246]. Moreover, next to the aforementioned interfacing of the TI samples with a ferromagnetic layer for spin pumping experiments, the Regensburg MBE cluster opens a broad spectrum of possibilities for incorporating the TI growth developed in this thesis into more complex devices. For example, the cluster allows the preparation of semiconductor nanowires, that could subsequently be equipped in-situ with a topological insulator shell and ferromagnetic or superconducting contacts. These technical capabilities in combination with the deep understanding of the electronic properties of our topological insulator materials generated through the investigations presented in this thesis provide an ideal basis for all of these future fields of research.

IV

Appendices

A

Parameters for molecular beam epitaxy

In the following, the key parameters for the molecular beam epitaxy will be provided, details concerning the growth procedure are described in Sec. 4. Since almost all samples discussed in the main text of this thesis were grown on $SrTiO_3$, only the parameters for this growth procedure will be given. When the Bi_2Se_3 seed layer is implemented the parameters are transferable to other substrates. Since the parameters for $(Bi_{1-x}Sb_x)_2Te_3$ and $(Bi_{1-x}Sb_x)_2(Te_{1-y}Se_y)_3$ depend highly on the targeted stoichiometry of the alloy, only intervals will be provided below. In A.3 the parameters for $(Bi_{1-x}Sb_x)_2(Te_{1-y}Se_y)_3$ with a stoichiometry of ($x = 0.7|y = 0.9$) are listed exemplarily, as this alloy ratio is utilized in chapters 7 and 8.

A.1 Pre-growth SrTiO$_3$ preparation

Instead of using larger wafers, usually three square STO pieces of 5×5 mm are transferred into the UHV of the TI MBE chamber via a load lock and placed onto the manipulator. The pre-growth preparation of the STO is crucial to enable high quality epitaxial sample preparation. The procedure is:

- heating of manipulator to 700°C with 15°C/min

- constant 700°C for 10 min

- cooling manipulator to targeted temperature for TI growth

- exposure with selenium flux for 2.5 min with selenium cell at $T = 180$°C

A.2 Growth parameters

A.2.1 $(Bi_{1-x}Sb_x)_2Te_3$

- manipulator: temperature ramp from $T = 245°C$ to $T = 270°C$ during growth with 10°C/min

- bismuth: $300°C \leq T \leq 345°C$

- antimony:
  - cracker: $T = 650°C$
  - reservoir: $260°C \leq T \leq 290°C$
  - valve opening: 25% - 66%

- tellurium: $T = 275°C$ independent of targeted stoichiometry

A.2.2 Bi_2Se_3 seed layer

- manipulator: $T = 190°C$

- selenium: $T = 180°C$, bismuth: $T = 350°C$

- exposure for 2.5 min

- ramping of manipulator to $T = 255°C$ in 6 min

- after this time 1 QL of seed layer finished, longer exposure for thicker seed layers

- after targeted seed layer thickness is reached: close bismuth shutter

- ramp of manipulator to $T = 290°C$

- annealing for 15 min

- cooling to growth temperature

A.2.3 $(Bi_{1-x}Sb_x)_2(Te_{1-y}Se_y)_3$ with seed layer

- after seed layer growth, manipulator set to $T = 255°C$

- bismuth: $315°C \leq T \leq 350°C$

- antimony:
  - cracker: $T = 700°C$
  - reservoir: $275°C \leq T \leq 280°C$

    – valve opening: 25% - 66%

- tellurium: $250°C \leq T \leq 290°C$

- selenium: $140°C \leq T \leq 180°C$

A.3 Example: $(Bi_{1-x}Sb_x)_2(Te_{1-y}Se_y)_3$ with (x=0.7 | y=0.9)

- after seed layer growth, manipulator set to $T = 255°C$

- bismuth: $T = 345°C$

- antimony:
  - cracker: $T = 700°C$
  - reservoir: $T = 280°C$
  - valve opening: 66%

- tellurium: $T = 280°C$

- selenium: $T = 150°C$

B

Sample fabrication

B.1 Optical lithography

To obtain the Hall-bar geometry used for the magnetotransport measurements in this thesis, the samples are fabricating using optical lithography patterning, ion-beam etching and e-beam Ti/Au evaporation. For front-gate implementation additionally plasma-enhanced chemical vapor deposition (PECVD) and atomic layer deposition (ALD) were employed. All processes were performed in clean room conditions and the optical lithography additionally under yellow light. In the following, the standard patterning recipe developed during this thesis is provided, before in B.1 some general remarks and common issues are provided.

B.1.1 Hall-bar patterning recipe

I. **Cutting samples in halves**

- spin coating with arbitrary optical resist for protection
- baking on heat plate (5', 80°C)
- gluing to Teflon disk using mounting wax (80°C)
- cutting of sample using a diamond saw
- removing sample from Teflon disk in warm acetone (60°C)
- thorough cleaning in acetone ultrasonic bath
- standard cleaning procedure: acetone, propanol, nitrogen drying

II. **Mesa patterning**

- resist spin coating

- resist: S1813
- parameters: 6000 rpm, 4000 rpm/s, 30"
- baking: 80°C, 5'

- mask aligner
    - mask: TI mask, Hall-bar structure
    - exposure: $\gtrsim$120", ~275 W
- development: 40" MF-26A, 30" H_2O, thorough nitrogen drying

III. **Mesa etching: CAIBE**

- Mounting to CAIBE, spot on sample holder according to machine book
- settings: recipe 21, MFC: 15% argon
- time: 2×30", 2' in-between break
- unmounting sample and checking of etching using two-point resistivity probe
- if necessary, additional etching step
- resist lift-off
    - >15' in acetone at 60°C
    - rinsing sample withe acetone using a syringe
    - if necessary, brief ultrasonic bath in acetone
    - standard cleaning procedure

IV. **Bond pad patterning**

- resist spin coating I
    - resist: LOR-3A
    - parameters: 4000 rpm, 2000 rpm/s, 45"
    - baking: 80°C, 5'
- resist spin coating II
    - resist: S1813
    - parameters: 8000 rpm, 4000 rpm/s, 30"
    - baking: 80°C, 5'
- mask aligner
    - mask: TI mask, Bond pad structure
    - alignment of mask directly above pad structures of mesa
    - exposure: $\gtrsim$120", ~275 W
- development: 45" MF-26A, 30" H_2O, thorough nitrogen drying

V. **Titanium/gold e-beam deposition**

- parameters according to machine book
- thickness: 10 nm Ti, 100 nm Au
- lift-off
    - 15' in RPG at 60°C
    - rinsing sample with RPG using a syringe
    - standard cleaning procedure

B.1.2 Front-gate implementation

The front-gate implementation requires additional clean room patterning steps, performed directly following the Hall-bar processing:

I. **Patterning of stripe for dielectric**

- resist spin coating I
    - resist: LOR-3A
    - parameters: 4000 rpm, 2000 rpm/s, 45"
    - baking: 80°C, 5'
- resist spin coating II
    - resist: S1813
    - parameters: 8000 rpm, 4000 rpm/s, 30"
    - baking: 80°C, 5'
- mask aligner
    - mask: TI mask, stripe structure
    - alignment of mask above main Hall-bar canal
    - exposure: $\gtrsim$120", ~275 W
    - two additional exposures creating a cross-pattern (see B.1)
- development: 45" MF-26A, 30" H_2O, thorough nitrogen drying

II. **Deposition of bilayer dielectric**

- SiO_2 deposition using PECVD
    - temperature: 80°C
    - thickness: 30 nm
    - procedure: default 3-step procedure saved at machine
- Al_2O_3 deposition using ALD

- temperature: 80°C

- thickness: ~ 80 nm (1000 cycles)

- procedure: recipe "zij57805_Al2O3_100nm_80C_66sPurge", 66" purge time

- lift-off

  - 15' in RPG at 60°C

  - rinsing sample with RPG using a syringe

  - standard cleaning procedure

III. **Ti/Au gate electrode**

- Patterning equivalent to Bond pad patterning of B.1 IV.

- Ti/Au e-beam deposition equivalent to B.1 V.

B.1.3 Back-gate implementation

For samples grown on SrTiO$_3$ substrates, the back-gate functionality is implemented by gluing the sample to the socket using two-component silver epoxy in a ratio of 1:1. To cure the glue the samples are placed on a heat plate at 80°C for ~90'. Electrical connection is established by wire bonding from one contact of the socket to the socket bottom.

B.1.4 Wire bonding

Electrical contacts between sample and socket are established by standard wire bonding utilizing a *tpt* wire bonder equipped with an aluminum wire of 25 µm diameter. The machine is used in manual wedgebond mode and the parameters can slightly vary from sample to sample, with typical ones being (ultrasonic / time [ms] / force [mN]):

- bond 1: 200 / 200 / 300

- bond 2: 200 / 200 / 350

The first bond is placed on the sample, the second on the socket.

B.1.5 General remarks and common issues

I. **All patterning processes have been optimized to not exceed temperatures of 80°C**

II. **Hall-bar patterning**

- patterning two Hall-bars per halved sample provides redundancy and allows direct testing for parasitic conduction through the substrate at $T \leq 4.2$ K in the measurement setup

- optical lithography
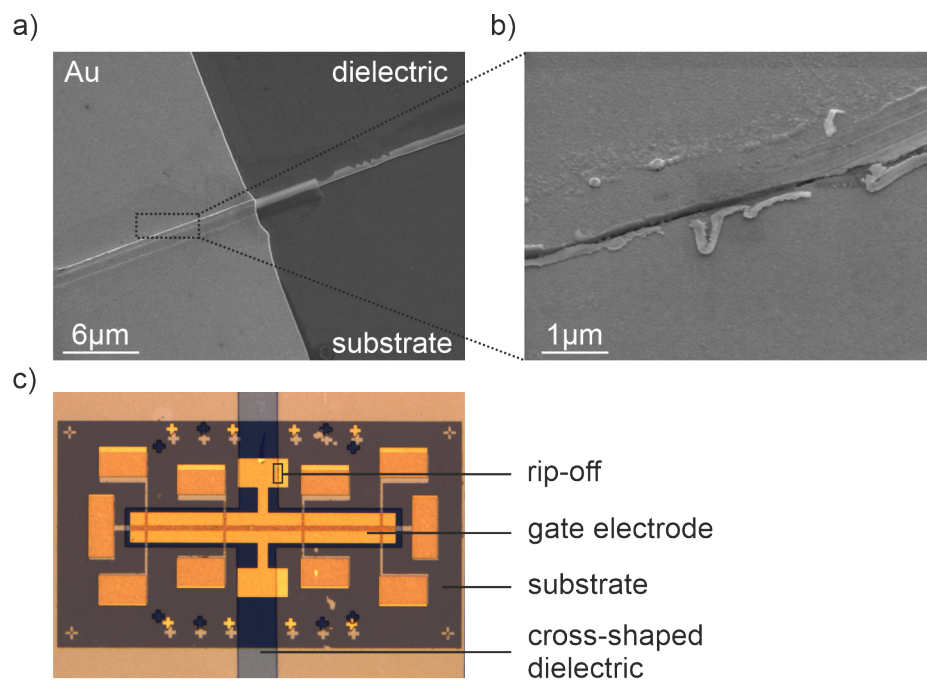
Figure B.1: Rip-off of Ti/Au electrode layer at the dielectric boundary. a) Scanning electron microscope image showing the rip-off, where the Ti/Au layer overlays the dielectric boundary. b) Zoom-in of a) visualizing the disruption of the electrical connection. c) Finished sample, where the dielectric (blue) is patterned in a cross-shape. The rip-off still happens at the dielectric edges, but enough space on the electrode bond pad is available for wire bonding.

- required exposure time is dependent on lamp output and can vary over time (check machine book)

- the comparatively large structures of the Hall-bar pattern are rather insensitive to slight overexposure → longer exposure times are recommended

- lift-off processes

  - application of ultrasonic bath is only recommended for lift-off processes not involving Ti/Au, due to possible damaging of areas that should not be removed

  - the dual-resist process utilizing LOR-3A and S1813 applied before Ti/Au deposition creates an undercut that eases the lift-off

  - every process involving LOR-3A requires RPG; if only S1813 is used, acetone is sufficient

  - RPG is more aggressive than e.g. acetone → samples should not be exposed to RPG for longer than necessary (usually ∼ 15′)

- ion-beam etching (CAIBE) and check for parasitic substrate conduction

  - etching in 30" intervals with breaks of 1.5' - 2' prevents burning of resist

  - if samples are grown on $SrTiO_3$ substrates, etching times have to optimized, since excessive ion-beam exposure of the STO can cause oxygen vacancies that create a parasitic conduction layer [247–249]

  - after etching samples need to be checked for parasitic substrate conduction using a two-point resistivity probe, where the tips have to be placed on suitable areas of TI material (placing tips directly on the substrate does not create sufficient contact and eventual parasitic conductance remains undetected)

  - since the parasitic substrate conduction can be temperature dependent, it should be checked again at liquid-helium temperatures before the measurement using a second Hall-bar

  - after unmounting the samples from the CAIBE, remaining glue has to be thoroughly removed from the back side

III. **Front-gate implementation**

- bilayer dielectric required to achieve higher reliability in terms of leakage currents

- if the sample is only partially covered by the dielectric, the subsequently deposited Ti/Au layer for the electrode breaks at the boundary of the dielectric disrupting the electrical connection (see Fig. B.1 a) and b)) → fixed by creating a dielectric cross-pattern as shown for a finished sample in Fig. B.1 c)

- alternatively the sample can be covered completely by the dielectric, which then requires an etching to facilitate reliable wire bonding

B.2 Electron-beam lithography

All samples discussed in the main text of this thesis were patterned by optical lithography. However, also successful fabrication using electron-beam lithography was performed on topological insulator samples and topological insulator/permalloy heterostructures. Below, the relevant lithography recipe is provided. All other patterning processes, like ion-beam etching or Ti/Au deposition including the corresponding lift-off process are applicable as presented in B.1. The e-beam lithography involves processes utilizing positive and negative resists. The positive steps are used to pattern areas for material evaporation, like Ti/Au deposition for alignment crosses, bond pads or waveguides. The negative steps define areas for etching purposes.

I. **Positive resist**
- resist spin coating I
    - resist: PMMA 50K / 12%
    - parameters: 8000 rpm, 1000 rpm/s, 30"
    - baking: 80°C, 5'
- resist spin coating II
    - resist: PMMA 200K / 9%
    - parameters: 8000 rpm, 1000 rpm/s, 30"
    - baking: 80°C, 5'
- lithography
    - EHT: 20 kV
    - aperture: 30 μm
    - area dose: 250 μC/cm^2 (140 μC/cm^2 for smaller structures ∼ 2 μm)
- development: 40" MIBK 1:3, 30" propanol, thorough nitrogen drying

II. **Negative resist**
- resist spin coating
    - resist: AR-N 7500.18 (negative resist, no exposure to ambient light!)
    - parameters: 6000 rpm, 1000 rpm/s, 30"
    - baking: 80°C, 5'
- lithography

- EHT: 20 kV

- aperture: 30 μm

- area dose: 150 μC/cm^2

- development: 90" AR300-47, 30" H$_2$O, thorough nitrogen drying
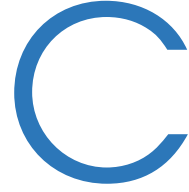
Magnetotransport details

To achieve comparable results in the electronic characterization of the TI samples, a standard procedure was established for the work presented in the main text of this thesis that prevents distortion of the results by measurement artefacts. Before this procedure will be given in C.1, the following will briefly discuss the main sources for error and explain how they can be avoided.

C.1 Standard electrical characterization procedure

C.1.1 Sources for error

Parasitic conduction and leakage currents

Every contribution to the conduction that does not stem from the TI sample obviously falsifies the obtained results. Such parasitic conduction channels can originate from a not completely insulating substrate (e.g. caused by too long etching times in the case of $SrTiO_3$) or leakage currents through the dielectric to the front-gate electrode. After the sample is cooled down to the desired measurement temperature, the front-gate should be tested via a leakage measurement and substrate conduction should be excluded by measuring the resistance between the two neighbouring Hall-bars.

Cool-down time

The velocity of the cool-down procedure can have an influence on the low temperature resistance of the sample. Figure C.1 illustrates this on an arbitrary TI heterostructure sample, where each pair of gray circle and red triangle represent a cool-down of the same sample from room temperature to $4.2\,\mathrm{K}$ during the respective time t. While the sheet resistance at room temperature (gray circles) and hence the starting point of the

measurement is constant for all runs, the resistance at low temperature (red triangles) is smaller for shorter cool-down times. However, for $t \gtrsim 125\,\text{s}$ the low temperature resistance saturates. Thus, extending the cool-down time to approximately 3 to 5 minutes yields reproducible results.
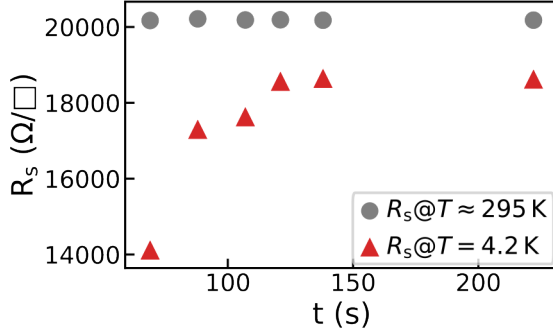
Figure C.1: Influence of the cool-down time on the low temperature resistance.

Back-gating: long-term effects

The unique dielectric properties of the $SrTiO_3$ substrate allow easy implementation of back-gating, but at the same time require accuracy in the measurement procedure to avoid unintended artefacts. First, after the back-gate voltage is changed, long-term effects lead to a further modulation of the electronic properties of the TI samples on a time scale of minutes. This is illustrated in Fig. C.2 a). At time $t < 0$, the back-gate voltage is set from 30 V to 0 V, after which the monitoring of the sample's sheet resistance is immediately started defining $t = 0$. Even though the gate voltage (and all other parameter) are not changed during $t > 0$, the resistance still shows a variation for several minutes. One of the possible subsequent measurement artefacts is shown in Fig. C.2 b), where the absolute magnetoresistance MR^{abs} of a heterostructure sample is shown measured at $T = 4.2\,\text{K}$. The usually axis-symmetric curve to $B = 0$ shows a bent shape for $B < 0$, due to the superposition of the magnetic field effect and the long-term influence on the resistance after a change of the back-gate. To avoid such artefacts, the resistance should be monitored after the back-gate voltage is changed and further measurements should only be started once it has saturated.
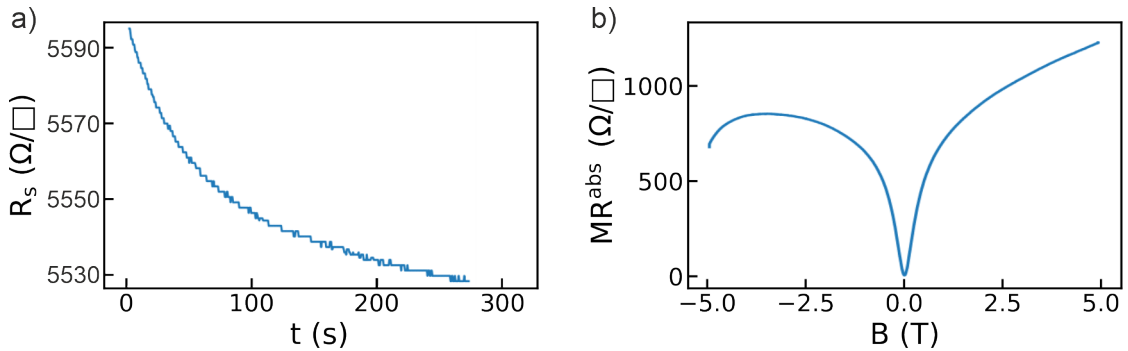
Figure C.2: a) Long-term effect on the sample's resistance induced by a change of the back-gate voltage. b) Subsequent artefact in the magnetoresistance.

Back-gating: hysteresis-effects

The second possible source of error in the back-gate measurements is the hysteresis of the gate. This is shown in Fig. C.3. The back-gate voltage V_{BG} is swept from $0\,V$ to $-32\,V$ (dark blue line) and back to $0\,V$ (light blue line). Due to the STO hysteresis, both curves do not coincide. The offset at $V_{BG} = -32\,V$ stems from the long-term effect stated above. To yield comparable back-gate studies, every measurement series should start at $V_{BG} = 0\,V$ and the voltage should always be monotonically increased or decreased. To erase the hysteresis, the sample has to be brought to room temperature and cooled down again at $V_{BG} = 0\,V$.

Figure C.3: Influence of the STO hysteresis on the sheet resistance of a sample measured at $T = 4.2\,K$.
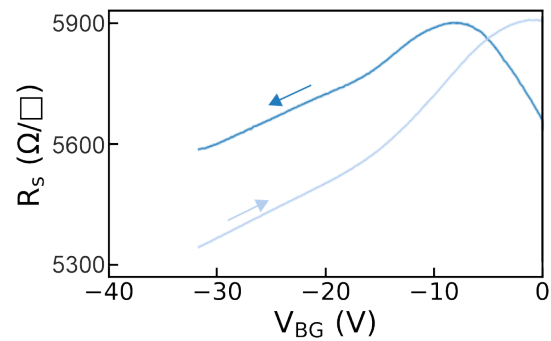
C.1.2 Standard procedure ^{4}He dewar

For the standard sample characterization procedure the ^{4}He dewar system is used as introduced in Sec. 5.1.4. It follows:

I. Test all contacts via a two point resistance measurement after sample is mounted to the dip stick

II. Connect the temperature sensor and the contacts needed for the measurement with the respective Lock-in or voltage source for gate operation, set all contacts to "float" on the switch box and switch on outputs of voltages source at $0\,V$

III. Start data acquisition and slowly lower dip stick into helium dewar on a time scale of 3 to 5 minutes, while always monitoring the current temperature (temperature decreases slowly in the beginning, but rapidly when the sample approaches the He bath)

IV. At $T = 4.2\,K$, check sample for leakage or parasitic currents

V. Sweep magnetic field to $5\,T$

VI. At $B = 5\,T$, where the highest signal of V_{xx} and V_{xy} is reached, optimize Lock-in settings

173

VII. Measure magnetic field sweep from +5 T to −5 T; from the sign of the slope of V_{xy} usually the sign of the gate voltage of the resistance maximum can be predicted

VIII. Sweep magnetic field to 0 T

IX. At $B = 0$ T measure gate sweep to positive or negative direction up to desired value; usually beyond the maximum in resistance

X. Sweep gate back to 0 V

XI. Bring sample to room temperature and let it warm up for some time

XII. Repeat cool-down procedure

XIII. If desired, measure gate sweep for opposite sign values; after measurement sweep gate back to 0 V and repeat warm-up and cool-down

XIV. Set gate to desired constant values, wait until resistance has saturated at the respective V_{BG} and measure magnetic field sweeps between ±5 T

XV. Sample has to be brought to room temperature, when magnetic field sweeps at opposite sign gate values are desired to be measured.

C.2 Symmetrization of Hall measurements

In the simplest case, the classical horizontal Hall resistance R_{xy} of a conductive material is a straight line. While the Hall curve can be non-linear in the presence of multiple conduction channels of different mobilities and types, it is always expected to be point-symmetric to $B = 0$ T and to fulfill $R_{xy} = 0\,\Omega$ at $B = 0$ T. In our measurements, however, we routinely obtained Hall curves that did not meet these expectations. An exemplary measurement is shown in Fig. C.4 a), where clearly a non-point-symmetric curve with a large offset from $R_{xy} = 0\,\Omega$ at $B = 0$ T can be observed. That this observation is an artefact from the measurement and has no physical origin can be easily illustrated by comparing the curve in panel a) with the one in panel b). As indicated by the insets, where the rectangles framed in red represent the used Hall-bar contacts, the only difference between the two measurements is the side of the contacts used to obtain the *longitudinal* voltage drop, the measurement of the horizontal voltage drop and the applied current are identical. As can be seen from the two measurements, changing the side of the contacts for the longitudinal voltage drop flips the measured curve of R_{xy} that is obtained from V_{xy}. The origin of this effect is a leakage current through the Lock-in that is utilized for the longitudinal measurement and that is caused by the high sample resistance. As indicated in Fig. C.4 c), this leakage current changes the potential landscape within the sample on that side, where the longitudinal voltage drops are contacted, which in turn influences the horizontal measurement. A practical solution of this issue is a post-measurement digital

Figure C.4: Illustration for the symmetrization of Hall curves. a),b) Measured Hall resistances on same sample with contacts connected as indicated in the insets. c) Sketch of potential landscape variation by connecting a Lock-in to measure the longitudinal voltage drop. d) Symmetrized measurements of a) and b) along with an un-symmetrized measurement, where no longitudinal contacts were connected. All curves yield identical results.

symmetrization of the V_{xy} data that extracts all components from the curve that are not point-symmetric to $B = 0\,\text{T}$ by

$$R_{xy}^{\text{sym}}(B) = \frac{R_{xy}(B) - R_{xy}(-B)}{2}.$$

That this procedure is physically justified is highlighted in Fig. C.4 d). The blue and orange curves correspond to the measurements of panels a) and b), respectively, after the digital symmetrization. The red curve represents the measurement of the same horizontal resistance, but with no segment to obtain V_{xx} connected to a Lock-in and *without symmetrization*. All three curves are identical, showing that the symmetrization procedure can eliminate the measurement artefact without falsifying the physical results. More details can be found in Ref. [250].

a)

b)
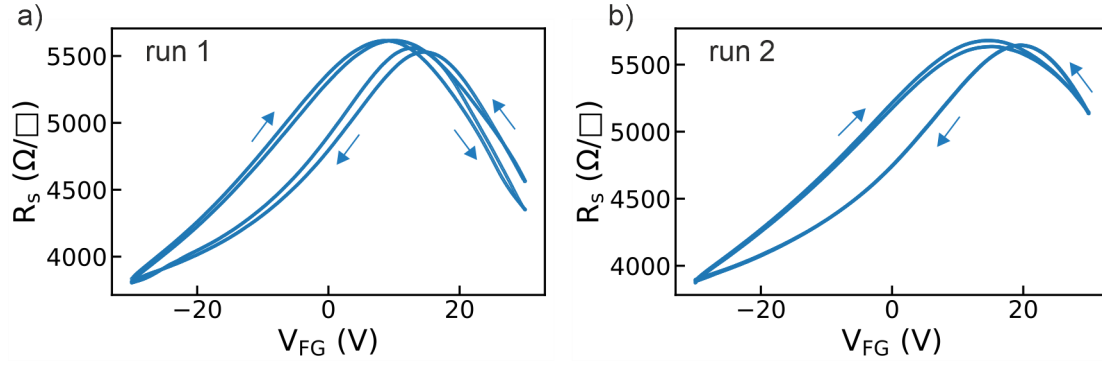
Figure C.5: Two runs of front-gate sweeps implemented before the dual-gated measurement to avoid hysteresis effects. a) Run 1: sweep of front-gate following +30V → -30V → +30V → -30V → +30V. b) Run 2 with identical sequence.

C.3 Dual-gated measurement

Figure 7.6 of section 7.3.1 showed a color plot of a dual-gated sample. The following will present the procedure conducted to obtain this plot.

Before the actual measurement, the sample was cooled to 4.2 K in the ^{4}He dewar system with both gates contacted to voltage sources with engaged output at 0 V. To ensure the absence of leakage currents through the front-gate dielectric, a leakage measurement was performed for $V_{FG} = \pm 30$ V. After bringing the sample back to room temperature and cooling down again to 4.2 K, the front-gate was swept twice from +30 V to -30 V in two runs to erase all front-gate hysteresis effects. The measured sheet resistance of the two runs are displayed in Fig. C.5. Whereas the first run shows some hysteresis effects, especially the two sweeps from +30 V to -30 V in run 2 coincide very well. Subsequently, the measurement to acquire the color plot of Fig. 7.6 in the main text only contains front-gate sweeps +30 V to -30 V. To obtain the color plot, the back-gate was varied from 0 V in steps of 1.5 V in positive direction. At each back-gate value and after a waiting time of 10 minutes to avoid long-term effects from the STO dielectric (see C.1), a front-gate sweep was measured from 30 V to -30 V with 60 mV/s. After the measurement at a back-gate voltage of +30 V, the BG was set to zero and the sample was brought to room temperature to reset both gates. After cool-down, the whole procedure was repeated (including the two runs to avoid the FG hysteresis) with the back-gate being set to negative values. Due to this required reset of the gates, a small discrepancy between the measurements for positive and negative back-gate direction is unavoidable. To account for this, the R_S values for positive back-gate voltage were shifted by 3.3 V front-gate in Fig. 7.6.

Bibliography

[1] C. Kittel, *Introduction to solid state physics*, 8th ed. (Wiley, 2004).

[2] L. LANDAU, *The Theory of Phase Transitions*, Nature **138**, 840–841 (1936).

[3] J. Tolédano, P. Tolédano, and E. Landau, *The Landau Theory of Phase Transitions: Application to Structural, Incommensurate, Magnetic, and Liquid Crystal Systems*, Lecture Notes in Physics Series (World Scientific, 1987).

[4] B. Bernevig and T. Hughes, *Topological Insulators and Topological Superconductors* (Princeton University Press, 2013).

[5] K. v. Klitzing, G. Dorda, and M. Pepper, *New Method for High-Accuracy Determination of the Fine-Structure Constant Based on Quantized Hall Resistance*, Phys. Rev. Lett. **45**, 494–497 (1980).

[6] M. Z. Hasan and C. L. Kane, *Colloquium: Topological insulators*, Rev. Mod. Phys. **82**, 3045–3067 (2010).

[7] J. M. Kosterlitz and D. J. Thouless, *Long range order and metastability in two dimensional solids and superfluids. (Application of dislocation theory)*, J. Phys. C: Solid State Phys. **5**, L124–L126 (1972).

[8] J. M. Kosterlitz and D. J. Thouless, *Ordering, metastability and phase transitions in two-dimensional systems*, J. Phys. C: Solid State Phys. **6**, 1181–1203 (1973).

[9] D. J. Thouless, M. Kohmoto, M. P. Nightingale, and M. den Nijs, *Quantized Hall Conductance in a Two-Dimensional Periodic Potential*, Phys. Rev. Lett. **49**, 405–408 (1982).

[10] F. D. M. Haldane, *Model for a Quantum Hall Effect without Landau Levels: Condensed-Matter Realization of the "Parity Anomaly"*, Phys. Rev. Lett. **61**, 2015–2018 (1988).

[11] C. L. Kane and E. J. Mele, *Quantum Spin Hall Effect in Graphene*, Phys. Rev. Lett. **95**, 226801 (2005).

[12] C. L. Kane and E. J. Mele, *Z_2 Topological Order and the Quantum Spin Hall Effect*, Phys. Rev. Lett. **95**, 146802 (2005).

[13] B. A. Bernevig and S.-C. Zhang, *Quantum Spin Hall Effect*, Phys. Rev. Lett. **96**, 106802 (2006).

[14] M. König, S. Wiedmann, C. Brüne, A. Roth, H. Buhmann, L. W. Molenkamp, X.-L. Qi, and S.-C. Zhang, *Quantum Spin Hall Insulator State in HgTe Quantum Wells*, Science **318**, 766–770 (2007).

[15] L. Fu and C. L. Kane, *Topological insulators with inversion symmetry*, Phys. Rev. B **76**, 045302 (2007).

[16] J. E. Moore and L. Balents, *Topological invariants of time-reversal-invariant band structures*, Phys. Rev. B **75**, 121306 (2007).

[17] R. Roy, *Topological phases and the quantum spin Hall effect in three dimensions*, Phys. Rev. B **79**, 195322 (2009).

[18] L. Fu and C. L. Kane, *Superconducting proximity effect and Majorana Fermions at the Surface of a Topological Insulator*, Phys. Rev. Lett. **100**, 096407 (2008).

[19] J. C. Y. Teo and C. L. Kane, *Majorana Fermions and Non-Abelian Statistics in Three Dimensions*, Phys. Rev. Lett. **104**, 046401 (2010).

[20] Y. Tanaka, T. Yokoyama, and N. Nagaosa, *Manipulation of the Majorana Fermion, Andreev Reflection, and Josephson Current on Topological Insulators*, Phys. Rev. Lett. **103**, 107002 (2009).

[21] J.-P. Xu et al., *Experimental Detection of a Majorana Mode in the core of a Magnetic Vortex inside a Topological Insulator-Superconductor Bi_2Te_3/$NbSe_2$ Heterostructure*, Phys. Rev. Lett. **114**, 017001 (2015).

[22] C. Schrade, A. A. Zyuzin, J. Klinovaja, and D. Loss, *Proximity-Induced π Josephson Junctions in Topological Insulators and Kramers Pairs of Majorana Fermions*, Phys. Rev. Lett. **115**, 237001 (2015).

[23] W. Tian, W. Yu, J. Shi, and Y. Wang, *The Property, Preparation and Application of Topological Insulators: A Review*, Materials **10**, 814 (2017).

[24] S. K. Banerjee, L. F. Register II, B. R. Sahu, P. Jadaun, and J. Chang, *Topological insulator-based field-effect transistor*, U.S. Patent US 8,629,427 B2 (2014).

[25] H. Liu and P. D. Ye, *Atomic-layer-deposited Al_2O_3 on Bi_2Te_3 for topological insulator field-effect transistors*, Appl. Phys. Lett. **99**, 052108 (2011).

[26] J. Son, K. Banerjee, M. Brahlek, N. Koirala, S.-K. Lee, J.-H. Ahn, S. Oh, and H. Yang, *Conductance modulation in topological insulator Bi_2Se_3 thin films with ionic liquid gating*, Appl. Phys. Lett. **103**, 213114 (2013).

[27] H. Zhang, C.-X. Liu, X.-L. Qi, X. Dai, Z. Fang, and S.-C. Zhang, *Topological insulators in Bi_2Se_3, Bi_2Te_3 and Sb_2Te_3 with a single Dirac cone on the surface*, Nat. Phys. **5**, 438–442 (2009).

[28] Y. Xu, I. Miotkowski, C. Liu, J. Tian, H. Nam, N. Alidoust, J. Hu, C.-K. Shih, M. Z. Hasan, and Y. P. Chen, *Observation of topological surface state quantum Hall effect in an intrinsic three-dimensional topological insulator*, Nat. Phys **10**, 956–963 (2014).

[29] F. Ortmann, S. Roche, and S. Valenzuela, *Topological Insulators: Fundamentals and Perspectives* (Wiley-VCH, 2015).

[30] G. Tkachov, *Topological Insulators: The Physics of Spin Helicity in Quantum Transport* (Jenny Stanford Publishing, 2015).

[31] M. Franz and L. Molenkamp, *Topological Insulators* (Elsevier Science, 2013).

[32] M. Fruchart and D. Carpentier, *An introduction to topological insulators*, Comptes Rendus Physique **14**, Topological insulators / Isolants topologiques, 779–815 (2013).

[33] D. Carpentier, "Topology of bands in solids", in *Dirac Matter. Progress in Mathematical Physics* (Springer International Publishing, 2014).

[34] M. Nakahara and M. Delbrück, *Differentialgeometrie, Topologie und Physik* (Springer Berlin Heidelberg, 2015).

[35] S. Hyde, B. W. Ninham, S. Anderson, K. Larsson, T. Landh, Z. Blum, and S. Lidin, "Chapter 1 - The Mathematics of Curvature", in *The Language of Shape* (Elsevier Science B.V., 1997).

[36] M. V. Berry, *Quantal phase factors accompanying adiabatic changes*, Proc. R. Soc. Lond. A **392**, 45–57 (1984).

[37] F. Ghahari et al., *An on/off Berry phase switch in circular graphene resonators*, Science **356**, 845–849 (2017).

[38] Y. Ando, *Topological Insulator Materials*, J. Phys. Soc. Japan **82**, 102001 (2013).

[39] A. Messiah, *Quantum Mechanics*, Quantum Mechanics Bd. 2 (Elsevier Science, 1981).

[40] J. Zak, *Berry's phase for energy bands in solids*, Phys. Rev. Lett. **62**, 2747–2750 (1989).

[41] D. Tong, *Lectures on the Quantum Hall Effect*, arXiv:1606.06687, V2 (2016).

[42] B. A. Bernevig, T. L. Hughes, and S.-C. Zhang, *Quantum Spin Hall Effect and Topological Phase Transition in HgTe Quantum Wells*, Science **314**, 1757–1761 (2006).

[43] M. König, S. Wiedmann, C. Brüne, A. Roth, H. Buhmann, L. W. Molenkamp, X.-L. Qi, and S.-C. Zhang, *Quantum Spin Hall Insulator State in HgTe Quantum Wells*, Science **318**, 766–770 (2007).

[44] L. Fu, C. L. Kane, and E. J. Mele, *Topological insulators in three dimensions*, Phys. Rev. Lett. **98**, 106803 (2007).

[45] R. Jackiw and C. Rebbi, *Solitons with fermion number 1/2*, Phys. Rev. D **13**, 3398–3409 (1976).

[46] C. Weyrich, *Electrical transport and magnetoresistance in MBE-grown 3D topological insulator thin films and nanostructures*, Dissertation at RWTH Aachen University (2019).

[47] Z. Alpichshev, J. G. Analytis, J.-H. Chu, I. R. Fisher, Y. L. Chen, Z. X. Shen, A. Fang, and A. Kapitulnik, *STM Imaging of Electronic Waves on the Surface of* Bi_2Te_3*: Topologically Protected Surface States and Hexagonal Warping Effects*, Phys. Rev. Lett. **104**, 016401 (2010).

[48] S. Kasap and P. Capper, *Springer Handbook of Electronic and Photonic Materials* (Springer International Publishing, 2017).

[49] R. Gross and A. Marx, *Festkörperphysik* (Oldenbourg Wissenschaftsverlag, 2012).

[50] T. Ihn, *Semiconductor Nanostructures: Quantum States and Electronic Transport* (OUP Oxford, 2010).

[51] J. S. Kim, S. S. A. Seo, M. F. Chisholm, R. K. Kremer, H.-U. Habermeier, B. Keimer, and H. N. Lee, *Nonlinear Hall effect and multichannel conduction in* $LaTiO_3/SrTiO_3$ *superlattices*, Phys. Rev. B **82**, 201407 (2010).

[52] C. Hurd, *The Hall Effect in Metals and Alloys* (Springer US, 2012).

[53] V. Gantmakher and L. Man, *Electrons and Disorder in Solids* (OUP Oxford, 2005).

[54] I. L. Aleiner, B. L. Altshuler, and M. E. Gershenson, *Interaction effects and phase relaxation in disordered systems*, Waves in Random Media **9**, 201–239 (1999).

[55] D. E. Prober, "Electron Coherence and Dephasing in Metal Films, Wires and Rings", in *Perspectives of mesoscopic physics* (World Scientific, 2010).

[56] J. J. Lin and J. P. Bird, *Recent experimental studies of electron dephasing in metal and semiconductor mesoscopic structures*, J. Phys. Condens. Matter **14**, R501–R596 (2002).

[57] Y. Takagaki, B. Jenichen, U. Jahn, M. Ramsteiner, and K.-J. Friedland, *Weak antilocalization and electron-electron interaction effects in Cu-doped* Bi_2Se_3 *films*, Phys. Rev. B **85**, 115314 (2012).

[58] C. Beenakker and H. van Houten, "Quantum Transport in Semiconductor Nanostructures", in *Semiconductor heterostructures and nanostructures*, Vol. 44 (Academic Press, 1991).

[59] H.-Z. Lu and S.-Q. Shen, *Weak localization and weak anti-localization in topological insulators*, Proc. SPIE Spintronics VII **9167**, 263–273 (2014).

[60] S. Hikami, A. I. Larkin, and Y. Nagaoka, *Spin-Orbit Interaction and Magnetoresistance in the Two Dimensional Random System*, Prog. Theor. Phys. **63**, 707–710 (1980).

[61] P. A. Lee and T. V. Ramakrishnan, *Disordered electronic systems*, Rev. Mod. Phys. **57**, 287–337 (1985).

[62] Aronov, A.G., *Electron Coherence and Interference in Disordered Conductors*, Europhys. News **24**, 98–101 (1993).

[63] B. Altshuler and A. Aronov, "Electron–Electron Interaction In Disordered Conductors", in *Electron–electron interactions in disordered systems*, Vol. 10 (Elsevier, 1985).

[64] P. Schwab, *Electron-Electron Interactions and Charge Transport in Mesoscopic Conductors*, Habilitation at the University of Augsburg (2007).

[65] C. L. Kane, R. A. Serota, and P. A. Lee, *Long-range correlations in disordered metals*, Phys. Rev. B **37**, 6701–6710 (1988).

[66] A. D. Stone, *Reduction of low-frequency noise in metals by a magnetic field: Observability of the transition between random-matrix ensembles*, Phys. Rev. B **39**, 10736–10743 (1989).

[67] B. L. Altshuler, A. G. Aronov, and D. E. Khmelnitsky, *Effects of electron-electron collisions with small energy transfers on quantum localisation*, J. Phys. C: Solid State Phys. **15**, 7367–7386 (1982).

[68] A. McNaught and A. Wilkinson, *IUPAC Compendium of Chemical Terminology* (IUPAC, 2003).

[69] D. H. Everett, *Manual of Symbols and Terminology for Physicochemical Quantities and Units, Appendix II: Definitions, Terminology and Symbols in Colloid and Surface Chemistry*, Pure Appl. Chem. **31**, 577–638 (1972).

[70] J. Laurer, *Spininjektion in Silizium: Von der epitaktischen Si/MgO-Tunnelstruktur zur Erzeugung und Detektion einer Spinakkumulation*, Dissertation at the University of Regensburg (2018).

[71] F. Tang, T. Parker, G.-C. Wang, and T.-M. Lu, *Surface texture evolution of polycrystalline and nanostructured films: RHEED surface pole figure analysis*, J. Phys. D: Appl. Phys. **40**, R427–R439 (2007).

[72] W. Braun, *Applied RHEED: Reflection High-Energy Electron Diffraction During Crystal Growth* (Springer Berlin Heidelberg, 1999).

[73] B. Joyce, P. Dobson, J. Neave, K. Woodbridge, J. Zhang, P. Larsen, and B. Bôlger, *RHEED studies of heterojunction and quantum well formation during MBE growth — from multiple scattering to band offsets*, Surf. Sci. **168**, 423–438 (1986).

[74] J. M. Hollander and W. L. Jolly, *X-ray photoelectron spectroscopy*, Acc. of Chem. Res. **3**, 193–200 (1970).

[75] C. Fadley, *X-ray photoelectron spectroscopy: Progress and perspectives*, J. Electron Spectrosc. Relat. Phenom. **178-179**, 2–32 (2010).

[76] P. van der Heide, *X-ray Photoelectron Spectroscopy: An introduction to Principles and Practices* (Wiley, 2011).

[77] D. Schroder, *Semiconductor Material and Device Characterization* (Wiley, 2015).

[78] N. Bansal, Y. S. Kim, M. Brahlek, E. Edrey, and S. Oh, *Thickness-Independent Transport Channels in Topological Insulator* Bi_2Se_3 *Thin Films*, Phys. Rev. Lett. **109**, 116804 (2012).

[79] H. Steinberg, D. R. Gardner, Y. S. Lee, and P. Jarillo-Herrero, *Surface State Transport and Ambipolar Electric Field Effect in Bi_2Se_3 Nanodevices*, Nano Lett. **10**, 5032–5036 (2010).

[80] T. Trivedi, S. Sonde, H. C. P. Movva, and S. K. Banerjee, *Weak antilocalization and universal conductance fluctuations in bismuth telluro-sulfide topological insulators*, J. of Appl. Phys. **119**, 055706 (2016).

[81] B. Xia, P. Ren, A. Sulaev, P. Liu, S.-Q. Shen, and L. Wang, *Indications of surface-dominated transport in single crystalline nanoflake devices of topological insulator $Bi_{1.5}Sb_{0.5}Te_{1.8}Se_{1.2}$*, Phys. Rev. B **87**, 085442 (2013).

[82] D. Backes, D. Huang, R. Mansell, M. Lanius, J. Kampmeier, D. Ritchie, G. Mussler, G. Gumbs, D. Grützmacher, and V. Narayan, *Disentangling surface and bulk transport in topological-insulator $p-n$ junctions*, Phys. Rev. B **96**, 125125 (2017).

[83] H. Fukuyama, *Anomalous Orbital Magnetism and Hall Effect of Massless Fermions in Two Dimension*, J. Phys. Soc. Japan **76**, 043711 (2007).

[84] D. Kim, S. Cho, N. P. Butch, P. Syers, K. Kirshenbaum, S. Adam, J. Paglione, and M. S. Fuhrer, *Surface conduction of topological Dirac electrons in bulk insulating Bi_2Se_3*, Nat. Phys. **8**, 459–463 (2012).

[85] G. Eguchi and S. Paschen, *Robust scheme for magnetotransport analysis in topological insulators*, Phys. Rev. B **99**, 165128 (2019).

[86] P. A. Fleury and J. M. Worlock, *Electric-Field-Induced Raman Scattering in $SrTiO_3$ and $KTaO_3$*, Phys. Rev. **174**, 613–623 (1968).

[87] K. A. Müller and H. Burkard, *$SrTiO_3$: An intrinsic quantum paraelectric below 4 K*, Phys. Rev. B **19**, 3593–3602 (1979).

[88] M. Schmalzbauer, *Heterostructure design of Si/SiGe two-dimensional electron systems for field-effect devices*, Dissertation at the University of Regensburg (2015).

[89] J. Loher, *Two-dimensional hole systems in indium-based quantum well heterostructures*, Dissertation at the University of Regensburg (2016).

[90] O. I. S. Limited, *Product guide Spektromag SM-4000*, (2004).

[91] F. J. Giessibl, *Advances in atomic force microscopy*, Rev. Mod. Phys. **75**, 949–983 (2003).

[92] D. Rugar and P. Hansma, *Atomic force microscopy*, Phys. today **43**, 23–30 (1990).

[93] R. Garcıa and R. Pérez, *Dynamic atomic force microscopy methods*, Surf. Sci. Rep. **47**, 197–301 (2002).

[94] G. Panaccione et al., *Advanced photoelectric effect experiment beamline at Elettra: A surface science laboratory coupled with Synchrotron Radiation*, Rev. of Sci. Instr. **80**, 043105 (2009).

[95] C. Bigi, *Understanding the electronic properties of quantum materials by means of photoemission with angular and spin resolution*, Dissertation at the University of Milan (2019).

[96] A. Damascelli, *Probing the Electronic Structure of Complex Systems by ARPES*, Phys. Scr. **T109**, 61 (2004).

[97] B. Lv, T. Qian, and H. Ding, *Angle-resolved photoemission spectroscopy and its application to topological materials*, Nat. Rev. Phys. **1**, 609–626 (2019).

[98] T. Ginley, Y. Wang, and S. Law, *Topological Insulator Film Growth by Molecular Beam Epitaxy: A Review*, Crystals **6**, 154 (2016).

[99] G. Mussler, *Molecular-Beam Epitaxy of 3D Topological Insulator Thin Films and Devices on Si Substrates*, Phys. Status Solidi B **257**, 2000007 (2020).

[100] Y. Xia et al., *Observation of a large-gap topological-insulator class with a single Dirac cone on the surface*, Nat. Phys. **5**, 398–402 (2009).

[101] Z.-H. Pan, E. Vescovo, A. V. Fedorov, D. Gardner, Y. S. Lee, S. Chu, G. D. Gu, and T. Valla, *Electronic Structure of the Topological Insulator Bi_2Se_3 Using Angle-Resolved Photoemission Spectroscopy: Evidence for a Nearly Full Surface Spin Polarization*, Phys. Rev. Lett. **106**, 257004 (2011).

[102] Scanlon, D. O. and King, P. D. C. and Singh, R. P. and de la Torre, A. and Walker, S. McKeown and Balakrishnan, G. and Baumberger, F. and Catlow, C. R. A., *Controlling bulk conductivity in topological insulators: key role of anti-site defects*, Adv. Mater. **24**, 2154–2158 (2012).

[103] P. Rüßmann, P. Mavropoulos, and S. Blügel, *Lifetime and surface-to-bulk scattering off vacancies of the topological surface state in the three-dimensional strong topological insulators Bi_2Te_3 and Bi_2Se_3*, J. phys. Chem. Solids **128**, 258–264 (2019).

[104] Y. L. Chen et al., *Experimental Realization of a Three-Dimensional Topological Insulator, Bi_2Te_3*, Science **325**, 178–181 (2009).

[105] Z. Ren, A. A. Taskin, S. Sasaki, K. Segawa, and Y. Ando, *Large bulk resistivity and surface quantum oscillations in the topological insulator Bi_2Te_2Se*, Phys. Rev. B **82**, 241306 (2010).

[106] D.-X. Qu, Y. S. Hor, J. Xiong, R. J. Cava, and N. P. Ong, *Quantum Oscillations and Hall Anomaly of Surface States in the Topological Insulator Bi_2Te_3*, Science **329**, 821–824 (2010).

[107]   J. Xiong, A. Petersen, D. Qu, Y. Hor, R. Cava, and N. Ong, *Quantum oscillations in a topological insulator Bi_2Te_2Se with large bulk resistivity ($6\Omega cm$)*, Physica E Low Dimens. Syst. Nanostruct. **44**, 917–920 (2012).

[108]   J. Zhang et al., *Band structure engineering in $(Bi_{1-x}Sb_x)_2Te_3$ ternary topological insulators*, Nat. Commun. **2**, 574 (2011).

[109]   S. Schreyeck, *Molecular Beam Epitaxy and Characterization of Bi-Based V_2VI_3 Topological Insulators*, Dissertation at the University of Würzburg (2016).

[110]   A. Koma and K. Yoshimura, *Ultrasharp interfaces grown with Van der Waals epitaxy*, Surf. Sci. **174**, 556–560 (1986).

[111]   A. Koma, *Van der Waals epitaxy — a new epitaxial growth method for a highly lattice-mismatched system*, Thin Solid Films **216**, 72–76 (1992).

[112]   P. H. Le, K. H. Wu, C. W. Luo, and J. Leu, *Growth and characterization of topological insulator Bi_2Se_3 thin films on $SrTiO_3$ using pulsed laser deposition*, Thin Solid Films **534**, 659–665 (2013).

[113]   K. van Benthem, C. Elsässer, and R. H. French, *Bulk electronic structure of $SrTiO_3$: Experiment and theory*, J. of Appl. Phys. **90**, 6156–6164 (2001).

[114]   R. C. Neville, B. Hoeneisen, and C. A. Mead, *Permittivity of Strontium Titanate*, J. of Appl. Phys. **43**, 2124–2131 (1972).

[115]   C. Weyrich et al., *Growth, characterization, and transport properties of ternary $(Bi_{1-x}Sb_x)_2Te_3$ topological insulator layers*, J. Condens. Matter Phys. **28**, 495501 (2016).

[116]   J. Tang et al., *Electrical Detection of Spin-Polarized Surface States Conduction in $(Bi_0.53Sb_0.47)_2Te_3$ Topological Insulator*, Nano Lett. **14**, 5423–5429 (2014).

[117]   X. He, H. Li, L. Chen, and K. Wu, *Substitution-induced spin-splitted surface states in topological insulator $(Bi_{1-x}Sb_x)_2Te_3$*, Sci. Rep. **5**, 8830 (2015).

[118]   F. Lüpke et al., *In situ disentangling surface state transport channels of a topological insulator thin film by gating*, npj Quantum Mater. **3**, 46 (2018).

[119]   D. Kong et al., *Rapid Surface Oxidation as a Source of Surface Degradation Factor for Bi_2Se_3*, ACS Nano **5**, 4698–4703 (2011).

[120]   A. J. Green, S. Dey, Y. Q. An, B. O'Brien, S. O'Mullane, B. Thiel, and A. C. Diebold, *Surface oxidation of the topological insulator Bi_2Se_3*, . Vac. Sci. Technol. A **34**, 061403 (2016).

[121]   M. Bianchi, D. Guan, S. Bao, J. Mi, B. B. Iversen, P. D. King, and P. Hofmann, *Coexistence of the topological state and a two-dimensional electron gas on the surface of Bi_2Se_3*, Nat Comm. **1**, 128 (2010).

[122]   J. Suh, D. Fu, X. Liu, J. K. Furdyna, K. M. Yu, W. Walukiewicz, and J. Wu, *Fermi-level stabilization in the topological insulators Bi_2Se_3 and Bi_2Te_3: Origin of the surface electron gas*, Phys. Rev. B **89**, 115307 (2014).

[123] T. Mayer, H. Werner, F. Schmid, R. Diaz-Pardo, J. Fujii, I. Vobornik, C. H. Back, M. Kronseder, and D. Bougeard, *Transport properties of band engineered p−n heterostructures of epitaxial* $Bi_2Se_3/(Bi_{1-x}Sb_x)_2(Te_{1-y}Se_y)_3$ *topological insulators*, Phys. Rev. Materials **5**, 014202 (2021).

[124] B. Ryu, B.-S. Kim, J. E. Lee, S.-J. Joo, B.-K. Min, H. Lee, S. Park, and M.-W. Oh, *Prediction of the band structures of* Bi_2Te_3*-related binary and Sb/Se-doped ternary thermoelectric materials*, J. Korean Phys. Soc. **68**, 115–120 (2016).

[125] Z. Zhang et al., *Transport properties of* Sb_2Te_3/Bi_2Te_3 *topological insulator heterostructures*, Phys. Status Solidi (RRL) **7**, 142–144 (2013).

[126] M. Eschbach et al., *Realization of a vertical topological p–n junction in epitaxial* Sb_2Te_3/Bi_2Te_3 *heterostructures*, Nat. Commun. **6**, 8816 (2015).

[127] B. Skinner, T. Chen, and B. I. Shklovskii, *Why Is the Bulk Resistivity of Topological Insulators So Small?*, Phys. Rev. Lett. **109**, 176801 (2012).

[128] T. Arakane, T. Sato, S. Souma, K. Kosaka, K. Nakayama, M. Komatsu, T. Takahashi, Z. Ren, K. Segawa, and Y. Ando, *Tunable Dirac cone in the topological insulator* $Bi_{2-x}Sb_xTe_{3-y}Se_y$, Nat. Commun. **3**, 636 (2012).

[129] B. Skinner, T. Chen, and B. I. Shklovskii, *Effects of bulk charged impurities on the bulk and surface transport in three-dimensional topological insulators*, J. Exp. Theor. Phys. **117**, 579–592 (2013).

[130] T. Chen and B. I. Shklovskii, *Anomalously small resistivity and thermopower of strongly compensated semiconductors and topological insulators*, Phys. Rev. B **87**, 165119 (2013).

[131] C. W. Rischau, A. Ubaldini, E. Giannini, and C. J. van der Beek, *Charge puddles in a completely compensated topological insulator*, New J. Phys. **18**, 073024 (2016).

[132] N. Borgwardt, J. Lux, I. Vergara, Z. Wang, A. A. Taskin, K. Segawa, P. H. M. van Loosdrecht, Y. Ando, A. Rosch, and M. Grüninger, *Self-organized charge puddles in a three-dimensional topological material*, Phys. Rev. B **93**, 245149 (2016).

[133] M. Brahlek, N. Koirala, N. Bansal, and S. Oh, *Transport properties of topological insulators: Band bending, bulk metal-to-insulator transition, and weak anti-localization*, Solid State Commun. **215-216**, 54–62 (2015).

[134] J. Wang, C. Gorini, K. Richter, Z. Wang, Y. Ando, and D. Weiss, *Two-Dimensional-Dirac Surface States and Bulk Gap Probed via Quantum Capacitance in a Three-Dimensional Topological Insulator*, Nano Lett. **20**, 8493–8499 (2020).

[135] T. Knispel, W. Jolie, N. Borgwardt, J. Lux, Z. Wang, Y. Ando, A. Rosch, T. Michely, and M. Grüninger, *Charge puddles in the bulk and on the surface of the topological insulator* $BiSbTeSe_2$ *studied by scanning tunneling microscopy and optical spectroscopy*, Phys. Rev. B **96**, 195135 (2017).

Bibliography

[136] O. Breunig, Z. Wang, A. A. Taskin, J. Lux, A. Rosch, and Y. Ando, *Gigantic negative magnetoresistance in the bulk of a disordered topological insulator*, Nat. Commun. **8**, 15545 (2017).

[137] B. F. Gao, P. Gehring, M. Burghard, and K. Kern, *Gate-controlled linear magnetoresistance in thin Bi_2Se_3 sheets*, Appl. Phys. Lett. **100**, 212402 (2012).

[138] W.-Y. Shan, H.-Z. Lu, and S.-Q. Shen, *Spin-orbit scattering in quantum diffusion of massive dirac fermions*, Phys. Rev. B **86**, 125303 (2012).

[139] H.-Z. Lu and S.-Q. Shen, *Finite-Temperature Conductivity and Magnetoconductivity of Topological Insulators*, Phys. Rev. Lett. **112**, 146601 (2014).

[140] J. Chen, X. Y. He, K. H. Wu, Z. Q. Ji, L. Lu, J. R. Shi, J. H. Smet, and Y. Q. Li, *Tunable surface conductivity in Bi_2Se_3 revealed in diffusive electron transport*, Phys. Rev. B **83**, 241304 (2011).

[141] J. Wang, A. M. DaSilva, C.-Z. Chang, K. He, J. K. Jain, N. Samarth, X.-C. Ma, Q.-K. Xue, and M. H. W. Chan, *Evidence for electron-electron interaction in topological insulator thin films*, Phys. Rev. B **83**, 245438 (2011).

[142] M. Liu et al., *Electron interaction-driven insulating ground state in Bi_2Se_3 topological insulators in the two-dimensional limit*, Phys. Rev. B **83**, 165440 (2011).

[143] X. Zhang, J. M. Woods, J. J. Cha, and X. Shi, *Crossover between weak antilocalization and weak localization in few-layer WTe_2: Role of electron-electron interactions*, Phys. Rev. B **102**, 115161 (2020).

[144] I. Garate and L. Glazman, *Weak localization and antilocalization in topological insulator thin films with coherent bulk-surface coupling*, Phys. Rev. B **86**, 035422 (2012).

[145] H. Steinberg, J.-B. Laloë, V. Fatemi, J. S. Moodera, and P. Jarillo-Herrero, *Electrically tunable surface-to-bulk coherent coupling in topological insulator thin films*, Phys. Rev. B **84**, 233101 (2011).

[146] M. Brahlek, N. Koirala, M. Salehi, N. Bansal, and S. Oh, *Emergence of Decoupled Surface Transport Channels in Bulk Insulating Bi_2Se_3 Thin Films*, Phys. Rev. Lett. **113**, 026801 (2014).

[147] W. J. Wang, K. H. Gao, and Z. Q. Li, *Thickness-dependent transport channels in topological insulator Bi_2Se_3 thin films grown by magnetron sputtering*, Sci. Rep. **6**, 25291 (2016).

[148] F. Yang, A. A. Taskin, S. Sasaki, K. Segawa, Y. Ohno, K. Matsumoto, and Y. Ando, *Dual-Gated Topological Insulator Thin-Film Device for Efficient Fermi-Level Tuning*, ACS Nano **9**, 4050–4055 (2015).

[149] V. Fatemi et al., *Electrostatic Coupling between Two Surfaces of a Topological Insulator Nanodevice*, Phys. Rev. Lett. **113**, 206801 (2014).

[150] Y. Xu, I. Miotkowski, and Y. P. Chen, *Quantum transport of two-species dirac fermions in dual-gated three-dimensional topological insulators*, Nat. Commun. **7**, 11434 (2016).

[151] Banerjee, Abhishek and Sundaresh, Ananthesh and Biswas, Sangram and Ganesan, R. and Sen, Diptiman and Anil Kumar, P. S., *Topological insulator n–p–n junctions in a magnetic field*, Nanoscale **11**, 5317–5324 (2019).

[152] K. S. Novoselov, A. K. Geim, S. V. Morozov, D. Jiang, Y. Zhang, S. V. Dubonos, I. V. Grigorieva, and A. A. Firsov, *Electric Field Effect in Atomically Thin Carbon Films*, Science **306**, 666–669 (2004).

[153] K. S. Novoselov, A. K. Geim, S. V. Morozov, D. Jiang, M. I. Katsnelson, I. V. Grigorieva, S. V. Dubonos, and A. A. Firsov, *Two-dimensional gas of massless Dirac fermions in graphene*, Nature **438**, 197–200 (2005).

[154] R. Yoshimi, A. Tsukazaki, Y. Kozuka, J. Falson, K. S. Takahashi, J. G. Checkelsky, N. Nagaosa, M. Kawasaki, and Y. Tokura, *Quantum Hall effect on top and bottom surface states of topological insulator $(Bi_{1-x}Sb_x)_2Te_3$ films*, Nat. Commun. **6**, 6627 (2015).

[155] A. L. Yeats, Y. Pan, A. Richardella, P. J. Mintun, N. Samarth, and D. D. Awschalom, *Persistent optical gating of a topological insulator*, Sci. Adv. **1** (2015).

[156] D. Kong et al., *Ambipolar field effect in the ternary topological insulator $(Bi_xSb_{1--x})_2Te_3$ by composition tuning*, Nat. Nanotechnol. **6**, 705–709 (2011).

[157] H.-T. He, G. Wang, T. Zhang, I.-K. Sou, G. K. L. Wong, J.-N. Wang, H.-Z. Lu, S.-Q. Shen, and F.-C. Zhang, *Impurity Effect on Weak Antilocalization in the Topological Insulator Bi_2Te_3*, Phys. Rev. Lett. **106**, 166805 (2011).

[158] Z. J. Yue, X. L. Wang, Y. Du, S. M. Mahboobeh, F. F. Yun, Z. X. Cheng, and S. X. Dou, *Giant and anisotropic magnetoresistances in p-type Bi-doped Sb_2Te_3 bulk single crystals*, EPL (Europhys. Lett.) **100**, 17014 (2012).

[159] Y. S. Kim, M. Brahlek, N. Bansal, E. Edrey, G. A. Kapilevich, K. Iida, M. Tanimura, Y. Horibe, S.-W. Cheong, and S. Oh, *Thickness-dependent bulk properties and weak antilocalization effect in topological insulator Bi_2Se_3*, Phys. Rev. B **84**, 073109 (2011).

[160] P. H. Le, P.-T. Liu, C. W. Luo, J.-Y. Lin, and K. H. Wu, *Thickness-dependent magnetotransport properties and terahertz response of topological insulator Bi_2Te_3 thin films*, J. Alloys Compd. **692**, 972–979 (2017).

[161] S.-P. Chiu and J.-J. Lin, *Weak antilocalization in topological insulator Bi_2Te_3 microflakes*, Phys. Rev. B **87**, 035122 (2013).

[162] V. M. Pereira, C. N. Wu, C.-A. Knight, A. Choa, L. H. Tjeng, and S. G. Altendorf, *Interfacing topological insulators and ferrimagnets: Bi_2Te_3 and Fe_3O_4 heterostructures grown by molecular beam epitaxy*, APL Mat. **8**, 071114 (2020).

[163] P. D. Dresselhaus, C. M. A. Papavassiliou, R. G. Wheeler, and R. N. Sacks, *Observation of spin precession in GaAs inversion layers using antilocalization*, Phys. Rev. Lett. **68**, 106–109 (1992).

[164] S. Pedersen, C. B. Sørensen, A. Kristensen, P. E. Lindelof, L. E. Golub, and N. S. Averkiev, *Weak localization in* $Al_{0.5}Ga_{0.5}As$/GaAs *p-type quantum wells*, Phys. Rev. B **60**, 4880–4882 (1999).

[165] T. Hassenkam, S. Pedersen, K. Baklanov, A. Kristensen, C. B. Sorensen, P. E. Lindelof, F. G. Pikus, and G. E. Pikus, *Spin splitting and weak localization in (110) GaAs/* $Al_xGa_{1-x}As$ *quantum wells*, Phys. Rev. B **55**, 9298–9301 (1997).

[166] J. B. Miller, D. M. Zumbühl, C. M. Marcus, Y. B. Lyanda-Geller, D. Goldhaber-Gordon, K. Campman, and A. C. Gossard, *Gate-Controlled Spin-Orbit Quantum Interference Effects in Lateral Transport*, Phys. Rev. Lett. **90**, 076807 (2003).

[167] R. K. Gopal, S. Singh, A. Mandal, J. Sarkar, and C. Mitra, *Topological delocalization and tuning of surface channel separation in* Bi_2Se_2Te *Topological Insulator Thin films*, Sci. Rep. **7**, 4924 (2017).

[168] A. Roy, S. Guchhait, S. Sonde, R. Dey, T. Pramanik, A. Rai, H. C. P. Movva, L. Colombo, and S. K. Banerjee, *Two-dimensional weak anti-localization in* Bi_2Te_3 *thin film grown on Si(111)-(7×7) surface by molecular beam epitaxy*, Appl. Phys. Lett. **102**, 163118 (2013).

[169] H.-Z. Lu and S.-Q. Shen, *Weak antilocalization and interaction-induced localization of Dirac and Weyl Fermions in topological insulators and semimetals*, Chin. Phys. B **25**, 117202 (2016).

[170] H.-Z. Lu and S.-Q. Shen, *Weak antilocalization and localization in disordered and interacting Weyl semimetals*, Phys. Rev. B **92**, 035203 (2015).

[171] Y.-H. Song et al., *Observation of Coulomb gap in the quantum spin Hall candidate single-layer 1T'-WTe2*, Nat. Commun. **9**, 4071 (2018).

[172] A. H. Castro Neto, F. Guinea, N. M. R. Peres, K. S. Novoselov, and A. K. Geim, *The electronic properties of graphene*, Rev. Mod. Phys. **81**, 109–162 (2009).

[173] V. N. Kotov, B. Uchoa, V. M. Pereira, F. Guinea, and A. H. Castro Neto, *Electron-Electron Interactions in Graphene: Current Status and Perspectives*, Rev. Mod. Phys. **84**, 1067–1125 (2012).

[174] B. L. Altshuler, A. G. Aronov, and P. A. Lee, *Interaction Effects in Disordered Fermi Systems in Two Dimensions*, Phys. Rev. Lett. **44**, 1288–1291 (1980).

[175] J. Liao, Y. Ou, H. Liu, K. He, X. Ma, Q.-K. Xue, and Y. Li, *Enhanced electron dephasing in three-dimensional topological insulators*, Nat. Commun. **8**, 16071 (2017).

[176] A. Banerjee, A. Sundaresh, R. Ganesan, and P. S. Anil Kumar, *Spatially varying electronic dephasing in three-dimensional topological insulators*, Phys. Rev. B **98**, 155423 (2018).

[177] G. Bergmann, *Weak localization in thin films: a time-of-flight experiment with conduction electrons*, Phys. Rep. **107**, 1–58 (1984).

[178] B. L. Altshuler, A. G. Aronov, A. I. Larkin, and D. E. Khmelnitskil, *Anomalous magnetoresistance in semiconductors*, Zh. Eksp. Teor. Fiz. **81**, 768 − 783(1981).

[179] G. M. Stephen, O. A. Vail, J. Lu, W. A. Beck, P. J. Taylor, and A. L. Friedman, *Weak Antilocalization and Anisotropic Magnetoresistance as a Probe of Surface States in Topological $Bi_2Te_xSe_{3x}$ Thin Films*, Sci. Rep. **10**, 4845 (2020).

[180] V. E. Sacksteder, K. B. Arnardottir, S. Kettemann, and I. A. Shelykh, *Topological effects on the magnetoconductivity in topological insulators*, Phys. Rev. B **90**, 235148 (2014).

[181] G. Tkachov and E. M. Hankiewicz, *Weak antilocalization in hgte quantum wells and topological surface states: massive versus massless dirac fermions*, Phys. Rev. B **84**, 035444 (2011).

[182] C. J. Lin et al., *Parallel field magnetoresistance in topological insulator thin films*, Phys. Rev. B **88**, 041307 (2013).

[183] P. Adroguer, D. Carpentier, J. Cayssol, and E. Orignac, *Diffusion at the surface of topological insulators*, New J. Phys. **14**, 103027 (2012).

[184] R. S. Akzyanov and A. L. Rakhmanov, *Surface charge conductivity of a topological insulator in a magnetic field: The effect of hexagonal warping*, Phys. Rev. B **97**, 075421 (2018).

[185] S.-H. Zheng, H.-J. Duan, J.-K. Wang, J.-Y. Li, M.-X. Deng, and R.-Q. Wang, *Origin of planar Hall effect on the surface of topological insulators: Tilt of Dirac cone by an in-plane magnetic field*, Phys. Rev. B **101**, 041408 (2020).

[186] R. Dey, T. Pramanik, A. Roy, A. Rai, S. Guchhait, S. Sonde, H. C. P. Movva, L. Colombo, L. F. Register, and S. K. Banerjee, *Strong spin-orbit coupling and Zeeman spin splitting in angle dependent magnetoresistance of Bi_2Te_3*, Appl. Phys. Lett. **104**, 223111 (2014).

[187] B. A. Assaf, T. Cardinal, P. Wei, F. Katmis, J. S. Moodera, and D. Heiman, *Linear magnetoresistance in topological insulator thin films: Quantum phase coherence effects at high temperatures*, Appl. Phys. Lett. **102**, 012102 (2013).

[188] S. X. Zhang, R. D. McDonald, A. Shekhter, Z. X. Bi, Y. Li, Q. X. Jia, and S. T. Picraux, *Magneto-resistance up to 60 Tesla in topological insulator Bi2Te3 thin films*, Appl. Phys. Lett. **101**, 202403 (2012).

[189] H. Köhler and E. Wöchner, *The g-factor of the conduction electrons in $BiSe_3$*, Phys. Status solidi B **67**, 665–675 (1975).

[190] Y.-S. Fu, T. Hanaguri, K. Igarashi, M. Kawamura, M. S. Bahramy, and T. Sasagawa, *Observation of Zeeman effect in topological surface state with distinct material dependence*, Nat. Commun. **7**, 10829 (2016).

[191] H.-C. Liu, H.-Z. Lu, H.-T. He, B. Li, S.-G. Liu, Q. L. He, G. Wang, I. K. Sou, S.-Q. Shen, and J. Wang, *Tunable Interaction-Induced Localization of Surface Electrons in Antidot Nanostructured Bi_2Te_3 Thin Films*, ACS Nano **8**, 9616–9621 (2014).

[192] Y. Lyanda-Geller, *Quantum Interference and Electron-Electron Interactions at Strong Spin-Orbit Coupling in Disordered Systems*, Phys. Rev. Lett. **80**, 4273–4276 (1998).

[193] J. Lin, S. Hsu, J. Lue, and P. Sheng, *Spin–orbit scattering effect on electron–electron interactions in disordered metals*, J. Phys. Chem. Solids **62**, 1813–1818 (2001).

[194] F. M. Mayeya and M. A. Howson, *Quantum interference and electron interaction effects in CaAl(Au,Ag) amorphous alloys*, J. Condens. Matter Phys. **4**, 9355–9366 (1992).

[195] B. Altshuler, A. Aronov, and A. Zuzin, *Spin relaxation and interaction effects in the disordered conductors*, Solid State Commun. **44**, 137–139 (1982).

[196] A. J. Millis and P. A. Lee, *Spin-orbit and paramagnon effects on magnetoconductance and tunneling*, Phys. Rev. B **30**, 6170–6173 (1984).

[197] S. J. Poon, K. M. Wong, and A. J. Drehman, *Localization and electron-interaction effects in metallic glasses*, Phys. Rev. B **31**, 1668–1670 (1985).

[198] A. Sahnoune, J. O. Ström-Olsen, and H. E. Fischer, *Influence of spin-orbit scattering on the magnetoresistance due to enhanced electron-electron interactions*, Phys. Rev. B **46**, 10035–10040 (1992).

[199] P. Lindqvist, Ö. Rapp, A. Sahnoune, and J. O. Ström-Olsen, *Magnetoresistance due to enhanced electron-electron interactions in amorphous $Ca_{70}(Mg,Al)_{30}$*, Phys. Rev. B **41**, 3841–3843 (1990).

[200] M. Li, Z. Wang, L. Yang, X. P. Gao, and Z. Zhang, *From linear magnetoresistance to parabolic magnetoresistance in Cu and Cr-doped topological insulator Bi_2Se_3 films*, J. Phys. Chem. Solids **128**, 331–336 (2019).

[201] L. Wei, Z. Wang, Z. Zhang, C.-W. Liu, and X. P. A. Gao, *Enhanced linear magneto-resistance near the Dirac point in topological insulator $Bi_2(Te_{1x}Se_x)_3$ nanowires*, Nano Res. **13**, 1332–1338 (2020).

[202] H. Tang, D. Liang, R. L. J. Qiu, and X. P. A. Gao, *Two-Dimensional Transport-Induced Linear Magneto-Resistance in Topological Insulator Bi_2Se_3 Nanoribbons*, ACS Nano **5**, 7510–7516 (2011).

[203] G. Zhang, H. Qin, J. Chen, X. He, L. Lu, Y. Li, and K. Wu, *Growth of Topological Insulator Bi_2Se_3 Thin Films on $SrTiO_3$ with Large Tunability in Chemical Potential*, Adv. Funct. Mater. **21**, 2351–2355 (2011).

[204] D. Nandi et al., *Signatures of long-range-correlated disorder in the magnetotransport of ultrathin topological insulators*, Phys. Rev. B **98**, 214203 (2018).

190

[205] H. Zhang, H. Li, H. Wang, G. Cheng, H. He, and J. Wang, *Linear positive and negative magnetoresistance in topological insulator Bi₂Se₃ flakes*, Appl. Phys. Lett. **113**, 113503 (2018).

[206] A. Narayanan et al., *Linear Magnetoresistance Caused by Mobility Fluctuations in n-Doped* Cd_3As_2, Phys. Rev. Lett. **114**, 117201 (2015).

[207] X. Wang, Y. Du, S. Dou, and C. Zhang, *Room Temperature Giant and Linear Magnetoresistance in Topological Insulator* Bi_2Te_3 *Nanosheets*, Phys. Rev. Lett. **108**, 266806 (2012).

[208] T. Liang, Q. Gibson, M. N. Ali, M. Liu, R. J. Cava, and N. P. Ong, *Ultrahigh mobility and giant magnetoresistance in the Dirac semimetal Cd₃As₂*, Nat. Mater. **14**, 280–284 (2015).

[209] N. V. Kozlova, N. Mori, O. Makarovsky, L. Eaves, Q. D. Zhuang, A. Krier, and A. Patanè, *Linear magnetoresistance due to multiple-electron scattering by low-mobility islands in an inhomogeneous conductor*, Nat. Commun. **3**, 1097 (2012).

[210] A. A. Abrikosov, *Quantum magnetoresistance*, Phys. Rev. B **58**, 2788–2794 (1998).

[211] M. M. Parish and P. B. Littlewood, *Non-saturating magnetoresistance in heavily disordered semiconductors*, Nature **426**, 162–165 (2003).

[212] M. M. Parish and P. B. Littlewood, *Classical magnetotransport of inhomogeneous conductors*, Phys. Rev. B **72**, 094417 (2005).

[213] V. Harimohan, A. Bharathi, P. Babu, R. Rajaraman, P. Magudapathy, C. David, and C. Sundar, *Validity of Kohler's rule for the magneto-resistance in pristine and irradiated NbAs₂*, Solid State Commun. **305**, 113734 (2020).

[214] J. Hu et al., *Evidence of topological nodal-line fermions in zrsise and zrsite*, Phys. Rev. Lett. **117**, 016602 (2016).

[215] L. Guo et al., *Extreme magnetoresistance and SdH oscillation in compensated semimetals of NbSb₂ single crystals*, J. Appl. Phys. **123**, 155103 (2018).

[216] P. Adroguer, W. E. Liu, D. Culcer, and E. M. Hankiewicz, *Conductivity corrections for topological insulators with spin-orbit impurities: Hikami-Larkin-Nagaoka formula revisited*, Phys. Rev. B **92**, 241402 (2015).

[217] W. E. Liu, E. M. Hankiewicz, and D. Culcer, *Weak Localization and Antilocalization in Topological Materials with Impurity Spin-Orbit Interactions*, Materials **10**, 807 (2017).

[218] L. J. van der Pauw, *A method of measuring the resistivity and Hall coefficient on lamellae of arbitrary shape*, Philips Techn. Rev. **20**, 220–224 (1958).

[219] F. Schmid, *Electronic transport study of band-structure engineered 3D tetradymite topological insulators*, Master thesis at the University of Regensburg (2021).

[220] Y. Zhang et al., *Crossover of the three-dimensional topological insulator Bi_2Se_3 to the two-dimensional limit*, Nat. Phys. **6**, 584–588 (2010).

[221] Y.-Y. Li et al., *Intrinsic Topological Insulator Bi_2Te_3 Thin Films on Si and Their Thickness Limit*, Adv. Mater. **22**, 4002–4007 (2010).

[222] N. W. Tideswell, F. H. Kruse, and J. D. McCullough, *The crystal structure of antimony selenide, Sb_2Se_3*, Acta Crystallogr. **10**, 99–102 (1957).

[223] Y.-J. Chen, Y.-C. Jhong, P.-Y. Chuang, C.-W. Chong, J.-C.-A. Huang, V. Marchenkov, and H.-C. Han, *The heterostructure and electrical properties of Sb_2Se_3/Bi_2Se_3 grown by molecular beam epitaxy*, Chin. J. Phys. **62**, 65–71 (2019).

[224] Y. Zhou et al., *Thin-film Sb_2Se_3 photovoltaics with oriented one-dimensional ribbons and benign grain boundaries*, Nat. Photonics **9**, 409–415 (2015).

[225] S. Das, A. Sirohi, G. Kumar Gupta, S. Kamboj, A. Vasdev, S. Gayen, P. Gup-tasarma, T. Das, and G. Sheet, *Discovery of highly spin-polarized conducting surface states in the strong spin-orbit coupling semiconductor Sb_2Se_3*, Phys. Rev. B **97**, 235306 (2018).

[226] R. Vadapoo, S. Krishnan, H. Yilmaz, and C. Marin, *Electronic structure of antimony selenide (Sb_2Se_3) from GW calculations*, Phys. Status Solidi B **248**, 700–705 (2011).

[227] Y. Satake, J. Shiogai, D. Takane, K. Yamada, K. Fujiwara, S. Souma, T. Sato, T. Takahashi, and A. Tsukazaki, *Fermi-level tuning of the Dirac surface state in $(Bi_{1--x}Sb_x)_2Se_3$ thin films*, J. Condens. Matter Phys. **30**, 085501 (2018).

[228] Z. Ren, A. A. Taskin, S. Sasaki, K. Segawa, and Y. Ando, *Optimizing $Bi_{2-x}Sb_xTe_{3-y}Se_y$ solid solutions to approach the intrinsic topological insulator regime*, Phys. Rev. B **84**, 165311 (2011).

[229] A. Torane, K. Rajpure, and C. Bhosale, *Preparation and characterization of electrodeposited Sb_2Se_3 thin films*, Mater. Chem. Phys. **61**, 219–222 (1999).

[230] Y. Rodríguez-Lazcano, Y. Peña, M. Nair, and P. Nair, *Polycrystalline thin films of antimony selenide via chemical bath deposition and post deposition treatments*, Thin Solid Films **493**, 77–82 (2005).

[231] C. N. Savory and D. O. Scanlon, *The complex defect chemistry of antimony selenide*, J. Mater. Chem. A **7**, 10739–10744 (2019).

[232] C. E. Patrick and F. Giustino, *Structural and Electronic Properties of Semiconductor-Sensitized Solar-Cell Interfaces*, Adv. Funct. Mater. **21**, 4663–4667 (2011).

[233] M. R. Filip, C. E. Patrick, and F. Giustino, *GW quasiparticle band structures of stibnite, antimonselite, bismuthinite, and guanajuatite*, Phys. Rev. B **87**, 205125 (2013).

[234] C. H. Lee et al., *Metal–insulator transition in variably doped $(Bi_{1x}Sb_x)_2Se_3$ nanosheets*, Nanoscale **5**, 4337–4343 (2013).

[235] J. Liu and D. Vanderbilt, *Topological phase transitions in $(Bi_{1-x}In_x)_2Se_3$ and $(Bi_{1-x}Sb_x)_2Se_3$*, Phys. Rev. B **88**, 224202 (2013).

[236] W. Li, X.-Y. Wei, J.-X. Zhu, C. S. Ting, and Y. Chen, *Pressure-induced topological quantum phase transition in Sb_2Se_3*, Phys. Rev. B **89**, 035101 (2014).

[237] W. Liu, X. Peng, C. Tang, L. Sun, K. Zhang, and J. Zhong, *Anisotropic interactions and strain-induced topological phase transition in Sb_2Se_3 and Bi_2Se_3*, Phys. Rev. B **84**, 245105 (2011).

[238] A. Bera, K. Pal, D. V. S. Muthu, S. Sen, P. Guptasarma, U. V. Waghmare, and A. K. Sood, *Sharp Raman Anomalies and Broken Adiabaticity at a Pressure Induced Transition from Band to Topological Insulator in* Sb_2Se_3, Phys. Rev. Lett. **110**, 107401 (2013).

[239] I. Efthimiopoulos, J. Zhang, M. Kucway, C. Park, R. C. Ewing, and Y. Wang, *Sb_2se_3 under pressure*, Sci. Rep. **3**, 2665 (2013).

[240] I. Efthimiopoulos, C. Buchan, and Y. Wang, *Structural properties of Sb2S3 under pressure: evidence of an electronic topological transition*, Scientific Reports **6**, 24246 (2016).

[241] G. Cao, H. Liu, J. Liang, L. Cheng, D. Fan, and Z. Zhang, *Rhombohedral* Sb_2Se_3 *as an intrinsic topological insulator due to strong van der Waals interlayer coupling*, Phys. Rev. B **97**, 075147 (2018).

[242] A. V. Matetskiy, V. V. Mararov, I. A. Kibirev, A. V. Zotov, and A. A. Saranin, *Trivial band topology of ultra-thin rhombohedral Sb_2Se_3 grown on Bi_2Se_3*, J. Condens. Matter Phys. **32**, 165001 (2020).

[243] A. A. Taskin, S. Sasaki, K. Segawa, and Y. Ando, *Manifestation of Topological Protection in Transport Properties of Epitaxial* Bi_2Se_3 *Thin Films*, Phys. Rev. Lett. **109**, 066803 (2012).

[244] N. H. Tu, Y. Tanabe, Y. Satake, K. K. Huynh, and K. Tanigaki, *In-plane topological p-n junction in the three-dimensional topological insulator $Bi_{2-x}Sb_xTe_{3-y}Se_y$*, Nat. Commun. **7**, 13763 (2016).

[245] K. M. M. Habib, R. N. Sajjad, and A. W. Ghosh, *Chiral Tunneling of Topological States: Towards the Efficient Generation of Spin Current Using Spin-Momentum Locking*, Phys. Rev. Lett. **114**, 176801 (2015).

[246] Y. Xie, Y. Tan, and A. W. Ghosh, *Spintronic signatures of Klein tunneling in topological insulators*, Phys. Rev. B **96**, 205151 (2017).

[247] D. W. Reagor and V. Y. Butko, *Highly conductive nanolayers on strontium titanate produced by preferential ion-beam etching*, Nature Materials **4**, 593–596 (2005).

[248] H. Gross, N. Bansal, Y.-S. Kim, and S. Oh, *In situ study of emerging metallicity on ion-bombarded $SrTiO_3$ surface*, J. Appl. Phys. **110**, 073704 (2011).

Bibliography

[249] M.-J. Jin, D. Choe, S. Y. Lee, J. Park, J. Jo, I. Oh, S.-I. Kim, S.-H. Baek, C. Jeon, and J.-W. Yoo, *Probing surface electronic properties of a patterned conductive STO by reactive ion etching*, Appl. Surf. Sci. **466**, 730–736 (2019).

[250] H. Werner, *Band structure engineering of 3D topological insulator heterostructures*, Master thesis at the University of Regensburg (2020).

List of publications

4. "Transport properties of band engineered p-n heterostructures of epitaxial $Bi_2Se_3/(Bi_{1-x}Sb_x)_2(Te_{1-y}Se_y)_3$ topological insulators", **T. Mayer**, H. Werner, F. Schmid, R. Diaz-Pardo, J. Fujii, I. Vobornik, C. H. Back, M. Kronseder, and D. Bougeard, *Phys. Rev. Materials 5, 014202* (2021)

3. "Magnetic damping in poly-crystalline Co 25 Fe 75 : Ferromagnetic resonance vs. spin wave propagation experiments", H. S. Körner, M. A. W. Schoen, **T. Mayer**, M. M. Decker, J. Stigloher, T. Weindler, T. N. G. Meier, M. Kronseder, and C. H. Back, *Appl. Phys. Lett. 111, 132406* (2017)

2. "Towards carbon nanotube growth into superconducting microwave resonator geometries", S. Blien, K. J. G. Götz, P. L. Stiller, **T. Mayer**, T. Huber, O. Vavra, and A. K. Hüttel, *Phys. Status Solidi B, 253: 2385-2390* (2016)

1. "Co-sputtered MoRe thin films for carbon nanotube growth-compatible supercon-ducting coplanar resonators", K. J. G. Götz, S. Blien, P. L. Stiller, O. Vavra, **T. Mayer**, T. Huber, T. N. G. Meier, M. Kronseder, Ch. Strunk, and A. K. Hüttel, *Nanotechnology 27 135202* (2016)

List of publications

Acknowledgements/Danksagung

Zuletzt möchte ich mich bei den vielen Personen bedanken, ohne deren Unterstützung diese Arbeit nicht möglich gewesen wäre. Danke an alle, die mit ihrem Mitwirken nicht nur zu den erreichten Ergebnissen, sondern vor allem auch zu meiner persönlichen Entwicklung und nicht zuletzt zu einer herausfordernden, lehrreichen und generell tollen Zeit beigetragen haben.

Allen voran möchte ich mich bei **Prof. Dr. Dominique Bougeard** bedanken für die Möglichkeit diese Dissertation durchzuführen, die herzliche Aufnahme in seine Gruppe, für das Vertrauen, das er mir entgegen gebracht hat und für sein außergewöhnliches Bemühen immer den bestmöglichen Rahmen für wissenschaftliche Arbeit zu schaffen. Danke darüber hinaus für die vielen, teilweise stundenlangen Diskussionen über die neuesten Ergebnisse, die wertvolle Hilfe bei deren Aufarbeitung und die oft notwendige und immer hilfreiche Anleitung bei deren Einordnung. Ich bedanke mich außerdem für das ehrliche und besondere Interesse, das er nicht nur für die wissenschaftliche Arbeit, sondern speziell auch an jeder Person in seiner Gruppe zeigt, was zu einer außergewöhnlichen Arbeitsatmosphäre beiträgt.

Ein weiterer großer Dank gilt **Dr. Matthias Kronseder**. Vielen Dank für das Wachsen von hunderten Proben, nicht zählbaren Diskussionen über die Resultate und mindestens ebenso vielen Gesprächen über Dinge abseits der Arbeit. Seine Freude an der Wissenschaft und seine darauf beruhende Arbeitswut war mit Sicherheit ansteckend und hat kombiniert mit seinem Ideenreichtum ganz entscheidend zu dieser Arbeit beigetragen. Danke aber besonders für die freundschaftliche Ebene unserer Zusammenarbeit, die die letzten Jahre extrem bereichert hat. Ohne sein Mitwirken hätte meine Arbeit nicht nur weniger Resultate hervorgebracht, sondern vor allem auch weniger Spaß gemacht.